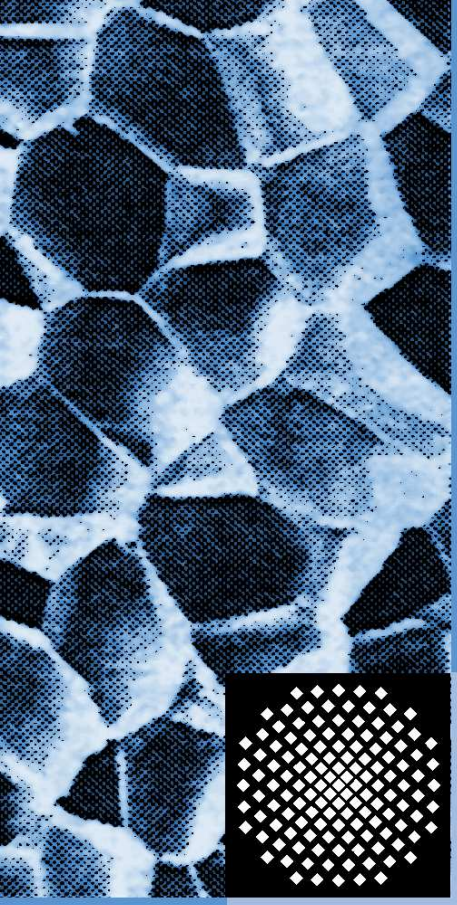

Universität Stuttgart
Germany

Institut für Mechanik (Bauwesen)
Lehrstuhl für Kontinuumsmechanik
Prof. Dr.-Ing. W. Ehlers

Extended Modelling of the Multiphasic Human Brain Tissue with Application to Drug-Infusion Processes

Arndt Wagner

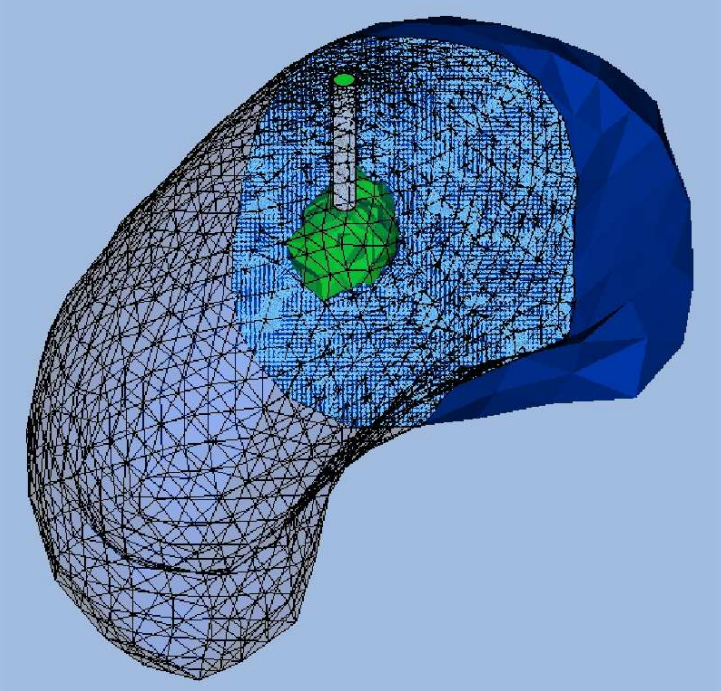

Report No.: II-27 (2014)

Extended Modelling of the Multiphasic Human Brain Tissue with Application to Drug-Infusion Processes

Von der Fakultät Bau- und Umweltingenieurwissenschaften
der Universität Stuttgart zur Erlangung der Würde
eines Doktor-Ingenieurs (Dr.-Ing.)
genehmigte Abhandlung

vorgelegt von

Dipl.-Ing. Arndt Wagner

aus
Waiblingen

Hauptberichter:	Prof. Dr.-Ing. Wolfgang Ehlers
Mitberichter:	Prof. Dr.-Ing. Tim Ricken

Tag der mündlichen Prüfung: 14. Juli 2014

Institut für Mechanik (Bauwesen) der Universität Stuttgart
Lehrstuhl für Kontinuumsmechanik
Prof. Dr.-Ing. W. Ehlers
2014

Report No. II-27
Institut für Mechanik (Bauwesen)
Lehrstuhl für Kontinuumsmechanik
Universität Stuttgart, Germany, 2014

Editor:
Prof. Dr.-Ing. W. Ehlers

Institut für Mechanik (Bauwesen)
Lehrstuhl für Kontinuumsmechanik
Universität Stuttgart
Pfaffenwaldring 7
70569 Stuttgart, Germany

ISBN 978 – 3 – 937399 – 27 – 5
(D 93 – Dissertation, Universität Stuttgart)

Acknowledgements

The work presented in this doctoral thesis was developed during my profession as an assistant lecturer and research assistant at the Institute of Applied Mechanics (Civil Engineering) Chair of Continuum Mechanics, at the University of Stuttgart. At this point, I want to take the opportunity to gratefully acknowledge numerous people who contributed in many ways to the realisation of this work.

First of all, I would like to express my deepest appreciation to Professor Wolfgang Ehlers for giving me the opportunity to prepare my thesis under his conscionable supervision and constant scientific support at his institute. Without his broad expertise this dissertation would certainly not have been possible. I am also particularly grateful to Professor Tim Ricken for taking the first co-chair in my dissertation procedure as well as for many fruitful conversations at conferences. Furthermore, I want to thank Professor Bernd Markert and Professor Oliver Röhrle for most valuable discussions which helped me to quickly enter into various related topics.

I will always remember Oliver Klar and his contagious enthusiasm. His decisive offer of a student assistant position initially inspired me to head into the field of mechanics. In my early days, Dr.-Ing. Nils Karajan supervised and taught me many important routine matters at the institute. Even today, I am very grateful to benefit from his broad knowledge. Moreover, I have truly enjoyed the outstanding atmosphere among colleagues at the institute, providing an excellent basis for a pleasant and efficient working environment. In particular, I want to thank David Koch for his selfless support, the open-minded discussions about technical and many other issues as well as the content-related proof-reading of this work. Equally, I would like to thank my colleagues Sami Bidier, Davina Otto, Maik Schenke, Kai Häberle, Patrick Schröder, Seyedmohammad Zinatbakhsh, Chenyi Luo, Joffrey Mabuma, Christian Bleiler, Thomas Heidlauf and Michael Sprenger for their true partnership, the willingness to face new challenges together and the always open and warm conversations. This, of course, also applies to my former colleagues Dr.-Ing. Ayhan Acartürk, Dr.-Ing. Okan Avci, Dr.-Ing. Tobias Graf, Dr.-Ing. Yousef Heider, Dr.-Ing. Irina Komarova and my long-time roommate Dr.-Ing. Hans-Uwe Rempler. Beyond that, I owe special thanks to my cousin Kerstin Brendle for the time-consuming linguistic proof-reading of the manuscript.

Finally, I want to thank my wonderful family and especially my parents for always believing and trusting in me. Their limitless support enabled me to reach this point of my life. Last but not least, I want to express my deepest gratitude to my beloved wife Sabine who essentially contributed to the successful completion of this work with her well-balanced mix of beneficial pressure and limitless support.

Stuttgart, July 2014 Arndt Wagner

Imagination is more important than knowledge.
For knowledge is limited, whereas imagination embraces the entire world,
stimulating progress, giving birth to evolution.

Albert Einstein (1879 – 1955)

Contents

Deutschsprachige Zusammenfassung

Motivation

Das Gehirn ist das wichtigste Organ des Menschen. Andere Organe können grundsätzlich ersetzt werden, doch der Hirntod (irreversibles Ende aller Hirnfunktionen) gilt heute als sicheres Todeszeichen und kennzeichnet daher auch den Zeitpunkt, ab dem eine mögliche Organentnahme zur Organtransplantation durchgeführt werden kann.

Das gesunde Gehirn nimmt durch seine zentrale Steuerung des Nervensystems eine Schlüsselrolle in der Informationsverarbeitung sowie der Kontrolle und Steuerung des menschlichen Körpers ein. Diese wichtigen Funktionen werden durch ein Netzwerk von Milliarden von Neuronen bereitgestellt, die miteinander über Signalimpulse kommunizieren. Um die Funktionalität des Gehirns aufrecht zu erhalten, werden die benötigten Stoffwechsel durch die zerebrale Zirkulation reguliert, welche alle Bereiche des Gehirns versorgt. In diesem Kreislauf wird sauerstoffreiches Blut (sowie Glucose und andere Nährstoffe) durch ein hochverzweigtes Netzwerk von Blutgefäßen transportiert. Der Austausch zwischen dem Blutgefäßsystem (intravaskular) und dem umliegenden Gewebe (extravaskular) findet im Kapillarbett statt. Anschließend entsorgt die venöse Drainage das nun sauerstoffarme Blut (sowie enthaltenes Kohlendioxid und andere Stoffwechselprodukte) und bringt dieses zurück zum Herz.

In der Regel ist das Gehirn durch seine Lage innerhalb des starren Schädels ausreichend gegen äußere Einwirkungen geschützt. Jedoch können innerhalb des Schädels durch (krankhafte) Veränderungen im Gehirn äußerst kritische Situationen entstehen. So kann beispielsweise eine lokale Störung der Blutversorgung zu einem Schlaganfall führen, der die Hirnfunktionen massiv beeinträchtigt. Eine weitere lebensgefährliche Bedrohung kann durch eine krankhafte Gewebewucherung entstehen, welche umgangssprachlich auch als Gehirntumor bezeichnet wird. Das hierbei auftretende abnormale Wachstum von Zellen kann entweder gutartiger (benigne) oder bösartiger (maligne) Natur sein. Gutartige Tumore wachsen langsam und verdrängen dabei das umliegende Gewebe. Sie sind dadurch gut abgrenzbar zu gesundem Gewebe und bilden keine Metastasen (Absiedlungen). Bösartige Tumore werden häufig auch als Krebs bezeichnet und durchwachsen (infiltrieren) schnell das umgebende Gewebe. Durch diesen invasiven Charakter kann ein bösartiger Tumor über den Blutkreislauf Metastasen in entferntes Gewebe absiedeln. Grundsätzlich sind aber beide Fälle aufgrund des begrenzten Raums innerhalb des starren Schädels kritisch und benötigen unbedingt eine geeignete medizinische Behandlung. Hirntumore treten in den meisten Fällen völlig unerwartet auf und sind in der Regel nicht von Risikofaktoren abhängig. Oftmals führen routinemäßig durchgeführte medizinische Untersuchungen (beispielsweise bei unerklärlichen Kopfschmerzen) zur Diagnose eines Hirntumors.

Bis heute sind die ablaufenden Prozesse bei einer Hirntumorerkrankung nicht vollständig wissenschaftlich verstanden. Aufgrund der hohen Relevanz dieses Themengebiets besteht ein dringender Forschungsbedarf, um Tumore frühzeitig zu erkennen und effektiv behandeln zu können. Heutzutage sind bereits vielfältige Möglichkeiten zur zuverlässigen Er-

kennung von Unregelmäßigkeiten im Gehirn durch die medizinische Bildgebung gegeben, wie beispielsweise die Verwendung der Computertomographie (CT) oder der Magnetresonanztomographie (MRT). Allerdings bleiben die möglichen Behandlungsoptionen nach einem medizinischen Befund oft unzufriedenstellend.

In diesem Zusammenhang bieten numerische Simulationen, die auf einer fundierten theoretischen Modellierung des Gehirns basieren, eine aussichtsreiche Möglichkeit, die auftretenden biomechanischen Effekte infolge unterschiedlicher Behandlungsoptionen zu bestimmen und dadurch sogar vorhersagen zu können. Eine solche Materialmodellierung trägt zum fundierten Verständnis der ablaufenden Prozesse im Gehirngewebe bei und bietet darüber hinaus die Möglichkeit, neuartige medizinische Behandlungsmöglichkeiten zu testen und dadurch die praktizierenden Chirurgen in der klinischen Anwendung zu unterstützen. Die patienten-spezifische Modellierung des menschlichen Gehirns stellt jedoch eine Herausforderung dar, welche nicht nur der dreidimensionalen strukturellen Komplexität des Gehirns geschuldet ist. Das Gehirngewebe besitzt zudem eine mehrphasige und mehrkomponentige Zusammensetzung mit elektro-chemischen Eigenschaften, wobei der anisotrope und heterogene Aufbau des Gehirngewebes eine erweiterte Materialbeschreibung zwingend erfordert.

Stand der Forschung, Vorgehensweise und Zielsetzung

Seit jeher haben Menschen das Bedürfnis, das faszinierende Gehirn besser zu verstehen, um beispielsweise mehr über das Verhalten oder das Wesen der Intelligenz zu erfahren. Daher ist es nicht weiter verwunderlich, dass die Geschichte der Hirnforschung viele Jahrhunderte weit zurück reicht. Ihr Ursprung kann bis ins alte Ägypten zurückverfolgt werden, wo bereits vor mehr als 5000 Jahren erste chirurgische Eingriffe durchgeführt wurden. In der Antike und im Mittelalter wurde jedoch aufgrund des Verbots der anatomischen Präparation (durch religiöse und politische Autoritäten) eine Erweiterung dieses Wissens fast unmöglich. Dieser Zustand änderte sich entscheidend im Zeitalter der Renaissance, welches durch einen sehr starken wissenschaftlichen Drang gekennzeichnet war. Im fünfzehnten Jahrhundert untersuchte das italienische Universalgenie Leonardo da Vinci die Schädelhöhle mit flüssigem Wachs und erstellte aufwendige grafische Darstellungen des Gehirns. Ihm folgte im siebzehnten Jahrhundert der englische Arzt Thomas Willis mit seinen bedeutenden Entdeckungen zur Gefäßversorgung des Gehirns. Bis zur heutigen Zeit wurde die anatomische Struktur immer detaillierter erforscht, wobei im zwanzigsten Jahrhundert durch die Etablierung von medizinischen, bildgebenden Verfahren ein entscheidender Schritt zur patienten-spezifischen Echtzeitvisualisierung des lebenden Gehirns gemacht wurde. Heute ist die Anatomie des menschlichen Gehirns nahezu vollständig bekannt und in umfangreichen Werken zusammengestellt, siehe Schünke *et al.* [142] oder Lippert [100].

Im Gegensatz zu den primär lastabtragenden Komponenten des menschlichen Körpers, wie beispielsweise den Knochen oder Muskeln, entstanden Studien über das mechanische Materialverhalten des weichen Hirngewebes (von Schweinen) erst vor etwa fünfzig Jahren (Franke [68]). Untersuchungen an totem menschlichen Gehirngewebe wurden in den

letzten Jahren realisiert (Fallenstein *et al.* [65]). Die experimentellen Ergebnisse gaben dabei Hinweise auf eine Post-mortem-Änderung des mechanischen Verhaltens. Umfangreiche Experimente von Miller [111] und Miller & Chinzei [112, 113] zeigten am Hirngewebe des Schweins ein unterschiedliches, nicht-lineares Spannungs-Dehnungs Verhalten bei behinderter oder unbehinderter Kompression sowie bei Extension. Zudem wurde eine starke Verformungsratenabhängigkeit festgestellt. Darüber hinaus spielen weitere spezifische Eigenschaften des Gewebes eine maßgebende Rolle, insbesondere die anisotropen (richtungsabhängigen) Eigenschaften des Hirngewebes aufgrund der mikroskopischen Architektur der Nervenfasern, siehe Margulies & Prange [104]. Dies kann Auswirkungen auf das Verformungsverhalten sowie auf die Strömungs- und Diffusionsprozesse im Gewebe haben. Ein Meilenstein bei der Identifikation der Mikroarchitektur markiert die Etablierung der sogenannten Diffusion-Tensor-Imaging-Technik (DTI) in der Mitte der neunziger Jahre, siehe Basser *et al.* [12] oder Le Bihan *et al.* [94]. Diese Erweiterung, basierend auf der Standard-MRT-Messung, ermöglicht eine in-vivo und nicht-invasive Identifikationsmöglichkeit der Nervenfaserbahnen im Gehirn (Basser *et al.* [13]). Dadurch können, wie in Tuch *et al.* [161] beschrieben, die Permeabilitätseigenschaften des porösen Gewebeskeletts abgeschätzt werden.

Grundsätzlich lassen sich die in der Literatur verfügbaren theoretischen Modelle zur Beschreibung des Materialverhaltens des Gehirns in Ein- oder Mehrkomponentenmodelle unterteilen. Dabei ist die Wahl des verwendeten Modellansatzes immer stark mit den Anforderungen des betrachteten Anwendungsbereichs verknüpft. Aufgrund des Bedarfs, Prozesse innerhalb des Gehirngewebes zu beschreiben, sowie aus physiologischen und anatomischen Gesichtspunkten, kommen im Rahmen dieser Monographie nur Mehrkomponentenmodelle in Betracht. Diesbezüglich gehen die ersten Überlegungen zurück auf Hakim & Adams [73] und Fallenstein *et al.* [65]. Die ersten mathematischen Beschreibungen, welche die Hirnsubstanz als poröses Medium mit einer viskosen Flüssigkeit im extrazellulären Raum (ECS) beschreiben, wurden von Nagashima *et al.* [118] und Tada & Nagashima [155] formuliert und durch erste numerische Untersuchungen ergänzt. Allerdings bestätigten erst die von Franceschini *et al.* [67] durchgeführten Oedometerversuche an totem menschlichen Hirngewebe das mehrkomponentige Materialverhalten. Durch diese Studien an drainierten Hirngewebeproben war es möglich, zwischen einem einphasigen, viskosen Materialverhalten und einem Konsolidierungsvorgang eines mehrphasigen Materials zu unterscheiden. Konsequenterweise berücksichtigt der Modellierungsansatz für totes Hirngewebe von Franceschini *et al.* [67] das Festkörperskelett sowie die interstitielle Flüssigkeit. Allerdings wird die Blutkomponente vernachlässigt, welche für eine Modellierung von lebendem Hirngewebe berücksichtigt werden sollte. Ansätze, die den Blutfluss in biologischem Gewebe beschreiben, finden sich bei hierarchischen porösen Medien (Vankan *et al.* [162, 163]) oder bei detaillierten (halbautomatisch erstellten) mikromechanischen Modellen (Linninger *et al.* [96]).

Der Wunsch nach einer ganzheitlichen Beschreibung des komplexen Blutgefäßsystems, den Strömungs- und Transportprozessen im ECS sowie des umgebenden Festkörperskellets in einem makroskopischen Modell motiviert die Verwendung der Theorie Poröser Medien (TPM), siehe de Boer [20, 21, 22], Bowen [26, 27, 28] oder Ehlers [44, 50, 51]. Im Laufe der Zeit ist die TPM erfolgreich in einer breiten Variation von biomechanischen An-

wendungen eingesetzt worden, siehe beispielsweise die Arbeiten von Acartürk [3], Ehlers [51], Ehlers *et al.* [55], Karajan [87], Ricken & Bluhm [130] oder Ricken *et al.* [132, 133]. Darüber hinaus können aber auch relevante Erkenntnisse aus dem verwandten Bereich der geomechanischen Problemstellungen, wie beispielsweise von Strömungs- und Transportprozessen in ungesättigten Böden, übertragen werden, siehe beispielsweise Graf [70] oder Ehlers [51].

Bezüglich der Medikamentenverabreichung zur Hirntumorbehandlung enstanden bemerkenswerte Forschungarbeiten in den letzten Jahrzehnten. Die begrenzte räumliche Verteilung von Wirkstoffen bei der Verwendung von Implantaten (Bobo *et al.* [18], Groothuis *et al.* [72], Kawakami *et al.* [88]) motivierte eine direkte (invasive) Infusion zur gezielten und effektiven therapeutischen Verabreichung. Diese sogenannte Konvektionstherapie, auch bekannt als „convection-enhanced drug delivery“ (CED), wurde erstmals in den frühen neunziger Jahren von Bobo *et al.* [18] vorgestellt und bei Katzen angewendet. Bereits drei Jahre später wurden experimentelle (trial and error) Studien an sterbenskranken Patienten durchgeführt, um Ausbreitung und therapeutische Wirkung zu testen, siehe Laske *et al.* [93]. Bei weiteren vorklinischen und klinischen Studien wurde das große Potenzial für die klinische Anwendung dokumentiert (Hall *et al.* [74], Kunwar *et al.* [92], Shahar *et al.* [144], Voges *et al.* [165]). Allerdings ist die Verwendung von CED (Ding *et al.* [39], Raghavan *et al.* [125], Vogelbaum [164]) heute immer noch weit von einem medizinischen Standardverfahren zur Tumorenbehandlung entfernt, und die herkömmlichen Behandlungsmethoden (operative Entfernung des Tumors in Kombination mit Bestrahlungstherapie und/oder Chemotherapie) werden üblicherweise vorgezogen.

Zur Berechnung und Simulation des chirurgischen CED-Eingriffs wurden verschiedene Modelle entwickelt. Analytische (zylinder oder kugelförmig symmetrische) Ansätze wurden von Basser [11], Kaczmarek *et al.* [85], Morrison *et al.* [116], Smith & Humphrey [147] oder Wirth & Sobey [171] entwickelt. Numerische Modelle, welche unter anderem auch die Möglichkeit zur Berücksichtigung von anisotropen Durchlässigkeiten durch die Einbeziehung von medizinischen (DTI) Daten bieten, wurden beispielsweise von Linninger *et al.* [97, 98, 99], Støverud *et al.* [152] oder Ehlers & Wagner [59, 60] und Wagner & Ehlers [168, 169, 170] vorgestellt. In diesem Zusammenhang sind auch die voxelbasierten Modelle mit regulärem Berechnungsgitter von Chen & Sarntinoranont [34], Kim *et al.* [91], Magdoom *et al.* [103], Pishko *et al.* [123] und Sarntinoranont *et al.* [135] zu nennen. Begleitend zu numerischen Berechnungen wurden Experimente in gehirnähnlichen (Agarose) Gelen zur Verifizierung und zur Validierung solcher Modelle durchgeführt (Chen *et al.* [35], Darcis [37], Ivanchenko *et al.* [81], Sindhwani *et al.* [146]). Mittlerweile besteht sogar die Möglichkeit, die CED-Infusion im Sinne eines Black-box-Verfahrens mittels eines kommerziellen chirurgischen Softwarepackets (iPlan®Flow, BrainLAB, Feldkirchen, Deutschland) zu simulieren, siehe hierzu auch die zugrundeliegenden Arbeiten von Chen *et al.* [35], Morrison *et al.* [115, 116] und Sampson *et al.* [134]. Demzufolge scheint die Vorhersage der Medikamentenverteilung im menschlichen Hirngewebe bereits erreicht. Allerdings verbleiben immer noch offene Punkte, um den CED-Vorgang und alle daraus resultierenden Effekte vollständig zu beschreiben.

Bis heute sind der Einfluss der Deformation und die damit verbundene Beanspruchung auf das Hirngewebe nicht ausreichend geklärt. In der Regel wird vereinfachend von ei-

nem starren Festkörperskelett ausgegangen. Bei kurzzeitigem (oder auch lang andauerndem) Einbringen therapeutischer Flüssigkeit in ein räumlich begrenztes Gebiet, welches bereits durch das vollständig gesättigte Hirngewebe ausgefüllt ist, ergibt sich jedoch zwangsläufig immer eine Festkörperdeformation. Daher muss eine ausreichende Modellierung des Hirngewebes grundsätzlich die Beschreibung von Verformungen einbeziehen. Bei raumfordernden Prozessen, wie Hirnödemen, Hydrocephalus (Wasserkopf), Tumorwachstum oder sogar aktiv initiierten Vorgängen infolge computerintegrierter Chirurgie (CIS), kann es zu großen (aber quasi-statischen) Deformationen kommen. Dies kann wiederum die ursprünglichen Gewebeeigenschaften und dadurch auch die Ausbreitung eingebrachter Medikamente beeinflussen. Demzufolge wird für die hier entwickelte Modellierung ein vollständig gekoppelter Ansatz aller maßgebenden Effekte gewählt.

Die Vorgehensweise beinhaltet eine thermodynamisch konsistente Modellformulierung des menschlichen Gehirns, wobei alle anatomischen und physiologischen Gegebenheiten konstitutiv berücksichtigt werden. Dieses Model beeinhaltet eine finite anisotrope Materialformulierung des Festkörperskeletts mit anisotropen und heterogenen Durchströmungseigenschaften für die flüssigen Komponenten Blut und interstitielle Flüssigkeit. Darauf aufbauend wird durch die monolithische Lösung des Systems von gekoppelten Differentialgleichungen mittels erweiterten finiten Elementen eine numerische Simulation ermöglicht. Dies erlaubt es, alle Interaktionsprozesse während eines Infusionsprozesses in einer ganzheitlichen und eleganten Art und Weise zu beschreiben. Das Ziel dieser Monographie ist demnach die Entwicklung eines möglichst vielseitigen und robusten Simulationswerkzeugs. Auf diese Weise entsteht eine virtuelle Testumgebung für die Untersuchung verschiedenster Fragestellungen. Ein spezifischer Fokus in der klinischen Anwendung ist auf das Medikamentenverabreichungsproblem bei der Behandlung von schweren Gehirntumorerkrankungen gelegt. Das im Rahmen dieser Arbeit vorgestellte Modell ermöglicht es, zur Beantwortung offener Fragen im bedeutenden und faszinierenden Gebiet der Gehirntumortherapien beizutragen. Das entwickelte Modell ist dabei flexibel anpassbar und erweiterbar und lässt sich somit auch auf die Untersuchung anderer biologischer Materialien übertragen, siehe beispielsweise Wagner *et al.* [166] zur Simulation von Knochenzementeinspritzungen in osteoporose Wirbelkörper. Als Konsequenz aus solchen numerischen Simulationen kann der praktizierende Chirurg vor sowie bei der Planung von Operationen unterstützt und bei seinen Entscheidungen begleitet werden.

Gliederung der Arbeit

Das einleitende **Kapitel 1** stellt die Motivation, den Stand der Forschung sowie die Ziele dieser Arbeit zusammen. In **Kapitel 2** wird eine kurze Einführung in die Anatomie und Physiologie des menschlichen Gehirns gegeben. Der Schwerpunkt liegt auf der für die Modellbildung des Gehirns grundlegenden Zusammensetzung des Gewebeaggregats sowie den spezifischen Eigenschaften der einzelnen beteiligten Komponenten. Im Hinblick auf eine angemessene Behandlung bei Tumorerkrankungen wird ein Überblick zu konventionellen und neuartigen Behandlungsmöglichkeiten gegeben. Medizinische Bildgebungsverfahren werden vorgestellt, welche durch den Einblick in lebendes Gewebe eine Möglichkeit zur Ermittlung von patientenspezifischen Materialparametern bereitstellen.

Die kontinuumsmechanischen Grundlagen für die mehrphasige und mehrkomponentige Beschreibung des Gehirns werden in **Kapitel 3** eingeführt. Dabei wird das Konzept der TPM auf das Gehirngewebe angewandt. Es wird ein Vier-Komponenten-Modell entwickelt, welches aus drei nicht mischbaren Konstituierenden und einer mischbaren Komponente besteht. Die nicht mischbaren Konstituierenden sind durch das Festkörperskelett (Gewebezellen und Gefäßwände), das Blut und die gesamte interstitielle Flüssigkeit gegeben. Dabei wird die Letztere durch eine reale Mischung eines flüssigen Lösungsmittels mit einem gelösten therapeutischen Stoff modelliert. Zur Behandlung mischbarer Komponenten im Rahmen der TPM muss diese zusätzlich um Elemente der Theorie der Mischungen erweitert werden. Ferner werden die kinematischen Relationen der überlagerten Komponenten dargestellt sowie die beschreibenden Bilanzgleichungen für das Gesamtaggregat als auch für ihre miteinander interagierenden Komponenten zusammengestellt.

In **Kapitel 4** werden die materialunabhängigen Bilanzgleichungen durch geeignete konstitutive Einstellungen vervollständigt. Dazu werden konstitutive Beziehungen über eine thermodynamisch konsistente Betrachtung aus der Entropieungleichung entwickelt und ermöglichen somit die charakteristische Materialbeschreibung des Gehirngewebes. Abschließende Bemerkungen kommentieren das Schließungsproblem des gekoppelten kontinuumsmechanischen Problems.

Das Ziel von **Kapitel 5** ist die numerische Umsetzung des theoretischen Modells. Hierzu wird die (erweiterte) Finite-Elemente-Methode zur Lösung des gekoppelten partiellen Differentialgleichungssystems verwendet. Ausgehend von den schwachen Formulierungen der beschreibenden Bilanzgleichungen folgt eine Diskretisierung in Raum und Zeit sowie die Vorstellung der gewählten Lösungsstrategie. Die numerische Realisierung wird im Programmpaket PANDAS implementiert, welches am Institut für Mechanik (Lehrstuhl für Kontinuumsmechanik) an der Universität Stuttgart gepflegt und weiterentwickelt wird.

In **Kapitel 6** werden die theoretischen und numerischen Entwicklungen bei Simulationen des menschlichen Gehirns zur Anwendung gebracht. Hierzu werden zunächst die Möglichkeiten zur Bestimmung der erforderlichen Simulationsparameter untersucht. Anschließend werden zwei Optionen zur Generierung von geeigneten patienten-spezifischen Geometrien zur Simulation von realistischen Randwertproblemen beschrieben. Die Realisierung von ausgewählten numerischen Beispielen demonstriert die Leistungsfähigkeit und Bandbreite des entwickelten Modells. Nach der Diskussion des grundlegenden Materialverhaltens wird eine detaillierte numerische Studie zur invasiven (CED) Verabreichung von Medikamenten durchgeführt. Darüber hinaus werden der Einfluss verschiedener Simulationsparameter durch eine lokale numerische Sensitivitätsanalyse untersucht sowie weitere Effekte betrachtet, die einen Einfluss auf die Verabreichung haben können.

Eine abschließende Zusammenfassung der Arbeit sowie ein Ausblick auf Erweiterungsmöglichkeiten des vorgestellten Modells sind in **Kapitel 7** gegeben.

Zusätzliche Informationen werden zur Ergänzung, aber auch zur besseren Übersicht und Lesbarkeit der Arbeit, im Anhang aufgeführt. Dabei sind benötigte mathematische Aspekte der Tensorrechnung in **Anhang A** und mechanische Ergänzungen in **Anhang B** zusammengestellt.

Nomenclature

The common notation of modern tensor calculus is used in this monograph, cf. Ehlers [45] and de Boer [19]. Moreover, the particular symbols are chosen according to the established nomenclature of related works, cf., e. g., de Boer [21] and Ehlers [44, 50].

Conventions

General conventions

$(\bullet)$			placeholder for arbitrary quantities
$a, b, \ldots$	or	$\phi, \psi, \ldots$	scalars (zero-order tensors)
$\mathbf{a}, \mathbf{b}, \ldots$	or	$\boldsymbol{\phi}, \boldsymbol{\psi}, \ldots$	vectors (first-order tensors)
$\mathbf{A}, \mathbf{B}, \ldots$	or	$\boldsymbol{\Phi}, \boldsymbol{\Psi}, \ldots$	tensors of second order

Index and suffix conventions

$i, j, k, n, \ldots$	indices (control variables) as super- or subscripts
$(\bullet)_\alpha$	subscripts indicate kinematical quantities of a constituent within porous-media or mixture theories
$(\bullet)^\alpha$	superscripts indicate non-kinematical quantities of a constituent within porous-media or mixture theories
$(\bullet)^\alpha_{0\alpha}$	initial values of non-kinematical quantities with respect to the referential configuration of a constituent
$\dot{(\bullet)} = \mathrm{d}(\bullet)/\mathrm{d}t$	total time derivatives with respect to the overall aggregate φ
$(\bullet)'_\alpha = \mathrm{d}_\alpha(\bullet)/\mathrm{d}t$	material time derivatives following the motion of φ^α
$\mathrm{d}(\bullet)$	differential operator
$\partial(\bullet)$	partial derivative operator
$\delta(\bullet)$	test functions of primary unknowns
$\hat{(\bullet)}$	production terms of mechanical quantities
$\check{(\bullet)}$	quantities in a rotated reference configuration
$\overset{*}{(\bullet)}$	quantities in a rotated actual configuration
$\bar{(\bullet)}$	prescribed quantities (boundary conditions)
$(\bullet)^\alpha_E$	extra (effective) quantities of a constituent φ^α
$(\bullet)^\alpha_{E\mathrm{dis.}}$, $(\bullet)^\alpha_{E\mathrm{mech.}}$	dissipative and purely mechanical parts of extra quantities
$(\bullet)^h$	spatially discretised quantities within numerical investigations
$(\bullet)_m$	molar quantities of miscible components
$(\bullet)_n$, $(\bullet)_{n+1}$	discretised quantities in time within numerical investigations
$(\bullet)^{\mathrm{n}}$	quantities based on medical imaging at an evaluated voxel

Symbols

Greek letters

Symbol	Unit	Description
α		constituent identifier for S, B and I in super- and subscript
$\tilde{\alpha}^B$	$[\,\mathrm{N/m^2}\,]$	material parameter in the constitutive equation of ψ^B
β		identifier for the pore-liquids B and I in super- and subscript
$\tilde{\beta}^B$	[-]	material parameter in the constitutive equation of ψ^B
γ		component identifier for L and D in super- and subscript
$\gamma^{\beta R}$	$[\,\mathrm{N/m^3}\,]$	effective weight of a liquid constituent φ^B
$\gamma^{\mathrm{n}}_{i\,\mathrm{awd}}$	$[\,\mathrm{m^2/s}\,]$	eigenvalues of the apparent water-diffusion tensor
$\gamma^{\mathrm{n}}_{\mathrm{max}}$	$[\,\mathrm{m^2/s}\,]$	largest eigenvalue of the apparent water-diffusion tensor
$\bar{\gamma}^{\mathrm{n}}_{\mathrm{awd}}$	$[\,\mathrm{m^2/s}\,]$	mean value of the eigenvalues $\gamma^{\mathrm{n}}_{i\,\mathrm{awd}}$
$\tilde{\gamma}^S_1$	[-]	parameter of the anisotropic part of the solid strain energy
Γ, Γ_{dof}		domain boundary and domain boundary of a primary variable
Γ^{dof}_D		Dirichlet boundary with essential boundary conditions
$\Gamma^{(\cdot)}_N$		Neumann boundary with natural boundary conditions
δ^j_i		Kronecker symbol or Kronecker delta
ε, ε^α	$[\,\mathrm{J/kg}\,]$	mass specific internal energy of φ and φ^α
$\hat{\varepsilon}^\alpha$	$[\,\mathrm{J/m^3\,s}\,]$	volume specific direct energy production of φ^α
$\varepsilon_{\mathrm{tol.}}$		pre-defined tolerance used in the Newton solver
$\hat{\zeta}^\alpha$	$[\,\mathrm{J/K\,m^3\,s}\,]$	volume specific direct entropy production of φ^α
η, η^α	$[\,\mathrm{J/K\,kg}\,]$	mass specific entropy of φ and φ^α
$\hat{\eta}$, $\hat{\eta}^\alpha$	$[\,\mathrm{J/K\,m^3\,s}\,]$	volume specific total entropy production of φ and φ^α
θ^i_S		general contravariant curvilinear solid coordinate lines
θ, θ^α	$[\,\mathrm{K}\,]$	absolute Kelvin's temperature of φ and φ^α
κ	[-]	exponent governing the deformation dependency of $\tilde{K}^{S\beta}$
$\lambda_{\alpha(k)}$	[-]	eigenvalues of the deformation tensors
λ^S_0	$[\,\mathrm{N/m^2}\,]$	second Lamé constant of φ^S
μ^β, $\mu^{\beta R}$	$[\,\mathrm{N\,s/m^2}\,]$	partial and effective dynamic viscosity of φ^β
μ^S_0	$[\,\mathrm{N/m^2}\,]$	first Lamé constant of φ^S
$\tilde{\mu}^S_1$	$[\,\mathrm{N/m^2}\,]$	parameter of the anisotropic part of the solid strain energy
μ^γ_{0m}, μ^γ_m	$[\,\mathrm{J/kg}\,]$	constant standard and molar chemical potential of φ^γ
ξ_i		local coordinates of a referential finite element
π, π^γ	$[\,\mathrm{N/m^2}\,]$	osmotic pressures of the aggregate φ and a component φ^γ
ρ	$[\,\mathrm{kg/m^3}\,]$	density of the overall aggregate φ
ρ^α, $\rho^{\alpha R}$	$[\,\mathrm{kg/m^3}\,]$	partial and effective (realistic) density of φ^α

ρ_I^γ	$[\,\mathrm{kg/m^3}\,]$	partial pore density of φ^γ related to the interstitial pore space
$\hat{\rho}^\alpha$	$[\,\mathrm{kg/m^3\,s}\,]$	volume-specific mass production term of φ^α
σ, σ^α		scalar-valued supply terms of mechanical quantities
σ_η, σ_η^α		volume specific external entropy supply of φ and φ^α
σ_V^S		von Mises equivalent stress
Υ		arbitrary field function (steady and steady differentiable)
φ, φ^α		entire aggregate model and particular constituent
ϕ_{dof}^j		global basis function of a degree of freedom
ψ, ψ^α	$[\,\mathrm{J/kg}\,]$	mass-specific Helmholtz free energy of φ and φ^α
$\tilde{\psi}_0^B$	$[\,\mathrm{J/kg}\,]$	constant standard state potential of φ^B
Ψ, Ψ^α	$[\,\cdot/\mathrm{m^3}\,]$	volume-specific densities of scalar mechanical quantities
Ψ_I^I, Ψ_I^γ	$[\,\mathrm{J/m^3}\,]$	Helmholtz free energy of φ^I and φ^γ
$\hat{\Psi}$, $\hat{\Psi}^\alpha$	$[\,\cdot/\mathrm{m^3}\,]$	volume-specific productions of scalar mechanical quantities
Ω, $\partial\Omega$		spatial domain and boundary of the aggregate body $\mathcal{B}$
Ω_e, Ω^h		a finite element and the discretised finite element domain
Ω_e^ξ		reference finite element described in local coordinates
$\boldsymbol{\xi}_i$		local coordinate system of a referential finite element
$\boldsymbol{\sigma}$, $\boldsymbol{\sigma}^\alpha$		vector-valued supply terms of mechanical quantities
$\boldsymbol{\Upsilon}$		arbitrary field function (steady and steady differentiable)
$\boldsymbol{\phi}$, $\boldsymbol{\phi}^\alpha$		vector-valued efflux terms of mechanical quantities
$\boldsymbol{\phi}_\eta$, $\boldsymbol{\phi}_\eta^\alpha$	$[\,\mathrm{J/K\,m^2\,s}\,]$	entropy efflux vector of φ and φ^α
$\boldsymbol{\phi}_{\mathrm{dof}}^j$		global basis function of a degree of freedom
$\boldsymbol{\phi}_{\mathrm{geo}}^j$		basis functions of the geometry transformation
$\boldsymbol{\chi}_\alpha$, $\boldsymbol{\chi}_\alpha^{-1}$		motion and inverse motion functions of the constituents φ^α
$\boldsymbol{\Psi}$, $\boldsymbol{\Psi}^\alpha$	$[\,\cdot/\mathrm{m^3}\,]$	volume-specific densities of vectorial mechanical quantities
$\hat{\boldsymbol{\Psi}}$, $\hat{\boldsymbol{\Psi}}^\alpha$	$[\,\cdot/\mathrm{m^3}\,]$	volume-specific productions of vectorial mechanical quantities
$\boldsymbol{\tau}$, $\boldsymbol{\tau}^\alpha$	$[\,\mathrm{N/m^2}\,]$	Kirchhoff stress tensors of φ and φ^α
$\boldsymbol{\Phi}$, $\boldsymbol{\Phi}^\alpha$		general tensor-valued mechanical quantities

Latin letters

Symbol	Unit	Description
B		identifier for the blood constituent φ^B
c_m^γ	$[\,\mathrm{mol/m^3}\,]$	molar concentration of a component φ^γ
d^{voxel}	$[\,\mathrm{m}\,]$	distance of a voxel information to the considered Gauss point
$\mathrm{d}m^\alpha$, $\mathrm{d}m^\gamma$	$[\,\mathrm{kg}\,]$	local mass element of φ^α and φ^γ
$\mathrm{d}n_m^\gamma$	$[\,\mathrm{mol}\,]$	local number of moles of a component φ^γ
$\mathrm{d}t$	$[\,\mathrm{s}\,]$	time increment

$\mathrm{d}v$, $\mathrm{d}v^\alpha$	$[\,\mathrm{m}^3\,]$	actual volume element of φ and φ^α
$\mathrm{d}v_\xi$	$[\,\mathrm{m}^3\,]$	actual volume element of the reference element Ω_e^ξ
$\mathrm{d}V_\alpha$	$[\,\mathrm{m}^3\,]$	reference volume element of φ^α
D		identifier for the dissolved therapeutic solute φ^D (drug)
$\bar{D}^D$	$[\,\text{-}\,]$	reference value for the calibration of the drug's diffusivity
$\hat{e}^\alpha$	$[\,\mathrm{J/m^3\,s}\,]$	volume specific total energy production of φ^α
E	$[\,\text{-}\,]$	number of non-overlapping finite elements Ω_e
E^*		attached finite element to a respective node P^j
h_n	$[\,\mathrm{s}\,]$	actual time step in a temporal discretisation scheme
I		identifier for the interstitial fluid constituent φ^I
$I_{\alpha1}$, $I_{\alpha2}$, $I_{\alpha3}$	$[\,\text{-}\,]$	principal invariants of the deformation tensors
$\bar{j}^D$	$[\,\mathrm{mol/m^2\,s}\,]$	area-specific therapeutic efflux of φ^D over the boundary
J_{S1}, J_{S2}, J_{S3}	$[\,\text{-}\,]$	basic invariants of the deformation tensors
J_{S4}, J_{S5}	$[\,\text{-}\,]$	mixed basic invariants of $\mathbf{C}_S$ and $\boldsymbol{\mathcal{M}}^S$
J_α, $\bar{J}$	$[\,\text{-}\,]$	Jacobian determinant of φ^α and of a reference element Ω_e^ξ
K_G		integration points for the Gaussian quadrature scheme
$\bar{K}^I$	$[\,\text{-}\,]$	reference value for the calibration of the permeability of φ^I
$\tilde{K}^{S\beta}$	$[\,\text{-}\,]$	prefactor for deformation-dependent permeability
$\tilde{K}_{ij}^{K_G}$		weighted scalar voxel information at the Gauss point K_G
L		identifier for the liquid solvent φ^L within φ^I
M	$[\,\mathrm{kg}\,]$	mass of the overall aggregate φ
M_m^γ	$[\,\mathrm{kg/mol}\,]$	molar mass of a mixture component φ^γ
n^α, n^β	$[\,\text{-}\,]$	volume fractions of φ^α and φ^β
n^F	$[\,\text{-}\,]$	porosity, composed of n^I (ECS) and n^B (intravascular space)
n^S	$[\,\text{-}\,]$	solidity, volume fraction of φ^S
N, N_e	$[\,\text{-}\,]$	number of nodal points for Ω^h and Ω_e
N_A	$[\,\cdot/\mathrm{mol}\,]$	Avogadro's constant
p, $p^{\beta R}$	$[\,\mathrm{N/m^2}\,]$	overall pore pressure and liquid pore pressures
$p_{\text{dif.}}$	$[\,\mathrm{N/m^2}\,]$	differential pressure of the pore liquids
P^j		nodal point in a finite element Ω_e within the set $\mathcal{N}$
Q	$[\,\mathrm{m^3/s}\,]$	application rate during the CED application
r, r^α	$[\,\mathrm{J/kg\,s}\,]$	mass-specific external heat supply (radiation) of φ and φ^α
R	$[\,\mathrm{J/mol\,K}\,]$	universal gas constant
R_{K_G}	$[\,\mathrm{m}\,]$	influence radius for the weighting of voxel information
s^β	$[\,\text{-}\,]$	saturation function of the pore liquids φ^β
s_{voxel}	$[\,\mathrm{m}\,]$	uniform voxel size of the medical-imaging grid
S		identifier for the solid skeleton constituent φ^S

$S_{R,P}$	[-]	local sensitivity indicator
t, t_n, t_{n+1}	[s]	actual time and temporally discretised time steps
T	[s]	specific (final) time within an evaluated time interval
U_0^S	[N/m^2]	volumetric extension term in the isotropic solid strain energy
$\bar{v}^\beta$	[m^3/m^2 s]	area-specific volume efflux of φ^β over the boundary
V, V_α	[m^3]	overall volume of $\mathcal{B}$ and partial volume of $\mathcal{B}^\alpha$
w_k	[-]	weight for the Gaussian quadrature scheme
w^{voxel}	[-]	weight for the voxel information at the considered K_G
W^S	[J/m^3]	volume specific solid strain energy function
W^S_{iso}	[J/m^3]	isotropic part of the volume specific solid strain energy W^S
W^S_{aniso}	[J/m^3]	anisotropic part of the volume specific solid strain energy W^S
x^γ_m	[-]	mole fraction of a mixture component φ^γ
$\mathbf{a}_0^S$	[-]	unit vector pointing in the fibre direction
$\mathbf{a}_{Si}$, $\mathbf{a}_S^i$	[-]	co- and contravariant solid actual basis vector
$\mathbf{b}$, $\mathbf{b}^\alpha$	[m/s^2]	mass specific body force vector
$\mathbf{d}_\alpha$	[m/s]	diffusion velocity vector of φ^α
$\mathbf{d}_{\gamma I}$	[m/s]	pore-diffusion velocity vector of φ^γ with respect to φ^I
d$\mathbf{a}$, d$\bar{\mathbf{a}}$	[m^2]	oriented and weighted actual area element
d$\mathbf{A}_\alpha$	[m^2]	oriented reference area element of φ^α
d$\mathbf{k}^\alpha_O$, d$\mathbf{k}^\alpha_V$	[N]	contact and volume force increment of φ^α
d$\mathbf{x}$	[m]	actual line element
d$\mathbf{X}_\alpha$	[m]	reference line element of the constituent φ^α
$\mathbf{e}_i$	[-]	(Cartesian) basis of orthonormal vectors
$\mathbf{f}^\alpha$	[N]	volume force vector acting on $\mathcal{P}^\alpha_\mathcal{B}$ from a distance
$\mathbf{g}$	[m/s^2]	constant gravitation vector
$\mathbf{h}$	[kg/m s]	local moment of momentum of the overall aggregate φ
$\mathbf{h}_{Si}$, $\mathbf{h}_S^i$	[-]	co- and contravariant solid reference basis vector
$\hat{\mathbf{h}}^\alpha$	[N/m^2]	volume-specific total angular momentum production of φ^α
$\mathbf{k}^\alpha$, $\mathbf{k}^\alpha_O$, $\mathbf{k}^\alpha_V$	[N]	total, contact and volume force element of φ^α
$\mathbf{l}$	[kg/m^2 s]	local momentum of the overall aggregate φ
$\hat{\mathbf{m}}^\alpha$	[N/m^2]	volume-specific direct angular momentum production of φ^α
$\mathbf{m}_{\alpha(k)}$	[-]	eigenvectors of $\mathbf{C}_\alpha$ related to the reference configuration
$\mathbf{n}$	[-]	outward-oriented unit surface normal vector
$\mathbf{n}_{\alpha(k)}$	[-]	eigenvectors of $\mathbf{B}_\alpha$ related to the actual configuration
$\hat{\mathbf{p}}^\alpha$, $\hat{\mathbf{p}}^\alpha_E$	[N/m^3]	volume-specific direct and extra momentum production of φ^α
$\mathbf{q}$, $\mathbf{q}^\alpha$	[J/m^2 s]	heat influx (convection) vector of φ and φ^α
$\hat{\mathbf{s}}^\alpha$	[N/m^3]	volume-specific total momentum production of φ^α

$\bar{\mathbf{t}}$	$[\mathrm{N/m^2}]$	external load vector acting on the boundary
$\mathbf{t}^\alpha$	$[\mathrm{N/m^2}]$	surface traction vector of φ^α
$\mathbf{u}_S$	$[\mathrm{m}]$	solid displacement vector
$\mathbf{v}_i^{\mathrm{n}}$	$[\text{-}]$	eigenvectors of the apparent water-diffusion tensor
$\mathbf{w}_\beta$, $\mathbf{w}_\gamma$	$[\mathrm{m/s}]$	seepage velocity vector of φ^β and φ^γ
$\mathbf{x}$	$[\mathrm{m}]$	actual position vector of φ
$\mathbf{X}_\alpha = \mathbf{x}_{0\alpha}$	$[\mathrm{m}]$	reference position vector of $\mathcal{P}^\alpha$
$\dot{\mathbf{x}}$, $\overset{\prime}{\mathbf{x}}_\alpha$	$[\mathrm{m/s}]$	velocity vector of the aggregate φ and the constituent φ^α
$\ddot{\mathbf{x}}$, $\overset{\prime\prime}{\mathbf{x}}_\alpha$	$[\mathrm{m/s^2}]$	acceleration vector of the aggregate φ and the constituent φ^α
$\mathbf{A}_\alpha$	$[\text{-}]$	contravariant Almansian strain tensor of φ^α (AC)
$\mathbf{B}_\alpha$	$[\text{-}]$	covariant left Cauchy-Green deformation tensor of φ^α (AC)
$\mathbf{C}_\alpha$	$[\text{-}]$	contravariant right Cauchy-Green deformation tensor (RC)
$\mathbf{D}_\alpha$	$[\cdot/\mathrm{s}]$	symmetric deformation velocity tensor of φ^α
$\mathbf{D}_{\mathrm{awd}}$	$[\mathrm{m^2/s}]$	apparent water-diffusion tensor obtained by DTI
$\mathbf{D}^\gamma$, $\mathbf{D}_0^\gamma$	$[\mathrm{m^2/s}]$	diffusion and initial diffusion tensor of the component φ^γ
$\overset{3}{\mathbf{E}}$	$[\text{-}]$	Ricci permutation tensor (third-order fundamental tensor)
$\mathbf{E}_\alpha$	$[\text{-}]$	contravariant Green-Lagrangean strain tensor (RC)
$\mathbf{F}_\alpha$	$[\text{-}]$	material deformation gradient of φ^α
$\mathbf{H}$	$[\text{-}]$	symmetric transformation tensor in the group of $\mathcal{MG}_3 \in \mathcal{O}_e$
$\mathbf{I}$	$[\text{-}]$	identity tensor (second-order fundamental tensor)
$\overset{\mathrm{R}}{\mathbf{K}}_\alpha$, $\mathbf{K}_\alpha$	$[\text{-}]$	covariant Karni-Reiner strain tensor in RC and AC
$\mathbf{K}^\beta$	$[\mathrm{m/s}]$	Darcy (or hydraulic) permeability of φ^β
$\mathbf{K}^\beta_{\mathrm{spec.}}$	$[\mathrm{m^4/N\,s}]$	specific permeability tensor of φ^β
$\mathbf{K}^{S\beta}$	$[\mathrm{m^2}]$	(anisotropic) intrinsic permeability of φ^β
$\mathbf{K}^\gamma$	$[\mathrm{J/kg}]$	tensor of chemical potential of a component φ^γ
$\mathbf{L}$, $\mathbf{L}_\alpha$	$[\cdot/\mathrm{s}]$	spatial velocity gradient of φ and φ^α
$\mathbf{M}_\alpha$	$[\text{-}]$	eigentensor of $\mathbf{C}_\alpha$ related to the reference configuration
$\hat{\mathbf{M}}^\alpha$	$[\mathrm{N/m^2}]$	coupling tensor, skew-symmetric part of the partial stress
$\mathbf{N}_\alpha$	$[\text{-}]$	eigentensor of $\mathbf{B}_\alpha$ related to the actual configuration
$\mathbf{P}$, $\mathbf{P}^\alpha$	$[\mathrm{N/m^2}]$	first Piola-Kirchhoff or nominal stress tensors of φ and φ^α
$\mathbf{Q}$	$[\text{-}]$	arbitrary rigid body rotation in the group of $\mathcal{O}_e$
$\mathbf{Q}^{\mathrm{n}}$	$[\text{-}]$	transformation tensor containing the coefficients of $\mathbf{v}^{\mathrm{n}}$
$\mathbf{R}_\alpha$	$[\text{-}]$	proper orthogonal rotation tensor of the polar decomp. of $\mathbf{F}_\alpha$
$\mathbf{S}$, $\mathbf{S}^\alpha$	$[\mathrm{N/m^2}]$	second Piola-Kirchhoff stress tensors of φ and φ^α
$\mathbf{S}^{\alpha\beta}$	$[\mathrm{N\,s/m^4}]$	friction tensor relating the constituents φ^α and φ^β
$\mathbf{T}$, $\mathbf{T}^\alpha$	$[\mathrm{N/m^2}]$	overall and partial Cauchy (true) stress tensor of φ and φ^α
$\mathbf{T}^\alpha_E$	$[\mathrm{N/m^2}]$	partial Cauchy extra stress tensor of φ^α

$\mathbf{T}^S_{E,\,\mathrm{iso}}$	$[\,\mathrm{N/m^2}\,]$	isotropic contribution to the solid's extra stresses $\mathbf{T}^S_E$
$\mathbf{T}^S_{E,\,\mathrm{aniso}}$	$[\,\mathrm{N/m^2}\,]$	anisotropic contribution to the solid's extra stresses $\mathbf{T}^S_E$
$\mathbf{U}_\alpha$, $\mathbf{V}_\alpha$	$[\,\text{-}\,]$	right and left stretch tensors of the polar decomposition of $\mathbf{F}_\alpha$
$\mathbf{W}_\alpha$	$[\,\cdot/\mathrm{s}\,]$	skew-symmetric spin tensor

Calligraphic letters

Symbol	Unit	Description
$\mathcal{A}^{\mathrm{dof}}$		ansatz (trial) functions of the primary variables
$\mathcal{B}$, $\mathcal{B}^\alpha$		aggregate body and body of the constituent φ^α
$\mathcal{D}$	$[\,\mathrm{J/m^3\,s}\,]$	dissipative part in the entropy inequality
$\mathcal{G}_{\mathrm{dof}}$		weak formulation of a governing equation related to a dof
$\mathcal{H}$	$[\,\mathrm{J/K}\,]$	entropy in a body $\mathcal{B}$
$\mathcal{H}^1(\Omega)$		Sobolev space
$\mathcal{I}_S$	$[\,\text{-}\,]$	set of scalar basic and mixed invariants of $\mathbf{C}_S$ and $\boldsymbol{\mathcal{M}}^S_a$
$\mathcal{K}$	$[\,\mathrm{kg\,m^2/s^2}\,]$	kinetic energy of a body $\mathcal{B}$
$\mathcal{L}_a$	$[\,\mathrm{N\,m/s}\,]$	external mechanical power of a body $\mathcal{B}$
$\mathcal{L}_S$	$[\,\text{-}\,]$	set of principal invariants of $\mathbf{C}_S$ or $\mathbf{B}_S$
$\mathcal{MG}_3$		symmetry group within the group of $\mathcal{O}_e$
$\mathcal{N}$		set of all nodes for the FE discretisation of Ω^h
$\mathcal{O}$		origin of a coordinate system
$\mathcal{O}_e$		group of proper orthogonal rotations
$\mathcal{P}$, $\mathcal{P}^\alpha$		material points of φ and φ^α
$\mathcal{P}^\alpha_{\mathcal{S}}$, $\mathcal{P}^\alpha_{\mathcal{B}}$		material points of φ^α on the surface $\mathcal{S}$ and inside a body $\mathcal{B}$
$\mathcal{P}$	$[\,\mathrm{N/m^2}\,]$	Lagrangean multiplier
$\mathcal{Q}_a$	$[\,\mathrm{N\,m/s}\,]$	external non-mechanical power of a body $\mathcal{B}$
$\mathcal{R}$		set of response functions
$\mathcal{s}$		reduced subset of independent process variables within $\mathcal{V}$
$\mathcal{S}$, $\mathcal{S}^\alpha$		surface of the overall and the constituent body
$\mathcal{T}^{\mathrm{dof}}$		test functions of the primary variables
$\mathcal{S}_a$	$[\,\mathrm{J/K\,s}\,]$	external change of entropy in a body $\mathcal{B}$
$\mathcal{S}_i$	$[\,\mathrm{J/K\,s}\,]$	internal entropy production in a body $\mathcal{B}$
$\mathcal{V}$		set of independent process variables
$\mathrm{D}\boldsymbol{\mathcal{F}}^k_{n+1}$		global residual tangent
$\boldsymbol{f}$		generalised force vector
$\boldsymbol{\mathcal{F}}$		vector containing the global and local system of equations
$\boldsymbol{\mathcal{G}}^h_{(\cdot)}$		abstract function vectors containing the weak forms
$\boldsymbol{k}$		generalised stiffness vector

$\boldsymbol{y}$	abstract vector containing the nodal unknowns of each dof
$\Delta\boldsymbol{y}_{n+1}^{k}$	vector of stage increments at the current Newton step k
$\boldsymbol{\mathcal{D}}$	generalised damping matrix
$\boldsymbol{K}$	generalised stiffness matrix
$\boldsymbol{\mathcal{M}}^{S}$	general structural tensor on the reference configuration
$\boldsymbol{\mathcal{M}}_{a}^{S}$	structural tensor constructed by unit fibre vectors $\mathbf{a}_{0}^{S}$

Selected acronyms

Symbol	Description
2-d	two-dimensional
3-d	three-dimensional
dof	degree of freedom
AC	actual configuration
ASCII	American standard code for information interchange
BBB	blood-brain barrier
BC	boundary condition
CB	cerebral blood pressure
CAD	computer-aided design
CED	convection-enhanced (drug) delivery
CIS	computer-integrated surgery
CNS	central nervous system
CSF	cerebrospinal fluid
(μ)CT	(micro)computed tomography
DAE	differential-algebraic equations
DOF	degrees of freedom
DTI	diffusion-tensor imaging
ECS	extracellular space
FEM	finite-element method
GBM	glioblastoma multiforme
GUI	graphical user interface
IBVP	initial-boundary-value problem
ICP	intracranial pressure
IGES	initial graphics exchange specification
IHP	interstitial hydrostatic pressure
ISF	interstitial fluid
ISO	International Organization for Standardization

LBB	Ladyshenskaya-Babuška-Brezzi
MRA	magnetic-resonance angiography
MRE	magnetic-resonance elastography
MRI	magnetic-resonance imaging
NA^+	sodium ion
NMR	nuclear-magnetic resonance
NRRD	nearly raw raster data
ODE	ordinary differential equations
PANDAS	porous media adaptive nonlinear finite element solver based on differential algebraic systems
PDE	partial differential equations
PU	partition-of-unity principle
RC	referential configuration
REV	representative elementary volume
RKI	Robert-Koch Institute
ROI	region of interest
SI	international system of units
STEP	standard for the exchange of product model data
TOF	time-of-flight
TPM	Theory of Porous Media
WHO	World Health Organization
XFEM	extended finite-element method
XTPM	extended Theory of Porous Media

Chapter 1:
Introduction and overview

1.1 Motivation

The brain is the most significant and complex organ of human beings and plays a key role as the control centre of the nervous system. This outstanding property is provided by a network of billions of neurons, which are connected to several thousand other neurons via synapses. As a result, these neurons mutually communicate by their axon terminals, carrying trains of signal pulses in order to process information and to control any behaviour of the human body. In order to maintain the functionality of the brain, the metabolic demands are regulated by the cerebral circulation, supplying all domains of the brain with the essentials. In particular, this is achieved via the perfusion of oxygenated blood as well as glucose and other nutrients through a highly branched network of blood vessels. Afterwards, the venous drainage removes the deoxygenated blood, including carbon dioxide and other metabolic products, and brings it back again to the heart.

At first glance, the brain seems to be adequately protected against external influences by the rigid skull. However, severe situations may arise if the functionality of the system is compromised within the intracranial cavity itself. For example, strokes can attack the brain's function, resulting from a local disturbance of the blood supply. Another life-threatening disease is caused by solid neoplasm, commonly known as brain tumours. The occurring abnormal growth of cells can be either malignant or benign. Malignant tumours (often denoted as cancer) grow fast and in an invasive and infiltrative manner. In contrast, benign (non-cancerous) tumours grow slower and do not spread metastases. Yet, both cases are inherently serious due to the limited space within the skull. In the majority of cases, the occurrence of a brain tumour is unexpected and not influenced by any risk factor. Hence, it can generally affect anyone. Frequently, medical examinations due to, e. g., epileptic shocks or unexplained headaches, result in the diagnosis of a brain tumour. Certainly, this causes an incredibly demanding physical and psychological stress for the patient and his social environment. The desolate point is that the occurring processes are still not fully understood. This motivates the research rationale to circumvent and treat such serious diseases. Today, several sophisticated possibilities of medical imaging, e. g., computed tomography (CT) or magnetic resonance imaging (MRI), are provided, allowing a reliable detection of brain diseases. However, the treatment options after a medical detection often remain unsatisfactory.

It is obvious that an adequate theoretical modelling of the brain allows a simulation of the occurring biomechanical effects under certain circumstances. This contributes to a profound understanding of the complex processes within the tissue aggregate. Moreover, it provides the possibility to numerically study new medical treatment options and their clinical results in order to support and assist the practising surgeons. However, the biomechanical modelling of the brain is a challenging task. Certainly, this is caused

by the patient-specific structural complexity of the three-dimensional (3-d) anatomical shape of the brain. Moreover, the brain-tissue aggregate is a complex subject of multi-component nature with electro-chemical properties. In this respect, the tissue characteristics of the brain-matter constituents show significant anisotropic and heterogeneous properties, which require an extended description within the framework of porous materials.

1.2 State of the art, scope and aims

Humans have always felt an urge to explore the mystery of the brain to answer open questions, such as the source of behaviour or of intelligence. Therefore, it is not surprising that the history of brain research reaches back many centuries. Its origin trace back to the Ancient Egypt, where surgical interventions (such as trepanning) were already performed more than five thousand years ago, as reported in the prehistoric "Edwin Smith Papyrus", cf. the English translation of Breasted [30]. This hieroglyphic text is supposed to be the oldest known surgical treatise report, including also first anatomical descriptions of the human brain. In Ancient Times and the Middle Ages, the gain of knowledge became nearly impossible, not least due to the prohibition of anatomical dissections preserved by religious and political authorities. This circumstance crucially changed in the Age of Renaissance, which is characterised by a strong scientific drive. In this regard, the Italian polymath Leonardo da Vinci explored the cranial cavity with liquid wax and prepared laborious graphical representations of the brain during the fifteenth century, cf. the historical review of Tamaraz & Comair [156]. A further important pioneer of neuroanatomy was Thomas Willis, an English doctor living in the seventeenth century. Surely, his major contribution was the discovery of the vascular supply at the brain's base via a circle of arteries, the so-called "Circle of Willis" (named after him). Over time, the anatomical structure of the brain has been studied increasingly. A remarkable step forward was made by the upcoming modern medical imaging methods in the twentieth century, such as the application of CT or MRI, enabling an accurate in-vivo visualisation. Today, it can be said that the anatomy of the human brain is fully explored. Hence, the current anatomical knowledge is provided in a comprehensive manner in several textbooks, cf., e. g., Lippert [100], Schünke *et al.* [142] or Tamaraz & Comair [156].

The intended material modelling of the brain's tissue, within the scope of this monograph, basically aims at other issues, rather than brain imaging purposes or the currently high-recognised neuro-scientific projects, such as, e. g., the "Human Brain Project[1]". This initiative faces the complete reconstruction of a human brain using supercomputers in order to mimic the brain's architecture and its functionality.

In contrast to primary load-bearing parts of the human body, e. g. bones or muscles, studies concerning the mechanical behaviour of the (non-load-transmitting) soft brain tissue started only fifty years ago. First, studies concentrated on animals, e. g., on the whole

[1]The Human Brain Project (see http://www.humanbrainproject.eu for detailed information) is a ten-year one billion Euro Flagship initiative of the European Commission headed by Henry Markram, which is also the director of the "Blue Brain Project" at the École Polytechnique Fédérale de Lausanne.

porcine brain (Franke [68]). Only in recent years, initial studies related to human brain tissue were realised by Fallenstein *et al.* [65]. In this contribution, the authors studied the dynamic shear properties using in-vitro tissue samples. Thereby, the experimental results already indicate a change in the mechanical behaviour during the post-mortem time. Subsequently, various further experiments and measuring devices were applied to (porcine) brain tissue in confined and unconfined compression, as well as in tension, by the group of Miller, cf., e. g., Miller [111] and Miller & Chinzei [112, 113]. As a result, a non-linear stress-strain relation and a strong strain-rate dependence were found and the description using a visco-elastic and single-phasic continuum was proposed. Moreover, Miller & Chinzei [113] indicated that the material behaviour of brain tissue is completely different in an extension or in a compression state. These issues already indicate a complex material behaviour, but further specific properties of the tissue aggregate need to be considered. In particular, Margulies & Prange [104] reported anisotropic properties of brain tissue for small sample sizes at the length-scale of millimetres. At such a small length-scale, the fibrous nature causes direction-dependent tissue properties which can also influence the macroscopical response, regarding the deformation as well as the flow and diffusion behaviour. In order to identify the tissue's microstructure, the establishment of the so-called "Diffusion Tensor Imaging (DTI)" represents a milestone in the middle of the nineties, cf., e. g., Basser *et al.* [12] or Le Bihan *et al.* [94]. This medical imaging application provides an in-vivo and non-invasive possibility for the tracking of fibres within the brain's nervous tissue, cf., e. g., Basser *et al.* [13]. Moreover, the identification of permeability characteristics of the tissue skeleton is feasible, cf. Tuch *et al.* [161].

During the historical development of the first theoretical models, which were mainly related to the hydrocephalus problem, researchers always discussed intensively whether to use singlephasic or multiphasic models for a proper description of the mechanical behaviour of the soft brain tissue, cf. Dutta-Roy *et al.* [41], Franceschini *et al.* [67], Miller [110], Taylor & Miller [157]. Certainly, the most appropriate choice of the model is always based on the requirements of the intended application. From a physiological and anatomical point of view, the multicomponent nature of brain tissue appears straightforward. Moreover, it is necessary for the issues under consideration to describe processes occurring within the tissue aggregate. Thus, only multicomponent models are considered for the purpose of this monograph. In this regard, the origin of multicomponental considerations trace back to Hakim & Adams [73] who stated in 1965 that the occurring effects during hydrocephalus can only be described by the interplay of several brain-tissue components. Heading in the same direction, Fallenstein *et al.* [65] use the analogy that the overall brain might be considered as an inflated or pressurised structure with a tough covering and filled with a gel-like material. Moreover, they assumed that the large number of blood vessels, which are under pressure, help to lend rigidity to the soft brain structure. The first mathematical approach, assuming the brain matter to be a porous medium containing a viscous fluid in the extra-cellular space (ECS) was carried out by Nagashima *et al.* [118] and Tada & Nagashima [155] in 1987. These contributions were complemented by a course numerical study of a two-dimensional (2-d) brain slice. In recent years, experimental studies were carried out by the group of Holzapfel [67] on dead human brain tissue and gave evidence to an (at least) biphasic nature. For this purpose, a uni-axial strain machine with properly defined draining conditions was used. Consequently, it was

possible to distinguish between a viscous behaviour of a singlephasic material and an ongoing consolidation process of a multiphasic material. The work of Franceschini *et al.* [67] also provides a modelling approach for dead human brain tissue. In this regard, the compartments of the brain-tissue skeleton and the interstitial fluid were incorporated in the proposed model, but the blood constituent was omitted. This was sufficient for the in-vitro studies considered in Franceschini *et al.* [67] but represents a somehow incomplete approach for in-vivo studies of human brain tissue, which is still used in recent simulations of human brain tissue. In this regard, a complete modelling approach should also include the blood constituent in a fully coupled manner in order to describe in-vivo brain tissue properly. Initial biphasic approaches have already been applied to blood perfusion of biological tissue in terms of hierarchical porous media, cf. Vankan *et al.* [162, 163]. Recently, Linninger *et al.* [96] focused on a detailed micromechanical modelling of the cortical microcirculatory system to study the oxygen exchange between the blood vessels and the brain cells. As a result, extremely complex geometrical structures need to be (semi-automatically) reconstructed, due to the highly branched blood-vessel system.

Hence, a macroscopical modelling of the complex brain-tissue aggregate appears suitable. In order to be able to describe flow and transport processes within the extracellular matrix essentially motivates the application of the Theory of Porous Media (TPM), cf. the fundamental works of Bowen [26, 27, 28], de Boer [20, 21, 22] and Ehlers [44, 50, 51]. Meanwhile, a wide field of biomechanical applications of the TPM have been derived. Such as the works of, e. g., Ricken *et al.* [133] and Ricken & Bluhm [130] for remodelling and growth phenomena of biological tissues, Acartürk [3] and Ehlers [51] for swelling processes of electro-chemically active materials, Ehlers *et al.* [55, 56] and Karajan [87] for intervertebral disc mechanics or Ricken *et al.* [132] for the modelling of liver perfusion characteristics, just to name a few. Relevant fundamentals can also be adopted from the wide field of geomechanical problems, such as flow and transport processes in unsaturated soils, cf., e. g., the monograph of Graf [70] or Ehlers [51]. For the numerical investigation of the arising coupled problems of porous materials within a finite-element (FE) solution procedure, the capabilities of the research code PANDAS[2] are of immense benefit for the implementation of TPM-models. In this regard, fundamental works were subsequently developed at the Institute of Applied Mechanics (Continuum Mechanics) at the University of Stuttgart, cf., e. g., Ehlers & Ellsiepen [53], Ellsiepen [63] and Ammann [7].

In terms of the drug-delivery problem for the treatment of brain diseases, such as tumours, remarkable research developed in the last decades. The selective properties of the vascular walls within an intravascular medication and the limited spatial distribution of therapeutics via purely diffusion from intracranial implants, cf., e. g., Bobo *et al.* [18], Groothuis *et al.* [72] and Kawakami *et al.* [88], motivated the direct (invasive) infusion for a targeted and effective therapeutical administration. This so-called convection-enhanced drug delivery (CED) was proposed in a pioneering work by Bobo *et al.* [18] in the early nineties. Therein, the application of CED was demonstrated at cats. Subsequently, Blasberg *et al.* [16] applied this promising method to rhesus monkeys, representing anthropoid primates. Basically, these purely experimental investigations were carried out in the manner of trial

[2] Porous media Adaptive Nonlinear finite element solver based on Differential Algebraic Systems, cf. Ellsiepen [63], the manual [1] and http://www.get-pandas.com .

and error tests, where infusions were made in several (somehow arbitrary) regions and analysed in order to gain knowledge of the arising distribution profile. Only three years after the foundation of CED, first trials on humans were investigated, cf. Laske *et al.* [93]. These studies highlighted a great potential for the clinical application and, hence, preclinical studies and clinical trials were continued and reported, e. g., by Hall *et al.* [74], Kunwar *et al.* [92], Shahar *et al.* [144] and Voges *et al.* [165]. Nowadays, however, the application of CED is still far away from being a standard medical procedure, when it comes to the treatment of brain tumours. Instead, the conventional treatment options are still preferred, proceeding (if possible) from a (complete) removal of the tumour in combination with the opportunities of radiotherapy and chemotherapy. For a comprehensive review on CED the interested reader is referred to, e. g., Ding *et al.* [39], Raghavan *et al.* [125], Vogelbaum [164] and citations therein. Within these reviews, issues concerning the administered drugs, accompanying medical imaging techniques to monitor drug delivery (e. g., Mehta *et al.* [109]) and recent computer simulations (assisting the implementation of catheters in patients) are discussed in detail.

Until now, various modelling approaches were developed for the prognosis of a CED-intervention. For example, analytical ones by Basser [11], Morrison *et al.* [116], Kaczmarek *et al.* [85], Smith & Humphrey [147] or Wirth & Sobey [171] on (cylindrically or spherically) symmetrical models of the brain. In order to verify and validate such distribution models, accompanying isotropic experiments with brain-phantom (agarose) gels were realised, e. g., by Chen *et al.* [35], Darcis [37], Ivanchenko *et al.* [81] and Sindhwani *et al.* [146]. More enhanced theoretical and numerical models, including also the possibility to estimate anisotropic tissue permeabilities and drug diffusivities, e. g. based on medical (DTI) data, are investigated by, e. g., Linninger *et al.* [97, 98, 99], Støverud *et al.* [152], Ehlers & Wagner [59, 60] and Wagner & Ehlers [168, 169, 170]. Voxelised models exhibiting a fixed computation mesh related to the medical-imaging resolution are developed by, e. g., Sarntinoranont *et al.* [135], Chen & Sarntinoranont [34], Kim *et al.* [91], Pishko *et al.* [123] or Magdoom *et al.* [103]. Presently, the possibility to simulate an infusion process is also provided by the commercial surgical planning software iPlan®Flow[3]. Hence, the prediction of drug distribution in human brain tissue seems to be achieved. Nevertheless, up to now these investigations are somehow insufficient to describe the CED process and the accompanying effects in its entirety. To the author's best knowledge, the underlying model (and simulation algorithm) of the above mentioned software was initially given by Morrison *et al.* [116] and further specified in Chen *et al.* [35] and Sampson *et al.* [134]. As described in Sampson *et al.* [134], the distribution of the infused therapeutic agent is computed via the volume balance (volume conservation) of the incompressible interstitial fluid. Therein, the so-called "Darcy filter law" is used for the fluid velocity field, describing the flow in a porous material. In a second equation, the temporal change of the drug's concentration is approximated by the summation of diffusion, changes caused by convection and losses. Afterwards, this set of equations is sequentially solved in a decoupled manner. The influence of a solid deformation is only considered in a pre-calculation step, where the pressure distribution along the catheter shaft is evaluated with a poroelastic model (Morrison *et al.* [115]) and subsequently applied via boundary conditions to the

[3]BrainLAB, Feldkirchen, Germany, cf. http://www.brainlab.com .

adopted volume balance.

In conclusion, one of the factors that has not been adequately addressed so far is the influence of the tissue deformation. In the case of a bolus (or a prolonged) injection of a liquid (therapeutical) volume into the somehow confined domain of the skull, which is equipped by the fully saturated tissue, inevitably results in solid deformations. Therefore, it is generally necessary to include deformation effects. In addition, space-demanding processes, e. g. caused by cerebral oedema, hydrocephalus (Lewin [95]), tumour growth or even actively initiated by computer-integrated surgery (CIS), may result in large but quasi-static deformations. Hence, the tissue properties and the spreading of an infused therapeutic agent may be influenced. Beyond that, there are still several open questions, e. g., concerning further significantly influencing effects or the proper description of the deformable porous tissue and its entire pore content in a fully coupled manner. In this regard, a thermodynamically consistent constitutive framework and a numerical investigation to solve the arising set of coupled partial differential equations in a monolithic manner are still missing. Such a framework is desirable in order to apply it to all interaction processes occurring during an infusion process into the brain tissue. Therefore, the scope of this monograph is the development of a versatile simulation tool, which is based on a sophisticated continuum-mechanical modelling approach for the complex multicomponent tissue aggregate. By this means, the numerical investigations provide a virtual testbed for the computational study of various issues, such as, e. g., the material behaviour combined with flow and diffusion states under prescribed conditions. In order to face clinically relevant applications for the treatment of serious brain-cancer diseases, a specific focus is placed on drug-delivery purposes within the brain-tissue. Thus, a suitable model requires to include all relevant physical components. Consequently, it is based on the well-founded TPM in order to describe the multicomponent nature of brain tissue in a comprehensive and elegant manner. In particular, a finite anisotropic material model of the brain's solid skeleton is derived. Furthermore, it additionally includes the overall interstitial fluid mixture and the blood constituent. Since the tissue aggregate exhibits anisotropic and heterogeneous properties, microscopical tissue characteristics are considered via suitable medical-imaging data. The ambitious aim of this thesis is to contribute, at least in parts, to the solution of open questions, remaining in the important and fascinating field of brain-tumour therapies. Beyond these issues, the opportunity to study further relevant diseases or enhance the level of complexity is generally given. As a consequence from numerical studies, such as the distribution of infused therapeutic agents, the practising surgeon can be pre-operatively assisted in planning the medical intervention and foster his decisions.

1.3 Outline of the thesis

After this introductory **Chapter 1**, the relevant anatomical and physiological aspects of the human brain are briefly summarised in **Chapter 2**. Therein, the main focus is placed on the composition of the brain's tissue-aggregate and the specific characteristics of its components, as far as needed for the modelling approach. The research rationale is considered by means of tumour diseases and their current treatment options. Related

medical-imaging methods are introduced, which enable an insight into living tissues and, therefore, provide the possibility for a patient-specific determination of material parameters.

The continuum-mechanical fundamentals, required for the description of the brain matter, are given in **Chapter 3**. Therefore, the basic concept of the TPM is applied to the multicomponent tissue-aggregate. In particular, a four-constituent model is investigated, which consists of three immiscible phases and one miscible component. The immiscible phases of the tissue-aggregate are represented by the solid skeleton (i. e. the glial and nervous tissue cells in a compound with the vascular walls), the blood (in the vessels) and the overall interstitial fluid (in the ECS). Moreover, the interstitial fluid is constituted by a liquid solvent and a dissolved therapeutic solute (as a result of a medical administration). For this purpose, elements of the Theory of Mixtures are embedded in the standard TPM in order to enable the description of miscible components. Furthermore, the kinematical relations of superimposed constituents are provided, and the balance equations for the overall aggregate as well as for its particular constituents are presented.

In **Chapter 4**, the specific adaptation of the material-independent balance equations by an appropriate constitutive setting is discussed. Therefore, constitutive relations (response functions) are derived, which describe the characteristic material behaviour of the brain's tissue. In this regard, the constitutive assumptions for the constituents involved, is examined by means of a thermodynamically consistent framework in terms of an evaluation process of the entropy inequality. Concluding remarks comment on the closure problem of the fully coupled continuum-biomechanical problem.

On this basis, the objective of **Chapter 5** is the numerical realisation of the developed theoretical model. Therefore, the finite-element method is chosen as a suitable numerical methodology to approximate the solution of the arising set of coupled partial differential equations. For this purpose, the weak formulations of the governing balance relations are discretised in space and time. This numerical chapter is concluded by the description of the applied monolithic solution strategy.

The application of the derived theoretical and numerical investigations to the human brain is carried out in **Chapter 6**. Therein, capabilities for a patient-specific estimation of required simulation parameters, such as local (anisotropic) permeabilities and diffusivities, are studied in detail. Next, the possibilities for a customised creation of geometries for the simulation of realistic initial-boundary-value problems are discussed. This finally allows the study of selected numerical examples, demonstrating the feasibility of the presented modelling approach. These examples start with the basic material behaviour of brain tissue and then face the invasive delivery process of therapeutics (CED). In this regard, the therapeutical distribution is shown at a realistic 3-d brain hemisphere and, afterwards, discussed in detail at a simplified (quasi 2-d) horizontal slice. Furthermore, a grid convergence study for different finite-element discretisations and a survey on the influence (by a local numerical sensitivity analysis) of several involved simulation parameters is examined. The chapter is closed by pointing out further effects, which may have an influence on the efficiency of the therapeutical distribution, such as backflow.

Finally, a summary and an outlook are given in **Chapter 7**, reflecting the presented contribution and showing the extension potential of the proposed model.

For the sake of convenience, additional information regarding the mathematical aspects of tensor calculus required in this monograph are collected in **Appendix A**. Further mechanical supplements are given in **Appendix B**.

Chapter 2:
Anatomy and physiology of the human brain

The purpose of this chapter is to review the basic anatomy and physiology of the human brain by means of introducing relevant issues for the continuum-mechanical modelling, discussed in Chapter 3. Therefore, the anatomy and physiology are summarised, as a short excerpt from comprehensive medical literature, cf., e. g., Gray [71], Lippert [100] or Schünke *et al.* [142]. In addition, a useful introduction into the considered topics is given by Brooks *et al.* [32] and Schlegel & Wiestler [139]. Afterwards, this chapter provides an overview about brain-tumour diseases occurring in the human brain tissue, complemented by its treatment limitations and restrictions. Finally, several relevant medical-imaging techniques, which provide the possibility to explore the brain-tissue characteristics are briefly assessed.

2.1 Composition of the human brain

The human brain constitutes the upper part of the central nervous system (CNS), which is responsible for a variety of tasks such as the processing of sensory impressions or the coordination of complex behaviours. Consequently, it is without doubt the most important organ of human beings. All other organs can be transplanted in principle and today the death of a human is generally identified with the death of its brain.

The human brain is located in the rigid skull, cf. Figure 2.1 (a). This rigid boundary provides a reliable protection against external influences. However, this also implies that space-consuming diseases within the rigid skull cannot be compensated and may result in life-threatening intracranial pressure increases. The domain between the skull and the brain's surface is covered by basically three meninges. Therein, the cerebrospinal fluid (CSF) is situated in the subarachnoidal space of the cranial meninges and encompasses the entire brain. Basically, the CSF protects the delicate brain from vibrations and somehow

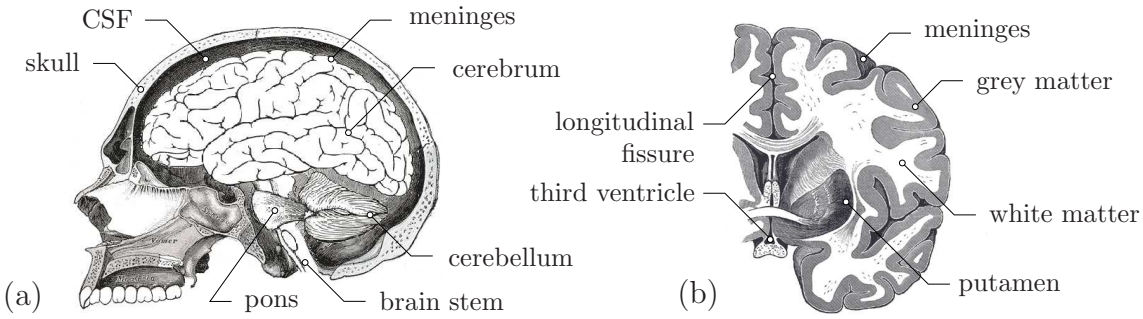

Figure 2.1: *(a) sketch of the human brain situated in the rigid skull and (b) coronal section of the brain. Lithographs are taken from Gray's Anatomy [71].*

provides a weightlessness[1], preventing the brain of stress peaks which would occur in the case of bearing. Furthermore, the CSF is also found in filled inner cavities of the brain, the so-called ventricles. As shown in Figure 2.1 (a), the macroscopical parts of the brain are given by the cerebrum, the cerebellum and the brain stem. The cerebrum occupies the main part of the intracranial domain and can be regarded as an assembly of several lobes, which are assigned by means of specific areas of responsibility. The cerebellum plays a central role in the coordination of body motion and the brain stem provides the nervous pathway connections between the human brain and the spinal cord. Additionally, the brain-tissue is entirely interveined by the complex blood-vessel system.

2.1.1 Neuroanatomical fundamentals

Commonly, the brain tissue is generally segmented into grey- and white-matter regions, cf. Figure 2.1 (b). This is motivated by the circumstance that freshly cut brain tissue exhibits areas which are coloured grey or white. In general, the grey matter is located at the cerebral cortex of the brain and encloses the white-matter tracts in the inside of the brain. The grey matter is composed of a complex dense network of interconnected cell bodies. Whereas, the information-transmitting extensions of the nervous cells bridge the white-matter regions by their myelinated axons.

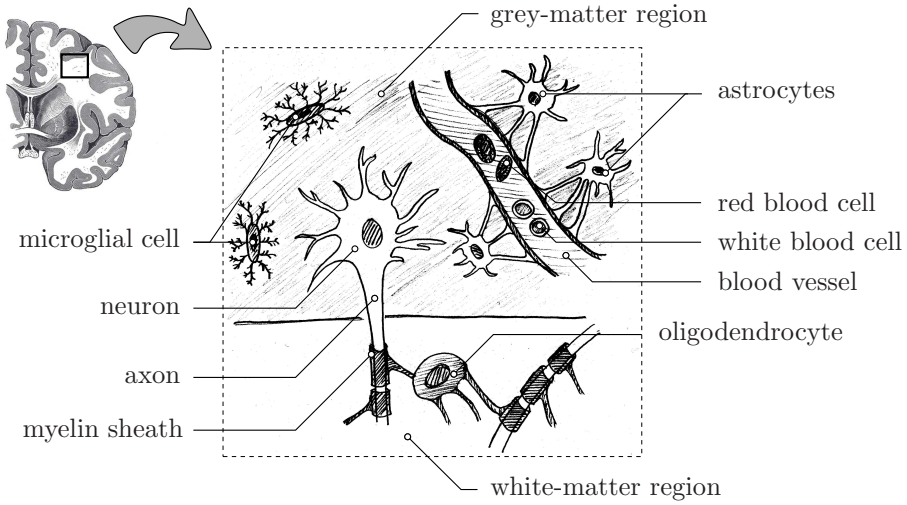

Figure 2.2: *Schematic illustration of the microscopical composition of the human brain tissue aggregate with different cell types, based on Brooks et al. [32].*

In general, the brain tissue consists of several cell types, cf. Figure 2.2. For the functionality and the structure of the brain, the most important ones are the nerve cells (neurons) and the glial cells, respectively, cf. Brooks *et al.* [32]. Moreover, there are various other cell types, such as the endothelial cells coating the vasculature from the inside, the ependyma cells coating the ventricles and the blood cells. However, the nervous system is in fact characterised by its nerve cells of varying shape and size, communicating with each other

[1]To be more precise, this is only valid for the overall brain since the gravitation acts on the volume of the brain, whereas, the pressure of the CSF is acting at the brain's surface.

through synaptic transmission. Yet, the majority of cells in the brain tissue are glial cells, which can be subdivided into three functionally distinct types. The astrocytes represent the most common type and play an important role by means of supporting cells for the neurons and surrounding the blood vessels of the brain. The second major type of glial cells are the oligodendrocytes, which form the myelin sheath that surrounds the axons of the neurons. The high-fat content of myelin gives it a white appearance in brain tissue and led to the above mentioned term white matter. Finally, the microglial cells take over tasks in the immune defense of the nervous system.

2.1.2 Blood-vessel system

The brain is highly vascularised by the well-branched blood-vessel system. The average distance between a microvessel and a neuron in the brain's grey matter is approximately $20\,\mu$m. This is in particular necessary, since the blood-vessel system is, e. g., responsible for an overall oxygen transport and provides the evacuation of pollutants. However, the averaged blood volume fraction of the overall brain's volume results an amount less than 3 % for healthy tissues, cf. Syková & Nicholson [154] and citations therein. In general, the blood supply is guaranteed by a complex system of cerebral arteries, which form an arterial circle (circle of Willis) at the base of the brain. Proceeding from there, the arteries supply all parts of the brain with blood, cf., e. g., Duvernoy *et al.* [42] or Schünke *et al.* [142]. In particular, the blood perfuses the nervous tissue subsequently from the arteries through the capillaries and is finally drained by the veins. Hereby, the blood flow is mainly driven by the pressure gradient of the cardiovascular system. Hence, a pulsatile effect can be measured in the arteries, which is widely damped via passing the arterioles. Moreover, the blood pressure is high in arteries and decreases through passing the capillary bed to low pressure values in the veins, cf., e. g., Cacioppo *et al.* [33]. Due to its corresponding tasks, the blood velocity is relatively high in arterioles and veins (providing an effective blood transport) and very low in the capillary bed (allowing for an exchange with the surrounding tissue).

2.1.3 Microscopical tissue composition and fluid spaces

At this point, the brain-tissue spaces, which are of specific interest, are introduced here for the sake of clarity. In particular, these are the interstitial fluid space, the intra- and extracellular space as well as the intra- and extravascular space, cf. Figure 2.3.

The attributes of the ECS are completely described in the review of Syková & Nicholson [154]. For the purpose in this monograph, all relevant issues are introduced in a compact manner. The ECS is filled by the interstitial fluid, where a bridge to the CSF is given at the surfaces of the ventricles. Thus, these fluids exhibit a similar composition. In total, the ECS typically occupies a volume fraction of 20 % of the brain's volume. However, this can vary between 15 % and 30 % and even falls to 5 % during global ischaemia. In order to maintain the functionality of the brain, the ECS provides a sufficient amount of extracellular ions, which is necessary for a stable electrical signalling of the nervous cells. Furthermore, this includes the possibility for diffusion, as well as a combined bulk-flow

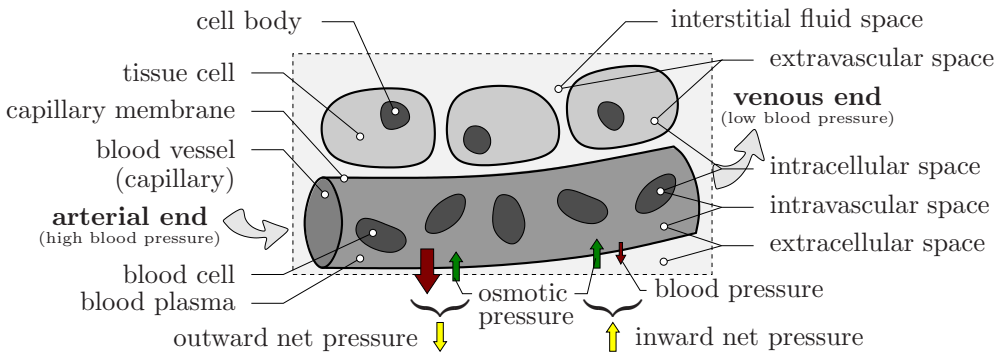

Figure 2.3: *Sketch of different fluid spaces and microscopical composition in the capillary bed of the brain tissue.*

transport of substances within the interstitial fluid through the connected pore space of the ECS, cf. Abbott [2].

In general, the capillary membrane (wall) is highly selective and governs the passing of molecules from the intravascular to the extravascular space. The movement of substances across the so-called blood-brain barrier (BBB) generally occurs due to a difference between the blood pressure and the osmotic pressure in the capillary bed. Thereby, substances are expelled from the capillary by means of clefts at the arterial end, and are taken into the vessels again at the venous end. In particular, this is caused by the circumstance that the blood pressure at the arterial side is higher than the osmotic pressure, resulting in a net outward pressure. Therefore, the brain tissue is supplied by the required oxygen and nutrients. In contrast, the blood pressure at the venous side is lower than the osmotic pressure, thus the blood can absorb metabolic products from the extra-vascular space. In this regard, the net movement between the intra- and extravascular compartments could be described via the Starling equation, cf., e. g., Kedem & Katchalsky [89] or Jain [82].

The cerebral blood pressure (CB) denotes the pressure in the vascular system and depends on its hierarchical position. The range in the capillary bed varies between 10 mmHg[2] (1333 N/m^2) at the venous end and 30 mmHg (4000 N/m^2) at the arterial end. The intracranial pressure (ICP) is known as the pressure in the CSF occurring in the mobile liquid around the brain. Normal values range from 0 to 10 mmHg (0 - 1333 N/m^2). In this context, an abnormal increase in the interstitial fluid is called edema. The interstitial hydrostatic pressure (IHP) describes the liquid pressure in the interstitial fluid space (tissue pressure) and has a normal value of 6 mmHg (800 N/m^2).

2.2 Tumour diseases in human brain tissue

The colloquially used expression “cancer” is the generic name for malignant neoplasms or tumours, caused by changes in the cell structures. In general, cancers of the cen-

[2]Due to clinical measurements, pressures are often given in millimetres of mercury (mmHg). This manometric unit descends from the excess pressure, generated by a one-millimetre column of mercury. One mmHg corresponds to 133.322387415 N/m^2. Even though it is not an SI unit, mmHg is still routinely used in the field of medicine.

tral nervous system (CNS) affect the brain up to 95% of brain cancer diseases. These changes influence the genome of the involved cells and can cause a faster cell division, compromising the surrounding tissue. The current state of research does not allow any statement about environmental or lifestyle influences, cf., e. g., the study by the Robert-Koch Institute (RKI) [84]. This means, that there is no verified relationship with, e. g., smoking, excessive alcohol consumption or the use of mobile phones. Rather, as known for other cancer diseases, genetic factors can play a role. However, it is difficult to assess its contribution to the individual human being. In general, cancer diseases in the brain are relatively rare, cf. Figure 2.4, but may occur at any age and are responsible for more than 20 % of all cancers in infancy. In Germany, approximately 7000 people are diagnosed with brain tumours each year, cf. Kaatsch *et al.* [84] or Schlegel & Wiestler [139]. This represents only 1.5 % of all occurring cancer cases, cf. Figure 2.4 (b), which is relatively low in relation to other cancer diseases, such as, e. g. lung cancer. However, the cases of death resulting from cancer in the CNS with 2.6 % are significantly higher, cf. Figure 2.4 (c). This may indicate the still inadequate treatment options for brain tumours in comparison to cancer diseases situated at other sites. These representative statistics, evaluated for Germany by the RKI [84], are generally comparable to other industrialised western countries. For instance, the World Health Organization (WHO) reports for the United States [40] an overall incidence rate of 20.59 per 100000 people affected by primary brain tumours. Brain tumours, indicated by abnormal growth of cells, result an intracranial solid neoplasm in the inside of the skull, which affects the brain directly or

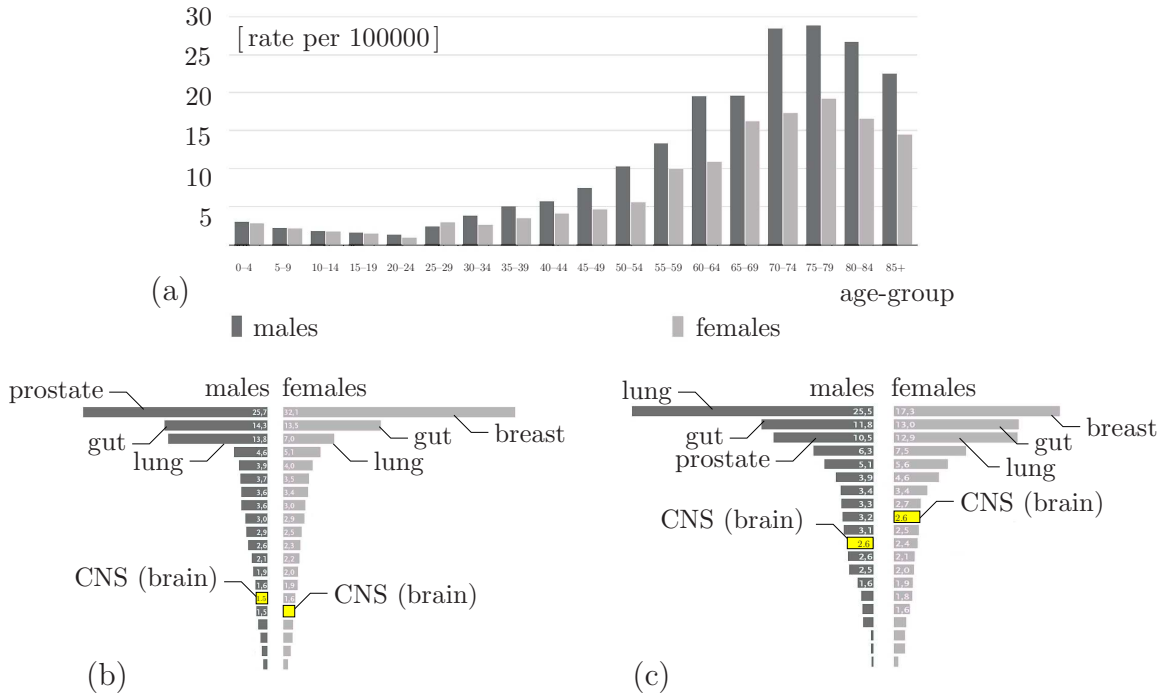

Figure 2.4: *(a) age-specific morbidity rate of cancers of the central nervous system (ICD-10 C70-72), (b) percentage of frequent tumour sites in newly diagnosed cancer patients and (c) percentage of frequent tumour sites of all cancer deaths. Excerpt of the 2007/2008 report of cancer in Germany, published by the RKI [84].*

indirectly. In any case, each kind of tumour growth seriously affects the brain and causes a life-threatening situation. The particular classification of specific brain tumours is based on the type of cell from which the brain tumour has developed. The most frequently used brain-tumour classification (WHO classification) provides four different degrees (grade I - IV) according to the seriousness of the disease. In conclusion, WHO grade I denotes a very benign, slow-growing tumour with a favourable prognosis, whereas, a WHO grade IV tumour represents a malignant, fast-growing tumour with a poor prognosis. This kind of classification guides the necessary treatment options. Usually, WHO grade I tumours are preferably treated by a surgical removal, whereas WHO grade IV tumours are additionally treated by radiation, mostly in combination with chemotherapy.

The most common primary brain tumours in adults are gliomas and meningiomas. However, brain tumours may also spread from cancers primarily located in other organs denoted as brain metastases. Moreover, medulloblastoma is a frequent tumour disease which may arise in the cerebellum during childhood. In general, nervous cells do not divide after birth and cause extremely rare brain tumours, which are known as neuromas and usually consist of nerve fibres. As mentioned above, gliomas represent the majority of brain tumours and account for about half of all diseases. These gliomas arise from the glial cells. In this regard, a subdivision into gliomas stemming from astrocytes, oligodendrocytes or ependymal cells is carried out. Most frequent are the astrocytomas, which may occur in each of the four WHO-classification grades. An especially malignant tumour representative of WHO grade IV is the so-called glioblastoma multiforme (GBM), which unfortunately is also the most frequently occurring glioma.

2.3 Brain tumour treatment and its limitations

In general, the treatment of cancer improves, but there is still an urgent clinical need for advanced therapies to oppose brain tumours such as the GBM. After a medical finding, the conventional treatment proceeds from a highly invasive removal of the tumour in a combination with radiotherapy or chemotherapy. However, the healing process is still

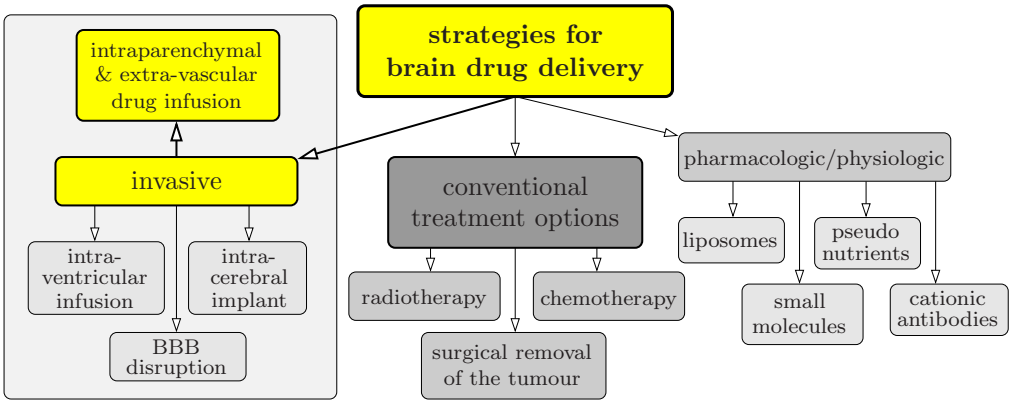

Figure 2.5: *Strategies for brain drug delivery, adjusted based on Pardridge [121]. The route of strategy of studied applications within this monograph is colour-coded in yellow.*

unsatisfactory since malignant tumours are strongly resistant and regrowth occurs frequently. In this regard, the work of Pardridge [121] provides a good overview concerning several strategies for brain drug delivery, which is illustrated in Figure 2.5. Basically, it is assumed that a suitable therapeutic agent, which is able to reach a malignant brain tumour, can have the desired treatment effect. However, the main issue lies in the question how to transport the drug to the targeted brain region. Unfortunately, the GBM under consideration is commonly situated deep within the brain, close to the corpus callosum, cf. Figure 2.6 (a). Due to this circumstance, it is highly challenging for the practising surgeon to reach the affected domain without compromising the functionality of the nervous tissue. Moreover, it is well known that the BBB is highly selective and prohibits the passing of molecules with high molecular masses from the intravascular to the extravascular space, cf. Figure 2.6 (b). Without any disruption of the BBB, this excludes the possibility

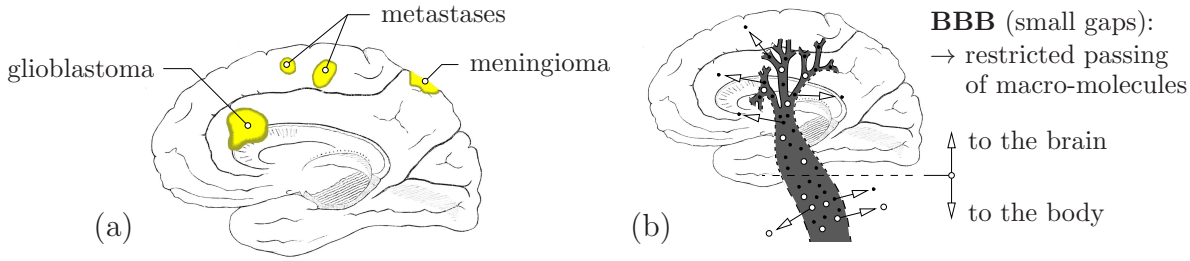

Figure 2.6: *(a) sketch of brain tumour locations and (b) limitations and characteristics of an intra-vascular medication.*

of an intravenous application of commonly used macromolecular therapeutic agents via the blood circulation to the target area. Furthermore, an intraventricular drug infusion is also an unsuitable option for the drug delivery to the brain parenchyma. A possible solution for the drug-delivery problem is provided by the direct insertion of therapeutic agents into the extra-vascular space in order to bypass the BBB. Herein, two different basic approaches can be distinguished, the intracerebral implantation of release systems, on the one hand, and the intracerebral parenchymal infusion of a solution containing the dissolved therapeutic agent, on the other hand. Implants are disapproved in comparison to infusions, since they allow the delivery of drugs only in a very limited environment as shown in Figure 2.7 (a) and discussed in, e. g., Bobo *et al.* [18], Groothuis *et al.* [72] or Kawakami *et al.* [88]. Therefore, the direct therapeutical infusion represents a promising approach and is studied in detail within this monograph.

2.3.1 Convection-enhanced drug delivery

The direct application of an extra-vascular drug infusion into the brain parenchyma is generally known as convection-enhanced drug delivery (CED) and was proposed in a fundamental paper of Bobo *et al.* [18] in the early nineties. It is astonishing that such a theoretically promising approach has not been established in current brain tumour treatment. Presumably, the main reason for this may be found in the lack of reliable prediction of the therapeutical spreading. Certainly, the main attention in this monograph is placed

on the treatment options of this pioneering method for malignant tumour diseases. However, several other serious diseases, e. g., epilepsy or Parkinson's desease, could also be treated by CED therapies. A detailed and comprehensive review on CED is provided by, e. g., the work of Ding *et al.* [39] and citations therein, which discusses the developed principles to model CED, administered experimental drugs, medical imaging techniques to monitor the drug delivery and investigated computer simulations assisting the implementation of CED catheters in patients. The treatment foresees the practising surgeon to

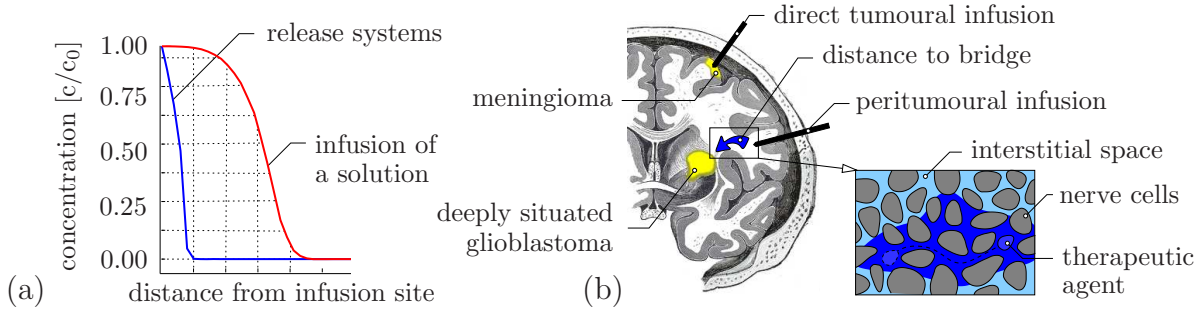

Figure 2.7: *(a) qualitative comparison of diffusion-driven (release system) and convection-enhanced (infusion) distribution. (b) illustration of the drug infusion set-up within convection-enhanced drug delivery and exemplarily therapeutic spreading of macromolecular drugs.*

drill small holes into the skull and to place up to four infusion catheters directly into the extravascular space of the brain parenchyma. A pressure gradient generated by external medical pumps initiates an interstitial fluid flow and, therewith, the distribution of the therapeutic agents. Within a long-lasting infusion, large target areas can be supplied, cf. Figure 2.7 (a). However, the prediction of the distribution profile remains challenging since the spreading is affected by the complex nature of living brain tissue. In general, the infusion may be applied directly to tumours situated at the cerebral cortex or in the easy-to-reach outer domains of the brain, like meningioma or metastases, cf. Figure 2.7 (b). In the case of the deeply situated GBM, it is essential to apply the infusion in a somewhat distant application site and try to reach the GBM by transport of the infused therapeutics. In this regard, a sophisticated theoretical model of the brain's tissue support a reliable simulation tool and possesses the potential to contribute to the successful planning of a surgical intervention.

In general, the application of CED represents the last (final) treatment option and the mean of survival remains still low. However, a clinical example presented by Rainov & Heidecke [126] reports on a 27-year-old male patient with a recurrent malignant glioma after surgery and adjuvant radiation and chemotherapy. The recurrence was treated with an intratumoral infusion via CED. This treatment resulted in a long-term survival of three years.

2.4 Imaging brain tissue characteristics

With regard to the constitutive modelling of the brain's tissue, there are several possibilities to explore the brain tissue in vivo via medical-imaging tools. The relevant techniques

are briefly summarised in this subsection.

To start with, **magnetic resonance imaging (MRI)** is a medical-imaging technique which is mainly used in the diagnosis of hydrated biological tissues, cf., e. g., Effelsberg [43]. MRI bases on nuclear magnetic resonance (NMR), cf. Schick [138]. With respect to the brain, MRI images provide a good contrast, due to the fact that brain tissue consists of a lot of water. Hence, the included protons get aligned within the applied magnetic field. Therefore, MRI is especially useful for imaging the brain in comparison to other commonly used medical-imaging techniques such as **computed tomography (CT)** or **X-rays**, which are widely used for bony structures. In contrast to CT-scans or traditional X-rays, MRI does not use ionising radiation. For the purposes under consideration, MRI images can be suitably used for generating patient-specific geometries of the brain and build the basis for further imaging methods.

In particular, Basser *et al.* [12] proposed the estimation of macroscopic diffusion characteristics from NMR-spin-echo experiments, commonly known as **diffusion tensor imaging (DTI)**. As depicted in the figures 2.1 (b) and 2.2, the brain tissue exhibits an internal fibrous structure, provided by the neural axons with a distinct orientation in the white-matter tracts. In accordance to this, local neuroarchitecture water diffuses more rapidly in the axon-aligned direction and much more slowly in the perpendicular directions, respectively. DTI provides a well established and meaningful tool for the detection of the micro-structural information of the neural axons. This includes the outstanding feature of DTI, namely, the possibility to determine the local diffusion tensor of water molecules in living biological tissue[3]. The obtained patient-specific (voxel) information can be consequently used in a suitable modelling approach. For an intuitive illustration of the anisotropic structure of the tissue, the measured apparent water-diffusion tensor can be visualised at each evaluated voxel by an ellipsoid in order to identify white- or grey-matter areas as a result of the shape and the size of these ellipsoids, cf. Section 6.2.1. A comprehensive overview on this topic can be found in, e. g., Le Bihan *et al.* [94] or Hlawatsch *et al.* [78].

Magnetic resonance angiography (MRA) uses an imaging technology, such as CT or MRI, and optionally a contrast material to produce pictures of the major blood vessels within the brain tissue. MRA is commonly used to diagnose medical conditions like aneurysms or abnormal vascular anatomy. However, the results obtained by MRA are less accurate in comparison to invasive-catheter angiography but the patient is not exposed to ionising radiation and the overall procedure is extremely short. Finally, **magnetic resonance elastography (MRE)** represents a new medical-imaging technique in its infancy which enables the measurement of mechanical properties (stiffness) of soft tissues in a non-invasive manner by a direct visualisation of propagating acoustic strain waves using MRI, cf., e. g., Muthupillai *et al.* [117].

[3]However, the standard period of recording (e. g. the spin-spin relaxation time) is restricted to low time frames in the range of milliseconds. Since diffusion is a very slow process, meaningful results can generally only be obtained for small characteristic lengths of the microstructure, which are in the range of micrometers. In general, this seems to be sufficient for the issues considered in this monograph.

Chapter 3:
Fundamentals of multiphasic and multicomponent models

In this chapter, the required theoretical fundamentals for the continuum-mechanical description of multiphasic and multicomponent materials are provided. In particular, the basic concept of combining immiscible and miscible constituents within a holistic model is introduced. Furthermore, the finite kinematical relations of superimposed constituents are displayed, providing the introduction of relevant deformation and strain measures. Afterwards, the state of stress is discussed. Finally, this chapter is closed by the derivation of general balance relations for the overall aggregate as well as the particular constituents, resulting in restrictions for a consistent bridging.

3.1 The concept of the Theory of Porous Media

When describing the considered human brain-tissue-aggregate by means of its multiphasic composition, two fundamentally different approaches are basically possible, cf. Ehlers [44]. On the one hand, individual parts can be separated from the overall aggregate in terms of using the Eulerian cut principle and addressed separately via the classical continuum-mechanical framework of singlephasic materials. Whereas, on the other hand, an idealised macroscopical substitute of the overall aggregate can be investigated, proceeding from a continuum theory of the heterogeneous composite with internal interactions. The drawback of the first-mentioned approach is found in the circumstance that all geometric and physical transition conditions at the contact surfaces of the separated individual parts have to be known. This may be possible for ordinary or regular structures, but certainly not for the complex (human-specific) composition of the brain tissue. Based on these preliminary considerations, the latter approach encourages the application of the TPM, representing a well-suited way to model the brain's tissue aggregate.

Regarding the historical development of the TPM, an excellent overview is given in the works of de Boer [20], de Boer & Ehlers [24] and Ehlers [44]. Moreover, a comprehensive summary of the current understanding of the TPM is provided, e. g., by works of de Boer [22] and Ehlers [50, 51]. In general, the fundamentals of the TPM proceed from the combination of two basic arrangements. In particular, these are the treatment of multiphasic materials based on the classical Theory of Mixtures (cf. Truesdell & Toupin [160] and Bowen [26]) and the concept of volume fractions (cf. Stefan [150], Mills [114] and Bowen [27, 28]). In this regard, the enhancement by the volume fractions enables the consideration of the local composition of the overall aggregate.

For the treatment of multiphasic material in terms of a continuum-mechanical framework, it is initially required that the body with delimiting parts on the microscale is "smeared" over the control domain, yielding a macroscopical substitute of the overall aggregate.

By doing so, the modelling approach of the TPM idealises the underlying multiphasic material by assuming the particular constituents of the overall aggregate to be in an ideal disorder over the control space. Hence, the constituents simultaneously occupy the entire volume of the considered domain. All geometric and physical parameters of the overall aggregate, such as motion, deformation and stress are defined in the entire domain and, thus, have to be understood as statistical averages of actually occurring variables.

In order to avoid ambiguity in the further use of the expressions "component", "phase" and "constituent", these terms are clarified here for the understanding of the presented modelling approach. Regarding the original (real) constitution of the brain-tissue aggregate, several components are recognised. This interacting or interdependent components form the integrated whole of the overall brain. In general, each component can exist in different phase states, i. e. solid, liquid or gaseous. Consequently, the chemical state of aggregation is referred to as phase. Finally, the term constituent is rather used in the context of the applied (virtual) modelling process, in which all constituents add up to the entire theoretical model of the brain-tissue aggregate.

3.2 Modelling approach of human brain tissue

For the considered issues, the multiphasic and multicomponent nature of the human-brain-tissue aggregate is basically described by including its relevant existing physical components, discussed in Section 2.1.

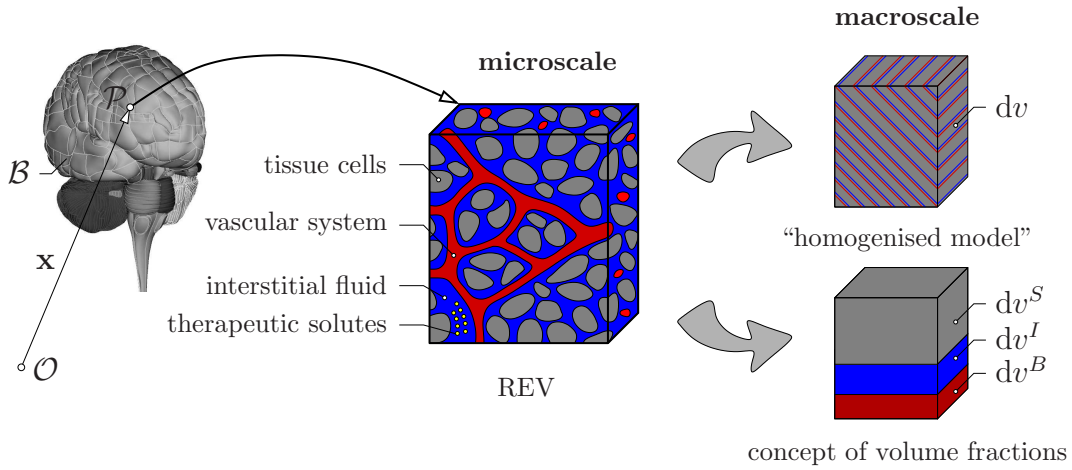

Figure 3.1: *Representative elementary volume with exemplarily displayed micro-structure of brain tissue and macroscopic multiphasic and multicomponental modelling approach.*

In this regard, the applied volumetrical homogenisation procedure (smearing) of the microscopical inner structure over a representative elementary volume (REV) of brain tissue yields a model on the macroscale, see Figure 3.1. Consequently, the initially ternary model is composed by its particular constituents, via

$$\varphi = \bigcup_{\alpha} \varphi^{\alpha} = \varphi^{S} \cup \varphi^{B} \cup \varphi^{I}, \quad \text{where} \quad \alpha = \{S, B, I\}. \tag{3.1}$$

Therein, the placeholder α indicates the solid constituent S, the blood constituent B and the interstitial fluid constituent I. In terms of the TPM, these constituents are understood as immiscible constituents. The solid skeleton φ^S is provided by the tissue cells and the vascular walls. Hence, this solid skeleton is perfused by the two mobile but generally separated pore-liquid constituents φ^β, indicated by $\beta = \{B, I\}$. On the one side, the blood constituent φ^B perfuses the brain's solid skeleton using the complex blood-vessel system. Whereas, on the other side, the overall interstitial fluid constituent φ^I is mobile within the ECS of the tissue. In order to provide the particular description of therapeutic agents within the overall interstitial fluid, this real mixture is furthermore treated as a chemical solution of two constituents (components of the solution), via

$$\varphi^I = \bigcup_\gamma \varphi^\gamma = \varphi^L \cup \varphi^D \,, \quad \text{where} \quad \gamma = \{L, D\} \,. \tag{3.2}$$

Therein, the liquid solvent φ^L and the dissolved therapeutic solute φ^D are the miscible components within the overall interstitial fluid solution. This represents an extension of the classical TPM approaches treating solely immiscible constituents by embedding elements of the Theory of Mixtures, yielding an extended Theory of Porous Media (XTPM). In conclusion, an insertion of (3.2) in (3.1) leads to the quaternary model

$$\varphi = \varphi^S \cup \varphi^B \cup \varphi^I = \varphi^S \cup \varphi^B \cup \varphi^L \cup \varphi^D \tag{3.3}$$

with four considered constituents. In terms of a meaningful consideration of the specific material properties of the constituents in (3.3), a constitutive setting is derived in Chapter 4.

3.2.1 Immiscible constituents

As mentioned before, the homogenisation of the microscopic physical quantities over a representative elementary volume (REV) leads to a model of superimposed and interacting continua. In order to account for the local compositions of the aggregate, scalar structure parameters are introduced by means of the concept of volume fractions, viz.:

$$n^\alpha := \frac{\mathrm{d}v^\alpha}{\mathrm{d}v} \,. \tag{3.4}$$

Therein, the volume fractions n^α are defined as the local ratios of the partial volume elements $\mathrm{d}v^\alpha$ with respect to the volume element $\mathrm{d}v$ of the overall aggregate. In this regard, the saturation condition

$$\sum_\alpha n^\alpha = n^S + n^B + n^I = 1 \tag{3.5}$$

needs to be satisfied[1]. In addition to the volume fractions, it is convenient to introduce further structural measures in terms of saturations s^β, viz.:

$$s^\beta := \frac{n^\beta}{n^F} \,, \qquad \text{with} \quad n^F = n^B + n^I \quad \text{and} \quad \sum_\beta s^\beta = s^B + s^I = 1 \,. \tag{3.6}$$

[1]Within this monograph, fully saturated conditions, i. e. no vacant space within the domain, are given.

Note that the definition of classical saturation measures, like in partially saturated soil mechanics, proceeds from the fact that one existing pore space is occupied by at least two different fluids. In contrast, the overall pore space in human brain tissue is made up of two separated pore spaces, the intravascular space and the interstitial fluid space. The former is filled by the blood plasma, while the latter contains the overall interstitial fluid. However, the structural measures s^β introduced in $(3.6)_1$ characterise the portion of a specific liquid in relation to the overall accumulated pore space n^F given in $(3.6)_2$. In accordance to the saturation condition (3.5), also the saturations s^β add up to one $(3.6)_3$. Due to the applied homogenisation, two different densities can be introduced, viz.:

$$\rho^{\alpha R} := \frac{\mathrm{d}m^\alpha}{\mathrm{d}v^\alpha} \qquad \text{and} \qquad \rho^\alpha := \frac{\mathrm{d}m^\alpha}{\mathrm{d}v}\,. \tag{3.7}$$

Therein, the realistic or material density $\rho^{\alpha R}$ is defined by the local mass element $\mathrm{d}m^\alpha$ with respect to its partial volume element $\mathrm{d}v^\alpha$, while the partial density ρ^α is defined by the local mass element $\mathrm{d}m^\alpha$ divided by the volume element $\mathrm{d}v$ of the overall aggregate. Based on the definitions in (3.7), it can easily be concluded from equation (3.4) that

$$\rho^\alpha = n^\alpha \rho^{\alpha R}\,. \tag{3.8}$$

In particular, this means that the property of material incompressibility ($\rho^{\alpha R} = \text{const.}$) will not necessarily lead to the property of bulk incompressibility ($\rho^\alpha = \text{const.}$). In fact, the partial density ρ^α of this constituent can still change due to a variation in its volume fraction n^α. Finally, the summation

$$\rho = \sum_\alpha \rho^\alpha \tag{3.9}$$

of all partial densities ρ^α yields the density ρ of the overall aggregate.

3.2.2 Miscible components

The scope of the investigated modelling approach requires the treatment of the overall interstitial fluid φ^I as a "real" mixture[2]. This solution consists of a liquid solvent φ^L and a dissolved therapeutic agent constituent φ^D. In this regard, the solvent φ^L represents the dominant volumetrical part. Whereas, the volumetrical contribution of the dissolved φ^D is extremely small. The basic thermodynamical fundamentals of such solutions are found in standard chemical textbooks, such as Adam *et al.* [4]. However, the incorporation of miscible components in the classical framework of the TPM requires an extension via elements of the classical mixture theory which are introduced in this subsection, according to Acartürk [3] and Ehlers [51].

Basic chemistry: In chemical solutions, the dissolved components are part of the whole fluid volume. Hence, their volume fractions cannot be measured. Moreover, the volume of a solution with dissolved components (such as a NaCl solution) change only minimally

[2]In this context, a "real" mixture refers to the physical combination of at least two substances in the form of a solution. The substances are mixed but not chemically combined through chemical reactions.

(in the order of $10^{-2}\,\%$ for a NaCl solution) between the unsaturated (pure solvent H_2O) and the completely saturated case, cf. Acartürk [3] and citations therein. Therefore, the indication of substances in a solution using volume fractions is commonly excluded. Instead, the number of dissolved molecules is used by means of concentrations. However, the total number of molecules in macroscopical systems is extremely high. For example, a physiological saline solution contains approximately 10^{23} Na^+-ions per litre. In order to avoid such high orders of magnitude, the quantity mol is introduced. In this regard, the amount of particles in one mole is given by $N_A = 6.022 \cdot 10^{23}\ \mathrm{mol}^{-1}$, which represents the so-called Avogadro's constant.

Following this idea, several molar quantities are introduced and denoted with the subscript $(\cdot)_m$. The molar concentration c_m^γ and the molar mass M_m^γ of a component φ^γ are defined, viz.:

$$c_m^\gamma := \frac{\mathrm{d}n_m^\gamma}{\mathrm{d}v^I} \qquad \text{and} \quad M_m^\gamma := \frac{\mathrm{d}m^\gamma}{\mathrm{d}n_m^\gamma}\,. \tag{3.10}$$

Therein, the local number of moles $\mathrm{d}n_m^\gamma$ is related to the local bulk fluid volume $\mathrm{d}v^I$ to obtain the molar concentration c_m^γ. Moreover, the molar mass M_m^γ relates the local mass element $\mathrm{d}m^\gamma$ of a component to its local number of moles $\mathrm{d}n_m^\gamma$. This measure represents a constant quantity for a specific component φ^γ. Furthermore, the total amount of molecules in a solution is constant. This can be seen by the so-called mole fractions

$$x_m^\gamma = \frac{\mathrm{d}n_m^\gamma}{\sum_\gamma \mathrm{d}n_m^\gamma} = \frac{c_m^\gamma}{\sum_\gamma c_m^\gamma}\,, \quad \text{where} \quad \sum_\gamma x_m^\gamma = 1\,. \tag{3.11}$$

Consideration of miscible components within the TPM: The density of the overall interstitial fluid φ^I, which is a solution of its components φ^γ, can be derived in analogy to (3.9) via

$$\rho^I = \sum_\gamma \rho^\gamma\,. \tag{3.12}$$

Proceeding from the basic chemical relations introduced above, the mixture components are not only considered by their partial densities ρ^γ but also by their partial pore densities ρ_I^γ defined with respect to the interstitial pore space, viz.:

$$\rho^\gamma =: n^I \rho_I^\gamma\,, \qquad \text{where} \quad \rho_I^\gamma = c_m^\gamma\, M_m^\gamma\,. \tag{3.13}$$

Therein, the partial pore density ρ_I^γ is given by the molar concentration c_m^γ multiplied with its corresponding molar mass M_m^γ. Regarding the considered solution of the overall interstitial fluid containing the dissolved therapeutic agent component as the only solute, its effective density

$$\rho^{IR} = \sum_{\gamma=L,D} \rho_I^\gamma = \rho_I^L + \rho_I^D \tag{3.14}$$

is given by the summation of the component's partial pore densities. In the case that the concentration of the solute within the overall solution represents only a very small part, the volume fraction of the solute can be neglected in comparison to the volume fraction of the overall solution. This means that changes in the solute's concentration do not change the volume fraction of the overall solution.

Remark: In principle, it is possible to apply the concept of volume fractions (3.4) for the specification of the composition of liquid-liquid solutions, where both parts are more similar. A prominent example of such a kind of mixture is known from the production of alcohol. In this context, the initial volumetrical amounts in a mixture of ethanol and water can be measured. However, the overall volume of the liquid-liquid mixture is slightly less than the sum of the particular volumes of its constituents. In order to account for that, the claimed amount of percent alcohol by volume is commonly obtained by mixing the desired volume units of ethanol with the required amount of water for the final volume of one hundred units. This shows that the overall volume of a liquid-liquid solution may fundamentally differ from the sum of the individual volumes, due to volume contraction and volume dilatation effects caused by a change in the chemical bonding forces.

3.3 Kinematics

This section introduces the state of motion of superimposed continua in the frame of finite kinematics. This represents a well-founded topic which is subject of various contributions. Hence, the focus is rather placed on the special requirements of the brain-tissue model. In this regard, the pursued objective is to provide the basic fundamentals and to combine already existing but isolated elements of suitable approaches to obtain the required kinematics for the proposed multi-constituent modelling approach. For a complete overview, the interested reader is referred to, e. g., Altenbach [5], Haupt [76] or Holzapfel [79] for singlephasic materials and Ehlers [44, 48, 50] for the treatment of multiphasic materials, respectively. Moreover, kinematical relations considering miscible components within the TPM are discussed in, e. g., Acartürk [3] and Ehlers [51].

3.3.1 Porous body and motion of superimposed constituents

In classical continuum mechanics of singlephasic materials, a body $\mathcal{B}$ is represented by the spatial manifold of its material points $\mathcal{P}$, where the set of material points $\mathcal{P}$ on the boundary composes the surface $\mathcal{S}$ of the body. In the context of the description of multiphasic materials, the smearing of the constituents over the whole domain implies

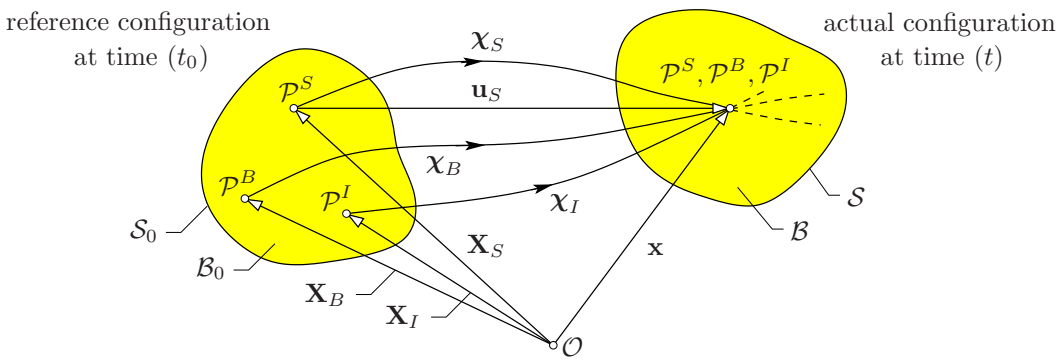

Figure 3.2: *Kinematics of a ternary model of superimposed continua.*

that in the actual configuration each spatial position $\mathbf{x}$ of the domain is simultaneously occupied by material points $\mathcal{P}^\alpha$ of all constituents. Thus, the relations of the classical continuum mechanics of singlephasic materials can be applied in accordance to each single constituent φ^α. In Figure 3.2, the kinematical relations of superimposed continua are shown. The requirement of independent states of motion of the constituents implies that the material points $\mathcal{P}^\alpha$ do not necessarily trace back to a common reference position, but can have individual reference positions $\mathbf{X}_\alpha$. Hence, each constituent φ^α (as well as φ^β and φ^γ) follows its own individual Lagrangean placement function $\boldsymbol{\chi}_\alpha(\mathbf{X}_\alpha, t)$, where the material points are identified with their initial position. In the actual configuration, the coincidence at time t for the current position

$$\mathbf{x} = \boldsymbol{\chi}_\alpha(\mathbf{X}_\alpha, t) \tag{3.15}$$

is given. Moreover, each material point at the current position is assigned to an unique reference position $\mathbf{X}_\alpha$ given by the Eulerian (spatial) description via the inverse motion function $\boldsymbol{\chi}_\alpha^{-1}$, viz.:

$$\mathbf{X}_\alpha = \boldsymbol{\chi}_\alpha^{-1}(\mathbf{x}, t) \quad \text{if} \quad J_\alpha := \det \frac{\partial \boldsymbol{\chi}_\alpha}{\partial \mathbf{X}_\alpha} \neq 0\,. \tag{3.16}$$

In order to guarantee the unique and uniquely invertible motion of the constituent, a mathematically sufficient condition is provided by a non-zero Jacobian J_α. Furthermore, the velocity and acceleration fields for each constituent are introduced by using the material time derivatives in a Lagrangean setting, viz.:

$$\overset{\prime}{\mathbf{x}}_\alpha = \frac{\partial \boldsymbol{\chi}_\alpha(\mathbf{X}_\alpha, t)}{\partial t} = \overset{\prime}{\mathbf{x}}_\alpha(\mathbf{X}_\alpha, t) \quad \text{and} \quad \overset{\prime\prime}{\mathbf{x}}_\alpha = \frac{\partial^2 \boldsymbol{\chi}_\alpha(\mathbf{X}_\alpha, t)}{\partial t^2} = \overset{\prime\prime}{\mathbf{x}}_\alpha(\mathbf{X}_\alpha, t)\,. \tag{3.17}$$

Moreover, for the Eulerian formulations the relations

$$\overset{\prime}{\mathbf{x}}_\alpha = \overset{\prime}{\mathbf{x}}_\alpha(\boldsymbol{\chi}_\alpha^{-1}(\mathbf{x}, t),\, t) = \overset{\prime}{\mathbf{x}}_\alpha(\mathbf{x},\, t) \quad \text{and} \quad \overset{\prime\prime}{\mathbf{x}}_\alpha = \overset{\prime\prime}{\mathbf{x}}_\alpha(\boldsymbol{\chi}_\alpha^{-1}(\mathbf{x}, t),\, t) = \overset{\prime\prime}{\mathbf{x}}_\alpha(\mathbf{x},\, t) \tag{3.18}$$

can be found by insertion of the inverse motion function (3.16) into (3.17). In the context of Eulerian formulations, it is necessary to consider material time derivatives. This is motivated by the fact that the temporal change of a field function also requires the consideration of inner (implicit) derivatives. In this regard, the total time derivative of an arbitrary, but steady and sufficiently steady differentiable, field function (scalar-valued Υ or vector-valued $\boldsymbol{\Upsilon}$) with respect to the overall aggregate φ is given via

$$\begin{aligned}
\dot{\Upsilon} &= \frac{\mathrm{d}}{\mathrm{d}t}\,\Upsilon(\mathbf{x}(t),\, t) = \frac{\partial \Upsilon}{\partial t} + \frac{\partial \Upsilon}{\partial \mathbf{x}}\frac{\partial \mathbf{x}}{\partial t} = \frac{\partial \Upsilon}{\partial t} + \operatorname{grad}\Upsilon \cdot \dot{\mathbf{x}}\,, \\
\dot{\boldsymbol{\Upsilon}} &= \frac{\mathrm{d}}{\mathrm{d}t}\,\boldsymbol{\Upsilon}(\mathbf{x}(t),\, t) = \frac{\partial \boldsymbol{\Upsilon}}{\partial t} + \frac{\partial \boldsymbol{\Upsilon}}{\partial \mathbf{x}}\frac{\partial \mathbf{x}}{\partial t} = \frac{\partial \boldsymbol{\Upsilon}}{\partial t} + (\operatorname{grad}\boldsymbol{\Upsilon})\,\dot{\mathbf{x}}\,.
\end{aligned} \tag{3.19}$$

Therein, $\operatorname{grad}(\,\cdot\,)$ denotes the spatial gradient operator with respect to the actual configuration. In analogy, the total time derivative with respect to the constituent φ^α yields

$$\begin{aligned}
(\Upsilon)'_\alpha &= \frac{\mathrm{d}_\alpha}{\mathrm{d}t}\,\Upsilon(\mathbf{x}(t),\, t) = \frac{\partial \Upsilon}{\partial t} + \operatorname{grad}\Upsilon \cdot \overset{\prime}{\mathbf{x}}_\alpha\,, \\
(\boldsymbol{\Upsilon})'_\alpha &= \frac{\mathrm{d}_\alpha}{\mathrm{d}t}\,\boldsymbol{\Upsilon}(\mathbf{x}(t),\, t) = \frac{\partial \boldsymbol{\Upsilon}}{\partial t} + (\operatorname{grad}\boldsymbol{\Upsilon})\,\overset{\prime}{\mathbf{x}}_\alpha\,.
\end{aligned} \tag{3.20}$$

Moreover, subtracting (3.19) from (3.20) and further use of the relation (3.23) yields the dependencies

$$(\Upsilon)'_\alpha \;=\; \dot{\Upsilon} \,+\, \operatorname{grad}\Upsilon \cdot \mathbf{d}_\alpha \quad \text{and} \quad (\boldsymbol{\Upsilon})'_\alpha \;=\; \dot{\boldsymbol{\Upsilon}} \,+\, (\operatorname{grad}\boldsymbol{\Upsilon})\,\mathbf{d}_\alpha\,. \tag{3.21}$$

The velocity of the overall aggregate (barycentric velocity) is introduced by the underlying idea[3] of conservating the local momentum of the overall aggregate with the sum of the local momenta of the constituents, yielding

$$\dot{\mathbf{x}} \;=\; \frac{1}{\rho}\sum_\alpha \rho^\alpha \overset{\prime}{\mathbf{x}}_\alpha\,. \tag{3.22}$$

Based on this introduction, the diffusion velocity $\mathbf{d}_\alpha$ relates the velocity of a constituent with respect to the barycentric velocity via

$$\mathbf{d}_\alpha \;:=\; \overset{\prime}{\mathbf{x}}_\alpha - \dot{\mathbf{x}}\,, \quad \text{where} \quad \sum_\alpha \rho^\alpha\,\mathbf{d}_\alpha \;=\; \sum_\alpha \rho^\alpha \overset{\prime}{\mathbf{x}}_\alpha \,-\, \dot{\mathbf{x}}\sum_\alpha \rho^\alpha \;=\; \mathbf{0}\,. \tag{3.23}$$

Therein, it can easily be concluded that the sum of the diffusion mass flow vanishes by inserting $(3.23)_1$ into $(3.23)_2$ and using the relations (3.9) and (3.22). Proceeding in analogy to (3.22), the velocity of the overall interstitial fluid mixture φ^I, composed by its miscible components φ^γ, is derived by using the relation (3.13), viz.:

$$\overset{\prime}{\mathbf{x}}_I \;=\; \frac{1}{\rho^I}\sum_\gamma \rho^\gamma \overset{\prime}{\mathbf{x}}_\gamma \;=\; \frac{1}{n^I\rho^{IR}}\sum_\gamma n^I\rho^\gamma_I \overset{\prime}{\mathbf{x}}_\gamma \;=\; \frac{1}{\rho^{IR}}\sum_\gamma \rho^\gamma_I \overset{\prime}{\mathbf{x}}_\gamma\,. \tag{3.24}$$

In (3.24), the pore densities ρ^γ_I are acting as weighting factors. When describing miscible components in terms of the XTPM, another important quantity is the pore-diffusion velocity $\mathbf{d}_{\gamma I}$ relating the velocity of a mixture component to the velocity of the overall interstitial fluid mixture, viz.:

$$\mathbf{d}_{\gamma I} \;:=\; \overset{\prime}{\mathbf{x}}_\gamma \,-\, \overset{\prime}{\mathbf{x}}_I\,, \quad \text{where} \quad \sum_\gamma \rho^\gamma_I\,\mathbf{d}_{\gamma I} \;=\; \sum_\gamma \rho^\gamma_I \overset{\prime}{\mathbf{x}}_\gamma \,-\, \overset{\prime}{\mathbf{x}}_I \sum_\gamma \rho^\gamma_I \;=\; \mathbf{0}\,. \tag{3.25}$$

Therein, the sum of the pore-diffusion mass flow vanishes by inserting $(3.25)_1$ into $(3.25)_2$ and using the relations (3.14) and (3.24).

In terms of porous-media theories including large solid deformations, it is suitable to use a Lagrangean description of the solid skeleton with respect to a basically given reference configuration. Therefore, the solid displacement field

$$\mathbf{u}_S \;:=\; \mathbf{x} \,-\, \mathbf{X}_S \tag{3.26}$$

is generally used as the primary kinematic variable. In contrast, the pore-liquid flow of the immiscible constituents is expressed in a modified Eulerian setting via the seepage velocities

$$\mathbf{w}_\beta \;:=\; \overset{\prime}{\mathbf{x}}_\beta \,-\, \overset{\prime}{\mathbf{x}}_S \tag{3.27}$$

[3]This relation is approved lateron, cf. $(3.80)_1$, by means of studying the relationships of the balance of momentum of the overall aggregate with its particular constituents.

describing the liquid velocities in relation to the velocity of the deforming solid skeleton. Regarding the description of the dissolved components in the overall interstitial fluid mixture, the seepage velocities

$$\mathbf{w}_\gamma := \overset{\prime}{\mathbf{x}}_\gamma - \overset{\prime}{\mathbf{x}}_S = \mathbf{d}_{\gamma I} + \overset{\prime}{\mathbf{x}}_I - \overset{\prime}{\mathbf{x}}_S = \mathbf{d}_{\gamma I} + \mathbf{w}_I \tag{3.28}$$

can be formulated with $(3.25)_1$ in terms of the pore-diffusion velocity $\mathbf{d}_{\gamma I}$ and the seepage velocity $\mathbf{w}_I$ of the overall interstitial fluid.

3.3.2 Deformation and strain measures

Certainly, the most important deformation quantity in continuum mechanics is provided by the material deformation gradient $\mathbf{F}_\alpha$. This results from its fundamental property to describe a change in motion and, thus, indicates the local deformation. Formally, $\mathbf{F}_\alpha$ and its inverse $\mathbf{F}_\alpha^{-1}$ are introduced via

$$\begin{aligned} \mathbf{F}_\alpha &= \frac{\partial \boldsymbol{\chi}_\alpha(\mathbf{X}_\alpha, t)}{\partial \mathbf{X}_\alpha} = \frac{\partial \mathbf{x}}{\partial \mathbf{X}_\alpha} = \operatorname{Grad}_\alpha \mathbf{x}\,, \\ \mathbf{F}_\alpha^{-1} &= \frac{\partial \boldsymbol{\chi}_\alpha^{-1}(\mathbf{x}, t)}{\partial \mathbf{x}} = \frac{\partial \mathbf{X}_\alpha}{\partial \mathbf{x}} = \operatorname{grad} \mathbf{X}_\alpha\,. \end{aligned} \tag{3.29}$$

Therein, the operator $\operatorname{Grad}_\alpha(\,\cdot\,)$ denotes the material gradient of φ^α with respect to its reference position. It follows directly from (3.29) that the material deformation gradient, in its capacity as a two-field tensor, maps a local line element of φ^α in a push-forward transformation from the reference configuration to the actual configuration yielding

$$\mathrm{d}\mathbf{x} = \mathbf{F}_\alpha\, \mathrm{d}\mathbf{X}_\alpha \quad \leftrightarrow \quad \mathrm{d}\mathbf{X}_\alpha = \mathbf{F}_\alpha^{-1}\, \mathrm{d}\mathbf{x}\,. \tag{3.30}$$

The so-called pull-back transformation in $(3.30)_2$ of an actual line element to the reference configuration is only feasible for existing inverse deformation gradients $\mathbf{F}_\alpha^{-1}$ as stated in $(3.16)_2$. Correspondingly, it can easily be concluded from the computation rule of the inverse

$$\mathbf{F}_\alpha^{-1} = \frac{(\operatorname{cof} \mathbf{F}_\alpha)^T}{\det \mathbf{F}_\alpha}\,, \qquad \text{that} \quad J_\alpha = \det \mathbf{F}_\alpha \neq 0 \tag{3.31}$$

needs to be fulfilled for the existence of the inverse deformation gradient. The specific calculations of the related operators, i. e., the cofactor $\operatorname{cof} \mathbf{F}_\alpha$ and the determinant $\det \mathbf{F}_\alpha$, are given in Appendix A.1. Moreover, investigating the initial condition of the deformation gradient results in

$$\mathbf{F}_\alpha(t = t_0) = \frac{\partial \mathbf{X}_\alpha}{\partial \mathbf{X}_\alpha} = \operatorname{Grad}_\alpha \mathbf{X}_\alpha = \mathbf{I} \quad \rightarrow \quad \det \mathbf{F}_\alpha(t_0) = \det \mathbf{I} = 1\,. \tag{3.32}$$

Therefore, it is concluded for the continuous and non-zero Jacobian that

$$J_\alpha = \det \mathbf{F}_\alpha > 0 \tag{3.33}$$

needs to be fulfilled. Based on the fundamental mapping (3.30), further transport theorems of referential area and volume elements are obtained via

$$\mathrm{d}\mathbf{a} \;=\; (\operatorname{cof}\mathbf{F}_\alpha)\,\mathrm{d}\mathbf{A}_\alpha \quad \text{and} \quad \mathrm{d}v \;=\; (\det\mathbf{F}_\alpha)\,\mathrm{d}V_\alpha\,. \tag{3.34}$$

Therein, $\mathrm{d}\mathbf{A}_\alpha$ and $\mathrm{d}V_\alpha$ denote area and volume elements in the referential configuration, whereas $\mathrm{d}\mathbf{a}$ and $\mathrm{d}v$ represent the corresponding elements in the actual configuration. Regarding $(3.34)_2$, the physical meaning of the Jacobian can be seen straightforwardly. In particular, a Jacobian greater than one represents a local volume extension, while values between one and zero imply a compaction. However, the shrinkage of an initial volume element of the reference configuration to a fictive mathematical point (without any volume) and beyond is excluded by (3.33).

As a next step, the introduction of deformation measures of φ^α is derived from the square of line elements in the actual and referential configurations and using the relations in (3.30), viz.:

$$\begin{aligned}
\mathrm{d}\mathbf{x}\cdot\mathrm{d}\mathbf{x} \;&=\; \mathrm{d}\mathbf{X}_\alpha\cdot(\mathbf{F}_\alpha^T\,\mathbf{F}_\alpha)\,\mathrm{d}\mathbf{X}_\alpha \;=:\; \mathrm{d}\mathbf{X}_\alpha\cdot\mathbf{C}_\alpha\,\mathrm{d}\mathbf{X}_\alpha \;\rightarrow\; \mathbf{C}_\alpha \;=\; \mathbf{F}_\alpha^T\,\mathbf{F}_\alpha\,,\\
\mathrm{d}\mathbf{X}_\alpha\cdot\mathrm{d}\mathbf{X}_\alpha \;&=\; \mathrm{d}\mathbf{x}\cdot(\mathbf{F}_\alpha^{T-1}\,\mathbf{F}_\alpha^{-1})\,\mathrm{d}\mathbf{x} \;=:\; \mathrm{d}\mathbf{x}\cdot\mathbf{B}_\alpha^{-1}\,\mathrm{d}\mathbf{x} \;\rightarrow\; \mathbf{B}_\alpha \;=\; \mathbf{F}_\alpha\,\mathbf{F}_\alpha^T\,.
\end{aligned} \tag{3.35}$$

Therein, $\mathbf{C}_\alpha$ and $\mathbf{B}_\alpha$ are introduced as the right and the left Cauchy-Green deformation tensors, respectively. Herein, the attributes right and left stem from the polar decomposition of $\mathbf{F}_\alpha$. Due to a separation of a local rigid body movement, a right and a left decomposition of $\mathbf{F}_\alpha$ is investigated in terms of

$$\mathbf{F}_\alpha \;=\; \mathbf{R}_\alpha\,\mathbf{U}_\alpha \;=\; \mathbf{V}_\alpha\,\mathbf{R}_\alpha\,, \quad \text{where} \quad \mathbf{V}_\alpha \;=\; \mathbf{R}_\alpha\,\mathbf{U}_\alpha\,\mathbf{R}_\alpha^T\,. \tag{3.36}$$

Therein, $\mathbf{R}_\alpha$ denotes a proper othogonal rotation with the properties

$$\mathbf{R}_\alpha^{-1} \;=\; \mathbf{R}_\alpha^T \qquad \text{and} \qquad \det\mathbf{R}_\alpha \;=\; 1\,. \tag{3.37}$$

Furthermore, the right stretch tensor $\mathbf{U}_\alpha$ and the left stretch tensor $\mathbf{V}_\alpha$ are symmetric and positive definite measures. This includes

$$\{\det\mathbf{U}_\alpha\,,\,\det\mathbf{V}_\alpha\} \;>\; 0 \qquad \text{and} \qquad \mathbf{U}_\alpha \;=\; \mathbf{U}_\alpha^T\,, \quad \mathbf{V}_\alpha \;=\; \mathbf{V}_\alpha^T\,. \tag{3.38}$$

Therefore, the insertion of $(3.36)_1$ in (3.35) using (3.37) and (3.38) results in further representations of the deformation tensors via

$$\mathbf{C}_\alpha \;=\; \mathbf{F}_\alpha^T\,\mathbf{F}_\alpha \;=\; \mathbf{U}_\alpha\,\mathbf{U}_\alpha\,, \quad \mathbf{B}_\alpha \;=\; \mathbf{F}_\alpha\,\mathbf{F}_\alpha^T \;=\; \mathbf{V}_\alpha\,\mathbf{V}_\alpha \quad \text{with} \quad \mathbf{B}_\alpha \;=\; \mathbf{R}_\alpha\,\mathbf{C}_\alpha\,\mathbf{R}_\alpha^T\,. \tag{3.39}$$

Note that the mathematical investigation of the polar decomposition in $(3.36)_1$ is derived by means of solving the eigenvalue problem of $\mathbf{C}_\alpha$ and $\mathbf{B}_\alpha$, cf. Appendix B.1.

Strain measures are introduced, proceeding from the difference of the squares of line elements. This is carried out again with respect to the reference and the actual configuration, using the relations (3.30) and (3.35):

$$\begin{aligned}
\mathrm{d}\mathbf{x}\cdot\mathrm{d}\mathbf{x} \;-\; \mathrm{d}\mathbf{X}_\alpha\cdot\mathrm{d}\mathbf{X}_\alpha \;&=\; \mathrm{d}\mathbf{X}_\alpha\cdot(\mathbf{C}_\alpha-\mathbf{I})\,\mathrm{d}\mathbf{X}_\alpha \;=:\; \mathrm{d}\mathbf{X}_\alpha\cdot 2\,\mathbf{E}_\alpha\,\mathrm{d}\mathbf{X}_\alpha\,,\\
\mathrm{d}\mathbf{x}\cdot\mathrm{d}\mathbf{x} \;-\; \mathrm{d}\mathbf{X}_\alpha\cdot\mathrm{d}\mathbf{X}_\alpha \;&=\; \mathrm{d}\mathbf{x}\cdot(\mathbf{I}-\mathbf{B}_\alpha^{-1})\,\mathrm{d}\mathbf{x} \;=:\; \mathrm{d}\mathbf{x}\cdot 2\,\mathbf{A}_\alpha\,\mathrm{d}\mathbf{x}\,.
\end{aligned} \tag{3.40}$$

Therein, $\mathbf{E}_\alpha$ denotes the Green-Lagrangean strain tensor and $\mathbf{A}_\alpha$ denotes the Almansian strain tensor. Although the introduction of the factor "2" in (3.40) may not initially appear motivated, this is typically done to obtain the traditional engineering strain as a result of a linearisation. In conclusion, it is found that

$$\mathbf{E}_\alpha = \tfrac{1}{2}(\mathbf{C}_\alpha - \mathbf{I}), \quad \mathbf{A}_\alpha = \tfrac{1}{2}(\mathbf{I} - \mathbf{B}_\alpha^{-1}), \quad \text{where} \quad \mathbf{A}_\alpha = \mathbf{F}_\alpha^{T-1}\,\mathbf{E}_\alpha\,\mathbf{F}_\alpha^{-1}. \tag{3.41}$$

In addition to the strain tensors given in (3.41), further strain measures can be introduced in terms of the referential and the spatial Karni-Reiner strain tensors of φ^α using a forward rotation of $\mathbf{E}_\alpha$ and a backward rotation[4] of $\mathbf{A}_\alpha$, yielding

$$\mathbf{K}_\alpha = \mathbf{R}_\alpha\,\mathbf{E}_\alpha\,\mathbf{R}_\alpha^T \quad \text{and} \quad \overset{\text{R}}{\mathbf{K}}_\alpha = \mathbf{R}_\alpha^T\,\mathbf{A}_\alpha\,\mathbf{R}_\alpha. \tag{3.42}$$

Therein, the referential ($\overset{\text{R}}{\mathbf{K}}_\alpha$) and the spatial ($\mathbf{K}_\alpha$) Karni-Reiner strain tensor can be described via

$$\overset{\text{R}}{\mathbf{K}}_\alpha = \tfrac{1}{2}\,(\mathbf{I} - \mathbf{C}_\alpha^{-1}), \quad \mathbf{K}_\alpha = \tfrac{1}{2}\,(\mathbf{B}_\alpha - \mathbf{I}), \quad \text{with} \quad \mathbf{K}_\alpha = \mathbf{F}_\alpha\,\overset{\text{R}}{\mathbf{K}}_\alpha\,\mathbf{F}_\alpha^T. \tag{3.43}$$

3.3.3 Finite kinematical relations of the solid skeleton

The kinematical relations derived so far can generally be applied to every kind of continua, such as solid, liquid or gaseous bodies. In the present context, the finite regime is applied to the solid skeleton which can exhibit large deformations. Furthermore, it represents the referential frame for all quantities through its primary kinematical variable $\mathbf{u}_S$. Hence, the solid's material deformation gradient $\mathbf{F}_S$ can be formulated in terms of the solid displacement vector $\mathbf{u}_S$ by inserting the relation (3.26) in (3.29), yielding

$$\begin{aligned} \mathbf{F}_S &= \frac{\partial \mathbf{x}}{\partial \mathbf{X}_S} = \frac{\partial(\mathbf{X}_S + \mathbf{u}_S)}{\partial \mathbf{X}_S} = \mathbf{I} + \operatorname{Grad}_S \mathbf{u}_S, \\ \mathbf{F}_S^{-1} &= \frac{\partial \mathbf{X}_S}{\partial \mathbf{x}} = \frac{\partial(\mathbf{x} - \mathbf{u}_S)}{\partial \mathbf{x}} = \mathbf{I} - \operatorname{grad} \mathbf{u}_S. \end{aligned} \tag{3.44}$$

Based on (3.44), the solid's deformation and strain measures are obtained in terms of the solid displacement vector $\mathbf{u}_S$, viz.:

$$\begin{aligned} \mathbf{C}_S &= \mathbf{I} + \operatorname{Grad}_S \mathbf{u}_S + (\operatorname{Grad}_S \mathbf{u}_S)^T + (\operatorname{Grad}_S \mathbf{u}_S)^T \operatorname{Grad}_S \mathbf{u}_S, \\ \mathbf{B}_S &= \mathbf{I} + \operatorname{Grad}_S \mathbf{u}_S + (\operatorname{Grad}_S \mathbf{u}_S)^T + \operatorname{Grad}_S \mathbf{u}_S\,(\operatorname{Grad}_S \mathbf{u}_S)^T, \\ \mathbf{C}_S^{-1} &= \mathbf{I} - \operatorname{grad} \mathbf{u}_S - (\operatorname{grad} \mathbf{u}_S)^T + \operatorname{grad} \mathbf{u}_S\,(\operatorname{grad} \mathbf{u}_S)^T, \\ \mathbf{B}_S^{-1} &= \mathbf{I} - \operatorname{grad} \mathbf{u}_S - (\operatorname{grad} \mathbf{u}_S)^T + (\operatorname{grad} \mathbf{u}_S)^T \operatorname{grad} \mathbf{u}_S, \\ \mathbf{E}_S &= \tfrac{1}{2}\left[\operatorname{Grad}_S \mathbf{u}_S + (\operatorname{Grad}_S \mathbf{u}_S)^T + (\operatorname{Grad}_S \mathbf{u}_S)^T \operatorname{Grad}_S \mathbf{u}_S\right], \\ \mathbf{A}_S &= \tfrac{1}{2}\left[\operatorname{grad} \mathbf{u}_S + (\operatorname{grad} \mathbf{u}_S)^T - (\operatorname{grad} \mathbf{u}_S)^T \operatorname{grad} \mathbf{u}_S\right], \\ \overset{\text{R}}{\mathbf{K}}_S &= \tfrac{1}{2}\left[\operatorname{grad} \mathbf{u}_S + (\operatorname{grad} \mathbf{u}_S)^T - \operatorname{grad} \mathbf{u}_S\,(\operatorname{grad} \mathbf{u}_S)^T\right], \\ \mathbf{K}_S &= \tfrac{1}{2}\left[\operatorname{Grad}_S \mathbf{u}_S + (\operatorname{Grad}_S \mathbf{u}_S)^T + \operatorname{Grad}_S \mathbf{u}_S\,(\operatorname{Grad}_S \mathbf{u}_S)^T\right]. \end{aligned} \tag{3.45}$$

[4] Another possibility is based on the difference of the squares of weighted area elements, cf. Ehlers [46].

Note in passing that in finite kinematics, it is often convenient to rewrite deformation and strain measures in terms of the natural basis representation. This allows for an intuitive association to adjacent (co- and contravariant) configurations, cf. Appendix B.2.

3.3.4 Velocity gradients and deformation rates

Although the description of rate-dependent material behaviour is not considered within this monograph, the subsequently derived quantities are of particular interest in thermodynamical issues. Proceeding either from a Lagrangean description of the velocity (3.17) or an Eulerian description of the velocity (3.18), the rate of the deformation gradient of φ^α results in

$$\begin{aligned}(\mathbf{F}_\alpha)'_\alpha \;=\; \frac{\mathrm{d}_\alpha}{\mathrm{d}t}\left(\frac{\partial \mathbf{x}}{\partial \mathbf{X}_\alpha}\right) \;&=\; \frac{\partial \overset{\prime}{\mathbf{x}}_\alpha(\mathbf{X}_\alpha,\, t)}{\partial \mathbf{X}_\alpha} \;=\; \mathrm{Grad}_\alpha \overset{\prime}{\mathbf{x}}_\alpha\,, \\ &=\; \frac{\partial \overset{\prime}{\mathbf{x}}_\alpha}{\partial \mathbf{x}}\,\frac{\partial \mathbf{x}}{\partial \mathbf{X}_\alpha} \;=:\; \mathbf{L}_\alpha\,\mathbf{F}_\alpha\,.\end{aligned} \tag{3.46}$$

Therein, the spatial velocity gradient is introduced via

$$\mathbf{L}_\alpha \;=\; \frac{\partial \overset{\prime}{\mathbf{x}}_\alpha(\mathbf{x},\, t)}{\partial \mathbf{x}} \;=\; \mathrm{grad}\,\overset{\prime}{\mathbf{x}}_\alpha \;=\; (\mathbf{F}_\alpha)'_\alpha\,\mathbf{F}_\alpha^{-1} \tag{3.47}$$

Furthermore, heading towards the constitutive modelling process, cf. Chapter 4, it is reasonable to additively split the spatial velocity gradient $\mathbf{L}_\alpha$ into a symmetric deformation velocity $\mathbf{D}_\alpha$ and a skew-symmetric spin tensor $\mathbf{W}_\alpha$, viz.:

$$\mathbf{L}_\alpha \;:=\; \mathbf{D}_\alpha + \mathbf{W}_\alpha\,, \qquad \text{with} \quad \left\{\begin{array}{lcl} \mathbf{D}_\alpha &=& \tfrac{1}{2}\,(\mathbf{L}_\alpha + \mathbf{L}_\alpha^T) \quad \text{and} \quad \mathbf{D}_\alpha \;=\; \mathbf{D}_\alpha^T\,, \\ \mathbf{W}_\alpha &=& \tfrac{1}{2}\,(\mathbf{L}_\alpha - \mathbf{L}_\alpha^T) \quad \text{and} \quad \mathbf{W}_\alpha \;=\; -\,\mathbf{W}_\alpha^T\,. \end{array}\right. \tag{3.48}$$

Based on the spatial velocity gradient $\mathbf{L}_\alpha$, the velocity of a line element is specified proceeding from (3.30). Further use of (3.47) yields

$$(\mathrm{d}\mathbf{x})'_\alpha \;=\; (\mathbf{F}_\alpha)'_\alpha\,\mathrm{d}\mathbf{X}_\alpha \;=\; \mathbf{L}_\alpha\,\mathbf{F}_\alpha\,\mathrm{d}\mathbf{X}_\alpha \;=\; \mathbf{L}_\alpha\,\mathrm{d}\mathbf{x}\,. \tag{3.49}$$

Analogously, the velocity of area and volume elements follows from (3.34), viz.:

$$\begin{aligned}(\mathrm{d}\mathbf{a})'_\alpha \;&=\; [\,(\mathbf{L}_\alpha \cdot \mathbf{I})\,\mathbf{F}_\alpha^{T-1} \,-\, \mathbf{L}_\alpha^T\,\mathbf{F}_\alpha^{T-1}\,]\,\det\mathbf{F}_\alpha\,\mathrm{d}\mathbf{A}_\alpha = [\,(\mathbf{L}_\alpha \cdot \mathbf{I})\,\mathbf{I} \,-\, \mathbf{L}_\alpha^T\,]\,\mathrm{d}\mathbf{a}\,, \\ (\mathrm{d}v)'_\alpha \;&=\; (\mathbf{L}_\alpha \cdot \mathbf{I})\,\det\mathbf{F}_\alpha\,\mathrm{d}V_\alpha \;=\; (\mathbf{L}_\alpha \cdot \mathbf{I})\,\mathrm{d}v \;=\; (\mathrm{div}\,\overset{\prime}{\mathbf{x}}_\alpha)\,\mathrm{d}v\,.\end{aligned} \tag{3.50}$$

Therein, the calculation rule (A.10) and the relations in (B.13) were used. Moreover, it is found due to the skew-symmetric spin tensor $\mathbf{W}_\alpha$ that

$$\mathbf{L}_\alpha \cdot \mathbf{I} \;=\; \mathbf{D}_\alpha \cdot \mathbf{I} \;=\; (\mathrm{grad}\,\overset{\prime}{\mathbf{x}}_\alpha) \cdot \mathbf{I} \;=\; \mathrm{div}\,\overset{\prime}{\mathbf{x}}_\alpha\,. \tag{3.51}$$

In order to obtain the rate of the right Cauchy-Green deformation tensor $(3.39)_1$ the material time derivative is applied, and a further use of (3.46) and (B.13) yields

$$\begin{aligned}(\mathbf{C}_\alpha)'_\alpha \;=\; (\mathbf{F}_\alpha^T\,\mathbf{F}_\alpha)'_\alpha \;&=\; (\mathbf{F}_\alpha^T)'_\alpha\,\mathbf{F}_\alpha \,+\, \mathbf{F}_\alpha^T\,(\mathbf{F}_\alpha)'_\alpha \\ &=\; \mathbf{F}_\alpha^T\,\mathbf{L}_\alpha^T\,\mathbf{F}_\alpha \,+\, \mathbf{F}_\alpha^T\,\mathbf{L}_\alpha\,\mathbf{F}_\alpha \;=\; 2\,\mathbf{F}_\alpha^T\,\mathbf{D}_\alpha\,\mathbf{F}_\alpha\,.\end{aligned} \tag{3.52}$$

3.4 The state of stress

The previous discussion on kinematical aspects are based on the existence of a (finite) deformation process, which is initiated by an external loading of the body. Therefore, the (inner) state of stress is introduced within this section.

3.4.1 Volume and surface forces

In general, each constituent φ^α of the overall material body $\mathcal{B}$ can be subjected to an individual volume force $\mathbf{f}^\alpha$ acting on all material points $\mathcal{P}_\mathcal{B}^\alpha$ from a distance, cf. Figure 3.3. For the purposes of this monograph, an a priori constitutive assumption is made for all constituents φ^α postulating that the body force is proportional to the partial density ρ^α. This yields the force inkrement

$$\mathrm{d}\mathbf{k}_V^\alpha = \mathbf{f}^\alpha \,\mathrm{d}v \quad \rightarrow \quad \mathbf{k}_V^\alpha = \int_\mathcal{B} \mathbf{f}^\alpha \,\mathrm{d}v\,, \quad \text{where} \quad \mathbf{f}^\alpha = \rho^\alpha \,\mathbf{b}^\alpha\,. \tag{3.53}$$

Therein, $\mathbf{b}^\alpha$ represents the external volume force per mass unit and is commonly induced as the gravitation. However, other effects such as magnetism may occur. In addition to volume forces, the material points $\mathcal{P}_\mathcal{S}^\alpha$ on the surface $\mathcal{S}$ of the body can also be affected by individual contact forces $\mathbf{t}^\alpha$ acting at the vicinity. This yields

$$\mathrm{d}\mathbf{k}_O^\alpha = \mathbf{t}^\alpha \,\mathrm{d}a \quad \rightarrow \quad \mathbf{k}_O^\alpha = \int_\mathcal{S} \mathbf{t}^\alpha \,\mathrm{d}a\,. \tag{3.54}$$

Therein, the contact (surface) force per surface area $\mathbf{t}^\alpha = \mathbf{t}^\alpha(\mathbf{x}, \mathbf{n}, t)$ depends not solely on the actual position $\mathbf{x}$ and time t but additionally on the outward-oriented unit surface normal vector $\mathbf{n}$. In conclusion, the summation of surface and volume forces yields the total force $\mathbf{k}^\alpha$ acting on the constituent φ^α, viz.:

$$\mathbf{k}^\alpha = \mathbf{k}_V^\alpha + \mathbf{k}_O^\alpha = \int_\mathcal{B} \rho^\alpha \,\mathbf{b}^\alpha \,\mathrm{d}v + \int_\mathcal{S} \mathbf{t}^\alpha \,\mathrm{d}a\,. \tag{3.55}$$

3.4.2 Partial stress tensors

Regarding the use of the surface force $\mathbf{t}^\alpha = \mathbf{t}^\alpha(\mathbf{x}, \mathbf{n}, t)$ as a stress measure, an undesired property is found in the dependency on the surface orientation $\mathbf{n}$. Therefore, the stress

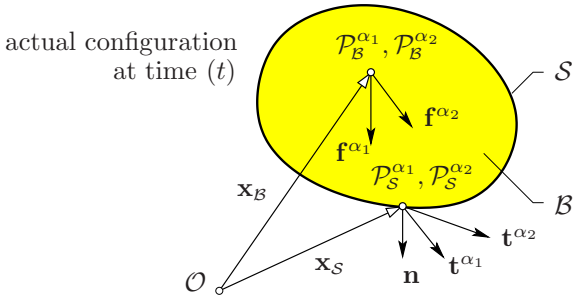

Figure 3.3: *Volume and surface forces acting on a multiphasic body.*

tensor concept is investigated to obtain a local stress measure, which is independent from the surface orientation. In a first step, Cauchy's lemma[5] is derived by a comparison of the resulting surface forces on a cut and its respective uncut body, yielding

$$\mathbf{t}^\alpha(\mathbf{x},\, t,\, \mathbf{n}) \;=\; -\,\mathbf{t}^\alpha(\mathbf{x},\, t,\, -\mathbf{n})\,. \tag{3.56}$$

Based on this lemma, Cauchy's theorem is obtained by studying the infinitesimal surrounding (tetrahedron) of a material point and neglecting the volume forces in comparison to the surface forces (due to a dimensional analysis). In particular, a static equilibrium and the use of (3.56) result in Cauchy's theorem, viz.:

$$\mathbf{t}^\alpha(\mathbf{x},\, t,\, \mathbf{n}) \;=\; [\,\mathbf{T}^\alpha(\mathbf{x},\, t)\,]\,\mathbf{n}\,. \tag{3.57}$$

Therein, $\mathbf{T}^\alpha$ is the partial Cauchy stress tensor of the constituent φ^α, also known as the so-called true stress, which relates the actual surface force element

$$\mathrm{d}\mathbf{k}_O^\alpha \;=\; \mathbf{t}^\alpha\,\mathrm{d}a \;=\; \mathbf{T}^\alpha\,\mathbf{n}\,\mathrm{d}a \;=\; \mathbf{T}^\alpha\,\mathrm{d}\mathbf{a} \tag{3.58}$$

to the oriented area element $\mathrm{d}\mathbf{a}$ of the actual configuration. Moreover, a further partial stress tensor is derived by relating the force element $\mathrm{d}\mathbf{k}_O^\alpha$ to a weighted area element of the actual configuration, yielding the Kirchhoff stress $\boldsymbol{\tau}^\alpha$, viz.:

$$\mathrm{d}\mathbf{k}_O^\alpha \;=\; \mathbf{t}^\alpha\,\mathrm{d}a \;=\; \boldsymbol{\tau}^\alpha\,\mathrm{d}\bar{\mathbf{a}}_\alpha\,, \quad \text{where} \quad \left\{\begin{array}{rcl} \boldsymbol{\tau}^\alpha &=& (\det\mathbf{F}_\alpha)\,\mathbf{T}^\alpha\,, \\ \mathrm{d}\bar{\mathbf{a}}_\alpha &=& (\det\mathbf{F}_\alpha)^{-1}\,\mathrm{d}\mathbf{a} \;=\; \dfrac{\mathrm{d}V_\alpha}{\mathrm{d}v}\,\mathrm{d}\mathbf{a}\,. \end{array}\right. \tag{3.59}$$

Relating the actual force element to an area element $\mathrm{d}\mathbf{A}_\alpha$ of the referential (undeformed) configuration yields the first Piola-Kirchhoff stress $\mathbf{P}^\alpha$, using the pull-back transformation (3.34) of the actual area element $\mathrm{d}a$, viz.:

$$\begin{aligned} \mathrm{d}\mathbf{k}_O^\alpha \;&=\; \mathbf{T}^\alpha\,\mathrm{cof}\,\mathbf{F}_\alpha\,\mathrm{d}\mathbf{A}_\alpha \;=\; \mathbf{P}^\alpha\,\mathrm{d}\mathbf{A}_\alpha\,, \\ &\text{with} \quad \mathbf{P}^\alpha \;=\; \det\mathbf{F}_\alpha\,\mathbf{T}^\alpha\,\mathbf{F}_\alpha^{T-1} \;=\; \boldsymbol{\tau}^\alpha\,\mathbf{F}_\alpha^{T-1}\,. \end{aligned} \tag{3.60}$$

Regarding (3.60), it is obvious that $\mathbf{P}^\alpha$ represents a two-field tensor. Accordingly, $\mathbf{P}^\alpha$ can be obtained by an incomplete covariant pull-back transformation (B.10) of the Kirchhoff stress $\boldsymbol{\tau}^\alpha$. Hence, $\mathbf{P}^\alpha$ (as well as all the other introduced stresses) are of covariant[6] nature by means of a natural basis representation. Since the first Piola-Kirchhoff stress is not symmetric, the symmetric second Piola-Kirchhoff stress $\mathbf{S}^\alpha$ is introduced by mapping $\mathbf{P}^\alpha$ entirely back to the reference configuration, yielding

$$\mathbf{S}^\alpha \;=\; \mathbf{F}_\alpha^{-1}\,\mathbf{P}^\alpha \;=\; \mathbf{F}_\alpha^{-1}\,\boldsymbol{\tau}^\alpha\,\mathbf{F}_\alpha^{T-1}\,. \tag{3.61}$$

Furthermore, the relation $\mathbf{F}_\alpha^{-1}\,\mathrm{d}\mathbf{k}_O^\alpha \;=\; \mathbf{S}^\alpha\,\mathrm{d}\mathbf{A}_\alpha$ is derived by inserting (3.61) in (3.60). This means, that $\mathbf{S}^\alpha\,\mathrm{d}\mathbf{A}_\alpha$ can be identified as the mapping of $\mathrm{d}\mathbf{k}_O^\alpha$ to the reference configuration. In conclusion, the covariant transport mechanisms are found, viz.:

$$\mathbf{S}^\alpha \;=\; \mathbf{F}_\alpha^{-1}\,\boldsymbol{\tau}^\alpha\,\mathbf{F}_\alpha^{T-1} \quad \text{and} \quad \boldsymbol{\tau}^\alpha \;=\; \mathbf{F}_\alpha\,\mathbf{S}^\alpha\,\mathbf{F}_\alpha^T\,. \tag{3.62}$$

[5] This corresponds to the famous interaction law "actio est reactio" (the third Newtonian law).

[6] This can also be found as a consequence from the contravariant nature of the oriented area elements.

3.5 Balance equations

The balance relations provide the basic set of equations for the solution of arbitrary continuum-mechanical problems. In general, these universal conservation laws are axiomatically introduced and base on reasonable physical observations. After the establishment of a general structure (master principle) of balance relations, evaluated for the overall aggregate as well as for the particular constituents, specific mechanical and thermodynamical balance relations are introduced. Based on this, a customised model for the brain's tissue requires a further completion by an appropriate constitutive modelling, which is strongly related to these considerations and continued in Chapter 4.

3.5.1 Preliminaries

Although the balance equations in terms of the TPM are of fundamental importance for the considered modelling approach, only a condensed review is given here. This is caused by the availability of various contributions treating these issues in a detailed manner, cf., e. g., Ehlers [48, 50, 51] and citations therein. The basis of the formulation of multiphasic balances is found in the classical Theory of Mixtures, cf., e. g., Bowen [25, 26], Kelly [90], Truesdell [158] and Truesdell & Toupin [160]. Fundamentally, the introduction of all specific balances is based on Truesdell's famous three "metaphysical principles" of mixture theories, cf. Truesdell [158]. They are introduced as:

(1) All properties of the mixture must be mathematical consequences of properties of the constituents.

(2) So as to describe the motion of a constituent, we may in imagination isolate it from the rest of the mixture, provided we allow properly for the actions of the other constituents upon it.

(3) The motion of the mixture is governed by the same equations as is a single body.

Note that in the present monograph the term mixture is used in the sense of a mixture of immiscible constituents, i. e., the overall aggregate. The basic idea is to proceed, according to the third principle, in analogy to the introduction of balance relations of singlephasic materials, cf. Ehlers [46], Haupt [76] or Holzapfel [79]. Moreover, the second principle indicates that care must be taken for the interaction mechanisms between the constituents by a proper inclusion of production terms. In particular, this is strongly required in order to obtain the overall model by means of the first principle.

Open and closed systems illustrated by the example of mass conversation: A thermodynamic system is defined as a particular quantity of matter or a particular region of space under consideration, cf. Rathakrishnan [127]. In general, the system is separated from its surroundings by its boundary, cf. Figure 3.4. In a closed system, the amount of mass stays always constant. This means that mass can not cross the (movable) boundary and leave (or enter) the domain of the system. In contrast, mass is able to cross the boundary of a system in terms of open systems. Thus, it is easily concluded that the

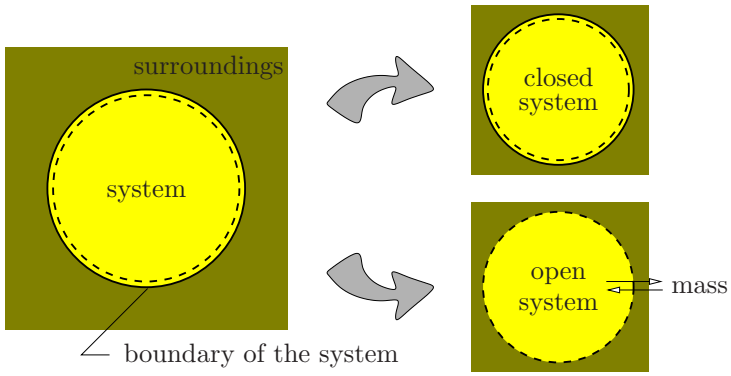

Figure 3.4: *Open and closed systems illustrated by the example of mass.*

mass in a closed system stays constant unless mass is somehow produced in the interior of the system. In conclusion, for the purposes of this monograph, the overall aggregate can be understood as a closed system, whereas open systems are applied for the included constituents.

3.5.2 General balance structure of the overall aggregate

As stated by Truesdell's third metaphysical principle, the global formulation of the general balance principle of the overall aggregate is postulated for volume-specific mechanical quantities[7] Ψ (scalar-valued) and $\boldsymbol{\Psi}$ (vector-valued), viz.:

$$\begin{aligned} \text{scalar-valued:} \quad & \frac{\mathrm{d}}{\mathrm{d}t}\int_{\mathcal{B}} \Psi \,\mathrm{d}v = \int_{\mathcal{S}} (\boldsymbol{\phi}\cdot\mathbf{n})\,\mathrm{d}a + \int_{\mathcal{B}} \sigma \,\mathrm{d}v + \int_{\mathcal{B}} \hat{\Psi}\,\mathrm{d}v\,, \\ \text{vector-valued:} \quad & \frac{\mathrm{d}}{\mathrm{d}t}\int_{\mathcal{B}} \boldsymbol{\Psi} \,\mathrm{d}v = \int_{\mathcal{S}} (\boldsymbol{\Phi}\,\mathbf{n})\,\mathrm{d}a + \int_{\mathcal{B}} \boldsymbol{\sigma} \,\mathrm{d}v + \int_{\mathcal{B}} \hat{\boldsymbol{\Psi}}\,\mathrm{d}v\,. \end{aligned} \tag{3.63}$$

Therein, the temporal change of the quantities Ψ and $\boldsymbol{\Psi}$ is in equilibrium with the sum of the effluxes $\boldsymbol{\phi}\cdot\mathbf{n}$ and $\boldsymbol{\Phi}\,\mathbf{n}$ (at the vicinity), the supply terms σ and $\boldsymbol{\sigma}$ (acting from a distance) and the production terms $\hat{\Psi}$ and $\hat{\boldsymbol{\Psi}}$ of the mechanical quantities. In general, the production term describes the interaction of the mechanical quantity with the surrounding of the system. However, regarding closed systems of the overall aggregate, the production terms vanish except for the entropy production. The local formulation (locally expressed at the material point) of the master balance principle is obtained by evaluating the global representation (3.63). Within this procedure, the left-hand side is subjected to the material time derivative[8]. On the right-hand side, the Gaussian integral theorem, cf., e. g., Ehlers [45], is applied in order to transform the only occurring surface integral into a

[7] Regarding the later evaluation of specific balances, Ψ is subsequently assigned to the local density ρ, the local internal energy $\rho\,\varepsilon$ and the local entropy $\rho\,\eta$, yielding the balances of mass, energy and entropy. The quantity $\boldsymbol{\Psi}$ is used in terms of the momentum $\mathbf{l}$ and the moment of momentum $\mathbf{h}$, resulting in the balances of momentum (linear momentum) and moment of momentum (angular momentum).

[8] In particular, the computation $\dfrac{\mathrm{d}}{\mathrm{d}t}\displaystyle\int_{\mathcal{B}} \Psi\,\mathrm{d}v = \int_{\mathcal{B}} \left[\dot{\Psi}\,\mathrm{d}v + \Psi\,(\mathrm{d}v)^{\cdot}\right] = \int_{\mathcal{B}} (\dot{\Psi} + \Psi\,\mathrm{div}\,\dot{\mathbf{x}})\,\mathrm{d}v$ is used.

volume integral. This yields, assuming steady and steadily differentiable integrands, the local formulations, viz.:

$$\begin{aligned} \dot{\Psi} \;+\; \Psi \operatorname{div} \dot{\mathbf{x}} \;&=\; \operatorname{div} \boldsymbol{\phi} \;+\; \sigma \;+\; \hat{\Psi}\,, \\ \dot{\boldsymbol{\Psi}} \;+\; \boldsymbol{\Psi} \operatorname{div} \dot{\mathbf{x}} \;&=\; \operatorname{div} \boldsymbol{\Phi} \;+\; \boldsymbol{\sigma} \;+\; \hat{\boldsymbol{\Psi}}\,. \end{aligned} \tag{3.64}$$

3.5.3 General balance structure of the particular constituents

Proceeding from Truesdell's second metaphysical principle, the master principle of the general balance relations for the particular constituents can be given based on the considerations made in (3.63), viz.:

$$\begin{aligned} \text{scalar-valued:}\quad \frac{\mathrm{d}_\alpha}{\mathrm{d}t} \int_{\mathcal{B}} \Psi^\alpha \,\mathrm{d}v \;&=\; \int_{\mathcal{S}} (\boldsymbol{\phi}^\alpha \cdot \mathbf{n}) \,\mathrm{d}a \;+\; \int_{\mathcal{B}} \sigma^\alpha \,\mathrm{d}v \;+\; \int_{\mathcal{B}} \hat{\Psi}^\alpha \,\mathrm{d}v\,, \\ \text{vector-valued:}\quad \frac{\mathrm{d}_\alpha}{\mathrm{d}t} \int_{\mathcal{B}} \boldsymbol{\Psi}^\alpha \,\mathrm{d}v \;&=\; \int_{\mathcal{S}} (\boldsymbol{\Phi}^\alpha \,\mathbf{n}) \,\mathrm{d}a \;+\; \int_{\mathcal{B}} \boldsymbol{\sigma}^\alpha \,\mathrm{d}v \;+\; \int_{\mathcal{B}} \hat{\boldsymbol{\Psi}}^\alpha \,\mathrm{d}v\,. \end{aligned} \tag{3.65}$$

In comparison to (3.63), the production terms $\hat{\Psi}^\alpha$ and $\hat{\boldsymbol{\Psi}}^\alpha$ can exist, even for closed systems of the overall aggregate, and describe the mutual interaction of the particular constituents. The local formulations are derived in analogy to (3.64), yielding

$$\begin{aligned} (\Psi^\alpha)'_\alpha \;+\; \Psi^\alpha \operatorname{div} \mathbf{x}'_\alpha \;&=\; \operatorname{div} \boldsymbol{\phi}^\alpha \;+\; \sigma^\alpha \;+\; \hat{\Psi}^\alpha\,, \\ (\boldsymbol{\Psi}^\alpha)'_\alpha \;+\; \boldsymbol{\Psi}^\alpha \operatorname{div} \mathbf{x}'_\alpha \;&=\; \operatorname{div} \boldsymbol{\Phi}^\alpha \;+\; \boldsymbol{\sigma}^\alpha \;+\; \hat{\boldsymbol{\Psi}}^\alpha\,. \end{aligned} \tag{3.66}$$

According to Truesdell's first metaphysical principle, the balances of the overall aggregate, gained by a summation of the particular balances (3.66), must provide the same statements as those given in (3.64). Therefore, accordances and restrictions between the particular constituents and the overall aggregate are obtained via

$$\begin{aligned} \Psi \;&=\; \textstyle\sum_\alpha \Psi^\alpha\,, \quad \phi \;=\; \sum_\alpha (\phi^\alpha - \Psi^\alpha \,\mathbf{d}_\alpha)\,, \qquad \sigma \;=\; \sum_\alpha \sigma^\alpha\,, \quad \hat{\Psi} \;=\; \sum_\alpha \hat{\Psi}^\alpha\,, \\ \boldsymbol{\Psi} \;&=\; \textstyle\sum_\alpha \boldsymbol{\Psi}^\alpha\,, \quad \boldsymbol{\Phi} \;=\; \sum_\alpha (\boldsymbol{\Phi}^\alpha - \boldsymbol{\Psi}^\alpha \otimes \mathbf{d}_\alpha)\,, \quad \boldsymbol{\sigma} \;=\; \sum_\alpha \boldsymbol{\sigma}^\alpha\,, \quad \hat{\boldsymbol{\Psi}} \;=\; \sum_\alpha \hat{\boldsymbol{\Psi}}^\alpha\,. \end{aligned} \tag{3.67}$$

Therein, the relations (3.21) and $(\mathrm{A}.11)_5$ are used to obtain the correlations for the efluxes.

3.5.4 Specific mechanical balance equations

The specific balance relations for the overall aggregate φ and the constituents φ^α are derived based on axiomatical introductions. A comparison of the postulated axioms with the global master formulations (3.63) and (3.65) enables the identification of the particular included quantities and results in the local formulation of the respective balance equation. Furthermore, a hierarchical structure guides the evaluation process in a distinct order.

Consequently, the evaluation proceeds from the so-called "lower" balance relations. The "higher" balance relations subsequently base on the accumulated previous findings.

Balance of mass: Proceeding from the axiomatical statement that in a closed system the mass M of the overall aggregate φ stays always constant, results in

$$M = \int_{\mathcal{B}} \rho \, \mathrm{d}v = \text{const.} \quad \rightarrow \quad \dot{M} = \frac{\mathrm{d}}{\mathrm{d}t} \int_{\mathcal{B}} \rho \, \mathrm{d}v = 0 \,. \tag{3.68}$$

In contrast, regarding an individual constituent φ^α, the temporal change of mass can differ from zero if mutual mass interactions between the constituents occur. This is postulated via

$$\frac{\mathrm{d}_\alpha}{\mathrm{d}t} \int_{\mathcal{B}} \rho^\alpha \, \mathrm{d}v = \int_{\mathcal{B}} \hat{\rho}^\alpha \, \mathrm{d}v \,, \tag{3.69}$$

where $\hat{\rho}^\alpha$ denotes the mass production per volume element. Comparing the axiomatical statements (3.68) and (3.69) with the corresponding global master balances $(3.63)_1$ and $(3.65)_1$, the following correlations are obtained:

$$\begin{aligned} &\Psi \;\rightarrow\; \rho \,, \quad \boldsymbol{\phi} \;\rightarrow\; \mathbf{0} \,, \quad \sigma \;\rightarrow\; 0 \,, \quad \hat{\Psi} \;\rightarrow\; 0 \,, \\ &\Psi^\alpha \;\rightarrow\; \rho^\alpha \,, \quad \boldsymbol{\phi}^\alpha \;\rightarrow\; \mathbf{0} \,, \quad \sigma^\alpha \;\rightarrow\; 0 \,, \quad \hat{\Psi}^\alpha \;\rightarrow\; \hat{\rho}^\alpha \,. \end{aligned} \tag{3.70}$$

Therefore, the local formulation of the mass balance of the overall aggregate φ is obtained by inserting the identified quantities $(3.70)_1$ into the general local form $(3.64)_1$, yielding

$$\dot{\rho} + \rho \operatorname{div} \dot{\mathbf{x}} = 0 \,. \tag{3.71}$$

Within an analogous procedure, the quantities assigned in $(3.70)_2$ are inserted in $(3.66)_1$. This yields the specific mass balance of the constituent φ^α, viz.:

$$(\rho^\alpha)'_\alpha + \rho^\alpha \operatorname{div} \overset{\prime}{\mathbf{x}}_\alpha = \hat{\rho}^\alpha \,. \tag{3.72}$$

A comparison of (3.70) with $(3.67)_1$, by means of Truesdell's first principle, yields (among others) the following important relations:

$$\rho = \sum_\alpha \rho^\alpha \,, \quad \sum_\alpha \hat{\rho}^\alpha = 0 \,. \tag{3.73}$$

Therein, the relation linking the overall density to the partial densities is reconfirmed, cf. (3.9). Moreover, a fundamental restriction for the mass production term $\hat{\rho}^\alpha$ is obtained, stating that the sum of mass supply is equal to zero.

The summation of all partial mass balances (3.72) results in the overall mass balance (3.71) as claimed by Truesdell's first principle, viz.:

$$\begin{aligned} \sum_\alpha \left\{ (\rho^\alpha)'_\alpha + \rho^\alpha \operatorname{div} \overset{\prime}{\mathbf{x}}_\alpha \right\} = \sum_\alpha \hat{\rho}^\alpha \;&=\; 0 \\ &=\; \sum_\alpha \left\{ \frac{\partial \rho^\alpha}{\partial t} + \operatorname{div} (\rho^\alpha \overset{\prime}{\mathbf{x}}_\alpha) \right\} \\ &=\; \frac{\partial \rho}{\partial t} + \operatorname{div} (\rho \dot{\mathbf{x}}) = \dot{\rho} + \rho \operatorname{div} \dot{\mathbf{x}} \,. \end{aligned} \tag{3.74}$$

Therein, the relations (3.22), $(3.19)_1$, (3.73) and $(A.11)_4$ have been used.

Balance of momentum: It is axiomatically stated for the overall aggregate φ that the temporal change of the local momentum $\mathbf{l} = \rho\,\dot{\mathbf{x}}$ is balanced by the sum of acting forces. Furthermore, the acting forces are separated into surface and body forces, cf. Section 3.4.1. This yields

$$\frac{\mathrm{d}}{\mathrm{d}t}\int\limits_{\mathcal{B}} \rho\,\dot{\mathbf{x}}\,\mathrm{d}v \;=\; \int\limits_{\mathcal{S}} (\mathbf{T}\,\mathbf{n})\,\mathrm{d}a \;+\; \int\limits_{\mathcal{B}} \rho\,\mathbf{b}\,\mathrm{d}v\,. \tag{3.75}$$

This axiom is analogously transferred to the temporal change of the momentum $\rho^\alpha\,{}'\mathbf{x}_\alpha$ of the constituent φ^α and further extended by the momentum production $\hat{\mathbf{s}}^\alpha$ of homogenised internal contact forces, viz.:

$$\frac{\mathrm{d}_\alpha}{\mathrm{d}t}\int\limits_{\mathcal{B}} \rho^\alpha\,{}'\mathbf{x}_\alpha\,\mathrm{d}v \;=\; \int\limits_{\mathcal{S}} (\mathbf{T}^\alpha\,\mathbf{n})\,\mathrm{d}a \;+\; \int\limits_{\mathcal{B}} \rho^\alpha\,\mathbf{b}^\alpha\,\mathrm{d}v \;+\; \int\limits_{\mathcal{B}} \hat{\mathbf{s}}^\alpha\,\mathrm{d}v\,. \tag{3.76}$$

In comparison to the vector-valued global master balances $(3.63)_2$ and $(3.65)_2$, the accordances for the overall aggregate φ and the constituent φ^α arise via

$$\begin{aligned} \boldsymbol{\Psi} &\;\to\; \rho\,\dot{\mathbf{x}}\,, \quad \boldsymbol{\Phi} \;\to\; \mathbf{T}\,, \quad \boldsymbol{\sigma} \;\to\; \rho\,\mathbf{b}\,, \quad \hat{\boldsymbol{\Psi}} \;\to\; \mathbf{0}\,, \\ \boldsymbol{\Psi}^\alpha &\;\to\; \rho^\alpha\,{}'\mathbf{x}_\alpha\,, \quad \boldsymbol{\Phi}^\alpha \;\to\; \mathbf{T}^\alpha\,, \quad \boldsymbol{\sigma}^\alpha \;\to\; \rho^\alpha\,\mathbf{b}^\alpha\,, \quad \hat{\boldsymbol{\Psi}}^\alpha \;\to\; \hat{\mathbf{s}}^\alpha\,. \end{aligned} \tag{3.77}$$

The local formulation of the momentum balance of the overall aggregate φ is obtained by inserting $(3.77)_1$ into $(3.64)_2$ and reformulating the left-hand side, using the mass balance (3.71). This results in

$$\rho\,\ddot{\mathbf{x}} \;=\; \operatorname{div}\mathbf{T} \;+\; \rho\,\mathbf{b}\,. \tag{3.78}$$

The same procedure is applied analogously to the individual constituent φ^α using $(3.77)_2$, $(3.66)_2$ and (3.72). This yields the local momentum balance of the constituent φ^α, viz.:

$$\rho^\alpha\,{}''\mathbf{x}_\alpha \;=\; \operatorname{div}\mathbf{T}^\alpha \;+\; \rho^\alpha\,\mathbf{b}^\alpha \;+\; \hat{\mathbf{p}}^\alpha\,, \quad \text{where} \quad \hat{\mathbf{s}}^\alpha \;=\; \hat{\mathbf{p}}^\alpha \;+\; \hat{\rho}^\alpha\,{}'\mathbf{x}_\alpha\,. \tag{3.79}$$

It can be seen that the direct momentum production term $\hat{\mathbf{p}}^\alpha$ constitutes, in a combination with a part resulting from the mass supply $\hat{\rho}^\alpha$, the total momentum production $\hat{\mathbf{s}}^\alpha$. A comparison of (3.77) with $(3.67)_2$, yields the following dependencies

$$\begin{aligned} \dot{\mathbf{x}} \;&=\; \frac{1}{\rho}\sum_\alpha \rho^\alpha\,{}'\mathbf{x}_\alpha \quad , \quad \mathbf{T} \;=\; \sum_\alpha \left(\mathbf{T}^\alpha \;-\; \rho^\alpha\,\mathbf{d}_\alpha \otimes \mathbf{d}_\alpha\right), \\ \rho\,\mathbf{b} \;&=\; \sum_\alpha \rho^\alpha\,\mathbf{b}^\alpha \quad , \quad \sum_\alpha \hat{\mathbf{s}}^\alpha \;=\; \sum_\alpha \left(\,\hat{\mathbf{p}}^\alpha \;+\; \hat{\rho}^\alpha\,{}'\mathbf{x}_\alpha\,\right) \;=\; \mathbf{0}\,. \end{aligned} \tag{3.80}$$

Therein, the relation for the velocity of the overall aggregate, introduced in (3.22) is verified again. Moreover, relations for the stress and the body forces (3.9) are obtained and the governing restriction for the total momentum production term $\hat{\mathbf{s}}^\alpha$ is recovered.

Balance of moment of momentum: The axiomatical statement of the third mechanical balance law postulates that the temporal change of the body moment of momentum equals the sum of moments of all forces acting on the body. Naturally, these quantities depend on an arbitrary but spatial fixed reference point. In this context, the origin $\mathcal{O}$ of the inertial basis system $\{0,\, \mathbf{e}_i\}$ is chosen for the sake of simplicity. Therefore, it follows for the overall aggregate φ that

$$\frac{\mathrm{d}}{\mathrm{d}t} \int\limits_{\mathcal{B}} \mathbf{x} \times (\rho\, \dot{\mathbf{x}})\, \mathrm{d}v \;=\; \int\limits_{\mathcal{S}} (\mathbf{x} \times \mathbf{T})\, \mathrm{d}\mathbf{a} \;+\; \int\limits_{\mathcal{B}} \mathbf{x} \times (\rho\, \mathbf{b})\, \mathrm{d}v\,, \tag{3.81}$$

and, accordingly, for the constituent φ^α that

$$\frac{\mathrm{d}_\alpha}{\mathrm{d}t} \int\limits_{\mathcal{B}} \mathbf{x} \times (\rho^\alpha\, {}'_{\alpha}\mathbf{x}_\alpha)\, \mathrm{d}v \;=\; \int\limits_{\mathcal{S}} (\mathbf{x} \times \mathbf{T}^\alpha)\, \mathrm{d}\mathbf{a} \;+\; \int\limits_{\mathcal{B}} \mathbf{x} \times (\rho^\alpha\, \mathbf{b}^\alpha)\, \mathrm{d}v \;+\; \int\limits_{\mathcal{B}} \hat{\mathbf{h}}^\alpha\, \mathrm{d}v\,. \tag{3.82}$$

Therein, $\hat{\mathbf{h}}^\alpha$ denotes the total production of the moment of momentum. In comparison with the global master balances (3.63) and (3.65) the accordances for the overall aggregate φ and for the constituent φ^α are obtained via

$$\begin{aligned} &\boldsymbol{\Psi} \;\to\; \mathbf{x} \times (\rho\, \dot{\mathbf{x}})\,, \quad \boldsymbol{\Phi} \;\to\; \mathbf{x} \times \mathbf{T}\,, \quad \boldsymbol{\sigma} \;\to\; \mathbf{x} \times (\rho\, \mathbf{b})\,, \quad \hat{\boldsymbol{\Psi}} \;\to\; \mathbf{0}\,, \\ &\boldsymbol{\Psi}^\alpha \;\to\; \mathbf{x} \times (\rho^\alpha\, {}'_{\alpha}\mathbf{x}_\alpha)\,, \quad \boldsymbol{\Phi}^\alpha \;\to\; \mathbf{x} \times \mathbf{T}^\alpha\,, \quad \boldsymbol{\sigma}^\alpha \;\to\; \mathbf{x} \times (\rho^\alpha\, \mathbf{b}^\alpha)\,, \quad \hat{\boldsymbol{\Psi}}^\alpha \;\to\; \hat{\mathbf{h}}^\alpha\,. \end{aligned} \tag{3.83}$$

An evaluation of $(3.83)_1$ in terms of $(3.64)_2$ and further reformulations using the mass and momentum balances (3.71), (3.78) leads to the key statement of the balance of moment of momentum for the overall aggregate φ, namely

$$\mathbf{0} = \mathbf{I} \times \mathbf{T} \quad \to \quad \mathbf{T} = \mathbf{T}^T\,. \tag{3.84}$$

In particular, the symmetry of the overall Cauchy stress tensor is obtained[9]. Accordingly, the statement of the balance of moment of momentum for the particular constituent φ^α is obtained by inserting $(3.83)_2$ in $(3.66)_2$ and using the "lower" balances (3.72) and (3.79). This results in

$$\mathbf{0} = \mathbf{I} \times \mathbf{T}^\alpha + \hat{\mathbf{m}}^\alpha \quad \to \quad (\mathbf{T}^\alpha)^T = \mathbf{T}^\alpha + \hat{\mathbf{M}}^\alpha\,, \tag{3.85}$$

where the direct production term $\hat{\mathbf{m}}^\alpha$ corresponds to the so-called coupling tensor $\hat{\mathbf{M}}^\alpha$, representing the skew-symmetric part of the partial stress tensor.

Remark: For non-polar materials (Cauchy-Boltzmann continua) with symmetric stresses on the microscale, a homogenisation procedure shows that the macroscopic stresses must also be symmetric, cf. Ehlers [50], Hassanizadeh & Gray [75]. Therefore, the statement of (3.85) is transferred to

$$\mathbf{T}^\alpha = (\mathbf{T}^\alpha)^T \quad \to \quad \hat{\mathbf{m}}^\alpha \equiv \mathbf{0}\,. \tag{3.86}$$

[9] To obtain $(3.84)_2$, the property of the axial vector (A.7) is used. The axial vector is assigned to the skew symmetric part of a tensor. Hence, the vanishing axial vector indicates the symmetry of the stess tensor.

In the framework of the micropolar theory (Cosserat continua), the balance of moment of momentum corresponds to the rotations (additional degrees of freedom) of particles. Since this contribution is restricted to non-polar constituents, the interested reader is referred to, e. g., Diebels [38], Ehlers [50], Ehlers *et al.* [58] or Scholz [140].

3.5.5 Specific thermodynamical balance laws

After the introduction of purely mechanical balances, the thermodynamical balance laws of energy and entropy are supplemented here. In this regard, the energy balance can serve as a governing equation in the treatment of thermodynamical problems, e. g., heat-transport processes. Since thermal effects are neglected in the developed brain-tissue model afterwards, the energy balance plays a minor role within this contribution. However, the arising entropy inequality plays a fundamental role in providing the frame for the development of thermodynamical consistent material laws, as it is described in Chapter 4.

Energy balance: The first law of thermodynamics axiomatically postulates that the sum of temporal changes of the internal energy $\mathcal{E}$ and kinetic energy $\mathcal{K}$ of a body balances the sum of external mechanical power $\mathcal{L}_a$ and non-mechanical power $\mathcal{Q}_a$, yielding

$$\frac{\mathrm{d}}{\mathrm{d}t}\left[\,\mathcal{E}(\mathcal{B},t)\,+\,\mathcal{K}(\mathcal{B},t)\,\right] \,=\, \mathcal{L}_a(\mathcal{B},t)\,+\,\mathcal{Q}_a(\mathcal{B},t)\,. \tag{3.87}$$

Therein, the introduced expressions in (3.87) are given via

$$\begin{aligned} \mathcal{E} &= \int_{\mathcal{B}} \varepsilon\,\rho\,\mathrm{d}v\,, & \mathcal{K} &= \int_{\mathcal{B}} \tfrac{1}{2}\,\dot{\mathbf{x}}\cdot\dot{\mathbf{x}}\,\rho\,\mathrm{d}v\,, \\ \mathcal{L}_a &= \int_{\mathcal{S}} \dot{\mathbf{x}}\cdot\mathbf{t}\,\mathrm{d}a \,+\, \int_{\mathcal{B}} \dot{\mathbf{x}}\cdot\rho\,\mathbf{b}\,\mathrm{d}v\,, & \mathcal{Q}_a &= -\int_{\mathcal{S}} \mathbf{q}\cdot\mathbf{n}\,\mathrm{d}a \,+\, \int_{\mathcal{B}} r\,\rho\,\mathrm{d}v\,. \end{aligned} \tag{3.88}$$

In terms of non-mechanical power, the convection term $\mathbf{q}$ (action at the vicinity) denotes the heat influx[10] through the surface, whereas the radiation r (action from a distance) represents the external heat supply. This leads to the local formulation of the energy balance of the overall aggregate φ and analogously to the constituent φ^α, viz.:

$$\begin{aligned} \rho\,\dot{\varepsilon} &= \mathbf{T}\cdot\mathbf{L} \,-\, \operatorname{div}\mathbf{q} \,+\, \rho\,r \quad \text{and} \\ \rho^\alpha\,(\varepsilon^\alpha)'_\alpha &= \mathbf{T}^\alpha\cdot\mathbf{L}_\alpha \,-\, \operatorname{div}\mathbf{q}^\alpha \,+\, \rho^\alpha\,r^\alpha \,+\, \hat{\varepsilon}^\alpha\,, \\ &\qquad \text{with} \quad \hat{e}^\alpha \,=\, \hat{\varepsilon}^\alpha \,+\, \hat{\mathbf{p}}^\alpha\cdot\overset{\prime}{\mathbf{x}}_\alpha \,+\, \hat{\rho}^\alpha\,(\,\varepsilon^\alpha \,+\, \tfrac{1}{2}\,\overset{\prime}{\mathbf{x}}_\alpha\cdot\overset{\prime}{\mathbf{x}}_\alpha\,)\,. \end{aligned} \tag{3.89}$$

Therein, the overall energy production term $\hat{e}^\alpha$ contains a direct part $\hat{\varepsilon}^\alpha$, a part stemming from the direct momentum production and a part induced by the density production (containing specific internal and kinetic energy).

[10] Note that the negative sign in front of $\mathbf{q}$ is introduced here due to the reverse orientation in relation to the efflux given in the master balance principle (3.63).

Entropy principle: It is axiomatically stated that the temporal change of the entropy $\mathcal{H}$ in a body equals the sum of the external change of entropy $\mathcal{S}_a$ and the internal entropy production $\mathcal{S}_i$, yielding

$$\frac{\mathrm{d}}{\mathrm{d}t}\,\mathcal{H}(\mathcal{B},t) \;=\; \mathcal{S}_a(\mathcal{B},t) \;+\; \mathcal{S}_i(\mathcal{B},t)\,. \tag{3.90}$$

Therein, the expressions

$$\mathcal{H} \;=\; \int\limits_{\mathcal{B}} \eta\,\rho\,\mathrm{d}v\,, \quad \mathcal{S}_a \;=\; \int\limits_{\mathcal{S}} \boldsymbol{\phi}_\eta \cdot \mathbf{n}\,\mathrm{d}a \;+\; \int\limits_{\mathcal{B}} \sigma_\eta\,\mathrm{d}v \quad \text{and} \quad \mathcal{S}_i \;=\; \int\limits_{\mathcal{B}} \hat{\eta}\,\mathrm{d}v \tag{3.91}$$

are used. In particular, these terms include the mass-specific entropy η, the entropy efflux $\boldsymbol{\phi}_\eta$ and the entropy supply σ_η, which are given by means of a priori constitutive assumptions, according to Ehlers [44, 47, 48, 50, 51] and citations therein, viz.:

$$\boldsymbol{\phi}_\eta \;=\; -\,\frac{\mathbf{q}}{\theta} \qquad \text{and} \qquad \sigma_\eta \;=\; \frac{\rho\,r}{\theta}\,. \tag{3.92}$$

As is already known, the insertion of (3.92) and (3.91) into the postulated axiomatical statement (3.90) enables the comparison to (3.63), yielding

$$\Psi \;\to\; \rho\,\eta\,, \quad \boldsymbol{\phi} \;\to\; -\,\frac{\mathbf{q}}{\theta}\,, \quad \sigma \;\to\; \frac{\rho\,r}{\theta}\,, \quad \hat{\Psi} \;\to\; \hat{\eta}\,. \tag{3.93}$$

Thus, it follows for the overall aggregate φ by insertion of (3.93) into $(3.64)_1$ and further reformulation of the left-hand side using the mass balance (3.71):

$$\rho\,\dot{\eta} \;=\; -\,\mathrm{div}\Big(\frac{\mathbf{q}}{\theta}\Big) \;+\; \frac{\rho\,r}{\theta} \;+\; \hat{\eta}\,. \tag{3.94}$$

Concerning the investigation of the entropy balance of the specific constituent φ^α, the same basic considerations are made for the individual constituents. This results in

$$\Psi^\alpha \;\to\; \rho^\alpha\,\eta^\alpha, \quad \boldsymbol{\phi}^\alpha \;\to\; -\,\frac{\mathbf{q}^\alpha}{\theta^\alpha}\,, \quad \sigma^\alpha \;\to\; \frac{\rho^\alpha\,r^\alpha}{\theta^\alpha}\,, \quad \hat{\Psi}^\alpha \;\to\; \hat{\eta}^\alpha\,. \tag{3.95}$$

Therefore, the entropy balance of φ^α is obtained by insertion of (3.95) into $(3.66)_1$ and inclusion of the constituent's mass balance (3.72), yielding

$$\rho^\alpha\,(\eta^\alpha)'_\alpha \;=\; -\,\mathrm{div}\,\Big(\frac{\mathbf{q}^\alpha}{\theta^\alpha}\Big) \;+\; \frac{\rho^\alpha\,r^\alpha}{\theta^\alpha} \;+\; \hat{\zeta}^\alpha\,, \quad \text{with} \quad \hat{\eta}^\alpha \;=\; \hat{\zeta}^\alpha \;+\; \hat{\rho}^\alpha\,\eta^\alpha\,. \tag{3.96}$$

Therein, $\hat{\zeta}^\alpha$ denote the volume specific direct entropy production of φ^α. Finally, the entropy inequality of the whole aggregate arises by an additional axiomatical statement, postulating that the total entropy production $\hat{\eta}$ is never negative. Proceeding from (3.96), the insertion into the restriction of the entropy production (3.67) yields

$$\hat{\eta} \;=\; \sum_\alpha \hat{\eta}^\alpha \;=\; \sum_\alpha \big[\,\rho^\alpha\,(\eta^\alpha)'_\alpha \;+\; \hat{\rho}^\alpha\,\eta^\alpha \;+\; \mathrm{div}\,\Big(\frac{\mathbf{q}^\alpha}{\theta^\alpha}\Big) \;-\; \frac{\rho^\alpha\,r^\alpha}{\theta^\alpha}\,\big] \;\geq\; 0\,. \tag{3.97}$$

Applying $(A.11)_6$, the energy balance $(3.89)_1$ and, in particular, the definition of the Helmholtz free energy

$$\psi^\alpha := \varepsilon^\alpha - \theta^\alpha \eta^\alpha \tag{3.98}$$

lead to the so-called Clausius-Duhem inequality, viz.:

$$\begin{aligned} \sum_\alpha \frac{1}{\theta^\alpha} \Big\{ \mathbf{T}^\alpha \cdot \mathbf{L}_\alpha - \rho^\alpha [\, (\psi^\alpha)'_\alpha + (\theta^\alpha)'_\alpha \, \eta^\alpha \,] - \hat{\mathbf{p}}^\alpha \cdot \overset{\prime}{\mathbf{x}}_\alpha - \\ - \hat{\rho}^\alpha \, (\psi^\alpha + \tfrac{1}{2} \overset{\prime}{\mathbf{x}}_\alpha \cdot \overset{\prime}{\mathbf{x}}_\alpha) - \frac{\mathbf{q}^\alpha}{\theta^\alpha} \cdot \operatorname{grad} \theta^\alpha + \hat{e}^\alpha \Big\} \geq 0 \,. \end{aligned} \tag{3.99}$$

For isothermal conditions (common constant temperature $\theta^\alpha \equiv \theta = \text{const.}$), as well as non-existent mass and energy production terms, the so-called Clausius-Planck inequality is obtained straightforward from (3.99), viz.:

$$\sum_\alpha \big[\, \mathbf{T}^\alpha \cdot \mathbf{L}_\alpha - \rho^\alpha \, (\psi^\alpha)'_\alpha - \hat{\mathbf{p}}^\alpha \cdot \overset{\prime}{\mathbf{x}}_\alpha \big] \geq 0 \,. \tag{3.100}$$

Note that any thermodynamically consistent process needs to satisfy the entropy inequality, which plays a fundamental role in the constitutive modelling process in Chapter 4.

Chapter 4:
Constitutive settings

The underlying fundamental principles of multiphasic models, presented in Chapter 3, enable the development of various kinds of customised models. Based on this general introduction, the purpose of this chapter is to present the particular investigations of the brain-tissue model under consideration. Therefore, several appropriate preliminary assumptions are made yielding a further specification (adaption) of the basic balance equations. Afterwards, the constitutive equations for the involved constituents are derived within a thermodynamically consistent manner via an evaluation process of the entropy inequality. In this regard, the objective of the derived constitutive setting is twofold. On the one hand, it is necessary to close the resulting set of governing equations and, on the other hand, it enables the description of the specific behaviour of the considered brain-tissue aggregate.

4.1 Preliminary model assumptions

In order to apply the previous findings to the modelling of brain tissue, the objective is to state meaningful a priori constitutive assumptions, yielding possible simplifications for the particularly focused issues within this monograph. Although the introduced preliminary assumptions induce certain limitations to the application range, they are necessary to simplify the modelling approach to a reasonable scope.

First, the solid constituent φ^S is assumed to be materially incompressible, implying a constant effective density ρ^{SR} of the solid skeleton. Note that the partial density ρ^S can still change due to variations of the volume fraction n^S, cf. (3.8). This commonly used assumption holds, since the volumetric bulk deformation of the porous solid material itself is, in general, much smaller than the pore-space dilatation or compression. Furthermore, the individual effective densities ρ^{BR}, ρ^{LR} and ρ^{DR} of the other constituents are also assumed to be constant under moderate pressures. This yields

$$\{\rho^{SR},\, \rho^{BR},\, \rho^{LR},\, \rho^{DR}\} \,=\, \text{const.}\,. \tag{4.1}$$

Regarding the overall interstitial fluid mixture φ^I, which is composed of materially incompressible components φ^L and φ^D, it is obvious that the effective density ρ^{IR} could change through varying concentrations c_m^L and c_m^D, although the molar masses M_m^L and M_m^D always remain constant. However, the overall interstitial fluid solution is predominantly composed of the liquid solvent and, therefore, the concentration of the therapeutic solutes is much lower than the concentration of the liquid solution itself, cf. Acartürk [3], Ehlers [51]. This yields the assumptions

$$n^D \ll n^L \approx n^I \quad \text{and} \quad c_m^D \ll c_m^L \approx \text{const.}\,. \tag{4.2}$$

Following this idea further and using the relations (3.13) and (3.24), it is concluded that

$$\rho_I^L \approx \rho^{IR} \quad \text{and} \quad \overset{\prime}{\mathbf{x}}_L \approx \overset{\prime}{\mathbf{x}}_I \quad \rightarrow \quad \mathbf{w}_L \approx \mathbf{w}_I \quad \text{and} \quad \mathbf{d}_{LI} \approx \mathbf{0}\,. \tag{4.3}$$

Based on these considerations, also the overall interstitial fluid mixture is assumed to be materially incompressible, yielding

$$\rho^{IR} = \text{const.}\,. \tag{4.4}$$

The next fundamental setting recalls that the overall aggregate is always fully saturated and consists of immiscible and miscible constituents, viz.:

$$n^S + n^B + n^I = n^S + n^B + \sum_{\gamma} n^\gamma = 1\,. \tag{4.5}$$

In this regard, the saturation condition acts as a restriction for the evaluation process of the entropy inequality. Moreover, the exclusion of mass exchanges, such as phase transitions or chemical reactions, is postulated by vanishing mass production terms, viz.:

$$\hat{\rho}^\alpha \equiv 0\,. \tag{4.6}$$

This assumption holds in general for healthy tissue[1]. Furthermore, quasi-static conditions are assumed for the overall aggregate as well as for the particular constituents, i. e., the overall and the constituent's acceleration terms are neglected, viz.:

$$\ddot{\mathbf{x}} \equiv \mathbf{0} \qquad \text{and} \qquad \overset{\prime\prime}{\mathbf{x}}_\alpha \equiv \mathbf{0}\,. \tag{4.7}$$

In particular, this restricts the validity of the model to slow processes. However, this represents a reasonable assumption since acceleration terms intentially do not come into play for the overall aggregate. This is caused by the circumstance that the patient is typically at rest during a clinical intervention. Moreover, the delicate infusions under CED-treatment are applied extremely slow. Beside that, uniform and constant gravitational (body) forces $\mathbf{b}^\alpha = \mathbf{g}$ are assumed for all constituents in a similar manner. Moreover, non-polar constituents with vanishing moment-of-momentum productions, i. e., $\hat{\mathbf{m}}^\alpha \equiv \mathbf{0}$, are postulated. Therefore, the statement of the balance of momentum results in the symmetry of the stress tensors, cf. Section 3.5. Finally, a common constant temperature (approximately 37°C) is assumed for all constituents of the living brain tissue, yielding

$$\theta^\alpha \equiv \theta = \text{const.}\,. \tag{4.8}$$

In conclusion, this leads to an isothermal model without an explicit need to consider the energy balance within the governing set of equations.

[1] $\hat{\rho}^\alpha \neq 0$ would be of importance, if mass exchanges between the constituents need to be considered. For example, the exchange of matter between the extra- and the intra-vascular space would require a mass production term $\hat{\rho}^\beta$ in the mass balances (3.72) of the liquid constituents, obeying local pressure conditions, cf. Section 2.1.3. However, in this monograph, a drug uptake is not included, since it is seen as a more or less negligible effect for the overall distribution of the therapeutics. Note in passing that results from clinical applications of CED by Voges *et al.* [165] indicate that an uptake of therapeutic agents into the blood vessel system may occur in the immediate vicinity of a brain tumour.

4.2 Adaption of balance relations

The basic formulation of balance equations is subjected to the previously discussed preliminary assumptions. This leads to a model, which is governed by the adapted mass and momentum balances of the constituents φ^α based on (3.72) and (3.79), viz.:

$$\begin{aligned} 0 &= (\rho^\alpha)'_\alpha + \rho^\alpha \operatorname{div} \overset{\prime}{\mathbf{x}}_\alpha \,, \\ \mathbf{0} &= \operatorname{div} \mathbf{T}^\alpha + \rho^\alpha \mathbf{g} + \hat{\mathbf{p}}^\alpha \,. \end{aligned} \tag{4.9}$$

As was mentioned in Subsection 3.5, the statements of the balances of moment of momentum serve for the symmetry of the stress tensors $\mathbf{T}^\alpha$. Moreover, the explicit consideration of the energy balances (3.89) is excluded since isothermal conditions are assumed, cf. (4.8). However, an implicit inclusion of the energy balances by means of rearranging the entropy inequality is applied. In this context, the entropy inequality serves as the restricting frame in terms of a thermodynamically consistent development of the required constitutive equations.

It can easily be seen that the system of equations given in (4.9) exhibits more unknowns than equations. In particular, four scalar-valued mass balance equations $(4.9)_1$ as well as four vector-valued (or twelve scalar-valued) momentum balance equations $(4.9)_2$ are available for the considered four-constituent model. In terms of a standalone viewing, these are 16 scalar-valued equations. However, the set of equations basically implies 55 scalar-valued unknowns, i. e., for the quantities ρ^α $(1 \cdot 4)$, $\overset{\prime}{\mathbf{x}}_\alpha$ $(3 \cdot 4)$, $\mathbf{T}^\alpha$ $(6 \cdot 4)$, $\mathbf{g}$ $(3 \cdot 1)$ and $\hat{\mathbf{p}}^\alpha$ $(3 \cdot 4)$. Hence, the existing gap needs to be closed (i. e., the closure problem) in terms of constitutive settings of the developed brain-tissue model.

Initially, a distinct choice of balance equations from (4.9) states the governing equations, which are linked to the so-called primary variables of the model. In this regard, the governing balance relations as well as the restrictive frame of the entropy inequality are further adapted. Afterwards, the constitutive modelling process provides the completion of the model. Therefore, all further unknowns (secondary variables) have to be found by combining the remaining balance equations with appropriate constitutive assumptions. Since this represents a somehow extensive procedure, a concluding summary of the model's coupling, reflecting the closure problem, is given in Section 4.6.

With regard to the adaption of the chosen governing balance equations, the general transformations[2]

$$(\,\cdot\,)'_\beta = (\,\cdot\,)'_S + \operatorname{grad}(\,\cdot\,) \cdot \mathbf{w}_\beta \qquad \text{and} \qquad (\,\cdot\,)'_\gamma = (\,\cdot\,)'_I + \operatorname{grad}(\,\cdot\,) \cdot \mathbf{d}_{\gamma I} \tag{4.10}$$

of material time derivatives with respect to a particular motion of a constituent are of immense benefit. Therein, material time derivatives with respect to the solid motion can be related to time derivatives with respect to other constituents and vice versa. The placeholder $(\,\cdot\,)$ in (4.10) is used for arbitrary scalar quantities.

[2]These reformulations are obtained by subtracting $(3.20)_1$ for the considered constituent from the linked constituent and using the relations (3.27) and (3.28).

4.2.1 Concentration balances of the interstitial fluid components

According to $(4.9)_1$, the local mass balances of the interstitial fluid components φ^γ is obtained via

$$(\rho^\gamma)'_\gamma \,+\, \rho^\gamma \operatorname{div} \overset{\prime}{\mathbf{x}}_\gamma \,=\, 0\,. \tag{4.11}$$

Considering the fact that the overall interstitial fluid represents a real mixture of its components, the specific density relations (3.13) of solutions are included, viz.:

$$n^I (\rho_I^\gamma)'_\gamma \,+\, (n^I)'_\gamma \, \rho_I^\gamma \,+\, n^I \rho_I^\gamma \operatorname{div} \overset{\prime}{\mathbf{x}}_\gamma \,=\, 0\,. \tag{4.12}$$

Expressing the partial pore densities ρ_I^γ of the mixture components in terms of the molar concentrations $(3.13)_2$, using the relations (4.10) and dividing by the constant molar masses leads to

$$(n^I c_m^\gamma)'_S \,+\, \operatorname{div} (n^I c_m^\gamma \, \mathbf{w}_\gamma) \,+\, n^I c_m^\gamma \operatorname{div} (\mathbf{u}_S)'_S \,=\, 0\,. \tag{4.13}$$

Therein, the leftmost term can be transformed further with the help of the time derivative of the saturation condition (3.5). In a combination with the assumption of materially incompressible constituents, cf. (4.1), this yields

$$(n^I)'_S \,=\, (n^S \,+\, n^B) \operatorname{div} (\mathbf{u}_S)'_S \,+\, \operatorname{div} (n^B \, \mathbf{w}_B)\,. \tag{4.14}$$

Finally, the concentration balances of the components φ^γ are obtained, viz.:

$$n^I (c_m^\gamma)'_S \,+\, c_m^\gamma \operatorname{div} (\mathbf{u}_S)'_S \,+\, \operatorname{div} (n^I c_m^\gamma \, \mathbf{w}_\gamma) \,+\, c_m^\gamma \operatorname{div} (n^B \, \mathbf{w}_B) \,=\, 0\,. \tag{4.15}$$

4.2.2 Volume balance of the overall interstitial fluid

Proceeding from the idea that the overall interstitial fluid is composed of its miscible components φ^γ, the mass balance of the overall interstitial fluid φ^I is derived by the summation over the partial mass balances (4.11) of its components φ^γ using the relations (3.12) and (3.24), yielding

$$\begin{aligned} \sum_\gamma [\, (\rho^\gamma)'_\gamma \,+\, \rho^\gamma \operatorname{div} \overset{\prime}{\mathbf{x}}_\gamma \,] \,&=\, \sum_\gamma [\, (\rho^\gamma)'_I \,-\, \operatorname{grad} \rho^\gamma \cdot \overset{\prime}{\mathbf{x}}_I \,+\, \operatorname{div} (\rho^\gamma \overset{\prime}{\mathbf{x}}_\gamma) \,] \,=\, 0 \\ \rightarrow \;\; (\rho^I)'_I \,+\, \rho^I \operatorname{div} \overset{\prime}{\mathbf{x}}_I \,&=\, 0\,. \end{aligned} \tag{4.16}$$

For the development of the volume balance of the overall interstitial fluid, the effective density ρ^{IR} is given according to (3.14), viz.:

$$\rho^{IR} \,=\, c_m^L \, M_m^L \,+\, c_m^D \, M_m^D\,. \tag{4.17}$$

As mentioned before in the preliminary assumptions (4.2), (4.3) and (4.4), the effective density ρ^{IR} is found to be constant for $c_m^D \ll c_m^L$. This yields

$$(n^I)'_I \,+\, n^I \operatorname{div} \overset{\prime}{\mathbf{x}}_I \,=\, 0 \quad \rightarrow \quad (n^I)'_S \,+\, \operatorname{div} (n^I \mathbf{w}_I) \,+\, n^I \operatorname{div} (\mathbf{u}_S)'_S \,=\, 0\,. \tag{4.18}$$

Therein, the material time derivative with respect to the overall interstitial fluid is formulated regarding the solid motion using $(4.10)_1$.

4.2.3 Volume balance of the blood plasma

According to the previous evaluation of the volume balance of the interstitial fluid (4.18), the local mass balance of the materially incompressible blood plasma φ^B simplifies to its volume balance, viz.:

$$(n^B)'_S + \operatorname{div}(n^B \mathbf{w}_B) + n^B \operatorname{div}(\mathbf{u}_S)'_S = 0\,. \tag{4.19}$$

Again, the material time derivative of the blood's volume fraction is formulated with respect to the solid motion using $(4.10)_1$.

4.2.4 Volume balance of the solid skeleton

Based on a materially incompressible solid skeleton, also the solid mass balance can be transferred to its volume balance, viz.:

$$(n^S)'_S + n^S \operatorname{div} \overset{\prime}{\mathbf{x}}_S = 0\,. \tag{4.20}$$

In general, the volume balance (4.20) is dedicated to compute the evolution of the volume fraction n^S. Therefore, the divergence term is reformulated using (A.4), (3.46) and (3.51), yielding

$$(\det \mathbf{F}_S)'_S = \operatorname{cof} \mathbf{F}_S \cdot (\mathbf{F}_S)'_S = \det \mathbf{F}_S\, \mathbf{F}_S^{T-1} \cdot \mathbf{L}_S\, \mathbf{F}_S = (\det \mathbf{F}_S) \operatorname{div} \overset{\prime}{\mathbf{x}}_S\,. \tag{4.21}$$

Based on this, the volume balance (4.20) is integrated via

$$\frac{(n^S)'_S}{n^S} = -\operatorname{div} \overset{\prime}{\mathbf{x}}_S = -\frac{(\det \mathbf{F}_S)'_S}{\det \mathbf{F}_S} \quad \rightarrow \quad \int_{t_0}^{t} \frac{(n^S)'_S}{n^S}\, \mathrm{d}\tilde{t} = -\int_{t_0}^{t} \frac{(\det \mathbf{F}_S)'_S}{\det \mathbf{F}_S}\, \mathrm{d}\tilde{t}\,, \tag{4.22}$$

and results in

$$\ln|n^S| - \ln|n^S_{0S}| = -\ln|\det \mathbf{F}_S| + \ln|\det \mathbf{I}| \quad \rightarrow \quad n^S = n^S_{0S} (\det \mathbf{F}_S)^{-1}\,. \tag{4.23}$$

Therein, n^S_{0S} is the solid's volume fraction in the solid's reference configuration.

4.2.5 Momentum balance of the overall aggregate

The quasi-static formulation of the momentum balance of the overall aggregate is derived by the summation of all particular momentum balances $(4.9)_2$ of the constituents φ^α yielding the overall momentum balance of φ, viz.:

$$\mathbf{0} = \operatorname{div} \mathbf{T} + \rho\, \mathbf{g}\,, \quad \text{where} \left\{ \begin{array}{rcl} \mathbf{T} & = & \mathbf{T}^S + \mathbf{T}^B + \mathbf{T}^I\,, \\ \rho & = & n^S \rho^{SR} + n^B \rho^{BR} + n^I \rho^{IR}\,. \end{array} \right. \tag{4.24}$$

Therein, the overall Cauchy stress tensor $\mathbf{T}$ and the density ρ of the overall aggregate are included. Furthermore, a uniform and constant gravitational force $\mathbf{g}$ is assumed and the

summation over all direct momentum production terms $\hat{\mathbf{p}}^\alpha$ is equal to zero for vanishing mass production terms ($\hat{\rho}^\alpha = 0$), cf. (3.80).

Remark: Note that the summation of the stress tensors towards $\mathbf{T}$ given in (4.24) differs from the relation given in $(3.80)_2$. Using $\mathbf{T}$ from (4.24) within the divergence operator is only valid if quasi-static conditions (4.7) and vanishing mass production terms (4.6) are assumed and thus

$$\begin{aligned} \rho\,\ddot{\mathbf{x}} &= \sum_\alpha \left[\, \rho^\alpha\, \overset{''}{\mathbf{x}}_\alpha \,-\, \operatorname{div}\left(\rho^\alpha\, \mathbf{d}_\alpha \otimes \mathbf{d}_\alpha\right) \,+\, \hat{\rho}^\alpha\, \overset{'}{\mathbf{x}}_\alpha \,\right] \\ &\rightarrow\; \operatorname{div}\Big(\sum_\alpha \rho^\alpha\, \mathbf{d}_\alpha \otimes \mathbf{d}_\alpha\Big) \,=\, 0\,. \end{aligned} \tag{4.25}$$

Therein, the relation $(4.25)_1$ is given according to de Boer & Ehlers [23], using the dependencies (3.23) and $(3.80)_1$, the transformation of time derivatives (3.21) as well as the mass balances of the overall aggregate (3.71) and the constituents (3.72).

4.2.6 Adaption of the entropy inequality

The constitutive equations for the set of involved constituents φ^α are derived based on the Clausius-Planck inequality (3.100). In particular, proceeding from its respective basic formulation in terms of the quaternary model, this inequality yields

$$\begin{aligned} &\mathbf{T}^S \cdot \mathbf{L}_S \,-\, \rho^S\,(\psi^S)'_S \,+\, \mathbf{T}^B \cdot \mathbf{L}_B \,-\, \rho^B\,(\psi^B)'_B \,-\, \hat{\mathbf{p}}^B \cdot \mathbf{w}_B \,+ \\ &+ \sum_\gamma \left[\, \mathbf{T}^\gamma \cdot \mathbf{L}_\gamma \,-\, \rho^\gamma\,(\psi^\gamma)'_\gamma \,-\, \hat{\mathbf{p}}^\gamma \cdot \mathbf{w}_\gamma \right] \,\geq\, 0\,. \end{aligned} \tag{4.26}$$

Therein, it is considered that the overall interstitial fluid $\varphi^I = \sum_\gamma \varphi^\gamma$ is a chemical solution composed by its miscible components φ^γ. Therefore, the mass-specific Helmholtz free energy ψ^γ of the components is formulated with respect to the overall interstitial fluid volume, cf. Ehlers [51]. Applying the relations of miscible components (3.13) yields

$$\rho^\gamma\,\psi^\gamma \,=\, n^I \rho^\gamma_I\,\psi^\gamma \,=:\, n^I\,\Psi^\gamma_I \qquad \rightarrow \quad \Psi^\gamma_I \,=\, \rho^\gamma_I\,\psi^\gamma\,. \tag{4.27}$$

Hence, the volume-specific Helmholtz free energy Ψ^γ_I of a component is related to the overall interstitial fluid. Furthermore, the summation of the component's Helmholtz free energies leads to the Helmholtz free energy of the overall interstitial fluid via

$$\Psi^I_I \,=\, \sum_\gamma \Psi^\gamma_I \,=\, \sum_\gamma \rho^\gamma_I\,\psi^\gamma\,. \tag{4.28}$$

Based on these considerations, the general formulation (4.26) is adjusted. In this regard, the temporal changes of the component's Helmholtz free energies are derived proceeding from the chain rule and using the relations (3.13), (4.10) and (4.12). This yields

$$\begin{aligned} \rho^\gamma\,(\psi^\gamma)'_\gamma \;&=\; n^I(\Psi^\gamma_I)'_\gamma \,-\, n^I\psi^\gamma(\rho^\gamma_I)'_\gamma \\ &=\; n^I\left[(\Psi^\gamma_I)'_I \,+\, \operatorname{grad}\Psi^\gamma_I \cdot \mathbf{d}_{\gamma I}\right] \,+\, \psi^\gamma\left[(n^I)'_\gamma\,\rho^\gamma_I \,+\, n^I\rho^\gamma_I\,\operatorname{div}\overset{'}{\mathbf{x}}_\gamma\right]. \end{aligned} \tag{4.29}$$

Therein, the time derivative of n^I with respect to a component φ^γ is computed using (4.5), (4.10) and the partial volume balances[3] (4.19) and (4.20), resulting in

$$\begin{aligned}(n^I)'_\gamma &= (n^I)'_I + \operatorname{grad} n^I \cdot \mathbf{d}_{\gamma I} = (n^I)'_S + \operatorname{grad} n^I \cdot \mathbf{w}_I + \operatorname{grad} n^I \cdot \mathbf{d}_{\gamma I} \\ &= n^S \operatorname{div} \overset{\prime}{\mathbf{x}}_S + n^B \operatorname{div} \overset{\prime}{\mathbf{x}}_B + \operatorname{grad} n^B \cdot \mathbf{w}_B + \operatorname{grad} n^I \cdot \mathbf{w}_\gamma \,.\end{aligned} \tag{4.30}$$

Hence, the time derivatives of the free Helmholtz energies of the components, required in (4.26), are obtained by the combination of (4.29) and (4.30) via

$$\begin{aligned}\rho^\gamma (\psi^\gamma)'_\gamma &= n^I (\Psi^\gamma_I)'_I + n^S \Psi^\gamma_I \mathbf{I} \cdot \mathbf{L}_S + n^B \Psi^\gamma_I \mathbf{I} \cdot \mathbf{L}_B + n^I \Psi^\gamma_I \mathbf{I} \cdot \mathbf{L}_\gamma + \\ &\quad + \Psi^\gamma_I \operatorname{grad} n^B \cdot \mathbf{w}_B + \Psi^\gamma_I \operatorname{grad} n^I \cdot \mathbf{w}_\gamma + \operatorname{grad} \Psi^\gamma_I \cdot (n^I \mathbf{d}_{\gamma I}) \,.\end{aligned} \tag{4.31}$$

Finally, the insertion of (4.31) into (4.26) yields an alternative formulation[4] of the general entropy inequality of the quaternary modelling approach, viz.:

$$\begin{aligned}&(\mathbf{T}^S - n^S \Psi^I_I \mathbf{I}) \cdot \mathbf{L}_S - \rho^S (\psi^S)'_S + (\mathbf{T}^B - n^B \Psi^I_I \mathbf{I}) \cdot \mathbf{L}_B - \rho^B (\psi^B)'_B - \\ &- (\hat{\mathbf{p}}^B + \Psi^I_I \operatorname{grad} n^B) \cdot \mathbf{w}_B + \sum_\gamma \Big[(\mathbf{T}^\gamma - n^I \Psi^\gamma_I \mathbf{I}) \cdot \mathbf{L}_\gamma - n^I (\Psi^I_I)'_I - \\ &- \operatorname{grad} \Psi^\gamma_I \cdot (n^I \mathbf{d}_{\gamma I}) - (\hat{\mathbf{p}}^\gamma + \Psi^\gamma_I \operatorname{grad} n^I) \cdot \mathbf{w}_\gamma \Big] \geq 0 \,.\end{aligned} \tag{4.32}$$

Constraining saturation condition: Moreover, the saturation condition (4.5) represents a mechanical constraint for the considered overall aggregate. In order to act as a restriction on the thermodynamical process, an incorporation into the entropy inequality is carried out. In this regard, the material time derivative $(\,\cdot\,)'_S$ is transformed with respect to the particular motion of the constituents, once the corresponding volume balances of the constituents are inserted, yielding

$$\begin{aligned}-(n^S + n^B + \sum_\gamma n^\gamma)'_S &= n^S \operatorname{div} \overset{\prime}{\mathbf{x}}_S + n^B \operatorname{div} \overset{\prime}{\mathbf{x}}_B + \operatorname{grad} n^B \cdot \mathbf{w}_B + \\ &\quad + \sum_\gamma (n^\gamma \operatorname{div} \overset{\prime}{\mathbf{x}}_\gamma + \operatorname{grad} n^\gamma \cdot \mathbf{w}_\gamma) = 0 \,.\end{aligned} \tag{4.33}$$

Since this expression equals to zero, a multiplication with a so-called Lagrangean multiplier[5] $\mathcal{P}$, cf. Liu [101], is feasible via

$$\begin{aligned}0 &= \mathcal{P} \Big[n^S \operatorname{div} \overset{\prime}{\mathbf{x}}_S + n^B \operatorname{div} \overset{\prime}{\mathbf{x}}_B + \operatorname{grad} n^B \cdot \mathbf{w}_B + \\ &\quad + \sum_\gamma (n^\gamma \operatorname{div} \overset{\prime}{\mathbf{x}}_\gamma + \operatorname{grad} n^\gamma \cdot \mathbf{w}_\gamma) \Big] \,.\end{aligned} \tag{4.34}$$

[3] In particular, the time derivative of the saturation condition (4.5) with respect to the solid motion by means of $(n^I)'_S = -(n^S)'_S - (n^B)'_S$ is used.

[4] Therein, the relation $\sum_\gamma n^I (\Psi^\gamma_I)'_I = n^I (\Psi^I_I)'_I = \sum_\gamma n^I (\Psi^I_I)'_I$ is used, cf. (4.28).

[5] The method of Lagrange multipliers provides the possibility of including constraints into a mathematical optimisation problem, which is represented here by the evaluation process of the entropy inequality.

After attaching this field equation to the entropy inequality (4.32), the following formulation is obtained, viz:

$$
\begin{aligned}
&(\underbrace{\mathbf{T}^S + n^S \mathcal{P}\mathbf{I}}_{\mathbf{T}^S_E} - n^S \Psi^I_I \mathbf{I}) \cdot \mathbf{L}_S - \rho^S (\psi^S)'_S + (\underbrace{\mathbf{T}^B + n^B \mathcal{P}\mathbf{I}}_{\mathbf{T}^B_E} - n^B \Psi^I_I \mathbf{I}) \cdot \mathbf{L}_B - \\
&- \rho^B (\psi^B)'_B - (\underbrace{\hat{\mathbf{p}}^B - \mathcal{P} \operatorname{grad} n^B}_{\hat{\mathbf{p}}^B_E} + \Psi^I_I \operatorname{grad} n^B) \cdot \mathbf{w}_B + \\
&+ \sum_\gamma \Big[(\underbrace{\mathbf{T}^\gamma + n^\gamma \mathcal{P}\mathbf{I}}_{\mathbf{T}^\gamma_E} - n^I \Psi^\gamma_I \mathbf{I}) \cdot \mathbf{L}_\gamma - n^I (\Psi^I_I)'_I - \operatorname{grad} \Psi^\gamma_I \cdot (n^I \mathbf{d}_{\gamma I}) - \\
&- (\underbrace{\hat{\mathbf{p}}^\gamma - \mathcal{P} \operatorname{grad} n^\gamma}_{\hat{\mathbf{p}}^\gamma_E} + \Psi^\gamma_I \operatorname{grad} n^I) \cdot \mathbf{w}_\gamma \Big] \geq 0 .
\end{aligned}
\tag{4.35}
$$

In the above representation of the entropy inequality (4.35), the so-called extra quantities are introduced, cf. Truesdell & Noll [159].

Extra quantities: Following the definition of extra quantities in (4.35), the partial stresses $\mathbf{T}^S$, $\mathbf{T}^B$ and $\mathbf{T}^\gamma$ as well as the direct momentum production terms $\hat{\mathbf{p}}^B$ and $\hat{\mathbf{p}}^\gamma$ are split into an undetermined part resulting from $\mathcal{P}$ and an extra (or effective) term indicated by the subscript E. The determination of the extra quantities is derived afterwards via appropriate constitutive equations. In summary, the introduced extra quantities are defined, viz.:

$$
\begin{aligned}
&\mathbf{T}^S_E := \mathbf{T}^S + n^S \mathcal{P}\mathbf{I}, \qquad \mathbf{T}^B_E := \mathbf{T}^B + n^B \mathcal{P}\mathbf{I}, \qquad \mathbf{T}^\gamma_E := \mathbf{T}^\gamma + n^\gamma \mathcal{P}\mathbf{I}, \\
&\hat{\mathbf{p}}^B_E := \hat{\mathbf{p}}^B - \mathcal{P} \operatorname{grad} n^B, \quad \hat{\mathbf{p}}^\gamma_E := \hat{\mathbf{p}}^\gamma - \mathcal{P} \operatorname{grad} n^\gamma .
\end{aligned}
\tag{4.36}
$$

Using these abbreviations yields the fundamental formulation of the entropy inequality for the considered quaternary model extended by the saturation constraint:

$$
\begin{aligned}
&(\mathbf{T}^S_E - n^S \Psi^I_I \mathbf{I}) \cdot \mathbf{L}_S - \rho^S (\psi^S)'_S + (\mathbf{T}^B_E - n^B \Psi^I_I \mathbf{I}) \cdot \mathbf{L}_B - \rho^B (\psi^B)'_B - \\
&- (\hat{\mathbf{p}}^B_E + \Psi^I_I \operatorname{grad} n^B) \cdot \mathbf{w}_B + \sum_\gamma \Big[(\mathbf{T}^\gamma_E - n^I \Psi^\gamma_I \mathbf{I}) \cdot \mathbf{L}_\gamma - n^I (\Psi^I_I)'_I - \\
&- \operatorname{grad} \Psi^\gamma_I \cdot (n^I \mathbf{d}_{\gamma I}) - (\hat{\mathbf{p}}^\gamma_E + \Psi^\gamma_I \operatorname{grad} n^I) \cdot \mathbf{w}_\gamma \Big] \geq 0 .
\end{aligned}
\tag{4.37}
$$

Proceeding from this formulation, the thermodynamical fundamentals are investigated in order to identify the relations for the involved quantities by means of a Coleman-Noll evaluation procedure.

4.3 Thermodynamical fundamentals of the constitutive modelling procedure

As was mentioned in Section 4.2, the adapted set of governing balance relations needs to be closed by constitutive equations describing the physical behaviour of the constituents as well as their mutual interactions. Within the constitutive modelling procedure, the basic thermodynamical principles must be taken into account by means of obtaining a thermodynamically consistent model. Therefore, the development of constitutive equations for multiphasic materials trace back to the same basic principles as applied in classical continuum mechanics of singlephasic materials, cf., e. g., Truesdell [158], Truesdell & Noll [159] and Truesdell & Toupin [160]. In particular, these are the principles of determinism, equipresence, local action, material frame indifference and dissipation, which are discussed in this section in order to develop the constitutive equations of the considered brain-tissue model. In general, the introduction of constitutive equations based on these principles is reasonable to avoid somehow arbitrary statements of the physical behaviour of the constituents.

4.3.1 Application of basic thermodynamical principles

Principle of determinism: Following the principle of determinism for the discussion of the basic entropy inequality (4.37), the set of undetermined response functions $\mathcal{R}$, which cannot determined from the balance equations with the knowledge of the full state of motion is found via

$$\mathcal{R} = \{\psi^S,\, \psi^B,\, \Psi_I^\gamma\,,\, \mathbf{T}_E^S\,,\, \mathbf{T}_E^B\,,\, \mathbf{T}_E^\gamma\,,\, \hat{\mathbf{p}}_E^B\,,\, \hat{\mathbf{p}}_E^\gamma\,\}\,. \tag{4.38}$$

Principle of equipresence: The principle of equipresence states that the response functions $\mathcal{R}(\mathcal{V})$ may depend on the whole set of constitutive (or process) variables $\mathcal{V}$ specifying the current and the initial state of the overall aggregate concerning the deformation, the structural composition, the chemical state and temperature. For a general multicomponental material, this set is basically given according to Ehlers [44], viz.:

$$\begin{aligned} \mathcal{V} \;=\; \{\, &\theta^\alpha,\, \operatorname{grad}\theta^\alpha,\, n^\alpha,\, \operatorname{grad} n^\alpha,\, \rho^{\alpha R},\, \operatorname{grad}\rho^{\alpha R},\\ &\mathbf{F}_\alpha,\, \operatorname{grad}\mathbf{F}_\alpha,\, \overset{\prime}{\mathbf{x}}_\alpha,\, \operatorname{grad}\overset{\prime}{\mathbf{x}}_\alpha,\, \boldsymbol{\mathcal{M}}^S,\, \mathbf{X}_S\}\,. \end{aligned} \tag{4.39}$$

Therein, the extension of the set by the structural tensor $\boldsymbol{\mathcal{M}}^S$, characterising the inherent anisotropic solid skeleton (caused by the nervous fibres) is investigated according to Karajan [87]. Proceeding from the general set $\mathcal{V}$, a reduced subset $\mathcal{s}$ of independent process variables is obtained by evaluating the preliminary assumptions, cf. Section 4.1. A detailed argumentation of the derived considerations for multicomponental materials is given in Ehlers [44, 50]. Furthermore, Karajan [87] discusses the specific consideration of an anisotropic solid skeleton. Moreover, the work of Acartürk [3] accounts, in particular, for the treatment of included miscible components. For the purposes of this monograph, the set of process variables is therefore described by

$$\mathcal{s} = \{\, \mathbf{F}_S,\, \boldsymbol{\mathcal{M}}^S,\, \mathbf{X}_S,\, n^\beta,\, \mathbf{w}_\beta,\, \mathbf{D}_\beta,\, c_m^\gamma\}\,. \tag{4.40}$$

Therein, isothermal conditions for an inhomogeneous aggregate with materially incompressible constituents and vanishing mass productions are assumed. Furthermore, the velocities $\overset{\prime}{\mathbf{x}}_\alpha$ are replaced by a description via the objective seepage velocities $\mathbf{w}_\beta$. Moreover, the symmetric parts of the velocity gradients $\mathbf{D}_\beta$ of the fluid components are used instead of the gradients of the fluid velocities in order to satisfy the principle of material frame indifference as described afterwards in the paragraph "material frame indifference".

Principle of local action: The principle of local action states, that the process variables consist only of local[6] values, i. e., the results of the response functions at time t are given at each material point $\mathbf{x}$ of the actual configuration by the values of the local process variables $\mathcal{s}(\mathbf{x}, t)$. Ehlers [44] proposed the principle of a constitutive (phase) separation of the constituents to describe practically oriented applications. In particular, this causes the constitutive statement that the Helmholtz free energies only depend on the non-dissipative process variables of the respective constituent itself. Therefore, the particular dependencies of the Helmholtz free energies of the constituents are stated, viz.:

$$\psi^S = \psi^S(\mathbf{F}_S,\, \boldsymbol{\mathcal{M}}^S,\, \mathbf{X}_S)\,, \quad \psi^B = \psi^B(s^B)\,, \quad \Psi_I^\gamma = \Psi_I^\gamma(c_m^\gamma)\,. \tag{4.41}$$

Material frame indifference: The principle of material frame indifference (material objectivity) accounts for the circumstance that a physical phenomenon[7] should not depend on the position of observation. In particular, this is mathematically achieved via invariant responses under rigid body rotations of the actual configuration, cf. Ehlers [44], Noll [119, 120]. Therefore, it is claimed that

$$\overset{*}{\mathcal{R}}(\mathcal{s}) \overset{!}{=} \mathcal{R}(\overset{*}{\mathcal{s}})\,. \tag{4.42}$$

Therein, the notation $(\overset{*}{\cdot})$ indicates quantities of the rotated actual configuration. The criteria (4.42) claim that it should be without consequences, if the response functions are applied by a rigid body rotation, to obtain $\overset{*}{\mathcal{R}}(\mathcal{s})$, or the actual configuration is initially rotated (variables $\mathcal{s}$ change to rotated variables $\overset{*}{\mathcal{s}}$) and the response functions $\mathcal{R}(\overset{*}{\mathcal{s}})$ are evaluated in the rotated actual configuration, afterwards. In general, all scalar-valued quantities, either in the referential or in the actual configuration, are material frame indifferent. Moreover, vector- and tensor-valued quantities which are completely related to the referential configuration are obviously not effected by a rotation of the actual configuration. Whereas, objects with a distinct orientation attached to the actual configuration need to be evaluated further. The investigations of material frame indifference proceed from the placement $\overset{*}{\mathbf{x}}$ of a material point in the rotated actual configuration, described by

$$\overset{*}{\mathbf{x}} = \mathbf{Q}\,\mathbf{x}\,, \quad \text{where} \quad \mathbf{Q} \in \mathcal{O}_e \quad \text{with} \quad \mathbf{Q}^T = \mathbf{Q}^{-1} \quad \text{and} \quad \det\mathbf{Q} = 1\,. \tag{4.43}$$

Therein, the arbitrary rigid body rotation $\mathbf{Q}$ is in the group $\mathcal{O}_e$ of proper orthogonal rotations. Proceeding from this idea, the rotated solid deformation gradient (in its property

[6] Non-local materials are not addressed in this monograph. In general, non-local effects caused by mutual interaction of the individual constituents are detected within the concept of second-grade materials.

[7] In this regard, the physical phenomena are described by the result obtained from any response function in the set (4.38).

of a two-field tensor) is obtained via

$$\overset{*}{\mathbf{F}}_S = \frac{\partial \overset{*}{\mathbf{x}}}{\partial \mathbf{X}_S} = \frac{\partial \overset{*}{\mathbf{x}}}{\partial \mathbf{x}} \frac{\partial \mathbf{x}}{\partial \mathbf{X}_S} = \mathbf{Q}\,\mathbf{F}_S\,, \quad \text{with} \quad \mathbf{Q} = \frac{\partial \overset{*}{\mathbf{x}}}{\partial \mathbf{x}}\,. \tag{4.44}$$

This already suggests that the solid's deformation gradient is not a suitable quantity by means of satisfying the restriction (4.42). In particular, this becomes evident by applying the principle of material frame indifference (4.42) to the scalar-valued (objective) Helmholtz energy of the solid skeleton, resulting the disagreement

$$\begin{aligned} \overset{*}{\psi}{}^S(\mathbf{F}_S\,, \boldsymbol{\mathcal{M}}^S, \mathbf{X}_S) &= \psi^S(\mathbf{F}_S\,, \boldsymbol{\mathcal{M}}^S, \mathbf{X}_S) \\ &\neq \psi^S(\overset{*}{\mathbf{F}}_S\,, \overset{*}{\boldsymbol{\mathcal{M}}}{}^S, \overset{*}{\mathbf{X}}_S) = \psi^S(\mathbf{Q}\,\mathbf{F}_S\,, \boldsymbol{\mathcal{M}}^S, \mathbf{X}_S)\,. \end{aligned} \tag{4.45}$$

Therein, the structural tensor $\boldsymbol{\mathcal{M}}^S$ and the initial placement $\mathbf{X}_S$ are referential quantities and, hence, invariant under rotations of the actual configuration. In order to overcome the conflict posed by the solid's deformation gradient in (4.45), a specific choice, namely $\mathbf{Q} = \mathbf{R}_S^T$, is made. In a combination with the polar decomposition theorem (3.36) of the solid's deformation gradient this results in

$$\overset{*}{\mathbf{F}}_S = \mathbf{Q}\,\mathbf{F}_S = \mathbf{R}_S^T\,(\mathbf{R}_S\,\mathbf{U}_S) = \mathbf{U}_S = \mathbf{C}_S^{\frac{1}{2}}\,. \tag{4.46}$$

It can easily be seen that the solid's Helmholtz free energy ψ^S should depend rather upon the referential stretch $\mathbf{U}_S$ of the solid's deformation gradient and, hence, on its corresponding deformation measure $\mathbf{C}_S$, yielding

$$\psi^S(\mathbf{F}_S\,, \boldsymbol{\mathcal{M}}^S, \mathbf{X}_S) \overset{!}{=} \psi^S(\mathbf{C}_S\,, \boldsymbol{\mathcal{M}}^S, \mathbf{X}_S)\,. \tag{4.47}$$

Thus, ψ^S needs to depend on $\mathbf{F}_S$ in such a manner that this dependence can be also expressed via $\mathbf{C}_S$. It is obviously found from $(3.35)_1$ and (4.44) that $\mathbf{C}_S$, being a referential measure, is independent from any rotation of the actual configuration, viz.:

$$\overset{*}{\mathbf{C}}_S = \overset{*}{\mathbf{F}}_S^T\,\overset{*}{\mathbf{F}}_S = (\mathbf{Q}\,\mathbf{F}_S)^T\,(\mathbf{Q}\,\mathbf{F}_S) = \mathbf{F}_S^T\,\mathbf{Q}^T\,\mathbf{Q}\,\mathbf{F}_S = \mathbf{F}_S^T\,\mathbf{F}_S = \mathbf{C}_S\,. \tag{4.48}$$

In terms of further relevant response functions included in the set (4.40), the non-scalar seepage velocity $\mathbf{w}_\beta$ fulfils the invariance condition. According to Karajan [87], its material frame indifference is shown via

$$\begin{aligned} &\overset{*}{\mathbf{w}}_\beta = \mathbf{Q}\,\mathbf{w}_\beta = \mathbf{Q}\,[\,(\overset{*}{\mathbf{x}})'_S - (\overset{*}{\mathbf{x}})'_\beta\,] = \mathbf{Q}\,(\overset{\prime}{\mathbf{x}}_S - \overset{\prime}{\mathbf{x}}_\beta) = \mathbf{Q}\,\mathbf{w}_\beta\,, \\ &\text{with} \begin{cases} (\overset{*}{\mathbf{x}})'_S = (\mathbf{Q}\,\mathbf{x})'_S = \dot{\mathbf{Q}}\,\mathbf{x} + \mathbf{Q}\,\overset{\prime}{\mathbf{x}}_S\,, \\ (\overset{*}{\mathbf{x}})'_\beta = (\mathbf{Q}\,\mathbf{x})'_\beta = \dot{\mathbf{Q}}\,\mathbf{x} + \mathbf{Q}\,\overset{\prime}{\mathbf{x}}_\beta\,. \end{cases} \end{aligned} \tag{4.49}$$

Note in passing that the material time derivatives $\dot{\mathbf{Q}}$ and $(\mathbf{Q})'_\alpha$ are identical, since the rigid body rotation is independent of the constituent it is applied to. Moreover, it is found

for the symmetric deformation velocity that

$$\overset{*}{\mathbf{D}}_\beta = \mathbf{Q}\,\mathbf{D}_\beta\,\mathbf{Q}^T = \tfrac{1}{2}\,(\overset{*}{\mathbf{L}}_\beta + \overset{*}{\mathbf{L}}{}^T_\beta) = \tfrac{1}{2}\,(\mathbf{Q}\,\mathbf{L}_\beta\,\mathbf{Q}^T + \mathbf{Q}\,\mathbf{L}^T_\beta\,\mathbf{Q}^T) = \mathbf{Q}\,\mathbf{D}_\beta\,\mathbf{Q}^T\,,$$

$$\text{with} \left\{ \begin{array}{l} \overset{*}{\mathbf{L}}_\beta = (\overset{*}{\mathbf{F}}_\beta)'_\beta\,\overset{*}{\mathbf{F}}{}^{-1}_\beta = (\mathbf{Q}\,\mathbf{F}_\beta)'_\beta\,(\mathbf{Q}\,\mathbf{F}_\beta)^{-1} = \dot{\mathbf{Q}}\,\mathbf{Q}^T + \mathbf{Q}\,\mathbf{L}_\beta\,\mathbf{Q}^T, \\ \overset{*}{\mathbf{L}}{}^T_\beta = \overset{*}{\mathbf{F}}{}^{T-1}_\beta\,(\overset{*}{\mathbf{F}}{}^T_\beta)'_\beta = (\mathbf{Q}^{T-1}\,\mathbf{F}^{T-1}_\beta)\,(\mathbf{F}^T_\beta\,\mathbf{Q}^T)'_\beta = \mathbf{Q}\,\dot{\mathbf{Q}}^T + \mathbf{Q}\,\mathbf{L}^T_\beta\,\mathbf{Q}^T. \end{array} \right. \tag{4.50}$$

Therein, the relations (4.44) and (3.47) are used in order to proof the material frame indifference of the symmetric part of the velocity gradients $\mathbf{D}_\beta$ of the fluid constituents.

4.3.2 Evaluation of the entropy inequality (dissipation)

As mentioned before, the satisfaction of the previously discussed basic thermodynamical principles is crucial for a thermodynamically consistent model. Furthermore, every admissible thermodynamical process has to fulfil the entropy inequality of the overall aggregate in order to satisfy the principle of dissipation. In this regard, an approved constitutive modelling process is provided by the evaluation of the entropy inequality (4.35), following the procedure of Coleman & Noll [36]. Hence, the postulated constitutive assumptions[8] for the Helmholtz free energies

$$\psi^S = \psi^S(\mathbf{C}_S,\, \boldsymbol{\mathcal{M}}^S,\, \mathbf{X}_S)\,, \quad \psi^B = \psi^B(s^B) \qquad \text{and} \qquad \Psi^\gamma_I = \Psi^\gamma_I(c^\gamma_m) \tag{4.51}$$

enable the evaluation of the entropy inequality, where each part has to be greater (dissipation or non-equilibrium part) or equal (equilibrium part) to zero.

To begin with, the required terms of the entropy inequality (4.37) are evaluated. Applying the material time derivative to the solid's Helmholtz free energy $(4.51)_1$ yields

$$\rho^S(\psi^S)'_S = \rho^S\,\frac{\partial \psi^S}{\partial \mathbf{C}_S} \cdot (\mathbf{C}_S)'_S = 2\,\rho^S\,\mathbf{F}_S\,\frac{\partial \psi^S}{\partial \mathbf{C}_S}\,\mathbf{F}^T_S \cdot \mathbf{D}_S\,. \tag{4.52}$$

Therein, the dependency on the deformation rate of $\mathbf{C}_S$ is considered, cf. (3.52). Furthermore, the time independence of the structural tensor $\boldsymbol{\mathcal{M}}^S$ and the referential position vector $\mathbf{X}_S$ are utilised. Hence, these quantities can be dropped out in the formulation of (4.52). Moreover, the material time derivatives of the remaining Helmholtz free energies

[8] In particular, the considered process variables of the constituent's free energies are postulated.

in (4.37) are obtained proceeding from $(4.51)_{2,3}$, viz.:

$$\begin{aligned}
\rho^B\,(\psi^B)'_B &= \rho^B\,\frac{\partial\psi^B}{\partial s^B}(s^B)'_B \,=\, \rho^B\,\frac{\partial\psi^B}{\partial s^B}\,\frac{1}{n^F}\,\big[\,(n^B)'_B \,-\, s^B(n^F)'_B\,\big] \\
&= \rho^B\,\frac{\partial\psi^B}{\partial s^B}\,\frac{1}{n^F}\,\big[\,-\,n^B\mathrm{div}\,\overset{\prime}{\mathbf{x}}_B \,-\, s^B n^S\mathrm{div}\,\overset{\prime}{\mathbf{x}}_S \,+\, s^B\mathrm{grad}\,n^S\cdot\mathbf{w}_B\,\big]\,, \\
(\Psi_I^\gamma)'_I &= \frac{\partial\Psi_I^\gamma}{\partial c_m^\gamma}(c_m^\gamma)'_\gamma \,-\, \mathrm{grad}\,\Psi_I^\gamma\cdot\mathbf{d}_{\gamma I}\,, \qquad (4.53)\\
n^I(\Psi_I^I)'_I &= -\sum_\gamma \frac{\partial\Psi_I^\gamma}{\partial c_m^\gamma}\,c_m^\gamma\,\big[\,n^S\mathrm{div}\,\overset{\prime}{\mathbf{x}}_S \,+\, n^B\mathrm{div}\,\overset{\prime}{\mathbf{x}}_B \,+\, n^I\mathrm{div}\,\overset{\prime}{\mathbf{x}}_\gamma \,+ \\
&\qquad + \mathrm{grad}\,n^B\cdot\mathbf{w}_B \,+\, \mathrm{grad}\,n^I\cdot\mathbf{w}_\gamma\,\big] \,-\, \sum_\gamma n^I\mathrm{grad}\,\Psi_I^\gamma\cdot\mathbf{d}_{\gamma I}\,.
\end{aligned}$$

Subsequently, the insertion of the derivatives (4.52) and (4.53) of the Helmholtz free energies into the current formulation of the entropy inequality (4.37) yields

$$\begin{aligned}
&\underbrace{\Big(\underbrace{\mathbf{T}_E^S - n^S\,(\Psi_I^I - \sum_\gamma c_m^\gamma\,\frac{\partial\Psi_I^\gamma}{\partial c_m^\gamma})\,\mathbf{I} + s^B\rho^{BR}\,\frac{\partial\psi^B}{\partial s^B}\,s^B n^S\,\mathbf{I}}_{\mathbf{T}^S_{E\,\mathrm{mech.}}} - 2\,\rho^S\,\mathbf{F}_S\,\frac{\partial\psi^S}{\partial\mathbf{C}_S}\,\mathbf{F}_S^T\Big)\cdot\mathbf{D}_S \,+}_{\text{equilibrium part}\,=\,0} \\
&+\Big(\underbrace{\mathbf{T}_E^B - n^B\,(\Psi_I^I - \sum_\gamma c_m^\gamma\,\frac{\partial\Psi_I^\gamma}{\partial c_m^\gamma})\,\mathbf{I} \,+\, \rho^B\,\frac{\partial\psi^B}{\partial s^B}\,s^B\,\mathbf{I}}_{\mathbf{T}^B_{E\,\mathrm{dis.}}}\Big)\cdot\mathbf{D}_B + \\
&+\sum_\gamma\Big(\underbrace{\mathbf{T}_E^\gamma - n^I\,(\Psi_I^\gamma - c_m^\gamma\,\frac{\partial\Psi_I^\gamma}{\partial c_m^\gamma})\,\mathbf{I}}_{\mathbf{T}^\gamma_{E\,\mathrm{dis.}}}\Big)\cdot\mathbf{D}_\gamma - \qquad (4.54)\\
&-\Big(\underbrace{\hat{\mathbf{p}}_E^B + (\Psi_I^I - \sum_\gamma c_m^\gamma\,\frac{\partial\Psi_I^\gamma}{\partial c_m^\gamma})\,\mathrm{grad}\,n^B \,+\, s^B\rho^{BR}\,\frac{\partial\psi^B}{\partial s^B}\,s^B\,\mathrm{grad}\,n^S}_{\hat{\mathbf{p}}^B_{E\,\mathrm{dis.}}}\Big)\cdot\mathbf{w}_B - \\
&-\sum_\gamma\Big(\underbrace{\hat{\mathbf{p}}_E^\gamma + (\Psi_I^\gamma - c_m^\gamma\,\frac{\partial\Psi_I^\gamma}{\partial c_m^\gamma})\,\mathrm{grad}\,n^I}_{\hat{\mathbf{p}}^\gamma_{E\,\mathrm{dis.}}}\Big)\cdot\mathbf{w}_\gamma \,\geq\, 0\,.
\end{aligned}$$

Proceeding from the standard evaluation procedure of Coleman & Noll [36], all resulting parts in (4.54) have to satisfy the inequality on their own for arbitrary choices of the free process variables $\mathbf{D}_S$, $\mathbf{D}_B$, $\mathbf{D}_\gamma$, $\mathbf{w}_B$ and $\mathbf{w}_\gamma$. The first part in (4.54) is postulated as an

equilibrium (non-dissipative) part under the assumption of purely elastic behaviour. It can easily be concluded that this is solely achieved (for an arbitrary choice of $\mathbf{D}_S$) if the expression in parentheses (factored out in the first row) equals to zero. Consequently, this yields the solid's extra stress via

$$\begin{aligned} \mathbf{T}^S_{E\,\text{mech.}} &= \mathbf{T}^S_E - n^S\,(\Psi^I_I - \sum_\gamma c^\gamma_m\,\frac{\partial \Psi^\gamma_I}{\partial c^\gamma_m})\,\mathbf{I} + s^B\rho^{BR}\,\frac{\partial \psi^B}{\partial s^B}\,s^B n^S\,\mathbf{I} \\ &= 2\,\rho^S\,\mathbf{F}_S\,\frac{\partial \psi^S}{\partial \mathbf{C}_S}\,\mathbf{F}^T_S\,. \end{aligned} \tag{4.55}$$

In contrast, the remaining (dissipative) parts can be greater than zero due to possible dissipative effects. Therefore, the following abbreviations are made, viz.:

$$\begin{aligned} \mathbf{T}^B_{E\,\text{dis.}} &= \mathbf{T}^B_E - n^B\,(\Psi^I_I - \sum_\gamma c^\gamma_m\,\frac{\partial \Psi^\gamma_I}{\partial c^\gamma_m})\,\mathbf{I} + \rho^B\,\frac{\partial \psi^B}{\partial s^B}\,s^B\,\mathbf{I}\,, \\ \mathbf{T}^\gamma_{E\,\text{dis.}} &= \mathbf{T}^\gamma_E - n^I\,(\Psi^\gamma_I - c^\gamma_m\,\frac{\partial \Psi^\gamma_I}{\partial c^\gamma_m})\,\mathbf{I}\,, \\ \hat{\mathbf{p}}^B_{E\,\text{dis.}} &= \hat{\mathbf{p}}^B_E + (\Psi^I_I - \sum_\gamma c^\gamma_m\,\frac{\partial \Psi^\gamma_I}{\partial c^\gamma_m})\,\operatorname{grad} n^B + s^B\rho^{BR}\,\frac{\partial \psi^B}{\partial s^B}\,s^B\operatorname{grad} n^S\,, \\ \hat{\mathbf{p}}^\gamma_{E\,\text{dis.}} &= \hat{\mathbf{p}}^\gamma_E + (\Psi^\gamma_I - c^\gamma_m\,\frac{\partial \Psi^\gamma_I}{\partial c^\gamma_m})\,\operatorname{grad} n^I\,. \end{aligned} \tag{4.56}$$

In this regard, the remaining dissipation inequality is found via

$$\mathcal{D} = \underbrace{\mathbf{T}^B_{E\,\text{dis.}}\cdot\mathbf{L}_B + \sum_\gamma \mathbf{T}^\gamma_{E\,\text{dis.}}\cdot\mathbf{L}_\gamma - \hat{\mathbf{p}}^B_{E\,\text{dis.}}\cdot\mathbf{w}_B - \sum_\gamma \hat{\mathbf{p}}^\gamma_{E\,\text{dis.}}\cdot\mathbf{w}_\gamma}_{\text{dissipative or non-equilibrium part}} \geq 0\,. \tag{4.57}$$

However, the frictional stresses are neglected in comparison with the momentum productions by arguments of dimensional analysis, cf. Ehlers *et al.* [54]. This results in

$$\operatorname{div}\mathbf{T}^B_{E\,\text{dis.}} \ll \hat{\mathbf{p}}^B_{E\,\text{dis.}} \;\rightarrow\; \mathbf{T}^B_{E\,\text{dis.}} \approx \mathbf{0} \quad\text{and}\quad \operatorname{div}\mathbf{T}^\gamma_{E\,\text{dis.}} \ll \hat{\mathbf{p}}^\gamma_{E\,\text{dis.}} \;\rightarrow\; \mathbf{T}^\gamma_{E\,\text{dis.}} \approx \mathbf{0}\,. \tag{4.58}$$

In particular, this allows the formulation of the stresses in a thermodynamical consistent context, as it will be evaluated in (4.64) and (4.70) afterwards. Moreover, inserting (4.58) into (4.57) yields a further limitation of the dissipation inequality, viz.:

$$\mathcal{D} = -\,\hat{\mathbf{p}}^B_{E\,\text{dis.}}\cdot\,\mathbf{w}_B - \sum_\gamma \hat{\mathbf{p}}^\gamma_{E\,\text{dis.}}\cdot\,\mathbf{w}_\gamma \geq 0\,. \tag{4.59}$$

Hence, the present form of the entropy inequality (4.59) motivates the following choice, cf. Acartürk [3], for the blood and the interstitial fluid components, viz.:

$$\hat{\mathbf{p}}^B_{E\,\text{dis.}} = -\,\mathbf{S}^{BS}\,\mathbf{w}_B \qquad\text{and}\qquad \hat{\mathbf{p}}^\gamma_{E\,\text{dis.}} = -\sum_\alpha \mathbf{S}^{\gamma\alpha}\,(\overset{\prime}{\mathbf{x}}_\gamma - \overset{\prime}{\mathbf{x}}_\alpha)\,. \tag{4.60}$$

Therein, the proportionalities $\hat{\mathbf{p}}^{B}_{E\,\text{dis.}} \propto \mathbf{w}_B$ and $\hat{\mathbf{p}}^{\gamma}_{E\,\text{dis.}} \propto \mathbf{w}_\gamma$ for a sufficient fulfilment of (4.59) are utilised. In the ansatz of (4.60), the so-called friction tensors $\mathbf{S}^{\beta\alpha}$ are introduced, which describe the resistance (friction) of a relative movement between the constituents. In particular, the ansatz for the extra parts of the direct momentum production terms of the interstitial-fluid components is obtained via

$$\begin{aligned}
\hat{\mathbf{p}}^{L}_{E\,\text{dis.}} &= -\,\mathbf{S}^{LS}\,\mathbf{w}_L \,-\, \mathbf{S}^{LD}\,(\mathbf{w}_L \,-\, \mathbf{w}_D)\,,\\
\hat{\mathbf{p}}^{D}_{E\,\text{dis.}} &= -\,\mathbf{S}^{DS}\,\mathbf{w}_D \,-\, \mathbf{S}^{DL}\,(\mathbf{w}_D \,-\, \mathbf{w}_L) \,=\, -\,\mathbf{S}^{LD}\,(\mathbf{w}_D \,-\, \mathbf{w}_L)\,,\\
\hat{\mathbf{p}}^{I}_{E\,\text{dis.}} &= \sum_{\gamma} \hat{\mathbf{p}}^{\gamma}_{E\,\text{dis.}} \,=\, -\,\mathbf{S}^{LS}\,\mathbf{w}_L\,.
\end{aligned} \tag{4.61}$$

Therein, the friction between the solid skeleton and the therapeutic agent is neglected (in comparison to $\mathbf{S}^{LS}$), yielding $\mathbf{S}^{DS} \approx \mathbf{0}$. Moreover, the friction among the interstitial-fluid components is symmetric $\mathbf{S}^{LD} = \mathbf{S}^{DL}$. Since the blood phase and the overall interstitial fluid are situated in separated pore-spaces, the friction between the interstitial fluid components and the blood vanishes, i. e., $\mathbf{S}^{\gamma B} = \mathbf{0}$. To summarise, the insertion of the statements (4.60), (4.61) into the dissipation inequality (4.59) yields[9]

$$\begin{aligned}
\mathcal{D} &= \mathbf{S}^{BS}\,\mathbf{w}_B\cdot\mathbf{w}_B \,+\, \mathbf{S}^{LS}\,\mathbf{w}_L\cdot\mathbf{w}_L \,+\\
&\quad \mathbf{S}^{LD}\,(\mathbf{w}_L \,-\, \mathbf{w}_D)\cdot\mathbf{w}_L \,+\, \mathbf{S}^{LD}\,(\mathbf{w}_D \,-\, \mathbf{w}_L)\cdot\mathbf{w}_D \qquad (4.62)\\
&= \mathbf{S}^{BS}\,\mathbf{w}_B\cdot\mathbf{w}_B \,+\, \mathbf{S}^{LS}\,\mathbf{w}_L\cdot\mathbf{w}_L \,+\, \mathbf{S}^{LD}\,(\mathbf{w}_L \,-\, \mathbf{w}_D)\cdot(\mathbf{w}_L \,-\, \mathbf{w}_D) \,\geq\, 0\,.
\end{aligned}$$

Therefore, it can easily be concluded that the dissipation inequality is always fulfilled using the following constitutive approaches of the positive-definite (second-order) friction-tensors, viz.:

$$\begin{aligned}
\mathbf{S}^{BS} &= (n^B)^2\,\mu^{BR}\,(\mathbf{K}^{SB})^{-1}\,,\\
\mathbf{S}^{LS} &= (n^I)^2\,\mu^{LR}\,(\mathbf{K}^{SL})^{-1}\,,\\
\mathbf{S}^{LD} &= (n^I)^2\,R\theta\,c^D_m\,(\mathbf{D}^D)^{-1}\,.
\end{aligned} \tag{4.63}$$

Therein, $\mu^{\beta R}$ are the effective shear viscosities, while R and θ are the universal gas constant and the absolute Kelvin's temperature, respectively. In terms of the considered scope of the brain-tissue model, it is of fundamental importance to capture anisotropic perfusion conditions for the intrinsic permeabilities $\mathbf{K}^{S\beta}$ and the diffusivity $\mathbf{D}^D$ of the therapeutic agent via the description by second-order tensors. The postulation of friction tensors in (4.63) is based on constitutive correlations, which hold for the momentum exchanges in (4.60) and (4.61). In particular, the momentum exchange increases due to higher filter velocities and higher partial viscosities, cf. $(4.63)_{1,2}$. In addition, a smaller permeability results in an increase of the momentum exchange. Finally, the constitutive setting of the friction among the interstitial fluid components $(4.63)_3$ is chosen according to Ehlers [51].

[9] Therein, the second binomial formula is used to evaluate the right-hand side of the expression.

4.3.3 Chemical relations of the interstitial-fluid components

The subsequently derived statements for the overall interstitial fluid mixture and its components, arising from the evaluation process of the entropy inequality, are based on the investigations presented in Bowen [26, 27], Acartürk [3] and Ehlers [51]. Proceeding from vanishing frictional stresses $\mathbf{T}^{\gamma}_{E\,\mathrm{dis.}}$, cf. $(4.58)_2$, it is obtained from $(4.56)_3$ that the extra stresses of the interstitial fluid components read

$$\mathbf{T}^{\gamma}_{E} = -\,n^{I}\,(c^{\gamma}_{m}\,\frac{\partial\Psi^{\gamma}_{I}}{\partial c^{\gamma}_{m}} - \Psi^{\gamma}_{I})\,\mathbf{I} \quad\leftrightarrow\quad \mathbf{T}^{\gamma}_{E} - n^{I}\,\Psi^{\gamma}_{I}\,\mathbf{I} = -\,n^{I}\,c^{\gamma}_{m}\,\frac{\partial\Psi^{\gamma}_{I}}{\partial c^{\gamma}_{m}}\,\mathbf{I}\,. \tag{4.64}$$

Comparing the relation (4.64) with the formulation of the chemical potential tensor $\mathbf{K}^{\gamma}$ introduced by Bowen [27] with the relations (3.13) and (4.27) yields

$$\mathbf{K}^{\gamma} := \psi^{\gamma}\,\mathbf{I} - \frac{1}{\rho^{\gamma}}\,(\mathbf{T}^{\gamma}_{E})^{T} \quad\leftrightarrow\quad \mathbf{T}^{\gamma}_{E} - n^{I}\,\Psi^{\gamma}_{I}\,\mathbf{I} = -\,n^{I}\,c^{\gamma}_{m}\,M^{\gamma}_{m}\,\mathbf{K}^{\gamma}\,. \tag{4.65}$$

From the accordance of $(4.64)_2$ and $(4.65)_2$, it is concluded that the component φ^{γ} can be described by an isotropic scalar-valued tensor of chemical potential

$$M^{\gamma}_{m}\,\mathbf{K}^{\gamma} = \frac{\partial\Psi^{\gamma}_{I}}{\partial c^{\gamma}_{m}}\,\mathbf{I} = \mu^{\gamma}_{m}\,\mathbf{I}\,, \qquad \text{where} \quad \mu^{\gamma}_{m} = \frac{\partial\Psi^{\gamma}_{I}}{\partial c^{\gamma}_{m}} \tag{4.66}$$

represents the molar chemical potential μ^{γ}_{m}. Moreover, the so-called "extra pressure" of the component φ^{γ} is identified by the contribution of the component's osmotic pressure π^{γ} to the overall osmotic pressure π. Therefore, the osmotic pressures of the components π^{γ} are identified from $(4.64)_1$ via

$$\pi^{\gamma} = c^{\gamma}_{m}\,\frac{\partial\Psi^{\gamma}_{I}}{\partial c^{\gamma}_{m}} - \Psi^{\gamma}_{I} = c^{\gamma}_{m}\,\mu^{\gamma}_{m} - \Psi^{\gamma}_{I}\,, \qquad \text{where} \quad \pi = \sum_{\gamma}\pi^{\gamma} \tag{4.67}$$

denotes the overall osmotic pressure, which is given by a summation of the partial osmotic pressures. At this point, the Helmholtz free energies of the components are specified according to Acartürk [3] and Ehlers [51], viz.:

$$\Psi^{\gamma}_{I} = c^{\gamma}_{m}\,\mu^{\gamma}_{0m} + c^{\gamma}_{m}\,R\theta\,(\ln c^{\gamma}_{m} - 1)\,. \tag{4.68}$$

Therein, μ^{γ}_{0m} denotes the constant standard potential. Following this, the chemical potential of the component as well as the osmotic pressures are obtained by the evaluation of (4.68) with the previously introduced relations, viz.:

$$\begin{aligned} \mu^{\gamma}_{m} &= \frac{\partial\Psi^{\gamma}_{I}}{\partial c^{\gamma}_{m}} = \mu^{\gamma}_{0m} + R\theta\ln c^{\gamma}_{m}\,, \\ \pi^{\gamma} &= c^{\gamma}_{m}\,\mu^{\gamma}_{m} - \Psi^{\gamma}_{I} = R\theta\,c^{\gamma}_{m} \quad\rightarrow\quad \pi = \sum_{\gamma}\pi^{\gamma} = R\theta\sum_{\gamma}c^{\gamma}_{m}\,. \end{aligned} \tag{4.69}$$

4.3.4 Partial stress tensors and pore pressures of the constituents

In the next step, the constituent's stresses and pore pressures are established. Therefore, the assumption (4.58) combined with (4.36), (4.55), (4.56) and the relations in (4.67) yields the partial stresses of the constituents, viz.:

$$\begin{aligned}
\mathbf{T}^{\gamma} &= -\left(n^{\gamma}\,\mathcal{P} + n^{I}\,\pi^{\gamma}\right)\mathbf{I}\,,\\
\mathbf{T}^{I} &= -n^{I}\left(\mathcal{P} + \pi\right)\mathbf{I} =: -n^{I}\,p^{IR}\,\mathbf{I}\,,\\
\mathbf{T}^{B} &= -n^{B}\left(\mathcal{P} + \pi\right)\mathbf{I} - \rho^{B}\,\frac{\partial\psi^{B}}{\partial s^{B}}\,s^{B}\,\mathbf{I} =: -n^{B}\,p^{BR}\,\mathbf{I}\,,\\
\mathbf{T}^{S} &= \mathbf{T}^{S}_{E\,\mathrm{mech.}} - n^{S}\left(\mathcal{P} + \pi + s^{B}\rho^{BR}\,\frac{\partial\psi^{B}}{\partial s^{B}}\,s^{B}\right)\mathbf{I} = \mathbf{T}^{S}_{E\,\mathrm{mech.}} - n^{S}\,p\,\mathbf{I}\,.
\end{aligned} \tag{4.70}$$

Therein, the effective pore pressure of the overall interstitial fluid p^{IR} and the effective blood pressure p^{BR} can be identified from $(4.70)_{2,3}$ via

$$p^{IR} = \mathcal{P} + \pi \qquad \text{and} \qquad p^{BR} = p^{IR} + s^{B}\rho^{BR}\,\frac{\partial\psi^{B}}{\partial s^{B}}\,. \tag{4.71}$$

For the sake of convenience and with regard to the further development of constitutive relations, it can easily be concluded that the pressure difference $p_{\mathrm{dif.}}$ between these two pore pressures can be introduced via

$$p_{\mathrm{dif.}} = p^{BR} - p^{IR} = s^{B}\rho^{BR}\,\frac{\partial\psi^{B}}{\partial s^{B}}\,. \tag{4.72}$$

Finally, the overall Cauchy stress $\mathbf{T}$ which is, in particular, required in the governing balance of momentum of the overall aggregate (4.24), is derived by a summation of its partial stresses in (4.70), viz.:

$$\mathbf{T} = \mathbf{T}^{S}_{E\,\mathrm{mech.}} - p\,\mathbf{I}\,, \quad \text{with} \quad p = s^{B}\,p^{BR} + s^{I}\,p^{IR}\,. \tag{4.73}$$

Therein, the overall pore pressure p is found as a combination of the liquid pore-pressures, weighted by the corresponding saturations. Note in passing that this representation is entirely consistent with the well-known formulation of Dalton's law of partial pressures.

4.3.5 Direct momentum production terms

Including the knowledge of the previously introduced pressures in (4.71) and (4.72), the direct momentum productions stated in $(4.36)_{4,5}$ are recovered via

$$\begin{aligned}
\hat{\mathbf{p}}^{\gamma} &= \mathcal{P}\,\mathrm{grad}\,n^{\gamma} + \pi^{\gamma}\,\mathrm{grad}\,n^{I} + \hat{\mathbf{p}}^{\gamma}_{E\,\mathrm{dis.}}\,,\\
\hat{\mathbf{p}}^{I} &= \sum_{\gamma}\hat{\mathbf{p}}^{\gamma} = p^{IR}\,\mathrm{grad}\,n^{I} + \hat{\mathbf{p}}^{I}_{E\,\mathrm{dis.}}\,,\\
\hat{\mathbf{p}}^{B} &= p^{IR}\,\mathrm{grad}\,n^{B} - p_{\mathrm{dif.}}\,s^{B}\,\mathrm{grad}\,n^{S} + \hat{\mathbf{p}}^{B}_{E\,\mathrm{dis.}}\,.
\end{aligned} \tag{4.74}$$

As a conclusion of this subsection, the thermodynamical consistency of the brain's tissue model is provided via the appropriate evaluation of the entropy inequality. These investigations provide the framework of constitutive relations for all involved constituents. In particular, the constitutive setting is applied to the pore-liquid constituents and its components in Subsection 4.4 as well as to the material modelling of the solid skeleton in Subsection 4.5.

4.4 The fluid constituents and its components

4.4.1 Flow of the pore liquids

Overall interstitial fluid: For the description of the specific flow characteristics of the overall interstitial fluid, the constitutive ansatz for the extra momentum production term $\hat{\mathbf{p}}^I_{E\,\text{dis.}}$, cf. $(4.61)_3$, $(4.63)_2$ and $(4.74)_2$, and the partial stress tensor, cf. $(4.70)_2$ are inserted into the (quasi-static) momentum balance $(4.9)_2$ of the overall interstitial fluid, viz.:

$$\begin{aligned}
\mathbf{0} &= \operatorname{div}\mathbf{T}^I + \rho^I\,\mathbf{g} + \hat{\mathbf{p}}^I \\
&= \operatorname{div}\left(-\,n^I\,p^{IR}\,\mathbf{I}\right) + \rho^I\,\mathbf{g} + p^{IR}\operatorname{grad} n^I + \hat{\mathbf{p}}^I_{E\,\text{dis.}} \\
&= -\,n^I\operatorname{grad} p^{IR} + n^I\,\rho^{IR}\,\mathbf{g} - (n^I)^2\,\mu^{IR}\,(\mathbf{K}^{SI})^{-1}\,\mathbf{w}_I\,, \\
\rightarrow \quad n^I\,\mathbf{w}_I &= -\,\frac{\mathbf{K}^{SI}}{\mu^{IR}}\left(\operatorname{grad} p^{IR} - \rho^{IR}\,\mathbf{g}\right).
\end{aligned} \tag{4.75}$$

Therein, the circumstance that the dissolved therapeutic agent is negligible in its total amount in comparison to the liquid solvent, cf. (4.2) and (4.3), is included in such a manner that the mechanical properties of the overall interstitial fluid mixture φ^I are assumed to be equal to the mechanical properties of the solvent φ^L. As a result, a standard Darcy-like filter law is obtained.

Blood constituent: Accordingly, the previous procedure is also applied to the (quasi-static) momentum balance $(4.9)_2$ of the blood constituent via incorporating the momentum production relations $(4.60)_1$, $(4.63)_1$ and $(4.74)_3$ as well as the partial stress tensor $(4.70)_3$ of the blood constituent, yielding

$$\begin{aligned}
\mathbf{0} &= \operatorname{div}\mathbf{T}^B + \rho^B\,\mathbf{g} + \hat{\mathbf{p}}^B \\
&= \operatorname{div}\left(-\,n^B\,p^{BR}\,\mathbf{I}\right) + \rho^B\,\mathbf{g} + p^{IR}\operatorname{grad} n^B - p_{\text{dif.}}\,s^B\operatorname{grad} n^S + \hat{\mathbf{p}}^B_{E\,\text{dis.}}\,, \\
\rightarrow \quad n^B\,\mathbf{w}_B &= -\,\frac{\mathbf{K}^{SB}}{\mu^{BR}}\left[\operatorname{grad} p^{BR} - \rho^{BR}\,\mathbf{g} + \frac{p_{\text{dif.}}}{n^B}(s^I\operatorname{grad} n^B - s^B\operatorname{grad} n^I)\right] \\
&= -\,\frac{\mathbf{K}^{SB}}{\mu^{BR}}\left[\operatorname{grad} p^{BR} - \rho^{BR}\,\mathbf{g} + \frac{p_{\text{dif.}}}{s^B}\operatorname{grad} s^B\right].
\end{aligned} \tag{4.76}$$

Due to this rigorous proceeding, an additional term is obtained[10] in comparison to the standard Darcy-like formulation derived for the interstitial fluid flow in (4.75), cf. the rightmost part in the parenthesis of $(4.76)_{3,4}$. Although this part accounts for a consistent constitutive modelling process, it has, in general, little to no effect[11]. Note in passing that the downward compatibility to a standard Darcy-like relation for the blood perfusion is obtained in the case of a complete blood saturation ($s^B = 1$), cf. the last line in (4.76). Further discussions of neglecting the contribution of a volumetrical-fraction gradient are found, e. g., in Avci [10], Fredlund & Rahardjo [69] and Graf [70] for multiphasic flow processes and, e. g., in Heider [77] related to saturated porous-media dynamics. The latter neglected the gradient of the volume fraction by means of a higher-order term in a geometrically linear biphasic model.

Different anisotropic permeability measures: The usage of second-order intrinsic permeabilities $\mathbf{K}^{S\beta}$ in both pore-liquid-flow equations (4.75) and (4.76) plays a crucial role. In particular, this enables a seepage velocity $\mathbf{w}_\beta$ that can differ from the direction of the existing pressure gradient. Thus, it is required for the considered anisotropic fibrous tissue to include this property. Furthermore, it is necessary to use different intrinsic permeabilities due to the circumstance that the pore liquids are located in separated pore spaces. In this regard, the intrinsic permeabilities of the tissue perfusion through the ECS by the interstitial fluid is considered via $\mathbf{K}^{SI}$, whereas the blood flow through the blood-vessel system is captured via $\mathbf{K}^{SB}$. Regarding the evaluation of the initial values $\mathbf{K}^{S\beta}_{0S}$ of the spatially varying intrinsic permeabilities, appropriate medical imaging methods are utilised afterwards, cf. Section 6.2.

In general, the intrinsic permeability $\mathbf{K}^{S\beta}$ represents a suitable permeability measure, since this quantity is independent of the fluid properties and represents a purely structural quantity of the solid skeleton. Nevertheless, other kinds of permeability measures are commonly used. In particular, these are the positive-definite hydraulic (or Darcy) permeability tensor $\mathbf{K}^\beta$ and the positive-definite specific permeability $\mathbf{K}^\beta_{\text{spec.}}$. Their dependencies in relation to the intrinsic permeability $\mathbf{K}^{S\beta}$ are given by

$$\mathbf{K}^{S\beta} = \frac{\mu^{\beta R}}{\gamma^{\beta R}}\,\mathbf{K}^\beta = \mu^{\beta R}\,\mathbf{K}^\beta_{\text{spec.}}\ \left[\,\mathrm{m}^2\,\right] \quad \leftrightarrow \quad \begin{cases} \mathbf{K}^\beta = \dfrac{\gamma^{\beta R}}{\mu^{\beta R}}\,\mathbf{K}^{S\beta} & \left[\,\dfrac{\mathrm{m}}{\mathrm{s}}\,\right], \\ \mathbf{K}^\beta_{\text{spec.}} = \dfrac{\mathbf{K}^{S\beta}}{\mu^{\beta R}} & \left[\,\dfrac{\mathrm{m}^4}{\mathrm{N\,s}}\,\right]. \end{cases} \tag{4.77}$$

Therein, the hydraulic (or Darcy) permeability $\mathbf{K}^\beta$ depends on the fluid properties. The use of the specific permeability $\mathbf{K}^\beta_{\text{spec.}}$ results in the benefit of a single prefactor in the pore-liquid-flow equations (4.75) and (4.76). Note in passing that the order of magnitude generally varies[12] in a strong manner between the different kinds of permeabilities. In this regard, the corresponding units are given in (4.77), characterising the permeability measures. For a more detailed discussion on different permeability measures, the reader is referred to, e. g., Markert [106].

[10] Therein, the rightmost part in the parenthesis of $(4.76)_{3,4}$ can be rearranged via (B.14).

[11] In particular, this is obvious for a homogeneous blood saturation distribution, which is a reasonable assumption in many applications using a homogenisation of the complex blood-vessel system.

[12] For example, the Darcy permeability of water (with $\gamma^{WR} \approx 10\,000\,\mathrm{N/m^3}$ and $\mu^{WR} \approx 0.001\,\mathrm{Ns/m^2}$) is approximately seven orders of magnitude higher than its respective intrinsic permeability.

Deformation-dependent permeabilities: It is worth mentioning that the initial intrinsic permeabilities $\mathbf{K}_{0S}^{S\beta}$ can change during a (finite) deformation process of the tissue skeleton. Therefore, the intrinsic permeabilities in the actual configuration

$$\mathbf{K}^{S\beta} \;=\; \tilde{K}^{S\beta}\,\mathbf{F}_S\,\mathbf{K}_{0S}^{S\beta}\,\mathbf{F}_S^T \quad \text{with} \quad \tilde{K}^{S\beta} \;=\; \Big(\frac{n^\beta}{n_{0S}^\beta}\,\frac{n_{0S}^S}{n^S}\Big)^\kappa \;\text{ and }\; \kappa \geq 0 \tag{4.78}$$

are obtained via a push-forward transformation to the actual configuration. Furthermore, deformation-dependent permeability can be considered by the prefactor $\tilde{K}^{S\beta}$, including an additional material parameter κ. For a detailed description of deformation-dependent permeabilities of porous materials, the interested reader is referred to, e. g., Ateshian & Weiss [9], Federico [66] or Markert [106].

4.4.2 Diffusion of the therapeutic agent

The distribution law for the therapeutical component is derived by the insertion of the partial stress $\mathbf{T}^D$ and the direct momentum production $\hat{\mathbf{p}}^D$ of the therapeutic agent in the (quasi-static) formulation of the therapeutic agent's momentum balance $(4.9)_2$. In addition, the momentum production relations $(4.61)_2$, $(4.63)_3$ and $(4.74)_1$ as well as the therapeutic agent's stress tensor $(4.70)_1$ are used such that

$$\begin{aligned}
\mathbf{0} \;&=\; \operatorname{div}\mathbf{T}^D \,+\, \rho^D\,\mathbf{g} \,+\, \hat{\mathbf{p}}^D \\
&=\; -\,n^I\operatorname{grad}\pi^D \,-\, n^D\operatorname{grad}\mathcal{P} \,+\, \rho^D\,\mathbf{g} \,+\, \hat{\mathbf{p}}^D_{E\,\text{dis.}} \\
\rightarrow\quad n^I c_m^D\,\mathbf{d}_{DI} \;&=\; -\,\frac{\mathbf{D}^D}{R\theta}\,\big(\operatorname{grad}\pi^D \,+\, \rho_I^D\,\mathbf{g} \,+\, \frac{n^D}{n^I}\operatorname{grad}\mathcal{P}\,\big) \;\approx\; -\,\mathbf{D}^D\operatorname{grad}c_m^D\,.
\end{aligned} \tag{4.79}$$

Therein, the osmotic pressure π^D of the therapeutical component is replaced by its concentration using $(4.69)_2$. Furthermore, the second and third part in parenthesis can be neglected due to the argumentation in (4.2) and (4.3). This leads[13] to a standard Fick-like distribution law. Furthermore, using the kinematical relation (3.28) yields a corresponding expression for the therapeutic seepage velocity, viz.:

$$n^I c_m^D\,\mathbf{w}_D \;=\; -\,\mathbf{D}^D\operatorname{grad}c_m^D \,+\, n^I c_m^D\,\mathbf{w}_I\,. \tag{4.80}$$

Note in passing that the effective drug diffusivity $\mathbf{D}^D = \mathbf{F}_S\,\mathbf{D}_0^D\,\mathbf{F}_S^T$ can be evaluated based on its initial value $\mathbf{D}_0^D$, which is itself obtained via appropriate medical-imaging techniques, cf. Section 6.2.

4.4.3 Saturation of the blood constituent

It has not been considered so far that all volume fractions of the constituents are generally unknown. To determine the solid volume fraction, the evolution of n^S is derived by a formal integration of the volume balance of the solid skeleton, cf. (4.23). Furthermore,

[13] Here, the assumed constant temperature field θ, cf. (4.8), can be extracted from the gradient operator.

the volume fraction of the therapeutic agent is a priori neglected, cf. (4.2), but the volume fractions of the pore-liquids remain unknown. However, only one constitutive equation is available, i. e., the saturation condition (3.5). Hence, one additional constitutive equation needs to be specified in order to describe the partitioning of the liquid's volume fractions. This is comparable to the procedure within unsaturated soil mechanics. Therein, the capillary pressure, defined as the difference between the pressures of the non-wetting and the wetting fluid, is used to evaluate the saturations via capillary-pressure-saturation conditions, cf., e. g., Ehlers [51] or Ricken & de Boer [131]. However, in the present case, the blood and the interstitial fluid are not situated in the same pore compartment such that these relations cannot be applied. Instead, further assumptions are needed here in order to specify the blood's saturation s^B. In particular, two distinct approaches are proposed. These are the assumption of a constant volume fraction and a more sophisticated constitutive relation for the blood saturation, depending on the pressure difference of the pore liquids.

Constant volume fraction of the blood: In terms of modelling the therapeutic agent distribution in the extra-vascular space of the brain tissue, it is convenient to exclude any influence of the blood-vessel system in a first step. Therefore, a simple but definitely meaningful choice is the assumption of a constant blood volume fraction, viz.:

$$n^B = n^B_{0S} = \text{const.} \quad \rightarrow \quad n^I = 1 - n^S - n^B_{0S}\,. \tag{4.81}$$

This implies the assumption of an inherent stability of the blood-vessel system and results in a pure interaction between the solidity n^S and the interstitial fluid's volume fraction n^I during a deformation process. Reasonable values of the homogenised blood volume fraction n^B are in the range of approximately 3 % for healthy tissues, cf. the review article of Syková & Nicholson [154] based on, e. g., Jain [83]. In contrast, in tumour-affected domains, the range can vary between 1 % and 20 % .

Constitutive relation for the volume fraction of the blood: Nevertheless, more sophisticated approaches are often necessary by means of a suitable consideration of the blood constituent. In particular, this is the case for, e. g., a mutually volumetrical interaction caused by sufficiently soft elastic arterial walls. Therefore, a constitutively chosen ansatz for the Helmholtz free energy of the blood constituent is postulated, viz.:

$$\psi^B(s^B) = \frac{\tilde{\alpha}^B}{\rho^{BR}} \left((\tilde{\beta}^B + 1) \ln(s^B) + \frac{1}{s^B} - \ln(1 - s^B) \right) + \tilde{\psi}^B_0\,. \tag{4.82}$$

Therein, $\tilde{\psi}^B_0$ denotes the constant reference potential (standard state potential). This approach needs to satisfy the thermodynamical restrictions found in (4.72) and consequently yields the difference of the pore-pressures via

$$\begin{aligned} p_{\text{dif.}}(s^B) &= s^B \rho^{BR} \frac{\partial \psi^B}{\partial s^B} = \tilde{\alpha}^B \left(\frac{1 - 2\,s^B}{s^B (s^B - 1)} + \tilde{\beta}^B \right), \\ \text{where} \quad \frac{\partial \psi^B}{\partial s^B} &= \frac{\tilde{\alpha}^B}{\rho^{BR}} \left(\frac{\tilde{\beta}^B}{s^B} - \frac{1}{s^B (s^B - 1)} - \frac{1}{(s^B)^2} \right). \end{aligned} \tag{4.83}$$

Therein, $\tilde{\alpha}^B$ and $\tilde{\beta}^B$ denote material parameters, which allow via $\tilde{\alpha}^B$ for the adaption of the pore-pressure difference to typical pressure values as they exist in the skull and for

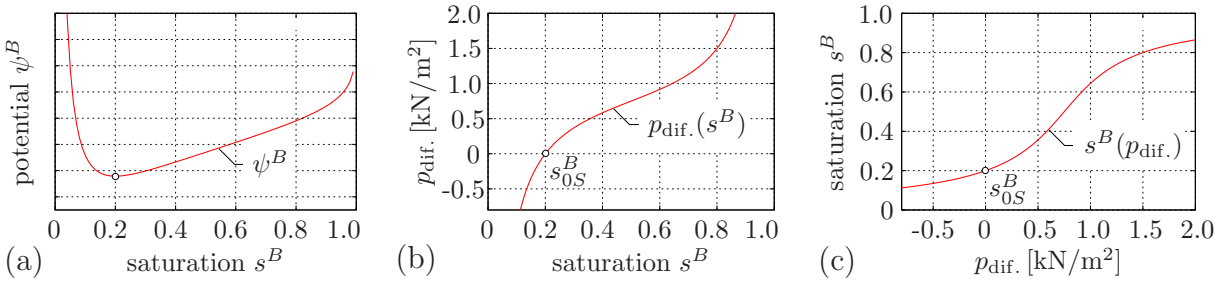

Figure 4.1: *Constitutive relation: (a) the Helmholtz free energy (potential) ψ^B of the blood constituent, (b) the differential pressure $p_{\text{dif.}}$ of the pore-liquid constituents, and (c) the blood saturation s^B.*

the initial blood saturation via $\tilde{\beta}^B$. The inversion of (4.83) leads to the blood saturation function. In particular,

$$s^B(p_{\text{dif.}}) = \frac{1}{2\left(\frac{p_{\text{dif.}}}{\tilde{\alpha}^B} - \tilde{\beta}^B\right)} \left(\left(\frac{p_{\text{dif.}}}{\tilde{\alpha}^B} - \tilde{\beta}^B - 2\right) + \sqrt{4 + \left(\frac{p_{\text{dif.}}}{\tilde{\alpha}^B} - \tilde{\beta}^B\right)^2} \right) \tag{4.84}$$

is found by rational investigations of a meaningful inversion of (4.83), which is a second-order function in s^B. This statement for the saturation (4.84) allows for a proper determination of the volume fractions from the saturation condition (3.5), viz.:

$$n^B = s^B\,(1 - n^S) \qquad \rightarrow \quad n^I = 1 - n^S - n^B\,. \tag{4.85}$$

To give an example, an equation satisfying both typical initial volume fractions of the brain tissue and typical pressure values as they exist in the skull is adapted by $\tilde{\beta}^B = 3.75$ and $\tilde{\alpha}^B = 200.0$ N/m^2, cf. Figure 4.1. This leads to a replacement of the interstitial fluid if the pressure difference $p_{\text{dif.}}$ is positive. Note in passing that a constant value of $n^B_{0S} = 0.05$ yields an initial value of $s^B_{0S} = 0.2$ and, as a result, $p_{\text{dif.}} = 0$. Moreover, it should be noted that the solid, when it deforms, rather pushes away the liquid with the lower pressure than the liquid with the higher pressure.

In conclusion, this constitutive consideration allows for the determination of the liquid volume fractions by means of an expression via the primary unknowns. Furthermore, also the relations for the time derivatives of the volume fractions can be evaluated. In particular, these quantities (also denoted as secondary variables) are requested in the adapted balance relations (4.18) and (4.19). In particular, proceeding from the time derivative of the saturation condition (3.5) with respect to the solid motion, it is found that

$$(n^F)'_S = -\,(n^S)'_S \qquad \text{with} \qquad (n^S)'_S = -\,n^S\,\text{div}\,(\mathbf{u}_S)'_S\,. \tag{4.86}$$

Furthermore, including the saturation relations (3.6) yields

$$\begin{aligned} (n^B)'_S &= (s^B n^F)'_S = (s^B)'_S\,n^F + s^B (n^F)'_S\,, \quad \text{where } (s^B)'_S = \frac{\partial s^B}{\partial p_{\text{dif.}}}\,(p_{\text{dif.}})'_S\,, \\ (n^I)'_S &= -\,(n^S)'_S - (n^B)'_S\,. \end{aligned} \tag{4.87}$$

It can easily be concluded from $(4.87)_1$ that the temporal change $(s^B)'_S$ of the blood saturation depends on the chosen constitutive formulation of the saturation relation.

4.5 The solid skeleton constituent

4.5.1 Material symmetry

Regarding the microscopic composition of human brain tissue, cf. Section 2.1, it is obvious that the solid skeleton belongs to the class of anisotropic materials due to a distinct fibre orientation caused by the myelinated nervous fibres. Although nervous fibres might cross each other at local positions in the brain-tissue, only one (the dominant) fibre family is taken into account. This specific class of material is generally known as transversely isotropic material, where the issue of material symmetry plays a major role. Therefore, the basic considerations made for material symmetry in terms of material modelling purposes are introduced in this section based on the fundamental works of, e. g., Truesdell & Noll [159], Spencer [148, 149] or Eringen [64]. Moreover, the proceeding is closely based on the contributions of Schröder [141], Ehlers [44] and Karajan [86, 87] and citations therein. Following the standard argumentation, an alternative reference configuration is introduced, viz.:

$$\check{\mathbf{X}}_S \;=\; \mathbf{H}\,\mathbf{X}_S\,. \tag{4.88}$$

Therein, $\mathbf{H}$ denotes a transformation between the standard reference configuration and its alternative. In particular, the symmetric transformation $\mathbf{H} \in \mathcal{MG}_3 \in \mathcal{O}_e$ maps between these two reference configurations and exhibits in general the same properties as postulated for the proper rotations $\mathbf{Q}$ used in terms of the material frame indifference, cf. Section 4.3.1. However, treating anisotropic material behaviour requires a stronger restriction by means of claiming the membership in the more specific symmetry group $\mathcal{MG}_3 \in \mathcal{O}_e$. In general, the symmetry group $\mathcal{MG}_3$ is represented by the set of all linear transformations that map the reference configuration into an alternative reference configuration, stating that the values of the response functions remain unchanged. For a more detailed discussion on selected symmetry groups, cf. Karajan [87].

Regarding the anisotropic (fibre-reinforced) brain-tissue, the stored elastic energy depends on the deformation and the orientation of the material, whereas the dependence on the referential position $\mathbf{X}_S$ is omitted[14]. Thus, an invariance condition, cf. (4.42), for the (scalar-valued) solid strain energy ψ^S can be formulated based on $(4.41)_1$, viz.:

$$\check{\psi}^S(\mathbf{C}_S,\,\boldsymbol{\mathcal{M}}^S) \;=\; \psi^S(\mathbf{C}_S,\,\boldsymbol{\mathcal{M}}^S) \;\stackrel{!}{=}\; \psi^S(\check{\mathbf{C}}_S,\,\check{\boldsymbol{\mathcal{M}}}^S)\,. \tag{4.89}$$

Therein, the notation $(\,\check{\cdot}\,)$ indicates quantities of the rotated reference configuration. These variables are subsequently reformulated, proceeding from the rotated (two-field) deformation gradient

$$\check{\mathbf{F}}_S \;=\; \frac{\partial \mathbf{x}}{\partial \check{\mathbf{X}}_S} \;=\; \frac{\partial \mathbf{x}}{\partial \mathbf{X}_S}\,\frac{\partial \mathbf{X}_S}{\partial \check{\mathbf{X}}_S} \;=\; \mathbf{F}_S\,\mathbf{H}^{-1}\,, \qquad \text{where} \quad \mathbf{H}^{-1} \;=\; \frac{\partial \mathbf{X}_S}{\partial \check{\mathbf{X}}_S}\,. \tag{4.90}$$

From this basis, it is concluded for the considered quantities in (4.89) of the alternative reference configuration that

$$\check{\mathbf{C}}_S \;=\; \check{\mathbf{F}}_S^T\,\check{\mathbf{F}}_S \;=\; \mathbf{H}\,\mathbf{C}_S\,\mathbf{H}^T \qquad \text{and} \qquad \check{\boldsymbol{\mathcal{M}}}^S \;=\; \mathbf{H}\,\boldsymbol{\mathcal{M}}^S\,\mathbf{H}^T\,. \tag{4.91}$$

[14] This is constitutively stated in accordance to Karajan [87] since inhomogeneous material behaviour is usually captured in an implicit manner via material parameters.

Hence, the insertion of (4.91) into the relation (4.89) yields

$$\psi^S(\mathbf{C}_S,\, \boldsymbol{\mathcal{M}}^S) \;=\; \psi^S(\mathbf{H}\,\mathbf{C}_S\,\mathbf{H}^T,\, \mathbf{H}\,\boldsymbol{\mathcal{M}}^S\,\mathbf{H}^T)\,. \tag{4.92}$$

The restriction above serves as a criterion for the identification of the structural tensor $\boldsymbol{\mathcal{M}}^S = \mathbf{H}\,\boldsymbol{\mathcal{M}}^S\,\mathbf{H}^T$ in its property to fulfil (4.92) for appropriate symmetry groups $\mathbf{H} \in \mathcal{MG}_3$. For the further constitutive modelling process, the solid strain energy

$$W^S(\mathbf{C}_S,\, \boldsymbol{\mathcal{M}}^S) \;:=\; \rho^S_{0S}\,\psi^S(\mathbf{C}_S,\, \boldsymbol{\mathcal{M}}^S) \tag{4.93}$$

is introduced, replacing the Helmholtz free energy in further considerations.

4.5.2 Thermodynamical inferences from the basic principles

Tracing back to the conflict arising in (4.92), a detailed discussion can be found, e. g. in Karajan [87] or Ricken *et al.* [133], for various kinds of structured porous materials, such as isotropic and transversely isotropic materials as well as orthogonally and prismatically symmetric materials. For the purposes of this monograph, the corresponding strategy for transversely isotropic materials is briefly introduced.

The procedure starts with selecting symmetry groups, satisfying (4.92) in terms of the observed quantities $\mathbf{C}_S$ and $\boldsymbol{\mathcal{M}}^S$. In case of the considered transversely isotropic material behaviour, the structural tensor $\boldsymbol{\mathcal{M}}^S_a$ is obtained by the dyadic product of the unit vector $\mathbf{a}^S_0$, indicating the fibre direction in the non-deformed reference configuration, viz.:

$$\boldsymbol{\mathcal{M}}^S_a \;=\; \mathbf{a}^S_0 \otimes \mathbf{a}^S_0\,, \qquad \text{with} \quad \begin{cases} \boldsymbol{\mathcal{M}}^S_a \;=\; (\boldsymbol{\mathcal{M}}^S_a)^T\,, \\ \boldsymbol{\mathcal{M}}^S_a \;=\; \boldsymbol{\mathcal{M}}^S_a\,\boldsymbol{\mathcal{M}}^S_a\,, \\ \operatorname{tr}\boldsymbol{\mathcal{M}}^S_a \;=\; 1\,. \end{cases} \tag{4.94}$$

Since the structural tensor $\boldsymbol{\mathcal{M}}^S_a$ is constructed by the unit fibre vector $\mathbf{a}^S_0$, this quantity needs to be defined in the reference configuration. This is investigated afterwards via the evaluation of medical-imaging data, cf. Section 6.2.1. In order to account for the tensorial arguments in (4.92), the theory of invariants is applied. In this regard, the set $\mathcal{I}_S = \{J_{S1}, J_{S2}, J_{S3}, J_{S4}, J_{S5}\}$ of scalar basic and mixed invariants is obtained from their respective integrity bases, cf. Table 4.1. Note in passing that further conceivable constellations of mixed invariants are omitted due to the properties of $\boldsymbol{\mathcal{M}}^S_a$ given in

tensorial arguments	basic and mixed invariants	usage
$\mathbf{C}_S$	$\operatorname{tr}\mathbf{C}_S\,,\ \operatorname{tr}(\mathbf{C}_S\,\mathbf{C}_S)\,,\ \operatorname{tr}(\mathbf{C}_S\,\mathbf{C}_S\,\mathbf{C}_S)$	isotropy
$\mathbf{C}_S\,,\ \boldsymbol{\mathcal{M}}^S_a$	$\operatorname{tr}\mathbf{C}_S\,,\ \operatorname{tr}(\mathbf{C}_S\,\mathbf{C}_S)\,,\ \operatorname{tr}(\mathbf{C}_S\,\mathbf{C}_S\,\mathbf{C}_S)$ $\operatorname{tr}(\boldsymbol{\mathcal{M}}^S_a\,\mathbf{C}_S)\,,\ \operatorname{tr}(\boldsymbol{\mathcal{M}}^S_a\,\mathbf{C}_S\,\mathbf{C}_S)$	transverse isotropy

Table 4.1: *Minimal integrity basis for isotropic and transversely isotropic materials, according to Karajan [87].*

$(4.94)_{3,4}$. In case of isotropic material behaviour, the set $\mathcal{L}_S = \{I_{S1}, I_{S2}, I_{S3}\}$ of principal invariants of $\mathbf{C}_S$ (or alternatively of $\mathbf{B}_S$) is used, cf. Appendix B.1. This leads to the following accordances

$$\begin{aligned} I_{S1} &= \operatorname{tr}\mathbf{C}_S\,, \quad I_{S2} = \operatorname{tr}(\operatorname{cof}\mathbf{C}_S)\,, \quad I_{S3} = \det\mathbf{C}_S\,, \\ J_{S1} &= \operatorname{tr}\mathbf{C}_S \quad J_{S2} = \operatorname{tr}(\mathbf{C}_S\,\mathbf{C}_S) \quad J_{S3} = \operatorname{tr}(\mathbf{C}_S\,\mathbf{C}_S\,\mathbf{C}_S) \\ &= I_{S1}\,, \qquad = I_{S1}^2 - 2\,I_{S1}\,, \qquad = I_{S1}^3 - 3\,I_{S1}\,I_{S2} + 3\,I_{S3}\,. \end{aligned} \tag{4.95}$$

Therefore, the solid strain energy can be formulated via the set of principal invariants $\mathcal{L}_S$ for the purely isotropic case, viz.:

$$W_{\text{iso}}^S(\mathbf{C}_S) \quad \rightarrow \quad W_{\text{iso}}^S(I_{S1}, I_{S2}, I_{S3})\,. \tag{4.96}$$

Furthermore, in terms of a further transversely isotropic consideration, the mixed invariants J_{S4} and J_{S5} are included, viz.:

$$\begin{aligned} J_{S4} &= \operatorname{tr}(\boldsymbol{\mathcal{M}}_a^S\,\mathbf{C}_S) = \mathbf{a}_0^S \cdot \mathbf{C}_S\,\mathbf{a}_0^S = \mathbf{F}_S\,\mathbf{a}_0^S \cdot \mathbf{F}_S\,\mathbf{a}_0^S = \mathbf{a}^S \cdot \mathbf{a}^S\,, \\ J_{S5} &= \operatorname{tr}(\boldsymbol{\mathcal{M}}_a^S\,\mathbf{C}_S^2) = \mathbf{a}_0^S \cdot \mathbf{C}_S^2\,\mathbf{a}_0^S = \mathbf{C}_S\,\mathbf{a}_0^S \cdot \mathbf{C}_S\,\mathbf{a}_0^S = \mathbf{F}_S^T\,\mathbf{a}^S \cdot \mathbf{F}_S^T\,\mathbf{a}^S\,. \end{aligned} \tag{4.97}$$

Therein, J_{S4} represents the squared fibre stretch in the direction of the mapped fibre direction $\mathbf{a}^S = \mathbf{F}_S\,\mathbf{a}_0^S$ within the actual configuration. In contrast, J_{S5} owns no direct physical interpretation but enables the inclusion of strain-energy effects of a fibre-matrix interaction. However, in this monograph, the nerve fibres of the brain are assumed to be neither capable of carrying compressive nor shear loads. Therefore, the corresponding strain energy depends only on the mixed invariant J_{S4} and the dependence on the mixed invariant J_{S5} is omitted.

This procedure consequently results in scalar-valued (and thus invariant) arguments of the so-called canonical solid's strain energy

$$W^S(\mathbf{C}_S, \boldsymbol{\mathcal{M}}_a^S) \quad \rightarrow \quad W^S(I_{S1}, I_{S2}, I_{S3}, J_{S4}) = W_{\text{iso}}^S(I_{S1}, I_{S2}, I_{S3}) + W_{\text{aniso}}^S(J_{S4})\,. \tag{4.98}$$

Therefore, the restriction claimed by (4.92) is always fulfilled a priori. In conclusion, the solid strain energy is additively split[15] into an isotropic W_{iso}^S and an anisotropic W_{aniso}^S part. Consequently, this also results in a split of the solid extra stress $\mathbf{T}_E^S$, which is derived within the concept of hyperelasticity from the evaluation of the principle of dissipation (4.55) by means of the solid strain energy (4.96) via

$$\begin{aligned} \mathbf{T}_E^S &= 2\,J_S^{-1}\,\mathbf{F}_S\,\frac{\partial W^S}{\partial \mathbf{C}_S}\,\mathbf{F}_S^T\,, \\ &\text{with} \quad J_S = \frac{\rho_{0S}^S}{\rho^S} = \det\mathbf{F}_S = (\det\mathbf{C}_S)^{\frac{1}{2}} = \sqrt{I_{S3}}\,. \end{aligned} \tag{4.99}$$

[15]Note that within a finite theory independent energies can be summed up but it is, in general, not admissible to apply the superposition theorem. However, it represents a meaningful and commonly used assumption, cf. Karajan [87] or Markert [105].

Note in passing that the solid Jacobian J_S is directly related to the basic invariant I_{S3}. In particular, this allows the determination of the solid's extra stress through postulating appropriate constitutive assumptions of the solid strain energy W^S in (4.98), i. e., for its isotropic and anisotropic contributions, as it is derived in the following.

Isotropic contribution: The isotropic strain energy W^S_{iso} of the solid skeleton describes the basic ground-elasticity of the tissue matrix using a Neo-Hookean approach, viz.:

$$\begin{aligned} W^S_{\text{iso}} &= \tfrac{1}{2}\,\mu^S_0\,(I_{S1} - 3) - \mu^S_0 \ln\sqrt{I_{S3}} + U^S_0\,, \\ &\text{where} \quad U^S_0 = \lambda^S_0\,(1 - n^S_{0S})^2 \left(\frac{J_S - 1}{1 - n^S_{0S}} - \ln\frac{J_S - n^S_{0S}}{1 - n^S_{0S}}\right). \end{aligned} \tag{4.100}$$

Therein, the volumetric extension term U^S_0 provides the consideration of the so-called compaction point[16] in case of an extensive compression state, cf. Ehlers & Eipper [52]. The parameters μ^S_0 and λ^S_0 denote the first and the second Lamé constants. Based on the constitutive choice (4.100), the extra part

$$\mathbf{T}^S_{E,\,\text{iso}} = 2\,\frac{\mu^S_0}{J_S}\,\mathbf{K}_S + \lambda^S_0\,(1 - n^S_{0S})^2 \Big(\frac{1}{1 - n^S_{0S}} - \frac{1}{J_S - n^S_{0S}}\Big)\,\mathbf{I} \tag{4.101}$$

of the solid's isotropic stress contribution is consequently derived from $(4.99)_1$ by using $(A.10)_{2,4}$ and (3.43).

Anisotropic contribution: According to the previous argumentation, the anisotropic strain energy W^S_{aniso} of the solid skeleton depends on the mixed principal invariant J_{S4} and accounts for the fibre reinforcement of the considered nervous brain tissue, viz.:

$$W^S_{\text{aniso}} = \frac{\tilde{\mu}^S_1}{\tilde{\gamma}^S_1}\,(J^{\tilde{\gamma}^S_1/2}_{S4} - 1) - \tilde{\mu}^S_1 \ln (J_{S4})^{\frac{1}{2}}\,. \tag{4.102}$$

In this regard, the anisotropic strain energy is formulated for the transversely isotropic case including one involved fibre family, cf. Karajan [87] and Markert *et al.* [107]. Therein, the fibre stiffness is governed by the material parameters $\tilde{\mu}^S_1$ and $\tilde{\gamma}^S_1$. Regarding the requirements for strain-energy functions, i. e., polyconvex conditions, $J_{S4} \geq 1$ has to be fulfilled. This restriction underlines the idea that the nerve-fibre reinforcement can only withstand tensile forces, while compressive forces are not supported. Therefore, the tension-compression non-linearity is included via the case differentiation

$$W^S_{\text{aniso}} = \begin{cases} 0 & , \text{for } J_{S4} < 1 \\ W^S_{\text{aniso}}(J_{S4}) \text{ from } (4.102)\,, & \text{for } J_{S4} \geq 1\,. \end{cases} \tag{4.103}$$

In particular, this represents a bimodal behaviour of the considered brain tissue in tension and compression, as was claimed (for brain-tissue of pigs) by Miller & Chinzei [113]. Finally, the extra-part of the anisotropic solid stress contribution is derived analogously to the derivation of (4.101) from $(4.99)_1$ evaluated with (4.102), yielding

$$\mathbf{T}^S_{E,\,\text{aniso}} = \frac{\tilde{\mu}^S_1}{J_S\,(\mathbf{a}^S \cdot \mathbf{a}^S)} \Big((\mathbf{a}^S \cdot \mathbf{a}^S)^{\tilde{\gamma}^S_1/2} - 1\Big)(\mathbf{a}^S \otimes \mathbf{a}^S)\,. \tag{4.104}$$

[16] The compaction point is reached if all pores are completely compressed within a porous material as a result of a deformation process.

Based on the previous investigations, the extra-stress $\mathbf{T}_E^S$ of the solid skeleton is constituted by an isotropic part $\mathbf{T}_{E,\mathrm{iso}}^S$ and an anisotropic (transversely isotropic) part $\mathbf{T}_{E,\mathrm{aniso}}^S$, viz.:

$$\mathbf{T}_E^S \;=\; \mathbf{T}_{E,\mathrm{iso}}^S + \mathbf{T}_{E,\mathrm{aniso}}^S \,. \tag{4.105}$$

In conclusion, a finite anisotropic material model is chosen, since the soft brain tissue can be generally subjected to large deformations, e. g., in the case of hydrocephalus. Note in passing that the modelling of soft tissues using a standard biphasic theory is sometimes criticised. In this regard, Miller [110] reminds the reader that using a non-dissipative (hyperelastic) solid phase is not capable of properly describing the dependence of the loading velocity and the tissue's response, i. e., a strong stress-strain-rate dependence. However, if the considered strain rates are nearly zero, as it is the case for the considered drug-infusion process, the application of a hyperelastic TPM model is absolutely reasonable. Therefore, it is mostly even sufficient to confine the model to small deformations within a linear theory. Nevertheless, the presented tissue model can be extended to finite viscoelasticity straightforwardly, cf. Markert [105], if required for a certain application.

4.6 The closure problem of the fully coupled model

In order to conclude and summarise Chapter 4, this section discusses the so-called closure problem of continuum-mechanics for the constitutive modelling of the fully coupled quaternary TPM model. In this regard, it is possible to proceed from eight materially independent balance equations of mass and momentum for the four considered constituents, collected in Figure 4.2 (top position, coloured in purple). Based on this availabe set of equations, four so-called governing equations are selected (cf. Figure 4.2, bottom left position, coloured in red). In particular, these are the momentum balance (4.24) of the overall aggregate φ, the volume balance (4.19) of φ^B, the volume balance (4.18) of the overall interstitial fluid φ^I and the concentration balance (4.15) of the therapeutic solute φ^D (serially numbered from one to four in Figure 4.2). These equations are adopted in Section 4.2 using the constitutive assumptions. With regard to the corresponding numerical solution derived in Chapter 5, this coupled system is governed by the primary variables $\mathbf{u}_S$, p^{IR}, p^{BR} and c_m^D. Generally, $\mathbf{u}_S$ corresponds to the overall momentum balance, whereas the effective pore pressures p^{IR} and p^{BR} belong to the volume balances of φ^I and φ^B, respectively. Finally, the molar concentration c_m^D is related to the concentration balance of the therapeutic agent. In a next step, the four remaining particular balance relations are combined with appropriate constitutive assumptions (cf. Figure 4.2, middle left position, coloured in brown). Thereby, the restrictions obtained from the evaluation process of the entropy inequality (cf. Figure 4.2, middle right position, coloured in green) need to be rigorously accounted in order to obtain thermodynamical consistency. This allows for the determination of the so-called secondary variables (cf. Figure 4.2, bottom right position, coloured in blue) required in the governing equations. Using essentially the kinematical relations (cd. Figure 4.2, upper middle left position, coloured in pink), it is finally possible to assign all included quantities of the quaternary model, cf. Figure 4.2. Hence, it is easily concluded that the overall system of equations is self-contained

(closed) and can be solved via a numerical solution strategy, as it is described in the next chapter.

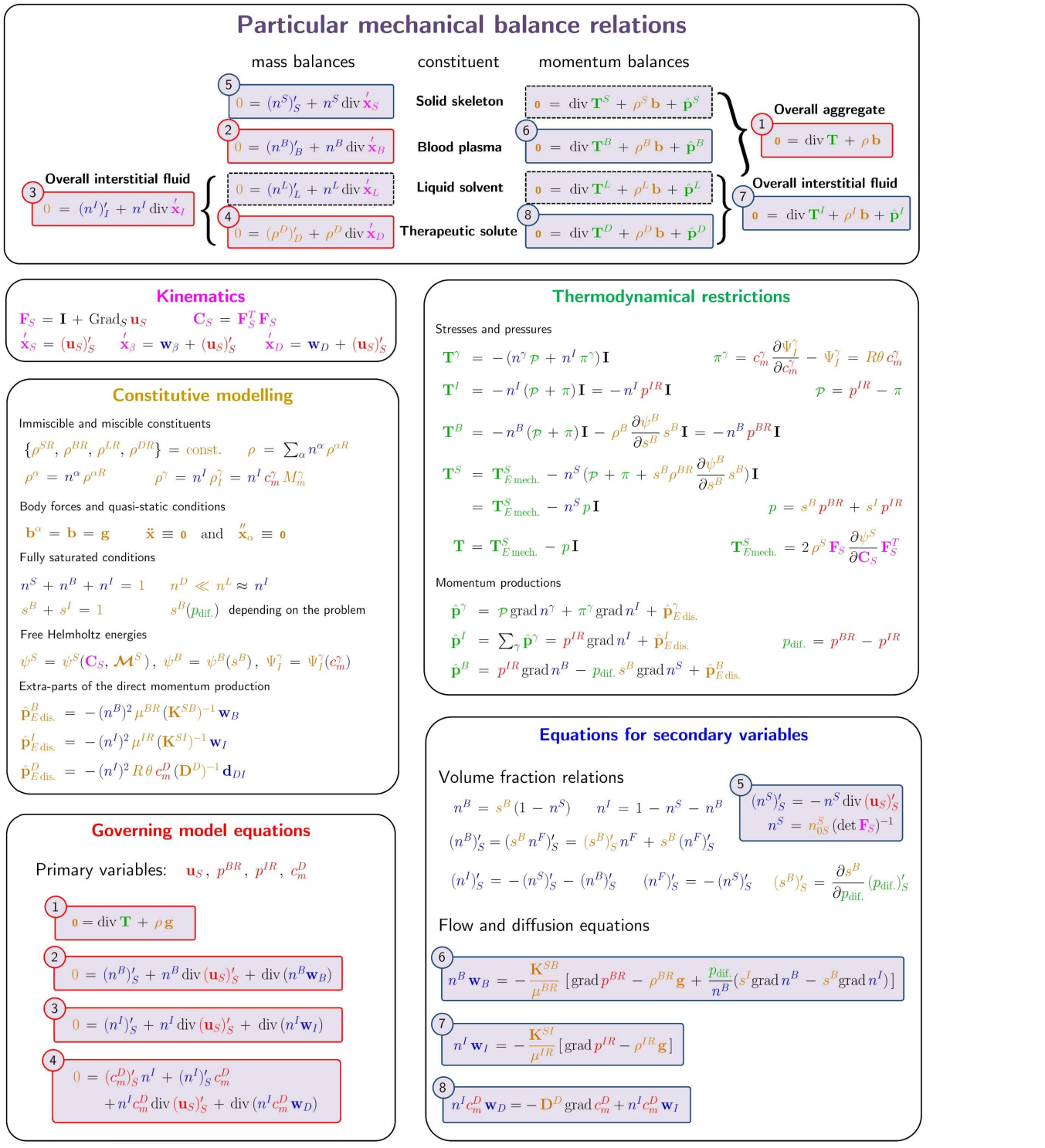

Figure 4.2: *The closure problem of the fully coupled quaternary TPM model.*

Chapter 5:
Numerical treatment

This chapter comprises the numerical treatment of the multicomponental brain-tissue model discussed in the previous chapter. For the numerical realisation of this model, the well-known finite-element method (FEM) is chosen as a suitable numerical methodology to approximate the solution of coupled partial differential equations (PDE). Therefore, the necessary weak formulations of the governing balance relations are presented, followed by the discretisation procedures in space and time, which are required for the numerical solution of the considered problem.

Basically, the FEM is established as a commonly used calculation method in all fields of engineering and provides somehow a standard solution procedure for solid mechanics. Accordingly, a broad variety of publications can be found in this field. For a comprehensive overview, the reader is referred to, e. g., the textbooks of Bathe [14], Braess [29], Schwarz [143] or Zienkiewicz & Taylor [173].

The treatment of multiphasic problems within the framework of the FEM is based on a continuously enhanced treatment at the Institute of Applied Mechanics (Chair of Continuum Mechanics) at the University of Stuttgart. In this regard, fundamental works for the numerical accessibility of porous media were subsequently investigated by Ellsiepen [63], Eipper [62] and Ammann [7]. Lateron, Acartürk [3] extended the basic formulations for the inclusion of real chemical mixtures. Concerning advanced visco-elastic material modelling at large strains, the reader is referred to the works of Markert [105] and Karajan [87]. Furthermore, Graf [70] and Avci [10] implemented the specific characteristics of elasto-plastic material behaviour of the solid skeleton and Rempler [129] enriched the field-describing quantities in terms of the so-called extended finite-element method (XFEM) in order to model evolving discontinuities, such as cracks.

5.1 Foundations of the finite-element method

Initial-boundary-value problem (IBVP): As stated in Chapter 4, the set of primary variables is given as follows:

$$\mathbf{u}_S\,,\ p^{BR}\,,\ p^{IR} \text{ and } c_m^D\,. \tag{5.1}$$

For each governing equation, so-called Neumann (natural) and Dirichlet (essential) boundary conditions need to be defined. Therefore, the boundary $\Gamma = \partial\Omega$ (surface of the body) is split for each of the four governing equations and related to the primary variables. The Dirichlet boundary Γ_D directly corresponds to the primary variables $\mathbf{u}_S$, p^{BR}, p^{IR} and c_m^D with essential boundary conditions. Whereas, the Neumann boundary Γ_N contains the natural boundary conditions. The restrictions, illustrated in Figure 5.1 state that Dirichlet and Neumann boundary conditions are mutually exclusive, i. e., they cannot be defined simultaneously for one specific primary variable. In contrast to this, overlapping

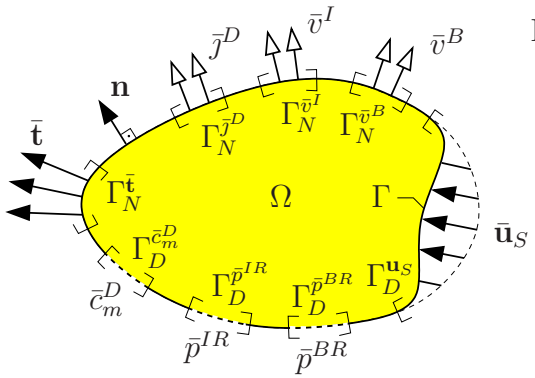

Restrictions for the boundary conditions:

$$\Gamma_S = \Gamma_D^{\mathbf{u}_S} \cup \Gamma_N^{\bar{\mathbf{t}}}, \quad \Gamma_B = \Gamma_D^{p^{BR}} \cup \Gamma_N^{\bar{v}^B},$$
$$\Gamma_I = \Gamma_D^{p^{IR}} \cup \Gamma_N^{\bar{v}^I}, \quad \Gamma_D = \Gamma_D^{c_m^D} \cup \Gamma_N^{\bar{j}^D},$$
$$\emptyset = \Gamma_D^{\mathbf{u}_S} \cap \Gamma_N^{\bar{\mathbf{t}}}, \quad \emptyset = \Gamma_D^{p^{BR}} \cap \Gamma_N^{\bar{v}^B},$$
$$\emptyset = \Gamma_D^{p^{IR}} \cap \Gamma_N^{\bar{v}^I}, \quad \emptyset = \Gamma_D^{c_m^D} \cap \Gamma_N^{\bar{j}^D}.$$

Figure 5.1: *Observed domain Ω and applied boundary conditions.*

boundary conditions between the primary variables are possible.

Ansatz and test functions: The ansatz (trial) functions of the primary variables in (5.1) with their corresponding Sobolev[1] spaces $\mathcal{H}^1(\Omega)$ are defined via

$$\begin{aligned}
\mathcal{A}^{\mathbf{u}_S}(t) &:= \{\ \mathbf{u}_S \in \mathcal{H}^1(\Omega)^d \ :\ \mathbf{u}_S(\mathbf{x}) = \bar{\mathbf{u}}_S(\mathbf{x},t) \ \text{ on } \Gamma_D^{\mathbf{u}_S}\ \}, \\
\mathcal{A}^{p^{BR}}(t) &:= \{\ p^{BR} \in \mathcal{H}^1(\Omega) \ :\ p^{BR}(\mathbf{x}) = \bar{p}^{BR}(\mathbf{x},t) \text{ on } \Gamma_D^{p^{BR}}\ \}, \\
\mathcal{A}^{p^{IR}}(t) &:= \{\ p^{IR} \in \mathcal{H}^1(\Omega) \ :\ p^{IR}(\mathbf{x}) = \bar{p}^{IR}(\mathbf{x},t) \text{ on } \Gamma_D^{p^{IR}}\ \}, \\
\mathcal{A}^{c_m^D}(t) &:= \{\ c_m^D \in \mathcal{H}^1(\Omega) \ :\ c_m^D(\mathbf{x}) = \bar{c}_m^D(\mathbf{x},t) \ \text{ on } \Gamma_D^{c_m^D}\ \}.
\end{aligned} \tag{5.2}$$

In $(5.2)_1$ the superscript $d \in \{1,2,3\}$ denotes the dimension of the problem. In general, $d = 3$ is choosen, relating to the 3-d space of real physical problems. The ansatz functions are restricted to result their Dirichlet values at the boundary. In addition, the test functions are defined, viz.:

$$\begin{aligned}
\mathcal{T}^{\mathbf{u}_S} &:= \{\ \delta\mathbf{u}_S \in \mathcal{H}^1(\Omega)^d \ :\ \delta\mathbf{u}_S(\mathbf{x}) = \mathbf{0} \text{ on } \Gamma_D^{\mathbf{u}_S}\ \}, \\
\mathcal{T}^{p^{BR}} &:= \{\ \delta p^{BR} \in \mathcal{H}^1(\Omega) \ :\ \delta p^{BR}(\mathbf{x}) = 0 \text{ on } \Gamma_D^{p^{BR}}\ \}, \\
\mathcal{T}^{p^{IR}} &:= \{\ \delta p^{IR} \in \mathcal{H}^1(\Omega) \ :\ \delta p^{IR}(\mathbf{x}) = 0 \text{ on } \Gamma_D^{p^{IR}}\ \}, \\
\mathcal{T}^{c_m^D} &:= \{\ \delta c_m^D \in \mathcal{H}^1(\Omega) \ :\ \delta c_m^D(\mathbf{x}) = 0 \text{ on } \Gamma_D^{c_m^D}\ \}.
\end{aligned} \tag{5.3}$$

5.2 Weak formulations of the governing equations

The local (strong) formulations of the governing balance equations are valid in an absolute sense at each material point $\mathcal{P}$. However, this represents a too restrictive requirement for solving this system of strongly-coupled differential-equations numerically. Therefore, it is essential to transform the strong formulations into so-called weak (integral) formulations

[1]The Sobolev space $\mathcal{H}^1(\Omega)$ corresponds to functions, whose first derivatives are square integrable within the domain Ω, cf., e. g., Bathe [14].

which fulfill the governing equations in an integral (distributed) manner. Following this, the quasi-static formulation of the overall momentum balance (4.24) is weighted by the test function $\delta\mathbf{u}_S$ and integrated over the spatial domain Ω, resulting in

$$\begin{aligned} \mathcal{G}_{\mathbf{u}_S}(\mathbf{u}_S, p^{BR}, p^{IR}, \delta\mathbf{u}_S) \;\equiv\; & \int_{\Omega} \mathbf{T} \cdot \operatorname{grad} \delta\mathbf{u}_S \, \mathrm{d}v \;-\; \int_{\Omega} \rho\, \mathbf{g} \cdot \delta\mathbf{u}_S \, \mathrm{d}v \;- \\ & - \int_{\Gamma_N^{\bar{\mathbf{t}}}} \overline{\mathbf{t}} \cdot \delta\mathbf{u}_S \, \mathrm{d}a \;=\; 0\,. \end{aligned} \tag{5.4}$$

Therein, the Gaußian integral theorem was used in order to transfer the last term in (5.4) to the boundary $\Gamma_N^{\bar{\mathbf{t}}}$ of the overall aggregate. In this regard, the stress vector $\overline{\mathbf{t}} = \mathbf{T}\,\mathbf{n}$ can be explicitly assigned via a Neumann boundary condition. The scalar multiplication of the strong forms of the pore liquid's volume balances (4.18) and (4.19) with their scalar test functions $\delta p^{\beta R}$ yields after the integration over the spatial domain Ω their corresponding weak formulations, viz.:

$$\begin{aligned} \mathcal{G}_{p^{BR}}(\mathbf{u}_S, p^{BR}, p^{IR}, \delta p^{BR}) \;\equiv\; & \int_{\Omega} \left[(n^B)'_S + n^B \operatorname{div} (\mathbf{u}_S)'_S \right] \delta p^{BR} \, \mathrm{d}v \\ & - \int_{\Omega} n^B \mathbf{w}_B \cdot \operatorname{grad} \delta p^{BR} \, \mathrm{d}v \;+\; \int_{\Gamma_N^{\bar{v}^B}} \bar{v}^B \, \delta p^{BR} \, \mathrm{d}a \;=\; 0\,, \\ \mathcal{G}_{p^{IR}}(\mathbf{u}_S, p^{BR}, p^{IR}, \delta p^{IR}) \;\equiv\; & \int_{\Omega} \left[(n^I)'_S + n^I \operatorname{div} (\mathbf{u}_S)'_S \right] \delta p^{IR} \, \mathrm{d}v \\ & - \int_{\Omega} n^I \mathbf{w}_I \cdot \operatorname{grad} \delta p^{IR} \, \mathrm{d}v \;+\; \int_{\Gamma_N^{\bar{v}^I}} \bar{v}^I \, \delta p^{IR} \, \mathrm{d}a \;=\; 0\,. \end{aligned} \tag{5.5}$$

Therein, $\bar{v}^\beta = n^\beta \, \mathbf{w}_\beta \cdot \mathbf{n}$ denotes the volumetric efflux out of the domain. Finally, the resulting weak formulation of (4.15) for the therapeutic component reads

$$\begin{aligned} \mathcal{G}_{c_m^D}(\mathbf{u}_S, p^{BR}, p^{IR}, c_m^D, \delta c_m^D) \;\equiv\; & \int_{\Omega} \left[n^I (c_m^D)'_S + c_m^D \operatorname{div} (\mathbf{u}_S)'_S + c_m^D \operatorname{div} (n^B \mathbf{w}_B) \right] \delta c_m^D \, \mathrm{d}v \;- \\ & - \int_{\Omega} n^I c_m^D \mathbf{w}_D \cdot \operatorname{grad} \delta c_m^D \, \mathrm{d}v \;+\; \int_{\Gamma_{\bar{J}^D}} \bar{J}^D \, \delta c_m^D \, \mathrm{d}a \;=\; 0\,, \end{aligned} \tag{5.6}$$

where $\bar{J}^D = n^I \, c_m^D \, \mathbf{w}_D \cdot \mathbf{n}$ denotes the molar efflux of the therapeutic agent.

5.3 Solution procedure of the coupled problem

5.3.1 Spatial discretisation

Within the framework of the FEM, the spatial discretisation of the continuous domain Ω requires its partition into E non-overlapping finite subdomains Ω_e, the so-called finite

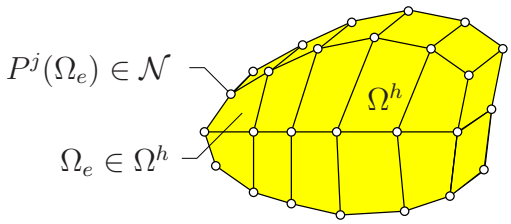

$$\Omega \approx \Omega^h = \bigcup_{e=1}^{E} \Omega_e$$

$$\mathcal{N} = \bigcup_{j=1}^{N} P^j(\Omega_e)$$

Figure 5.2: *Exemplary spatial discretisation of a certain domain.*

elements, as it is exemplarily shown in Figure 5.2. Therein, each finite element Ω_e is build of N_e nodal points, referred to as P^j, which can be mutually interconnected with shared nodes of neighbour elements. This spatial discretisation yields a finite-element mesh with (in total) N nodes, which approximates the discretised spatial domain Ω^h. Finally, $\mathcal{N}$ denotes the set of all nodes.

Mixed finite-element approach: Up to now, the weak formulations of the governing equations (5.4) - (5.6) are defined continuously in the infinite-dimensional spaces of the ansatz and test functions. For the purposes of this monograph, the procedure is discussed for the chosen displacement-pressure-pressure-concentration ($\mathbf{u}_S$ - p^{BR} - p^{IR} - c_m^D) formulation, cf. (5.1). In order to approximate these formulations on a mesh with N nodal points, the following discrete ansatz

$$\begin{aligned}
\mathbf{u}_S(\mathbf{x},t) &\approx \mathbf{u}_S^h(\mathbf{x},t) &&= \bar{\mathbf{u}}_S^h(\mathbf{x},t) &&+ \sum_{j=1}^{N} \boldsymbol{\phi}^j_{\mathbf{u}_S}(\mathbf{x})\, \mathbf{u}_S^j(t) && \in \mathcal{A}^{\mathbf{u}_S\, h}(t)\,, \\
p^{BR}(\mathbf{x},t) &\approx p^{BR\,h}(\mathbf{x},t) &&= \bar{p}^{BR\,h}(\mathbf{x},t) &&+ \sum_{j=1}^{N} \phi^j_{p^{BR}}(\mathbf{x})\, p^{BR\,j}(t) && \in \mathcal{A}^{p^{BR}\,h}(t)\,, \\
p^{IR}(\mathbf{x},t) &\approx p^{IR\,h}(\mathbf{x},t) &&= \bar{p}^{IR\,h}(\mathbf{x},t) &&+ \sum_{j=1}^{N} \phi^j_{p^{IR}}(\mathbf{x})\, p^{IR\,j}(t) && \in \mathcal{A}^{p^{IR}\,h}(t)\,, \\
c_m^D(\mathbf{x},t) &\approx c_m^{D\,h}(\mathbf{x},t) &&= \bar{c}_m^{D\,h}(\mathbf{x},t) &&+ \sum_{j=1}^{N} \phi^j_{c_m^D}(\mathbf{x})\, c_m^{D\,j}(t) && \in \mathcal{A}^{c_m^D\,h}(t)\,,
\end{aligned} \tag{5.7}$$

and the corresponding test functions

$$\begin{aligned}
\delta\mathbf{u}_S(\mathbf{x}) &\approx \delta\mathbf{u}_S^h(\mathbf{x}) &&= \sum_{j=1}^{N} \boldsymbol{\phi}^j_{\mathbf{u}_S}(\mathbf{x})\, \delta\mathbf{u}_S^j && \in \mathcal{T}^{\mathbf{u}_S\, h}\,, \\
\delta p^{BR}(\mathbf{x}) &\approx \delta p^{BR\,h}(\mathbf{x}) &&= \sum_{j=1}^{N} \phi^j_{p^{BR}}(\mathbf{x})\, \delta p^{BR\,j} && \in \mathcal{T}^{p^{BR}\,h}\,, \\
\delta p^{IR}(\mathbf{x}) &\approx \delta p^{IR\,h}(\mathbf{x}) &&= \sum_{j=1}^{N} \phi^j_{p^{IR}}(\mathbf{x})\, \delta p^{IR\,j} && \in \mathcal{T}^{p^{IR}\,h}\,, \\
\delta c_m^D(\mathbf{x}) &\approx \delta c_m^{D\,h}(\mathbf{x}) &&= \sum_{j=1}^{N} \phi^j_{c_m^D}(\mathbf{x})\, \delta c_m^{D\,j} && \in \mathcal{T}^{c_m^D\,h}
\end{aligned} \tag{5.8}$$

are defined. Therein, $\{\mathcal{A}^{\mathbf{u}_S\,h}\,,\mathcal{A}^{p^{BR}\,h}\,,\mathcal{A}^{p^{IR}\,h}\,,\mathcal{A}^{c_m^D\,h}\}$ and $\{\mathcal{T}^{\mathbf{u}_S\,h}\,,\mathcal{T}^{p^{BR}\,h}\,,\mathcal{T}^{p^{IR}\,h}\,,\mathcal{T}^{c_m^D\,h}\}$ are the discretised ansatz and test functions. As stated in (5.7) and (5.8), the same basis functions are used for both the ansatz and the test functions. This standard approach is well-known as the Bubnov-Galerkin method[2] (or simply Galerkin method). Moreover, $\{\bar{\mathbf{u}}_S^h\,,\bar{p}^{BRh}\,,\bar{p}^{IRh}\,,\bar{c}_m^{Dh}\}$ are the Dirichlet boundary conditions and $\{\boldsymbol{\phi}^j_{\mathbf{u}_S}\,,\phi^j_{p^{BR}}\,,\phi^j_{p^{IR}}\,,\phi^j_{c_m^D}\}$ are the global basis functions of the ansatz or test functions. The global basis functions of the solid displacement are understood as $\boldsymbol{\phi}^j_{\mathbf{u}_S} = [\,\phi^j_{u_{S1}},\,\phi^j_{u_{S2}},\,\phi^j_{u_{S3}}\,]^T$ (for the three dimensions). Finally, $\{u^j_{S1},\,u^j_{S2}\,,u^j_{S3}\,,p^{BRj}\,,p^{IRj}\,,c_m^{Dj}\}$ are the (scalar-valued) unknown nodal quantities, the so-called degrees of freedom (DOF) of the system. Each nodal point of the consistent finite-element mesh is assigned to a basis function $\boldsymbol{\phi}^j_{\mathrm{dof}}$ which supports only in finite elements E^* attached to the respective node P^j, cf., e. g., Ammann [7] or Rempler [129]. Thus,

$$\boldsymbol{\phi}^j_{\mathrm{dof}}(\mathbf{x}) \,=\, 0 \qquad \text{if} \quad \mathbf{x} \notin \bigcup_{e\,\in\,E^*} \Omega_e \qquad \text{and} \quad \boldsymbol{\phi}^j_{\mathrm{dof}}(\mathbf{x}_i) \,=\, \delta^j_i\,. \tag{5.9}$$

The consideration above yields so-called sparse matrices and enables an efficient implementation. Moreover, the basis functions $\boldsymbol{\phi}^j_{\mathrm{dof}}$ in (5.9) are normalised via the Kronecker symbol (for $\{i,j\} = 1,\,\ldots\,,N$), which gives the value 1 for $i = j$ and the value 0 otherwise. This guarantees at every nodal position $\mathbf{x}_i$ that the nodal quantities correspond exactly to the value of the approximated solution (except of Dirichlet boundary nodes). Recalling (5.4) - (5.6), the spatially discretised (variational) problem is formulated via

$$\text{Find} \left\{ \begin{array}{llll} \mathbf{u}_S^h & \in \mathcal{A}^{\mathbf{u}_S\,h} & \forall\,\delta\mathbf{u}_S^h & \in \mathcal{T}^{\mathbf{u}_S\,h} \\ p^{BR\,h} & \in \mathcal{A}^{p^{BR}\,h} & \forall\,\delta p^{BR\,h} & \in \mathcal{T}^{p^{BR}\,h} \\ p^{IR\,h} & \in \mathcal{A}^{p^{IR}\,h} & \forall\,\delta p^{IR\,h} & \in \mathcal{T}^{p^{IR}\,h} \\ c_m^{D\,h} & \in \mathcal{A}^{c_m^D\,h} & \forall\,\delta c_m^{D\,h} & \in \mathcal{T}^{c_m^D\,h} \end{array} \right\} \text{ such that } \left\{ \begin{array}{lll} \mathcal{G}^h_{\mathbf{u}_S} &=& \mathbf{0} \\ \mathcal{G}^h_{p^{BR}} &=& 0 \\ \mathcal{G}^h_{p^{IR}} &=& 0 \\ \mathcal{G}^h_{c_m^D} &=& 0 \end{array} \right\} \tag{5.10}$$

for a given set of Neumann boundary conditions at any time $t \in [\,0\,,T\,]$. Therein, an important property of the discrete test functions is the so-called Partition-of-Unity principle (PU), which ensures a proper bridge from local towards global quantities. In particular, this yields a system of linearly independent equations by setting one discrete test function to unity, while the remaining ones are set to zero.

Within this spatial discretisation of the considered strongly-coupled problem, the approximation of all primary variables (DOF) is investigated simultaneously in order to solve the problem straightforward in a monolithic manner. In general, it is also possible to solve this system of equations in a decoupled manner by applying a customised operator-splitting scheme, cf., e. g., Markert *et al.* [108]. However, the underlying physical properties of the considered problem, i. e., the values of the included material parameters, justify the application of a standard Galerkin procedure based on the same ansatz functions for both the field and the test functions. The main difficulty in the arising mixed formulation is

[2] In contrary, choosing different basis functions for the ansatz and the test functions is known as Petrov-Galerkin method. This somehow more general approach is often found in the context of numerical stabilisation techniques, cf. Ehlers *et al.* [54].

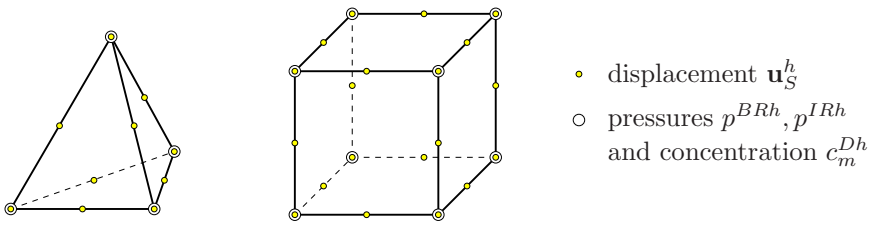

Figure 5.3: *Extended tetrahedral and hexahedral (3-d) Taylor-Hood elements.*

to find proper ansatz functions[3]. For the purposes of the derived choice, the argumentation follows the considerations made by Acartürk [3]. Looking at the governing overall momentum balance (4.24), the overall stress is constituted by the mechanical extra stress tensor of the solid skeleton, cf. (4.105), and the pore pressures of the liquids, cf. (4.73). The mechanical extra-stress tensor of the solid skeleton itself is obtained by the derivative of the solid displacement, through its dependence on the solid deformation gradient, cf. $(3.44)_1$. Since the divergence operator needs to be computed from the overall stress, equal order approximations are obtained for quadratic shape functions for the approximation of the solid displacement $\mathbf{u}_S$ and linear shape functions for the approximation of the pore-liquid pressures p^{IR} and p^{BR} as well as for the concentration c_m^D of the therapeutical agent. This type of elements is commonly denoted as extended Taylor-Hood type and exemplarily displayed in Figure 5.3 for a 3-d (10-noded) tetrahedron (left) and a (20-noded) hexahedron (right).

Geometry transformation and numerical integration: All essential quantities are evaluated locally on element level and assembled to the global system of equations, afterwards. Within this element-wise formulation, the necessary ansatz and test functions are always expressed with respect to a so-called reference element, which directly leads to the introduction of the geometry transformation and local coordinates $\boldsymbol{\xi}$, cf. Figure 5.4. Starting from an invariant reference element Ω_e^ξ described within its local coordinates $\boldsymbol{\xi}$,

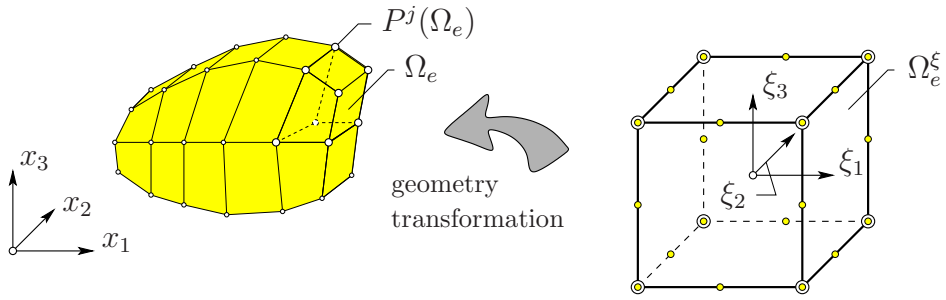

Figure 5.4: *Sketch of the geometry transformation for a reference (hexahedral) element Ω_e^ξ described within local coordinates $\boldsymbol{\xi}$.*

[3]In order to ensure the stability of the numerical solution, the chosen ansatz functions have to fulfil the so-called inf-sup condition (Ladyshenskaya-Babuška-Brezzi (LBB) condition). As far as the author is aware, this is not mathematically proven for the elements given in Figure 5.3 and the LBB-proof is only derived for the original (2-d) displacement-pressure (quadratic-linear) Taylor-Hood element with a middle node, cf. Hughes [80], so far. Nevertheless, the usage of the elements in Figure 5.3 shows satisfactory results. The reader, who is interested in the mathematical background is referred to the works of Brezzi & Fortin [31] and Hughes [80].

a relation to the physical (global) coordinates $\mathbf{x}$ is established via

$$\mathbf{x}(\boldsymbol{\xi}) \;=\; \sum_{j=1}^{N_e} \boldsymbol{\phi}^j_{\mathrm{geo}}(\boldsymbol{\xi})\, \mathbf{x}_j \;=\; \sum_{j=1}^{N_e} \boldsymbol{\phi}^j(\boldsymbol{\xi})\, \mathbf{x}_j \,. \tag{5.11}$$

Therein, $\mathbf{x}(\boldsymbol{\xi})$ describes an arbitrary position within an element depending on the local coordinates $\boldsymbol{\xi}$. Moreover, $\boldsymbol{\phi}^j_{\mathrm{geo}}(\boldsymbol{\xi})$ are the basis functions of the geometry transformation. In the present case, the mapping is investigated isoparametrically, yielding $\boldsymbol{\phi}^j_{\mathrm{geo}} = \boldsymbol{\phi}^j$. Furthermore, the quantities $\mathbf{x}_j$ given in (5.11) are the global (physical) coordinates of the nodal points in the finite element.

The weak formulations (5.4) - (5.6), which are the basis for the finite-element calculation, are expressed in an integral form. For the element-wise evaluation of these formulations, all integrals can be reformulated with respect to the local coordinates using the substitution rule

$$\int_{\Omega_e} f(\mathbf{x})\, \mathrm{d}v \;=\; \int_{\Omega_e^\xi} f(\mathbf{x}(\boldsymbol{\xi}))\, \bar{J}(\boldsymbol{\xi})\, \mathrm{d}v_\xi \qquad \text{with} \quad \bar{J}(\boldsymbol{\xi}) \;=\; \det\left(\frac{\mathrm{d}\mathbf{x}(\boldsymbol{\xi})}{\mathrm{d}\boldsymbol{\xi}}\right) . \tag{5.12}$$

Therein, $\mathrm{d}v_\xi$ is the incremental volume element of the reference element and $\bar{J}$ is the Jacobian determinant of the reference element. Finally, the numerical integration is obtained by the Gaußian quadrature scheme, viz.:

$$\int_{\Omega_e} f(\mathbf{x})\, \mathrm{d}v \;=\; \sum_{k=1}^{K_G} f(\mathbf{x}(\boldsymbol{\xi}_k))\, \bar{J}(\boldsymbol{\xi}_k)\, w_k \,. \tag{5.13}$$

Therein, the integration is substituted by a summation using the evaluation at the integration points K_G at fixed local positions $\boldsymbol{\xi}_k$ and its corresponding quadrature weights w_k. Note in passing that a suitable choice of the integration order is required for the accuracy of the solution.

5.3.2 Temporal discretisation and monolithic solution

Due to the spatial discretisation of the continuous weak formulations derived in the previous Section 5.3.1, the so-called semi-discrete system can be formulated in an abstract manner. Therefore, the only appearing material time derivative with respect to the deforming solid skeleton $(\,\cdot\,)'_S$ is expressed for convenience via $(\,\cdot\,)'$. This yields

$$\boldsymbol{\mathcal{F}}(t, \boldsymbol{y}, \boldsymbol{y}') \;=\; [\, \boldsymbol{\mathcal{D}}\, \boldsymbol{y}' \,+\, \boldsymbol{k}(\boldsymbol{y}) \,-\, \boldsymbol{f}\,] \;\stackrel{!}{=}\; \mathbf{0} \,. \tag{5.14}$$

Therein, all degrees of freedom of the system, namely the N nodal unknowns of each primary variable, are gathered in the abstract vector

$$\boldsymbol{y} \;=\; \left[\, (\, \mathbf{u}_S^1,\, p^{IR,\,1},\, p^{BR,\,1},\, c_m^{D,\,1}\,) \,,\; \ldots \,,\; (\, \mathbf{u}_S^N,\, p^{IR,\,N},\, p^{BR,\,N},\, c_m^{D,\,N}\,) \,\right]^T . \tag{5.15}$$

Note that in (5.15), the vectorial quantity $\mathbf{u}_S$ owns three elements, one for each spatial direction. The global system of equations (5.14) includes the generalised damping matrix

$\boldsymbol{\mathcal{D}}$, the generalised stiffness vector[4] $\boldsymbol{k}(\boldsymbol{y})$ and the generalised force vector $\boldsymbol{f}$ consisting of the Neumann boundary conditions. However, this semi-discrete system needs to be further discretised in the time domain. For the purpose of this thesis, a very compact introduction of this issue is chosen. Beyond that, the interested reader is referred to the detailed discussion of temporal discretisation methods within a coupled solution procedure by, e. g., Ellsiepen [63], Ammann [7] or Rempler [129].

Concerning the solution of (5.14), a so-called single-step method is preferred, where the numerical solution only depends on the previous time-step. Proceeding this idea further, the implicit Euler time-integration method is chosen from the general class of Runge-Kutta methods, suitable for index-1 systems of differential-algebraic equations (DAE). Within this method, the temporal discretisation of the unknowns $\boldsymbol{y}$ is based on the (backward) Taylor-series expansion, evaluated at the current time t_{n+1}, viz.:

$$\boldsymbol{y}_n \;=\; \boldsymbol{y}_{n+1} \;-\; h_n\, \boldsymbol{y}'_{n+1} \quad \longrightarrow \quad \boldsymbol{y}'_{n+1} \;=\; \frac{1}{h_n}\,\left(\boldsymbol{y}_{n+1} \;-\; \boldsymbol{y}_n\right) . \tag{5.16}$$

Therein, the most basic approximation is chosen, considering only the first series-expansion term and neglecting the remainder (higher-order terms). Furthermore, the introduced quantity $h_n \;=\; t_{n+1} \;-\; t_n \;>\; 0$ denotes the actual time-step, while the time t_n serves as the old (previous) time-step, respectively. This implicit and unconditionally stable (cf., e. g., Ehlers *et al.* [61]) time-integration strategy (5.16) is then applied to the basic set of differential-algebraic equations (5.14), yielding

$$\boldsymbol{\mathcal{F}}_{n+1}(t_{n+1}, \boldsymbol{y}_{n+1}, \boldsymbol{y}'_{n+1}(\boldsymbol{y}_{n+1})) \;=\; \left[\boldsymbol{\mathcal{D}}(\boldsymbol{y}_{n+1})\boldsymbol{y}'_{n+1} \;+\; \boldsymbol{k}(\boldsymbol{y}_{n+1}) \;-\; \boldsymbol{f}_{n+1}\right] \stackrel{!}{=} \boldsymbol{0} . \tag{5.17}$$

The resulting set of nonlinear equations (5.17) is solved with a Newton-iteration scheme at each time-integration step. Therefore, the required residual tangent

$$\mathrm{D}\boldsymbol{\mathcal{F}}^k_{n+1} \;:=\; \frac{\mathrm{d}\boldsymbol{\mathcal{F}}^k_{n+1}}{\mathrm{d}\boldsymbol{y}^k_{n+1}} \;=\; \frac{\partial \boldsymbol{\mathcal{F}}^k_{n+1}}{\partial \boldsymbol{y}^k_{n+1}} \;+\; \frac{1}{h_n}\,\frac{\partial \boldsymbol{\mathcal{F}}^k_{n+1}}{\partial (\boldsymbol{y}')^k_{n+1}} \tag{5.18}$$

of the system is computed numerically in this monograph, based on a central difference quotient. The main benefit of a numerical computation of the residual tangent (also known as the so-called Jacobian matrix) is found in its rather simple numerical implementation. However, using a numerical tangent may lead to instable numerical solutions in ranges close to the compaction point. In this regard, an analytical tangent could avoid numerical instabilities when required. Due to the knowledge of the global residual tangent $\mathrm{D}\boldsymbol{\mathcal{F}}^k_{n+1}$, the vector $\Delta\boldsymbol{y}^k_{n+1}$ of stage increments at the current Newton iteration step k can be solved via the linear system of equations

$$\mathrm{D}\boldsymbol{\mathcal{F}}^k_{n+1}\,\Delta\boldsymbol{y}^k_{n+1} \;=\; -\,\boldsymbol{\mathcal{F}}^k_{n+1} . \tag{5.19}$$

In particular, this can be achieved by direct or iterative solvers, cf., e. g., Ellsiepen [63]. Finally, the solution vector $\boldsymbol{y}^{k+1}_{n+1}$ is updated, and the procedure is repeated via the next

[4] Due to the nonlinear dependencies in $\boldsymbol{y}$, the generalised stiffness matrix $\boldsymbol{K}$ is obtained after a linearisation of the generalised stiffness vector $\boldsymbol{k}$. Afterwards, the matrix $\boldsymbol{K}$ exhibits a similar structure like the matrix $\boldsymbol{\mathcal{D}}$, but contains the particular blocks $\mathbf{K}_{ij} \;=\; \partial \boldsymbol{k}_i / \partial \boldsymbol{y}_j$.

Newton step, until the norm of the residuum is less than a certain pre-defined tolerance $\varepsilon_{\text{tol.}}$, viz.:

$$\boldsymbol{y}_{n+1}^{k+1} = \boldsymbol{y}_{n+1}^{k} + \Delta\boldsymbol{y}_{n+1}^{k}, \quad \text{until} \quad \left\|\boldsymbol{\mathcal{F}}_{n+1}^{k+1}\right\| < \varepsilon_{\text{tol.}}. \tag{5.20}$$

Based on these considerations concerning the numerical implementation, the applicability of the presented brain-tissue model is demonstrated by means of several initial-boundary-value problems (IBVP) discussed in the following Chapter 6.

Chapter 6:
Application to the human brain

This chapter discusses the application of the theoretical model derived in Chapter 4 as well as its numerical implementation investigated in Chapter 5 to the human brain. Therefore, it is necessary that further modelling issues are considered in order to adopt the model to the specific characteristics of the human brain tissue. First, two basic possibilities for the creation of appropriate patient-specific geometries for the simulation of realistic boundary-value problems are discussed. Next, a meaningful estimation of the included material parameters from medical-imaging techniques is the focus of investigations. In this regard, the evaluation of DTI-data is applied in terms of adapting the anisotropic and heterogeneous permeabilities and diffusivities. In a next step, it must be ensured that suitable algorithms are applied to map the obtained regularly structured data to the typically irregularly distributed nodes of the finite-element mesh. In terms of the blood perfusion, MRA-data is used in accordance to the implementations carried out for the inclusion of DTI-data. However, the quantitative determination of various in vivo material parameters is still subject of current research and remains unknown in some respects. Moreover, material parameters are selected based on typical choices in the related literature. In summary, this finally allows to study numerical examples, demonstrating the feasibility of the presented approach. In particular, the basic material behaviour of brain-tissue is studied via the evaluation of a consolidation process of a compressed tissue sample as well as finite-deformation processes in tension and compression applied to the fibre-reinforced soft-tissue material. Afterwards, the invasive extra-vascular delivery of therapeutics (CED) for innovative brain-tumour treatments is evaluated in detail. Tracing back to the previously mentioned lack of generally accepted material parameters, the specific simulation of various effects is accompanied by a numerical sensitivity analysis for the chosen parameters. Finally, further occurring effects influencing the therapeutical spreading within the complex tissue aggregate, such as backflow processes, are discussed.

6.1 Geometrical modelling

Certainly, the creation of a meaningful geometry of the brain represents a challenging task. Consequently, this leads to unavoidable difficulties due to the existing complex shape of the brain, exhibiting countless ridges and folds. In order to face the geometrical reconstruction, two possible ways are exemplarily displayed in this section. The first one focusses on the implementation of a patient-specific geometry, which is particularly required to enable individual case-specific statements for requested clinical applications. In contrary, the second procedure is concerned with the study of the general material behaviour and is, therefore, based on a preliminarily created and non-patient-specific brain.

6.1.1 Patient-specific reconstruction based on medical imaging

Having the clinical application – as a future challenge – in mind, the patient-specific determination of an appropriate geometry represents a crucially required feature. This is caused by the circumstance that various geometrical properties can vary significantly among individual brains. In this regard, image-based methods, which are applied in vivo, are most suited for patient-specific reconstructions. Nevertheless, the quality of the achieved results is always restricted by the provided image resolution and the faultless utilisation of the medical-imaging device. In the following, a possible evaluation sequence to obtain a patient-specific geometry is presented, which is basically applicable to several kinds of underlying image data, cf. Figure 6.1 for a schematic overview.

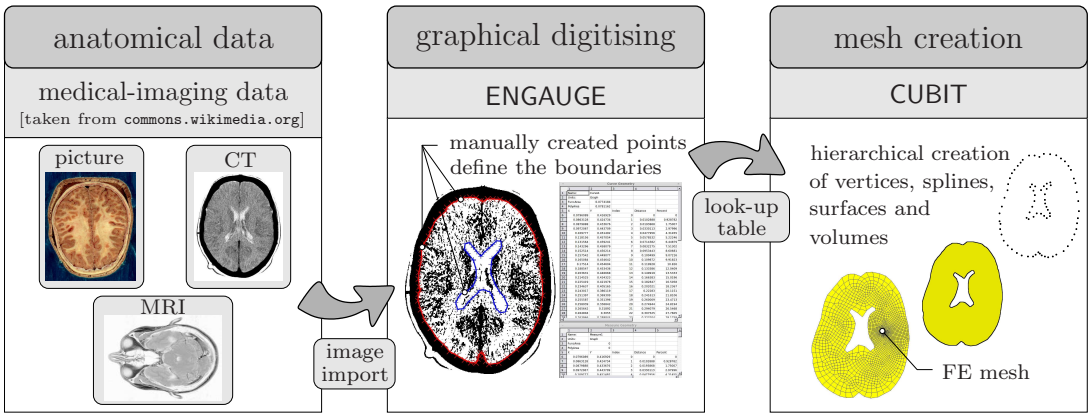

Figure 6.1: *Development of a patient-specific geometry based on medical-imaging data.*

In general, almost any kind of medical-imaging data can be used, where CT- or MRI-data are particularly suited. Proceeding from individual 2-d images, typically acting as slices within the corresponding 3-d image volume data set, the outer boundaries in each image are manually identified and marked by points. In this regard, it is convenient to use, e. g., the open-source software ENGAUGE[1]. Within this tool, a fixed coordinate system can be defined to specify the location of the selected points. Subsequently, the output data of ENGAUGE provides a list of (boundary) points with their actual positions. In order to take the third direction into account, while processing a stack of 2-d image slices, the respective values of the vertical coordinate of the images are determined by their position within the image volume data and manually added to the extracted point list. After this somehow laborious preliminary work[2], the points can be imported into the software toolkit CUBIT[3] as vertices. Therein, the corresponding vertices of each slice, i. e., the

[1]The name "Engauge" is assembled by "en" for "to make" and "gauge" for "to measure", cf. http://digitizer.sourceforge.net .

[2]Alternatively, there are current efforts, cf., e. g., the software ScanIP+FE Module of simpleware® (Simpleware Ltd., UK, cf. http://www.simpleware.com/software/fe-module) for an automatical evaluation of medical-imaging data based on its underlying grey values, i. e., its local X-ray resistance values. Therefore, the data can be segmented by means of a custom algorithm adapted to a certain prescribed limit, including the possibility of data compression and data smoothing. In this regard, a network of self-contained, free and non-penetrating triangular surfaces might provides a convenient meshing possibility without any further manual intervention.

[3]CUBIT (Sandia National Laboratories, Albuquerque, USA) is a geometry and mesh generation toolkit,

ones with the same vertical coordinate, are used to build splines by applying a built-in function of CUBIT. Subsequently, surfaces are generated with their respective boundaries, defined by the splines. To finish the geometry, volumes are lofted between each of these surfaces, and the overall volume is obtained by combining all particular subvolumes. The resulting volume can be further adopted to account for specific clinical issues, such as the placement of an infusion catheter for a scheduled infusion. Finally, CUBIT is used to obtain an appropriate finite-element mesh for the subsequent numerical solution. In this regard, CUBIT offers plenty of possibilities for meshing purposes, including the support to transfer the commonly used tetrahedral and hexahedral elements to the FE solver PANDAS. This is derived via the python-interface "mesh2pandas", cf. [1], developed at the Institute of Applied Mechanics (Chair of Continuum Mechanics) at the University of Stuttgart. The reader who is interested in the successful application of this procedure to a patient-specific geometrical evaluation from detailed microcomputed-tomography (μCT) data for a vertebral body is referred to the works of Bleiler [17] and Wagner *et al.* [166].

6.1.2 Utilisation of standard human brain geometry

Although the inclusion of a patient-specific geometry is generally feasible, as was shown in the previous subsection, it is often sufficient to proceed from a preliminary created geometry of a standard human-brain for the study of the general material behaviour. Therefore, non-patient-specific data is available, e. g., commercially provided by ANATOMIUM[4]. However, there is still need for further preparations of this data, cf. Figure 6.2 for a sketch of a possible processing sequence. Due to several circumstances, a direct meshing

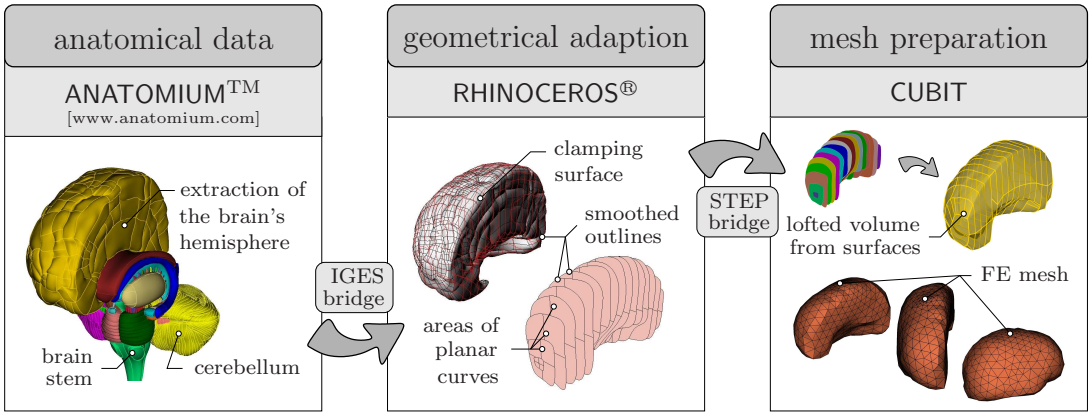

Figure 6.2: *Using a standard brain geometry for an appropriate finite-element mesh.*

is often not possible, i. e., due to redundant parts or surfaces involving intersecting triangles. Therefore, the initial geometry is rather pre-treated with, e. g., the CAD software

cf. http://cubit.sandia.gov.

[4] ANATOMIUM™ (21st Century Solutions Ltd. Media, Gibraltar, UK) provides human physiologically correct 3-d digital anatomy, cf. http://www.anatomium.com.

RHINOCEROS[5] using the IGES[6]-file format. In this regard, the desired body is covered by a clamping surface on which equidistant and closed contour lines (outlines) are individually defined. This provides the possibility for a manually smoothing[7] of the highly irregular cover layer of the brain's cortex, i. e., neglecting the ridges and folds. Afterwards the created areas of planar curves are exported via a STEP[8]-file into CUBIT for an appropriate meshing, in accordance to the considerations made in the previous Subsection 6.1.1. Note in passing that the meshing with tetrahedral elements usually provides a more appropriate spatial discretisation of non-regular 3-d geometries, such as the brain's hemisphere.

6.2 Estimation of material parameters

As a consequence of the enhanced constitutive modelling, a broad variety of simulation parameters is required in order to adopt the material behaviour of the tissue-aggregate constituents. Therefore, several approaches are explored, which provide the possibility to obtain suitable information. In particular, knowledge can be gained from appropriate medical-imaging methods, such as MRI, DTI or MRA. The fundamental principles of these methods were already briefly introduced in Section 2.4. Within this section, the specific utilisation of medical imaging data is rather presented, since these methods promise to contribute to the in-vivo evaluation of patient-specific parameters. In addition, material parameters which cannot be determined using these concepts are chosen according to the related literature on experiments and numerical studies.

6.2.1 Evaluation of diffusion-tensor-imaging data

It is obvious that several tissue properties are strongly characterised by their underlying microscopical architecture. In particular, this is the case in the white-matter tracts of the brain, exhibiting a heterogeneous and anisotropic nature, cf. Section 2.1. In order to estimate these permeability characteristics, Basser *et al.* [12] proposed an initial study on the basis of spin-echo experiments. This made it possible to gain in-vivo knowledge of the microscopical composition and to transfer this information in order to obtain macroscopic quantities. Hence, these quantities consider the underlying microstructure and can be conveniently used in the proposed macroscopical model. In this regard, the second-order permeability tensor $\mathbf{K}_{0S}^{SI}$ of the interstitial fluid in (4.75) and the diffusion tensor $\mathbf{D}_0^D$ of the therapeutic agent in (4.80) are derived based on evaluating patient-specific DTI.

[5] RHINOCEROS® (McNeel North America, Seattle, USA) is a powerful software tool with a large field of application (e. g., design, model or present), cf. http://www.rhino3d.com .

[6] The Initial Graphics Exchange Specification (IGES) is a data-file format, allowing for the digital information exchange among computer-aided design (CAD) systems.

[7] Otherwise, an enormous amount of finite elements is caused by the discretisation of the brain's outer surface, which results in inaccessible numerical costs and is, in particular, not necessary for the issues under consideration in this monograph.

[8] Standard for the Exchange of Product model data (STEP). An "International Organization for Standardization (ISO)" standard for computer-interpretable representation and exchange of geometrical information.

To begin with, the so-called apparent water-diffusion tensor $\mathbf{D}^{\mathrm{n}}_{\mathrm{awd}}$ is obtained at each evaluated voxel n as a result of DTI measurements, cf. Section 2.4. As a required property, these tensors $\mathbf{D}^{\mathrm{n}}_{\mathrm{awd}}$ are symmetric and positive-definite. In general, they can be expressed via

$$\mathbf{D}^{\mathrm{n}}_{\mathrm{awd}} \;=\; D^{\mathrm{n}}_{ik\,\mathrm{awd}}\,(\mathbf{e}_i \otimes \mathbf{e}_k) \;=\; \begin{bmatrix} D^{\mathrm{n}}_{11\,\mathrm{awd}} & D^{\mathrm{n}}_{12\,\mathrm{awd}} & D^{\mathrm{n}}_{13\,\mathrm{awd}} \\ D^{\mathrm{n}}_{21\,\mathrm{awd}} & D^{\mathrm{n}}_{22\,\mathrm{awd}} & D^{\mathrm{n}}_{23\,\mathrm{awd}} \\ D^{\mathrm{n}}_{31\,\mathrm{awd}} & D^{\mathrm{n}}_{32\,\mathrm{awd}} & D^{\mathrm{n}}_{33\,\mathrm{awd}} \end{bmatrix} (\mathbf{e}_i \otimes \mathbf{e}_k)\,. \tag{6.1}$$

For further use, this basic formulation (6.1) of $\mathbf{D}_{\mathrm{awd}}$ is transferred into an alternative representation, given by positive eigenvalues $\gamma^{\mathrm{n}}_{i\,\mathrm{awd}}$ and corresponding eigenvectors $\mathbf{v}^{\mathrm{n}}_i$ via a spectral decomposition procedure, cf. Appendix B.1, viz.:

$$\mathbf{D}^{\mathrm{n}}_{\mathrm{awd}} \;=\; \begin{bmatrix} \gamma^{\mathrm{n}}_{1\,\mathrm{awd}} & 0 & 0 \\ 0 & \gamma^{\mathrm{n}}_{2\,\mathrm{awd}} & 0 \\ 0 & 0 & \gamma^{\mathrm{n}}_{3\,\mathrm{awd}} \end{bmatrix} (\mathbf{v}^{\mathrm{n}}_i \otimes \mathbf{v}^{\mathrm{n}}_i)\,. \tag{6.2}$$

Hence, these tensors can be visualised at each evaluated position in space as ellipsoids, specified by its eigenvalues $\gamma^{\mathrm{n}}_{i\,\mathrm{awd}}$ and its eigenvectors $\mathbf{v}^{\mathrm{n}}_i$, cf. Figure 6.3. Therefore, it is possible to map the local diffusion characteristics, e. g., as exemplarily sketched for a coronal slice of the brain in Figure 6.3 (a). In particular, a distinct ellipsoid, cf. Figure 6.3 (b), exposes anisotropic conditions, whereas, a sphere indicates isotropic conditions, cf. Figure 6.3 (c). Furthermore, the initial local fibre direction $\mathbf{a}^{S,\mathrm{n}}_0$ is approximated at each voxel

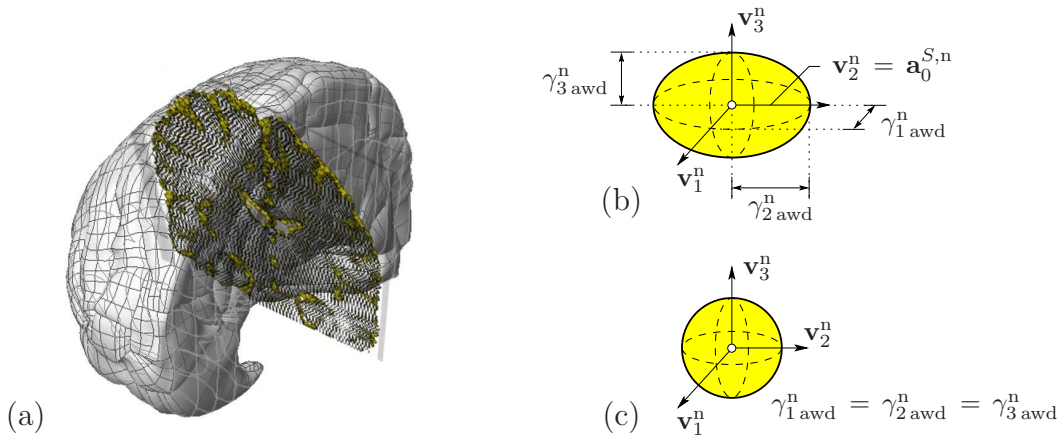

Figure 6.3: *Visualisation of the apparent diffusion tensors as ellipsoids at an exemplary coronal slice (a) with certain shapes, indicating (b) anisotropic and (c) isotropic characteristics.*

by the (dominant or principal) eigenvector corresponding to the eigenvalue of the largest magnitude via

$$\gamma^{\mathrm{n}}_{\mathrm{max}} \;=\; \max_i \gamma^{\mathrm{n}}_{i\,\mathrm{awd}} \quad\rightarrow\quad \mathbf{v}^{\mathrm{n}}_i(\gamma^{\mathrm{n}}_{\mathrm{max}}) \quad\rightarrow\quad \mathbf{a}^{S,\mathrm{n}}_0\,. \tag{6.3}$$

Note in passing that this method always reveals a macroscopic measure of a microscopic quantity, which is obtained via intravoxel averaging. In this regard, crossing fibre-tracts may result in a spherical representation as a result of a DTI measurement. Finally, it should be noted that the voxel dimensions consequently influence the measured apparent

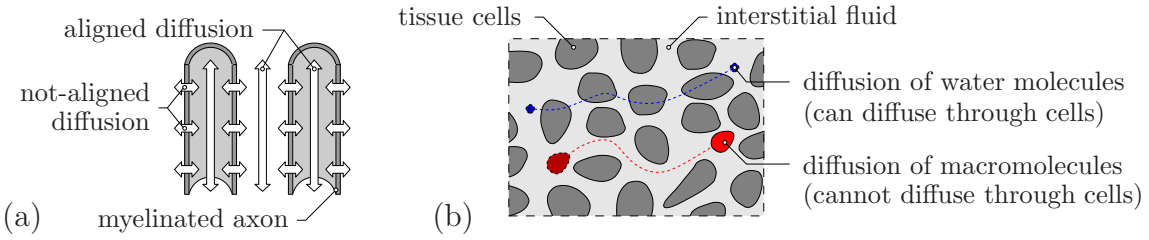

Figure 6.4: *Diffusion of water molecules and macromolecules (drugs) within brain tissue.*

diffusion tensors. However, this procedure is particularly suitable in terms of the TPM, using averaged macroscopic quantities from a homogenisation process over a REV.

Based on these general considerations, the DTI-data needs to be transferred in order to determine material parameters, which are used in the modelling approach. Based on Tuch *et al.* [161], the fundamental assumption is that the apparent water-diffusion tensor $\mathbf{D}_{\mathrm{awd}}$ possesses the same eigenvectors as the diffusion tensor $\mathbf{D}_0^D$ of the therapeutic agent and the permeability tensor $\mathbf{K}_{0S}^{SI}$ of the interstitial fluid. Hence, the underlying idea is that during DTI measurements, the deflected water-molecules are influenced by the tissue's micro-architecture in their (backward) movement in a similar manner as it would be the case for an arising motion (caused by an infusion) of the interstitial fluid φ^I and the dissolved therapeutics φ^D within the ECS, cf. Figure 6.4 (a). In general, this seems to be a reasonable assumption, but note in passing that water molecules can additionally diffuse through tissue cells, as it is schematically illustrated in Figure 6.4 (b), whereas the infused therapeutical macromolecules cannot, cf., e. g., Støverud [151] and citations therein. This may probably lead to a small inaccuracy in the distribution prediction. Nevertheless, following the idea of Tuch *et al.* [161] is a commonly used procedure, cf. Linninger *et al.* [98], Sarntinoranont *et al.* [135] or Støverud *et al.* [152], and is also considered as the most appropriate option in this monograph.

The task of transferring the apparent diffusion coefficients leads to a calibration procedure straightforwardly. In this regard, the diffusion coefficient of water within tissues is less than that of pure water, due to the circumstance that water molecules are obliged to move tortuously around obstructions presented mainly by the nervous fibres, cf. Sierra [145] and citations therein. Hence, the diffusion coefficient measured parallel to fibres can be up to three times larger than the diffusion coefficient perpendicular to fibres within the nervous brain tissue. Typical diffusion coefficients of water in the human brain cover the range from 10^{-4} to 10^{-3} mm^2/s, cf., e. g., Pierpaoli *et al.* [122]. Therefore, the eigenvalues of $\mathbf{D}_{\mathrm{awd}}^{\mathrm{n}}$ in (6.2) are linearly scaled in a first step in order to obtain the requested order of magnitude for the eigenvalues of $\mathbf{D}_0^{D,\mathrm{n}}$ and $\mathbf{K}_{0S}^{SI,\mathrm{n}}$, viz.:

$$\gamma^{\mathrm{n}}_{i\,\mathbf{D}_0^{D,\mathrm{n}}} = \bar{D}^D \frac{\gamma^{\mathrm{n}}_{i\,\mathrm{awd}}}{\bar{\gamma}^{\mathrm{n}}_{\mathrm{awd}}} \qquad \text{and} \qquad \gamma^{\mathrm{n}}_{i\,\mathbf{K}_{0S}^{SI,\mathrm{n}}} = \bar{K}^I \frac{\gamma^{\mathrm{n}}_{i\,\mathrm{awd}}}{\bar{\gamma}^{\mathrm{n}}_{\mathrm{awd}}} \,. \tag{6.4}$$

The main difficulty in applying (6.4) is to choose appropriate reference values $\bar{D}^D$ for the therapeutic agent and $\bar{K}^I$ for the interstitial fluid, respectively. Moreover, the calibration in (6.4) is investigated with respect to the mean of the eigenvalues, namely

$$\bar{\gamma}^{\mathrm{n}}_{\mathrm{awd}} = \tfrac{1}{3}(\gamma^{\mathrm{n}}_{1\,\mathrm{awd}} + \gamma^{\mathrm{n}}_{2\,\mathrm{awd}} + \gamma^{\mathrm{n}}_{3\,\mathrm{awd}}) \,. \tag{6.5}$$

Therefore, it can easily be concluded that this restricts the calibration to purely anisotropic results, omitting the description of locally varying heterogeneous quantities, exhibiting different orders of magnitude. If this is required, the calibration in (6.4) can be derived without the specific relation to the mean $\bar{\gamma}^{\mathrm{n}}_{\mathrm{awd}}$. Optionally, the anisotropic permeabilities can be manually increased in specific domains by a scalar factor in order to include damage effects, afterwards.

Finally, the calibration procedure (6.4) provides the initial diffusivity $\mathbf{D}_0^{D,\mathrm{n}}$ and the initial permeability tensor $\mathbf{K}_{0S}^{SI,\mathrm{n}}$ at each evaluated voxel in a compact manner, viz.:

$$\mathbf{D}^{D,\mathrm{n}}_{0,\,\mathrm{diag.}} = \sum_{i=1}^{3} \gamma^{\mathrm{n}}_{i\,\mathbf{D}_0^{D,\mathrm{n}}} \left(\mathbf{v}^{\mathrm{n}}_i \otimes \mathbf{v}^{\mathrm{n}}_i\right) \qquad \text{and} \qquad \mathbf{K}^{SI,\mathrm{n}}_{0S,\,\mathrm{diag.}} = \sum_{i=1}^{3} \gamma^{\mathrm{n}}_{i\,\mathbf{K}_{0S}^{SI,\mathrm{n}}} \left(\mathbf{v}^{\mathrm{n}}_i \otimes \mathbf{v}^{\mathrm{n}}_i\right). \tag{6.6}$$

The spectral representations given in (6.6) can be transferred to a description in terms of the Cartesian coordinate system $\mathbf{e}_i$ via the transformation rules

$$\mathbf{D}_0^{D,\mathrm{n}} = \mathbf{Q}^{\mathrm{n}}\, \mathbf{D}^{D,\mathrm{n}}_{0,\,\mathrm{diag.}} \left(\mathbf{Q}^{\mathrm{n}}\right)^{-1} \qquad \text{and} \qquad \mathbf{K}_{0S}^{SI,\mathrm{n}} = \mathbf{Q}^{\mathrm{n}}\, \mathbf{K}^{SI,\mathrm{n}}_{0S,\,\mathrm{diag.}} \left(\mathbf{Q}^{\mathrm{n}}\right)^{-1}. \tag{6.7}$$

Therein, the rotation tensor[9] $\mathbf{Q}^{\mathrm{n}} = Q^{\mathrm{n}}_{ji} \left(\mathbf{e}_j \otimes \mathbf{e}_i\right)$ contains the coefficients v^{n}_{ij} of the three eigenvectors $\mathbf{v}^{\mathrm{n}}_i = v^{\mathrm{n}}_{ij}\, \mathbf{e}_j$ (with $i = 1, 2, 3$) as column vectors within the coefficient matrix $Q^{\mathrm{n}}_{ji} = v^{\mathrm{n}}_{ij} = [v^{\mathrm{n}}_{1j},\, v^{\mathrm{n}}_{2j},\, v^{\mathrm{n}}_{3j}]$, cf. Ehlers [49].

For the sake of illustration, the application of this specific approach using a typical DTI data-set[10] is presented. In particular, a DTI-scan of a healthy human brain is studied, where the evaluated domain encompass 148 mm x 190 mm x 160 mm. Therein, the rectangular grid has a uniform voxel-size of $s_{\mathrm{voxel}} = 1\,\mathrm{mm}$ in each of the three spatial dimensions. Note that this exemplary data-set is used in order to demonstrate the general feasibility of the applied implementation approach. However, the same procedure can analogously be applied to any patient-specific data. In Figure 6.5, an implementation-sketch for the inclusion of voxel quantities is given. In this regard, the previously mentioned dataset is provided in a so-called NRRD[11] file format, consisting of a plain ASCII[12] header combined with a binary data file. In particular, there are seven values per voxel (32-bit floats, written in raw, big-endian) available. Therein, the first value represents the mask-image "confidence", which takes the value 1.0 in regions where the measured quantities are meaningful and 0.0 if the measured quantities are somehow noisy. Note in passing that these values allow the segmentation of the volumetric data and might enable the identification of bounding surfaces. Subsequently, the voxel arrays contain the values of the six unique coefficients of the apparent diffusion tensor $\mathbf{D}^{\mathrm{n}}_{\mathrm{awd}}$ in the specific order $D^{\mathrm{n}}_{11\,\mathrm{awd}}, D^{\mathrm{n}}_{12\,\mathrm{awd}}, D^{\mathrm{n}}_{13\,\mathrm{awd}}, D^{\mathrm{n}}_{22\,\mathrm{awd}}, D^{\mathrm{n}}_{23\,\mathrm{awd}}, D^{\mathrm{n}}_{33\,\mathrm{awd}}$. These quantities are described with respect to the $\mathbf{x}_i$-coordinate-system of the DTI-scanner's measurement frame. Due to the

[9] Furthermore, the rotation tensor $\mathbf{Q}^{\mathrm{n}}$ exhibits orthogonal properties. Hence, its inverse $(\mathbf{Q}^{\mathrm{n}})^{-1}$ can be replaced by its transpose $(\mathbf{Q}^{\mathrm{n}})^{T}$, which generally is more suitable for computational issues.

[10] Brain dataset courtesy of Gordon Kindlmann at the Scientific Computing and Imaging Institute, University of Utah, and Andrew Alexander, W. M. Keck Laboratory for Functional Brain Imaging and Behavior, University of Wisconsin-Madison, available at http://www.sci.utah.edu/∼gk/DTI-data.

[11] Nearly Raw Raster Data (NRRD) is file format designed to support scientific visualisation and image processing using high-dimensional raster data.

[12] American Standard Code for Information Interchange (ASCII) is a character-encoding scheme, originally based on the English alphabet, that encodes 128 specified characters.

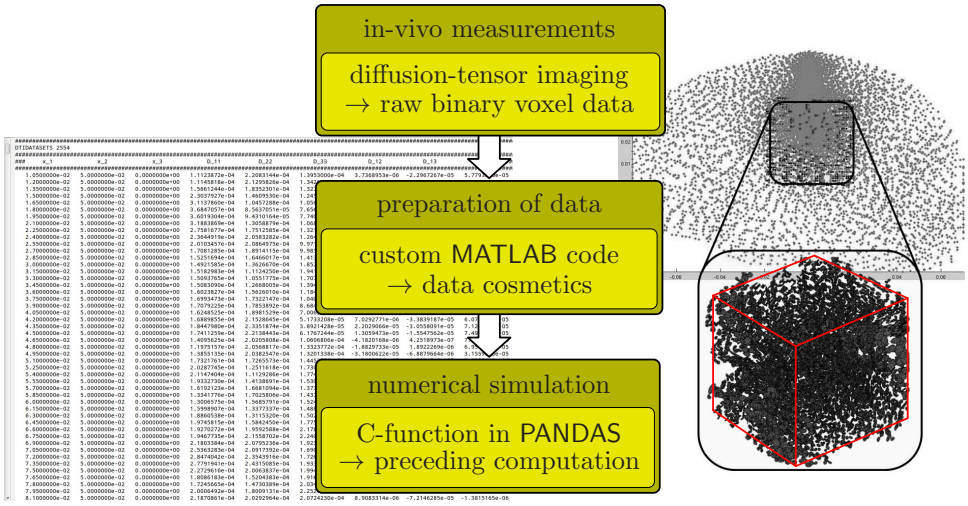

Figure 6.5: *Sketch of the implementation algorithm (middle), "look-up" table with diffusion coefficients (left) and visualisation of diffusion tensors with ellipsoids (right).*

unimaginable binary data in a distinct raster-ordering (fast-to-slow sampling of frame axes) and, moreover, the required transformation of the scanner's coordinate system, a customised MATLAB[13] code was developed for the purposes of this monograph. This tool enables an illustrative data interpretation and provides the visualisation of the voxel data. In this regard, the loaded DTI-data is initially cleaned via eliminating non-physical data-sets consisting of tensors with negative eigenvalues. Furthermore, the possibility to optionally restrict the data-set to a region of interest (ROI) is provided in order to economise calculation time. In particular, this is often reasonable since only data sufficiently close to the infusion site have a crucial influence on the therapeutic distribution.

For instance, the anisotropic diffusion characteristics are exemplarily evaluated at a random voxel position $\mathrm{n} = A$ in a representative horizontal slice of the brain, cf. Figure 6.6. As expected, highly anisotropic diffusion properties are revealed[14] at the position A due to its location in the white-matter domain. Although recognised by its ellipsoidal shape, this becomes evident from the eigenvalues of the diffusivity tensor $\mathbf{D}_0^{D,A}$. In this case, a preferred diffusion direction is indicated by the largest eigenvalue $\gamma_{2,\mathbf{D}_0^{D,A}}$. Hence, the assumed local fibre-direction $\mathbf{a}_0^{S,A}$ coincides with the corresponding eigenvector $\mathbf{v}_2^A$.

Due to the irregularly varying anisotropic parameters within the considered domain, it can easily be concluded that it is impossible to find a corresponding closed analytical (field) function for the considered brain tissue[15]. Hence, the available DTI-data is provided in

[13] MATLAB (Matrix Laboratory) is a commercial software, suitable for the numerical treatment of multi-dimensional arrays, including the support of raw files, cf. http://www.mathworks.de/products/matlab.

[14] The exemplarily given quantities are obtained from the calibration process, cf. (6.4)-(6.7). Moreover, the coefficients $D_{0\,ij}^{D,A}$ are related to the orthonormal basis system $\mathbf{e}_i$.

[15] Regarding further structured biological tissues, it often is possible to describe the occurring anisotropies in integrative algorithms. For instance, via location-dependent interpolation functions to describe the collagen-fibre distribution in the anulus fibrosus of the intervertebral disc, cf. Karajan [87]. As another example, an analytical function (closed-form) is commonly used for the initial depth-dependent distribution of fibre vectors in the cartilage of the femoral head, cf., e. g., Mabuma *et al.* [102].

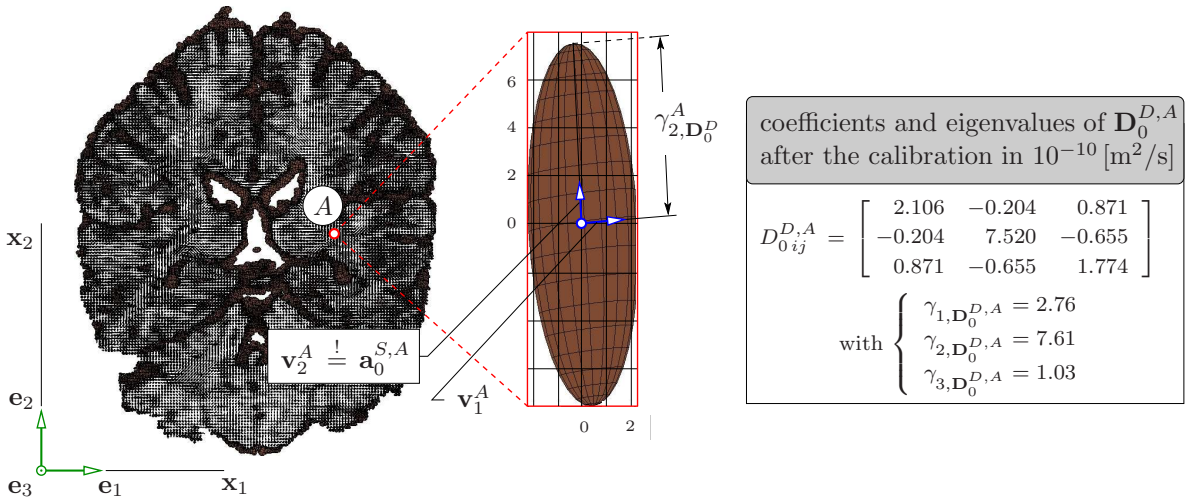

Figure 6.6: *Visualisation of the anisotropic diffusivity at a representative brain slice and at a random voxel position A.*

the manner of a "look-up" table, containing the evaluated voxel data. Based on this table, the spatially varying anisotropic (and inhomogeneous) properties of the underlying brain-tissue aggregate are loaded in PANDAS in a preceding calculation step. Afterwards, the tasks of the spectral decomposition (6.2) as well as the calibration procedure (6.4) are evaluated via a specific subroutine implemented in PANDAS.

Usually, the spatial discretisation of the finite-element grid is independent from the one of the voxel data, cf. Figure 6.7. Therefore, a specific algorithm allocates and stores the voxel information at each integration point K_G for the subsequent numerical simulation. In this regard, it is often sufficient that each Gauß point K_G is basically equipped with the closest voxel data available in space, cf. Figure 6.7 (c). However, a mismatch of integration

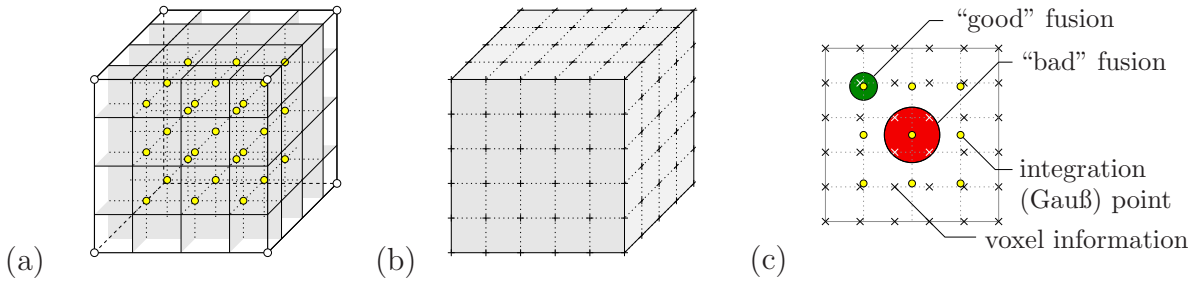

Figure 6.7: *(a) position of integration points for a 3×3×3 (27) Gaußian integration scheme, (b) uniform grid of evaluated voxels from DTI and (c) two-dimensional example of voxel-data-fusion to integration points.*

points combined with (sparse) voxel data can cause inaccurate results. Hence, a sufficient amount of voxel information, in terms of the chosen spatial discretisation, needs to be ensured. If this is not the case, the application of suitable averaging processes is optionally provided. In this case, voxel information, i. e., the (scalar-valued) permeability-coefficients

$K_{ij}^{K_G}$ are linearly weighted at the considered Gauß point K_G, viz.:

$$\tilde{K}_{ij}^{K_G} = \frac{\sum_{\mathrm{n}} K_{ij}^{\mathrm{voxel,n}}\, w^{\mathrm{voxel,n}}}{\sum_{\mathrm{n}} w^{\mathrm{voxel,n}}} \qquad \text{with} \quad w^{\mathrm{voxel,n}} = 1 - \frac{d^{\mathrm{voxel,n}}}{R_{K_G}}\,. \tag{6.8}$$

Therein, $d^{\mathrm{voxel,n}}$ is the distance of the voxel information to the considered K_G within a certain (influence) radius R_{K_G} for the K_G. Therefore, the included surrounding of K_G can either be chosen constant for the overall domain or location-dependent on the element size (via the Jacobian determinant $\bar{J}$ of the reference element). Related to this fusion problem of mapping medical-imaging data to a computation grid, Magdoom *et al.* [103] compared models using different mesh structures. In particular, the observed differences between a voxelised model with uniform rectangular elements and a non-voxelised model with an unstructured mesh are assumed to arise due to the tissue volume approximation (notably the curvature at tissue boundaries) and by varying resolutions.

6.2.2 Evaluation of magnetic-resonance-angiography data

Besides the previously investigated evaluation of the quantities $\mathbf{K}_{0S}^{SI}$ and $\mathbf{D}_0^D$ governing the flow and diffusion in the ECS, there is the additional need to account for the blood perfusion $\mathbf{K}_{0S}^{SB}$. As was already mentioned in Subsection 4.4.1, the solid skeleton of the brain-tissue aggregate exhibits two basically separated pore spaces. In this regard, the blood perfusion occurs within the complex system of vascular vessels. In order to include these underlying micro-structural informations into the macroscopical model, MRA provides an in-vivo approach to locate and image major blood vessels within the brain tissue, cf. Section 2.4. A basic approach for the implementation of MRA-data is sketched in Figure 6.8.

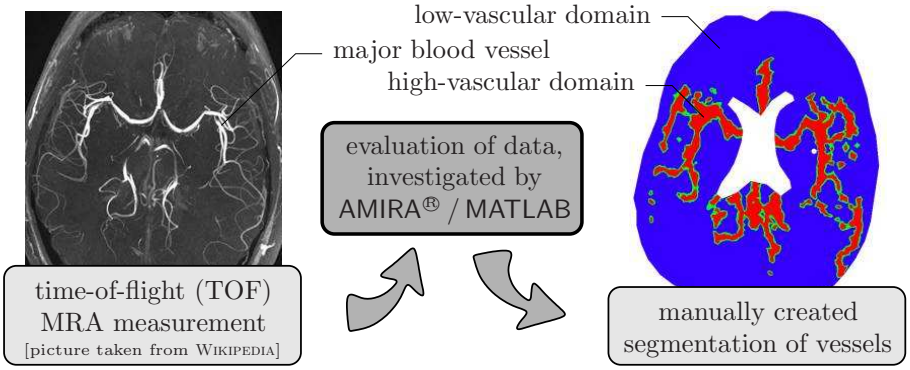

Figure 6.8: *Sketch of the implementation algorithm of MRA measurements.*

In a first step, the commercial medical-software AMIRA[16] is used in order to distinguish between intra-vascular and extra-vascular regions of the major blood vessels. Consequently, this allows a segmentation in high-vascular and low-vascular domains. For the purposes

[16] AMIRA® (FEI Visualization Sciences Group, Burlington, USA) is a powerful 3-d analysis software platform for visualising, manipulating, and understanding biomedical data originating from all types of sources and modalities, cf. http://www.vsg3d.com/amira.

of this monograph spatially varying (heterogeneous) isotropic[17] blood permeabilities $\mathbf{K}_{0S}^{SB}$ are assumed. Nevertheless, this approach is able to map anisotropic blood perfusion characteristics within the macroscopical model. Therefore, the local Gauß points of the spatial grid are assigned with higher permeabilities in high-vascular regions (major blood vessels) and lower permeabilities in low-vascular (capillary tissue) regions. Using MATLAB, this allocation is investigated in a similar manner as it is shown for the incorporation of DTI-data, cf. Section 6.2.1.

6.2.3 Collection of basic material parameters

As was shown in the previous investigations, certain patient-specific material parameters of the brain's tissue can be determined via in-vivo medical-imaging methods. However, a major drawback in computational biomechanics is still the task of obtaining all particularly required simulation parameters. Practically, this is beyond reach since it is almost impossible to realise experiments on living human brain tissue, not least due to ethical reasons. In contrast, an ex-vivo testing is conceivable, which was already performed, e. g., by Franceschini *et al.* [67]. Nevertheless, there are still ongoing discussions concerning the range and the validity of experimentally determined material parameters. In particular, this is mainly caused by the fact that brain-tissue properties change crucially in vitro. For example, the extra-cellular space shrinks after death, until there is no pore space left. Hence, the determination of permeability properties is extremely difficult and often leads to different quantitative statements in examined studies. In contrast, the initial (homogenised) volume fractions are generally accepted for (healthy) brain tissues, cf. Section 2.1. Here, 5 % are chosen for the blood phase and 20 % for the interstitial fluid. Therefore, the remaining part results in a solidity of 75 % via the saturation condition (3.5). In this regard, the solid skeleton mainly consists of cellular structure[18]. The material properties of the realistic density ρ^{IR} and viscosity μ^{IR} of the interstitial fluid are chosen in accordance to water. The material properties of the blood constituent are taken from "The Physics Hypertextbook"[19]. The elastic material constants μ_0^S and λ_0^S are small due to the soft brain tissue. Moreover, the constants $\tilde{\mu}_1^S$ and $\tilde{\gamma}_1^S$, governing the nervous-fibre stiffness of the reinforced soft tissue, are assumed to be even smaller. In particular, this is caused by the circumstance that the nervous fibres are rather designed as information-transmitting elements (signal pathways) than as structural elements by means of a mechanical functionality. Furthermore, gravity forces are neglected for the subsequently presented numerical examples. Following these parameter settings, it must be repeated that the main intention of this monograph is the development of a theoretical and a computational model, making numerical studies possible. Therefore, the accuracy is not claimed of all included values, which are collected in Table 6.1. To summarise, all pa-

[17] This assumption is caused by the MRA's low resolution, allowing only the detection of major vessels. Hence, this information is not sufficient to identify local anisotropies.

[18] Note in passing that the entire brain possesses approximately 80 % of water. However, the dominant part of this water is bounded within the tissue's cells and, hence, is assigned to the solid skeleton. This leads to a lower porosity as it is probably expected at first glance.

[19] Therein, an useful collection of mechanical parameters of various materials at different temperatures is given by Glenn Elert, cf. http://physics.info .

Collection of basic material parameter			
	value	unit	remark / reference
n_{0S}^{B}	0.05	[-]	according to Baxter & Jain [15]
n_{0S}^{I}	0.20	[-]	according to Syková & Nicholson [154]
n_{0S}^{S}	0.75	[-]	the initial solidity arises as a result of (3.5)
ρ^{BR}	$1.035 \cdot 10^{+3}$	[kg/m^3]	according to http://physics.info/density
ρ^{IR}	$0.993 \cdot 10^{+3}$	[kg/m^3]	chosen in accordance to water at 37°C
μ^{BR}	$3.5 \cdot 10^{-3}$	[Ns/m^2]	according to http://physics.info/viscosity
μ^{IR}	$0.7 \cdot 10^{-3}$	[Ns/m^2]	chosen in accordance to water at 37°C
μ_0^S	$1.0 \cdot 10^{+3}$	[N/m^2]	chosen in the order of magnitude, according to
λ_0^S	$5.0 \cdot 10^{+3}$	[N/m^2]	Chen & Sarntinoranont [34], Smith & Humphrey [147] and citations therein
$\tilde{\mu}_1^S$	$8.0 \cdot 10^{+1}$	[N/m^2]	assumed low fibre stiffness, since nervous fibres
$\tilde{\gamma}_1^S$	$1.0 \cdot 10^{+1}$	[-]	are not designed as supporting elements
g_i	0.0	[m/s^2]	gravity forces are neglected
$\tilde{\alpha}^B$	200	[N/m^2]	constitutive parameter in (4.83) and (4.84)
$\tilde{\beta}^B$	3.75	[-]	constitutive parameter in (4.83) and (4.84)
D_{ij}^{D}	10^{-9} - 10^{-10}	[m^2/s]	order of magnitude of spatially varying drug diffusion coefficient, according to Baxter & Jain [15] and citations therein
K_{ij}^{I}	10^{-7} - 10^{-8}	[m/s]	order of magnitude of spatial varying Darcy permeability for the interstitial fluid, according to Kaczmarek *et al.* [85]
K_{ii}^{B}	$3.0 \cdot 10^{-3}$	[m/s]	isotropic Darcy permeability coefficient, blood in vascular and
	$3.0 \cdot 10^{-5}$	[m/s]	lower-vascular regions, based on Su & Payne [153]

Table 6.1: *Collection of basic (referential) material parameters for the multicomponental simulation of human brain-tissue.*

rameters are chosen to the authors best knowledge from related literature on experiments or numerical studies on animals or gel-phantoms. Since there is still no general agreement concerning the quantification of several material parameters, a numerical sensitivity analysis is complemented in Section 6.3.3.

6.3 Numerical examples

First, the general material behaviour of the nervous brain-tissue aggregate is studied by means of two introductory examples, considering the basic multicomponental behaviour as well as finite deformation processes in tension and compression. Afterwards, the fo-

cus is placed on the main application of the proposed modelling approach, namely, the simulation of invasive infusions of therapeutical solutions into the ECS of the brain-tissue. Within these examples, the irregular spatial distribution of the therapeutic agents is observed. Moreover, several issues influencing the resulting profile of the therapeutical concentrations are considered and discussed in detail. For all intents and purposes, the coupled FE solver PANDAS is used for computations and the post-processing tool PANPOST (cf. Rempler [128]) for the visualisation of the numerical results.

6.3.1 General material behaviour of brain tissue

In this short introduction to the characteristical material behaviour of the complex multicomponent brain-tissue aggregate, two main aspects are selected. First, the interplay of the particular constituents during a so-called consolidation process and, second, the anisotropic and bimodal (i. e., the tension-compression non-linearity) behaviour within a finite-deformation process. Although Miller [110] addressed a word of caution to the application of modelling soft biological-tissues using biphasic (or multiphasic) theories, exactly this is (at least for the issues under consideration within this monograph) the most reasonable choice.

Consolidation process: The controversially and frequently discussed oedometric (quasi-static, uni-axially confined compression) experiments of Franceschini *et al.* [67] are studied here. Therein, in-vitro brain-tissue samples are taken from the parietal lobe[20] and tested under well-defined draining conditions. Due to this, Franceschini *et al.* [67] were able to distinguish between viscous singlephasic and multiphasic (consolidation) effects for the observed non-linear mechanical response. Consequently, it is stated in Franceschini *et al.* [67] that the brain's tissue behaves in the sense of a porous fluid-saturated medium.

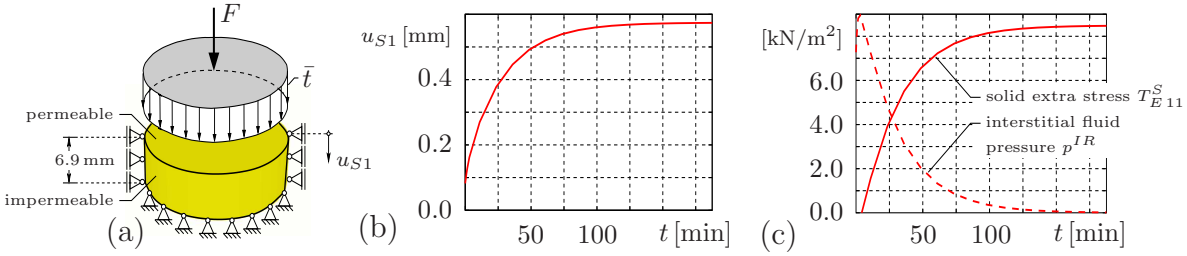

Figure 6.9: *(a) geometry and boundary conditions for the oedometric test, (b) vertical displacement of the top surface and (c) evolution of the interstitial fluid pressure p^{IR} and the solid extra stress $T^S_{E\,11}$ within the tissue sample.*

In this regard, a recalculation with a simplified biphasic model, omitting the blood phase, is investigated, cf. Wagner & Ehlers [167]. In order to obtain comparable results, similar boundary conditions and material parameters are chosen in accordance to the experiments of Franceschini *et al.* [67]. In particular, a free drainage of the bottom and the top surface is provided, whereas the side surface is rigidly supported (confined compression) and exhibits impermeable conditions for the interstitial fluid, cf. Figure 6.9 (a). Then,

[20] In this region, situated in the middle of the brain hemisphere, homogeneous samples of required dimensions (with 6.9 mm height and 30.0 mm in diameter) are available.

a distributed compressive load of $\bar{t} = 8488\,\mathrm{N/m^2}$ is applied to a brain-tissue sample, which corresponds to an external (total) force of $F = 6\,\mathrm{N}$. As a result of the numerical simulation, the downward-oriented displacement u_{S1} of the top surface increases over time due to the ongoing consolidation process, cf. Figure 6.9 (b). In this regard, the external load initially causes a high interstitial fluid pressure p^{IR}. As a consequence of the arising interstitial fluid efflux via the drained surfaces, the load is subsequently transferred to the solid skeleton and results in an increase of the solid's extra stress $T^S_{E\,11}$, cf. Figure 6.9 (c).

Finite deformation process: Besides consolidation phenomena, the soft brain tissue can principally be subjected to large deformations. In this context, the response of the fibre-reinforced tissue is bimodal, i. e., it differs in tension and compression states, cf., e. g., Miller [111], Miller & Chinzei [113]. This is included via the case distinction (4.103). In order to illustrate these characteristics in the material's response, an academic example is chosen. In particular, a rectangular, spatially fixed (at the bottom) tissue sample is tested, which exhibits a homogeneous fibre distribution under an initial fibre angle of 45°, cf. Figure 6.10 (left). The numerical results under finite stretch and compression

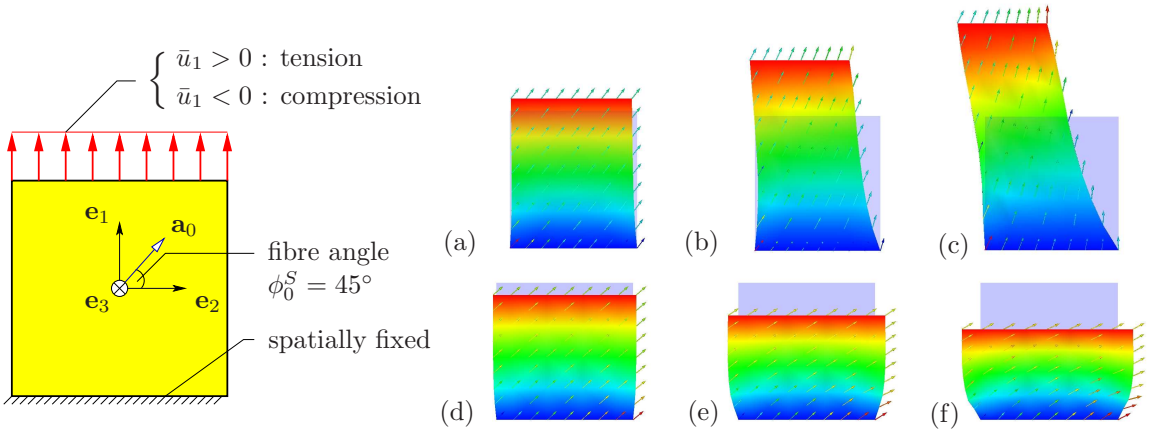

Figure 6.10: *Geometry, boundary conditions and initial fibre orientation of a tissue sample (left) and tissue sample under finite stretch (a)-(c) and compression (d)-(f), colour-coded in the vertical displacements, where the arrows display the actual fibre directions (right).*

are illustrated on the right of Figure 6.10 (a) - (c) and (d) - (f), respectively. Therein, the deformations are not scaled. As expected, pulling the top surface results in an additional horizontal displacement of the tissue-sample. In contrast, the material behaviour in (unconfined) compression is isotropic. Note in passing that the actual orientation of fibres, displayed via arrows in Figure 6.10 (right), change in dependence to the deformation state.

6.3.2 Invasive extra-vascular delivery of therapeutics

In this section, the distribution of infused therapeutics during the CED process is numerically studied. First, the application to a realistic 3-d brain-hemisphere, geometrically derived in Section 6.1, is investigated in order to show the full range of the presented model. However, a simplified (2-d) horizontal slice of a human brain is used afterwards for the sake of clarification in order to discuss in detail the specific circumstances, influ-

encing the irregular distribution of the infused drug. This includes a grid-convergence study for different finite-element discretisations. Furthermore, the influence of varying infusion rates as well as of the so-called backflow phenomenon on the distribution process are investigated.

CED applied to a 3-d human brain hemisphere: In order to apply the boundary conditions in a realistic manner to the geometrical model of the brain's hemisphere, cf. Section 6.1.2, a catheter shaft is incorporated within the geometry of the cerebrum, cf. Figure 6.11. This corresponds to the stereotactical placement of the infusion catheter in a surgical intervention. Afterwards, the body is meshed with approximately 7500

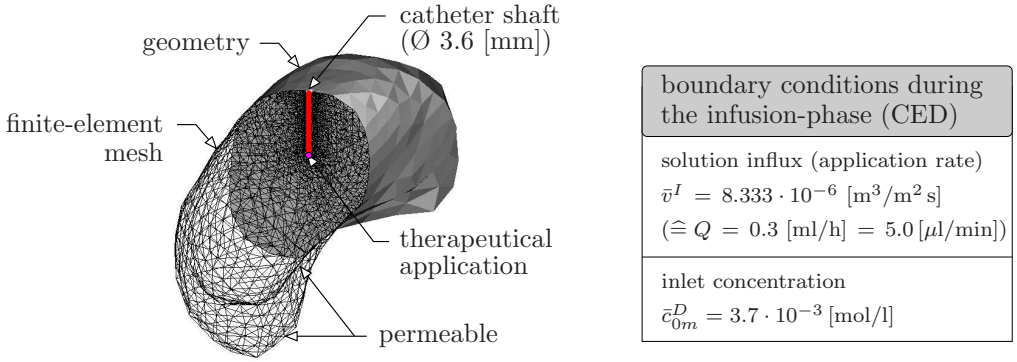

Figure 6.11: *Geometry and boundary conditions during CED in a 3-d brain hemisphere.*

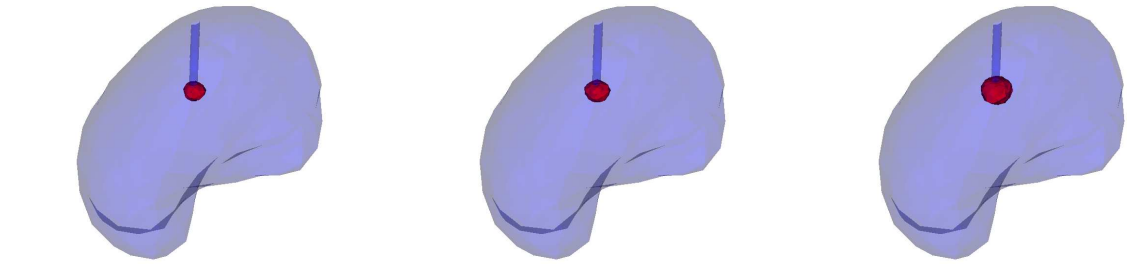

Figure 6.12: *Distribution of therapeutic agents during CED at (a) the beginning, (b) during and (c) at the end of the infusion process.*

tetrahedral elements, where in the vicinity of the catheter shaft and, especially around the catheter tip, the mesh is chosen finer to avoid numerical inaccuracies. In terms of appropriate boundary conditions, the brain's hemisphere is statically supported. At the brain's outside (cortex), an efflux of interstitial fluid through the surface is allowed. Here, the infusion site is given at the catheter tip[21], where the corresponding boundary conditions are applied, namely, an influx of the overall interstitial fluid volume with a constant inlet concentration of therapeutic agents. Thus, this corresponds to an infusion of a therapeutic solution containing the dissolved therapeutic agent. The resulting spatial

[21]Hence, the flow occurs anterograde into the neural tissue. Besides this standard catheter design, different modified catheter variants are used, e. g., with openings along the catheter shaft. However, the standard catheter is used for the purposes of this monograph.

and temporal spreading of the therapeutic agent within the brain's tissue is shown in Figure 6.12. Therein, the distribution front is displayed by a red-coloured isosurface of the therapeutic concentration.

CED applied to a (quasi 2-d) human brain-slice: As was already stated, the previously described 3-d model of a brain's hemisphere is further reduced, mainly caused by issues of numerical efficiency and illustration. In this regard, the considered layer is chosen on the horizontal level of the inner ventricles and contains the entire brain. Hence,

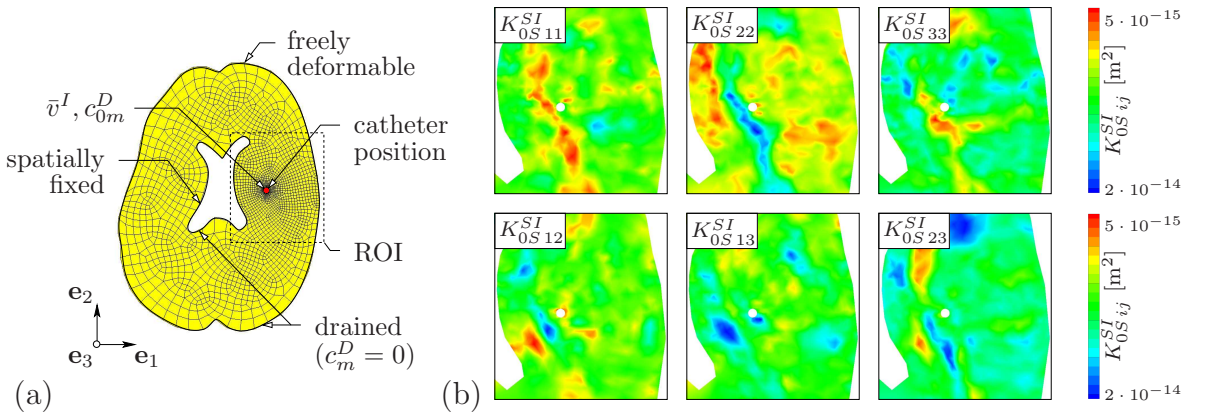

Figure 6.13: *(a) geometry and mesh of a horizontal brain section including the catheter position and boundary conditions. ROI (b) with values for the location-dependent coefficients of the anisotropic permeability tensor obtained via DTI.*

specific effects occurring during a CED infusion are studied in detail on a manually prepared geometry of a horizontal brain section, cf. Section 6.1.1. Using CUBIT, the quasi 2-d geometry is initially meshed with 2179 hexahedral elements with one element in the thickness direction, cf. Figure 6.13 (a). The spatial diversification of the underlying anisotropic permeability values are exemplary displayed in the ROI in Figure 6.13 (b). Regarding a CED application, the catheter is exemplarily placed within the brain tissue. This enables the application of the corresponding boundary conditions for the therapeutical infusion at the surface of the infusion site. In particular, a solution influx of $\bar{v}^I = 1.33 \cdot 10^{-6}$ m^3/m^2 s is combined with a therapeutical concentration of $c^D_{0m} = 3.7 \cdot 10^{-3}$ mol/l at the catheter tip. This chosen values correspond to a typical application dose[22] of $Q = 5$ μl/min (or 0.3 ml/h, respectively), cf., e. g., Ding *et al.* [39] of Voges *et al.* [165]. In addition, an efflux of interstitial fluid and therapeutic agents over the surfaces at the outside of the brain (the brain's cortex) and the inner ventricles is possible. In order to mechanically support the brain-slice, the geometry is spatially fixed at the surface of the inner ventricle, whereas, deformations are allowed at the brain's outer cortex[23]. In this example, the investigated period of time covers a long-lasting infusion, which is computed using adaptive time increments. As a result, the numerical simulation clearly displays the anisotropic spreading,

[22] Note in passing that an interstitial fluid excess pressure could be applied alternatively as a boundary condition at the infusion site, when requested.

[23] This corresponds to realistic conditions within the rigid skull. Therein, the brain's surrounding CSF is able to move via the spinal cord and, thus, allows for a somehow freely expansion of the brain's outer surface. In contrast, the inner ventricles are filled with CSF which cannot escape in a similar manner and, hence, hinders a free expansion.

as it is shown in Figure 6.14 at different time steps. In addition, the computations exhibit

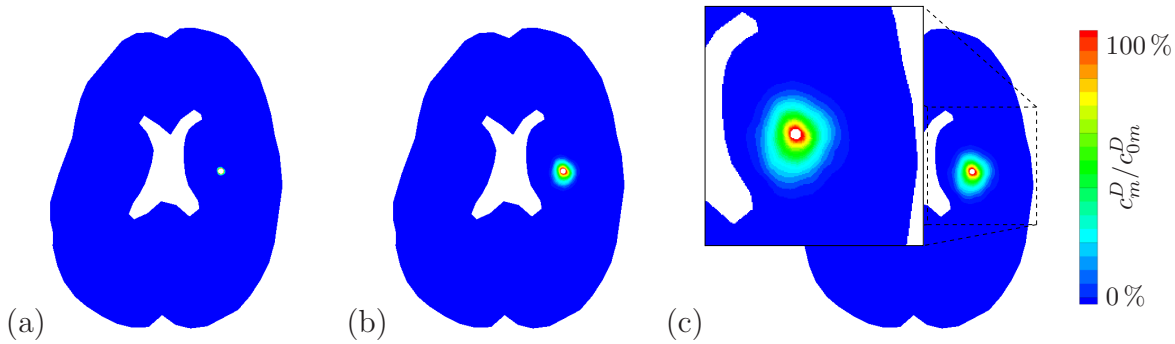

Figure 6.14: *Anisotropic distribution of the therapeutic agent during CED after 1 minute (a), 1 hour (b) and 3 hours (c), colour-coded by the normalised therapeutical concentration.*

an irregular propagation front, which obviously does not have a circular shape. Note in passing that the final state of application is reached at a certain time, depending on the site and rate of the injection. Besides the desired spreading of the therapeutical agents, several other coupled effects occur, which need to be considered carefully. In this regard, the stress and pressure distribution is of great interest during a CED application in order to perform a surgical intervention without incidents. In Figure 6.15 (a), it is seen that the pressure p^{IR} of the interstitial fluid naturally maximises at the infusion site of the catheter. In the present case, the resulting values are relatively low due to the moderate application dose. However, a notable pressure increase results as a consequence of higher infusion rates, as it is described in Section 6.3.3. The largest value of the interstitial fluid's volume fraction, cf. Figure 6.15 (b), is also found at the infusion site of the catheter, since the solid constituent is displaced as a result of the infused solution. To be more precise,

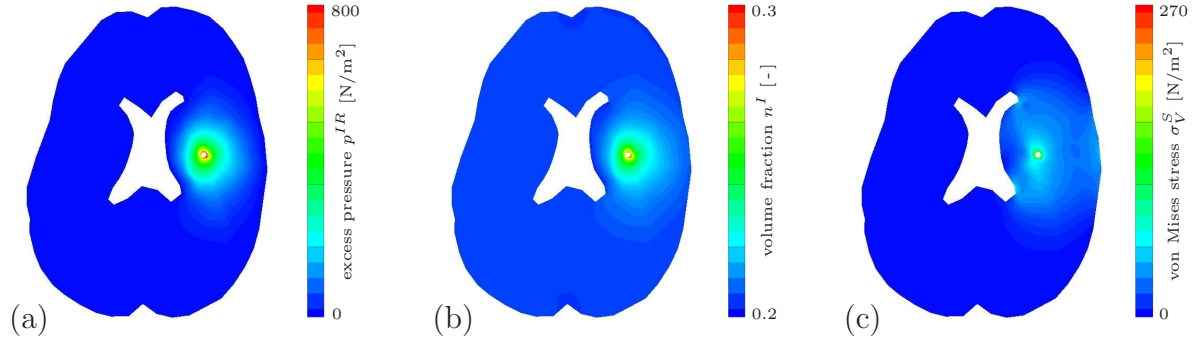

Figure 6.15: *(a) interstitial fluid excess pressure p^{IR}, (b) volume fraction n^I of the interstitial fluid and (c) von Mises stress σ_V^S during the infusion process.*

applying an amount of volume in a fully saturated domain leads basically to deformation processes of the solid skeleton. In order to obtain a local measure for the loading state of the solid skeleton of the tissue aggregate, the von Mises equivalent stress[24] is evaluated using the coefficients of the solid's extra-stress. In conclusion, this yields a scalar quantity, enabling the visualisation of the solid's local state of stress. Finally, the solid

[24] $\sigma_V^S = \sqrt{T_{E\,11}^S + T_{E\,22}^S + T_{E\,33}^S - T_{E\,11}^S T_{E\,22}^S - T_{E\,22}^S T_{E\,33}^S - T_{E\,11}^S T_{E\,33}^S + 3\,(T_{E\,12}^S + T_{E\,23}^S + T_{E\,13}^S)}$

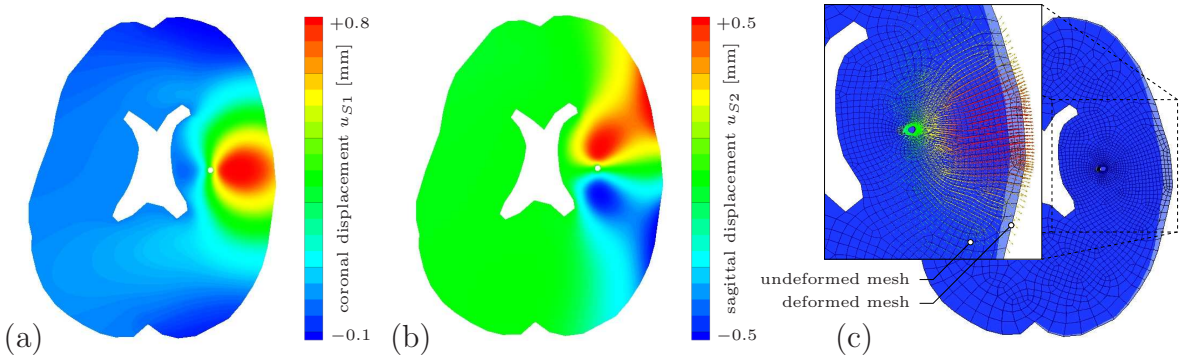

Figure 6.16: *(a) coronal and (b) sagittal displacements during CED. (c) visualisation of the deformation process, which is superelevated a thousand times. Therein, the deformed grid is given in light blue, whereas the undeformed (referential) grid is given in dark blue. Moreover, the displayed vectors indicate the local solid displacement* $\mathbf{u}_S$.

displacements are given in Figure 6.16. The coronal (corresponding to the $\mathbf{e}_1$-direction) and sagittal (corresponding to the $\mathbf{e}_2$-direction) solid displacements are shown in Figure 6.16 (a) and (b), respectively. Moreover, Figure 6.16 (c) illustrates the deformations of the considered brain slice. Note that the displacements are superelevated a thousand times due to the small measures. In this regard, the deformed mesh is displayed in light blue, whereas the undeformed (referential) grid is given in dark blue. In addition, the local solid-displacement vector $\mathbf{u}_S$ is indicated via vectors, which are colour-coded in the length (norm) of the occurring solid's displacement vector.

Quality of the spatial discretisation: For the verification of the quality of the chosen grid, i. e. the mesh (d) in Figure 6.17, the normalised therapeutic concentration is evaluated at an (arbitrarily chosen but fixed) spatial point P in the ROI. The results are compared with three further spatial-discretisation possibilities, cf. the meshes (a)-(c) in Figure 6.17. First, the relatively coarse mesh (a) with 561 hexahedral elements is considered having ten adjoining elements at the infusion site. Mesh (a) proves to be insufficient and produces non-physical results, i. e., at the beginning, slightly negative concentra-

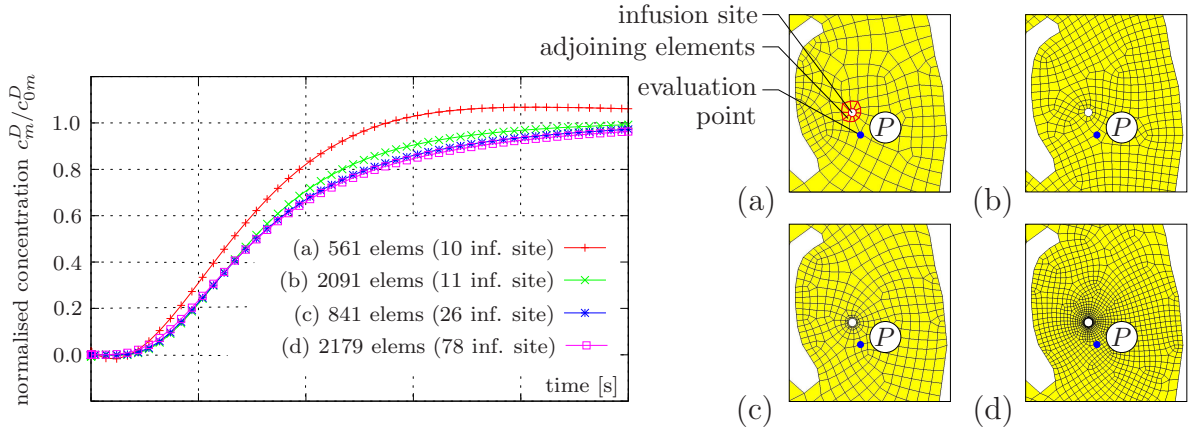

Figure 6.17: *Convergence study for the therapeutical concentration at the spatial location P in the vicinity of the infusion point (left) using different meshes (right).*

tions and a concentration-overstep in relation to the infused solution occur. Therefore, the mesh (a) is uniformly refined in the entire domain leading to the mesh (b) with 2091 elements (where 11 elements are located at the infusion site). Mesh (b) already yields qualitatively meaningful results. However, proceeding from a refinement of mesh (a), solely in the surrounding of the injection site and a coarser grid in the remainder of the ROI, cf. mesh (c) with 841 elements and mesh (d) with 2179 elements, leads to a convergence of the results for both meshes. The results of mesh (d) are recognised to be slightly more reliable due to a sufficient amount of finite elements, providing a stable numerical solution at the administration site. Therefore, it is highly recommended to use suitable meshes, like mesh (d). Note again that mesh (d) represents the chosen spatial discretisation of all (previous and following) investigations of the quasi 2-d brain slice and provides agreeable computational costs with a sufficiently fine spatial resolution of the considered domain.

6.3.3 Survey on the sensitivity of the involved parameters

This subsection concerns the survey of the influence of certain modelling parameters on the simulation result. First, the influence of the infusion rate is studied. This represents a quantity which can be (freely) chosen for the scheduled intervention and is applied as a boundary condition. In contrast, the values of material parameters, such as the diffusivities and the permeabilities, are basically given as patient-specific properties of the brain tissue. However, these quantities are not conclusively determined. Therefore, the variation in these material parameters is studied in order to detect their sensitivities on the computed results.

Influence of the infusion rate: As it can be seen in Figure 6.18, a duplication of the infusion rate between the referential (ref.) case and the case (i) results in a considerable extension of the therapeutical distribution. However, apart from this desired effect, the drawback lies in the side effect of also doubling the interstitial fluid pressure at the infusion site, cf. Figure 6.18 (a). Following this, one has to consider that, even when an efficient

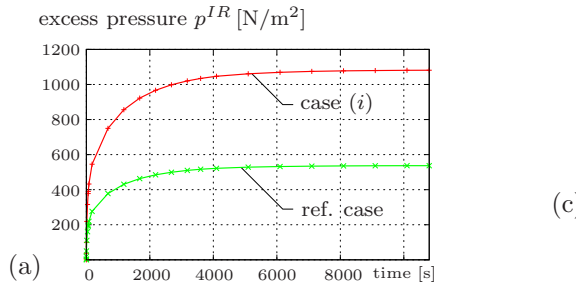

(a)

case	Q [μl/min]	$\bar{v}^I$ [m^3/m^{2}s]	c^D_{0m} [mol/l]
ref.	5.0 (0.3 ml/h)	$1.33 \cdot 10^{-6}$	$3.7 \cdot 10^{-3}$
(i)	10.0 (0.6 ml/h)	$2.65 \cdot 10^{-6}$	$3.7 \cdot 10^{-3}$

(b)

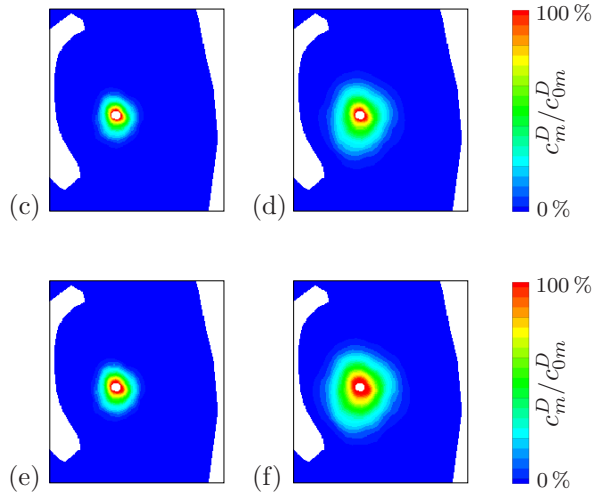

Figure 6.18: *Interstitial fluid excess pressure (a) for different infusion rates (b) and corresponding spatial drug distribution for the referential case: (c),(d) and the case (i): (e),(f) at 1 hour (left column) and 3 hours (right column).*

distribution of the therapeutic agent is requested, the local pressure should not exceed critical values in order to avoid severe complications.

Influence of the diffusivity and the permeability: The referential example of CED is generally set up with the referential set of material parameters given in Table 6.1. It has been noted before that the determination of reliable permeability values of the interstitial fluid is still subject of current research. Therefore, variations in the material properties are examined in order to study resulting effects. In particular, case (*ii*) analyses a higher Darcy permeability of the interstitial fluid in the range of $10^{-6} - 10^{-7}$ m/s. Furthermore, a lower drug diffusivity towards $10^{-10} - 10^{-11}$ m^2/s is considered in case (*iii*).

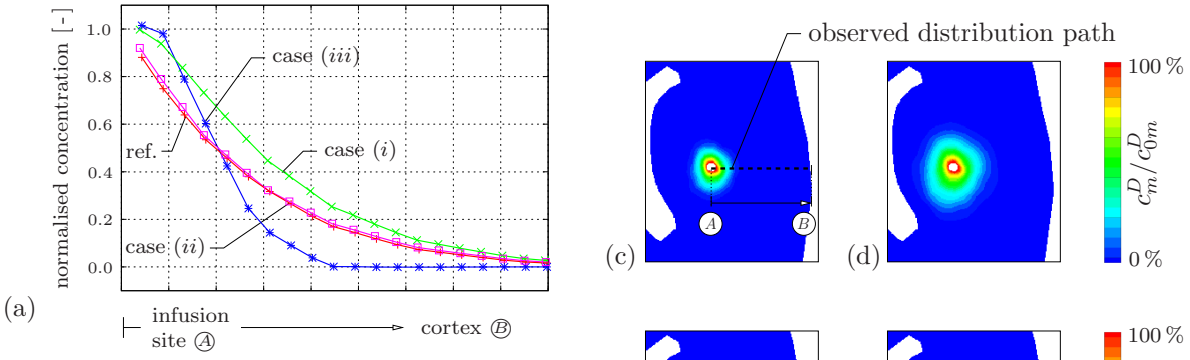

(b)

case	variation of material properties
(*ii*)	increase of interstitial fluid permeability
(*iii*)	decrease of drug diffusivity

Figure 6.19: *Drug distribution along an observed path (a) for variations in material properties (b) and spatial drug distribution for case (ii): (c), (d) and case (iii): (e), (f) after 1 hour (left column) and 3 hours (right column).*

The present example shows that a variation in the permeability of the interstitial fluid in case (*ii*) does not result in a measurable modification of the spatial distribution of the therapeutic agent compared with the referential case, cf. Figure 6.19 (a), (c) and (d). However, keeping the infusion rate constant as a boundary condition results in a decrease of the infusion pressure when the permeability is increased. For the medical application, the desired therapeutic impact can consequently be guaranteed by providing a constant application rate, but crucial infusion pressures need to be observed. Lowering the drug diffusivity in case (*iii*) results in a smaller distribution area of the therapeutic agent in combination with a thinner distribution front. But the low diffusivity also provides a high concentration of the therapeutic agent close to the infusion position, cf. Figure 6.19 (e) and (f). However, due to the low diffusivity, numerical instabilities may arise, as it is indicated by the small overshoot (non-physical concentration at the infusion site) in Figure 6.19 (a).

Sensitivity indicator: This paragraph concerns the formulation of a quantitative measure to indicate the specific influence of a certain parameter or boundary condition. Due to the numerical implementation, it is generally possible to study the sensitivity of the result as a consequence of a variation in a certain parameter via performing several computa-

tions. Note in passing that in contrast to the usual analytical computation of sensitivities, a numerical determination is investigated for the purpose of this monograph according to Karajan [87]. Therefore, a sensitivity indicator is introduced, viz.:

$$S_{R,P} = \frac{R - R_{\text{ref.}}}{R_{\text{ref.}}} \frac{P_{\text{ref.}}}{P - P_{\text{ref.}}} . \tag{6.9}$$

Therein, R denotes the computed result, which is related to its reference result $R_{\text{ref.}}$ by means of the percentage of the variation of the response. This result is further applied to the percentage of the variation of the parameter. Moreover, P and $P_{\text{ref.}}$ are the values of the corresponding modified and reference material parameters. In order to evaluate these sensitivities, the question has to be answered which response quantity R is of particular interest. Caused by the scope to model the therapeutical distribution within the brain's

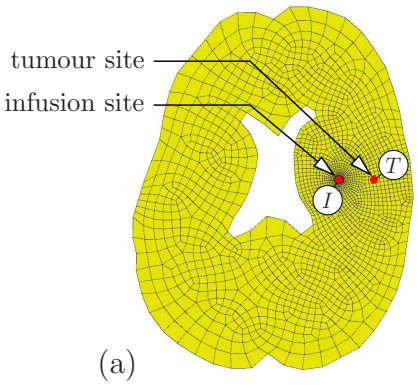

(a)

survey of the influence of involved parameters	
(i)	double the therapeutical influx $\bar{v}_I$
(ii)	increase the permeability K_{0S}^{SI} by a decade
(iii)	decrease the diffusivity D_0^D by a decade
(iv)	increase the solid skeleton stiffness: μ_0^S, λ_0^S
(v)	influence of the anisotropic characteristics

(b)

Figure 6.20: *(a) evaluation of sensitivity indicators at the infusion site I and the expected tumour site T and (b) tabular showing the investigated numerical cases.*

tissue, the responses R are chosen by the therapeutic concentration c_m^D, the interstitial fluid excess pressure p^{IR} and the von Mises equivalent stress σ_V^S. The sensitivity (6.9) is computed after three hours application time, i. e. at the end of the applied infusion process. In particular, the resulting effects are evaluated at the infusion site (I) and at an (assumed) tumour site (T), cf. Figure 6.20 (a). In addition to the preliminary introduced cases (i)-(iii), the cases (iv) and (v) are evaluated, cf. Figure 6.20 (b). The case (iv) concerns the solid's skeleton stiffness, i. e. a variation of the elastic constants, and the case (v) is related to the influence of the anisotropic (permeability and diffusivity) properties of the tissue's skeleton. Therefore, the corresponding mean quantities are utilised for the purely isotropical simplification.

Interpretation of the results: The computed absolute values are given in Table 6.2, whereas the corresponding sensitivities are collected in Table 6.3. For the purpose of this work, the following classification is used. Highly sensitive values are highlighted in red and indicated by numbers greater than 0.5. Moderate sensitive values are highlighted in orange, these are quantities in between 0.05 and 0.5, and non-sensitive quantities are smaller than 0.05. It is easily concluded for the case (i) that a doubling in the application rate crucially influences the distribution process of the infused therapeutic agents. This can be seen from a highly sensitive response at the tumour site. Furthermore, the interstitial pore pressure and the von Mises stress show a strong correlation to a change

	infusion site I			tumour site T		
	c_m^D [mol/l]	p^{IR} [N/m^2]	σ_V^S [N/m^2]	c_m^D [mol/l]	p^{IR} [N/m^2]	σ_V^S [N/m^2]
ref.-sol.	$3.7 \cdot 10^{-3}$	829.884	283.025	$1.1 \cdot 10^{-4}$	170.619	32.560
case (i)	$3.7 \cdot 10^{-3}$	1637.386	746.815	$1.7 \cdot 10^{-4}$	319.422	74.396
case (ii)	$3.7 \cdot 10^{-3}$	86.079	22.531	$1.4 \cdot 10^{-4}$	20.337	3.097
case (iii)	$3.7 \cdot 10^{-3}$	829.884	283.025	≈ 0.0[25]	170.619	32.560
case (iv)	$3.7 \cdot 10^{-3}$	860.784	224.955	$1.4 \cdot 10^{-4}$	203.365	31.027
case (v)	$3.7 \cdot 10^{-3}$	768.445	248.528	$1.3 \cdot 10^{-4}$	175.742	33.752

Table 6.2: *Computed response quantities R resulting from a variation of a certain parameter P for the cases (i)-(v).*

of the infusion boundary condition. This is seen at the infusion and the tumour site. Due to the setting of a flow boundary condition of the CED simulation, an increase of the permeability in case (ii) does not have a significant influence on the drug's spreading. In contrary, the influence on the interstitial pore pressure and the stress of the solid's skeleton is notable. This is caused by the circumstance that due to the lower permeability a higher driving pressure is needed to obtain the same flow as it is required for the chosen boundary condition.

evaluated location		infusion site I			tumour site T		
simulation parameter P / response quantity R		$S_{c_m^D,P}$	$S_{p^{IR},P}$	$S_{\sigma_V^S,P}$	$S_{c_m^D,P}$	$S_{p^{IR},P}$	$S_{\sigma_V^S,P}$
(i) application rate:	$\bar{v}_I$	0.00	0.97	1.64	0.52	0.87	1.28
(ii) permeability:	K_{0S}^{SI}	0.00	−0.10	−0.10	0.03	−0.10	−0.10
(iii) diffusivity:	D_0^D	0.00	0.00	0.00	1.11	0.00	0.00
(iv) elasticity:	μ_0^S, λ_0^S	0.00	0.00	−0.02	0.03	0.02	−0.01
(v) isotropic simplification		0.00	−0.07	−0.12	0.12	0.03	0.04

Table 6.3: *Computed sensitivities $S_{R,P}$ of parameters (columns) variations on certain responses (rows). Highly "sensitive" values are highlighted in red and moderate "sensitive" values in orange colour.*

As it is expected, a variation of the diffusivity in case (iii) does not change the interstitial fluid pressure and the solid's stress but has a dominant influence on the distribution front of the therapeutic spreading. This can be seen from the sensitivity for the therapeutic concentration at the tumour site, i. e. the therapeutic agent has not yet arrived. In case

[25] In particular, the computed value is approximately $-1.2 \cdot 10^{-9}$ mol/l. From the physical point, concentrations can be never negative. However, the negative sign is caused by numerical inaccuracies resulting from the low diffusivity. Due to the order of magnitude, this quantity can be neglected in comparison to the other concentrations at the tumour site T.

(iv), the influence of a stiffer solid skeleton is evaluated. It is found that this does not have a significant effect. Finally, in case (v) the effect of the anisotropic permeability and diffusivity properties on the spreading is studied. It is seen that in the vicinity of the infusion site an influence on the interstitial fluid pressure and the solid's extra stresses can be observed. In addition, the therapeutical distribution is effected at the tumour side. In contrast, the local effects on the pressure and the stress quantities is faded at the tumour side.

6.3.4 Further effects influencing the therapeutical distribution

Backflow along the catheter shaft: The case of backflow along the catheter shaft may occur due to a damage of the tissue caused by the insertion of the catheter or from an excessive inflow rate of the therapeutic solution. This compromises the targeted

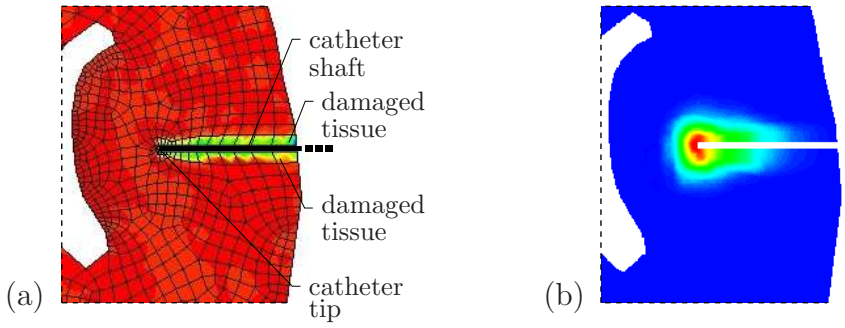

Figure 6.21: *(a) mesh, catheter placement and area of damaged tissue, (b) therapeutic spreading with consideration of backflow phenomena.*

drug delivery and consequently hampers the therapeutical success. In order to include this phenomenon in the modelling approach, the possibility of optionally increasing the permeabilities is provided. Therefore, the DTI-data of elements in the vicinity of the catheter shaft are modified by a custom MATLAB algorithm in the preliminary stage of a simulation. To set an example, the permeabilities in the damaged areas close to the catheter shaft, cf. Figure 6.21 (a), are chosen twenty times higher in comparison to their initial values. Note that this represents an arbitrarily chosen scalar factor in order to qualitatively show the resulting effects. In contrast to the calibration in (6.4), the eigenvalues are not calibrated here (with respect to their mean value) in order to allow for a quantitatively distinction in space. Hence, it is possible to map inhomogeneously distributed (anisotropic) properties. The resulting influence on the distribution profile of the therapeutic agent in the direction of the catheter shaft is clearly recognised in Figure 6.21 (b).

Incorporation of the blood-vessel system: The presented model also includes the description of the blood constituent. Therefore, it might be useful to give a prospect of future work of brain mechanics by outlining the blood flow within the brain tissue. In this regard, the incorporation of MRA-data, cf. Subsection 6.2.2, basically allows for the segmentation of the main vascular regions within the brain and, thus, the specific assignment of a location-dependent blood permeability $\mathbf{K}_{0S}^{SB}$. For this purpose, the per-

meabilities are set according to Table 6.1 by means of high values in vascular and low values in non-vascular regions, cf. Figure 6.22 (a). Within the considered IBVP, the ap-

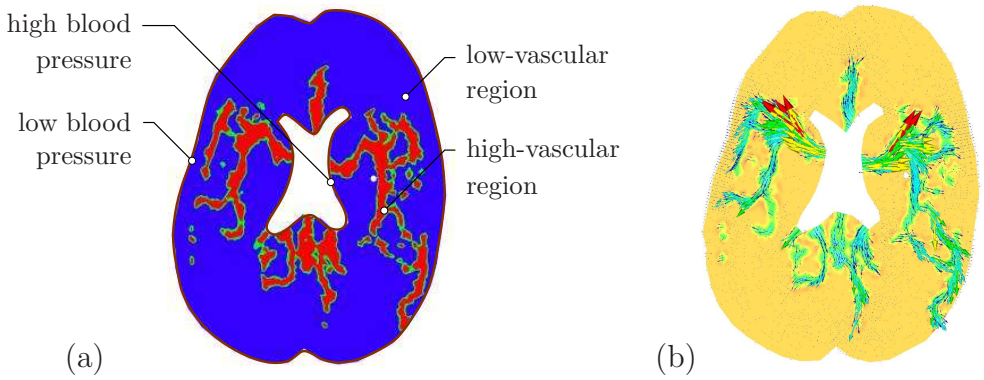

Figure 6.22: *(a) segmentation of vascular regions and (b) exemplary blood perfusion of the brain-tissue, where the displayed vectors indicate the local blood flow* $\mathbf{w}_B$.

plication of an external blood-pressure gradient (high blood pressure in the inside and low blood pressure at the outside of the brain) yields a gross idea of preferred blood perfusion pathways in the brain, cf. Figure 6.22 (b). However, this somehow artificially created scenario is surely not sufficient to map the full complexity of the blood-vessel system including the BBB. It rather serves as an outlook for further studies. Nevertheless, it clearly demonstrates the possibilities for a homogenised consideration of the blood-vessel system for those applications, where this might play an important role.

Chapter 7:
Summary and outlook

7.1 Summary

In this monograph, a suitable theoretical modelling procedure was presented, providing the numerical simulation of the material behaviour of brain tissue under certain situations. For that reason, it was initially necessary to survey the anatomical and physiological properties of the multicomponent tissue aggregate. Caused by the complex microscopical composition, this enforced an appropriate consideration of all relevant physical constituents by means of the TPM. It turned out that the TPM represents a well-suited way to include the enormous microscopical complexity of the brain-tissue architecture into a continuum-mechanical modelling approach. Proceeding from the derived multicomponent and multiphasic modelling approach, the numerical realisation enables a solid understanding of the brain's material behaviour. Moreover, the developed numerical tool provides the possibility to study (and predict scheduled) clinical applications in advance. In this regard, a novel and promising method for the effective treatment of malignant brain tumours, i. e., the direct extra-vascular infusion of therapeutic agents, was discussed in detail. Besides this considered application, the presented model can be easily adopted to the simulation of a broad variety of therapeutical medications in other (soft) biological tissues of living organisms.

For the desired simulation of such kind of applications, it was crucial to develop a customised multicomponent and multiphasic model. Although different immiscible phases are treated via standard elements of the classical TPM approach, it was additionally necessary to include miscible components in the model. Thus, elements from the Theory of Mixtures are utilised for the description of solutes by means of concentrations. In conclusion, the proposed modelling approach includes three immiscible phases, namely, the solid skeleton, the blood plasma and the overall interstitial fluid. Moreover, the overall interstitial fluid is treated as a real two-component mixture of a miscible liquid solvent and a dissolved therapeutic solute. This finally resulted in a quaternary model of brain tissue.

Regarding the constitutive modelling process, a thermodynamically consistent model was obtained via the evaluation procedure of the entropy inequality. This led to a restrictive frame, governing the constitutive settings for the specific constituents. In this context, the description of the solid skeleton was evaluated by a hyperelastic (transversely isotropic) approach, which enables for the description of finite and anisotropic deformation processes. Concerning the perfusion of the solid skeleton by the pore-liquids, a reasonable consideration of the local anisotropies and heterogeneities was integrated via a spatial diversification of the anisotropic permeability tensors, evaluated from (patient-specific) DTI data. In particular, this turned out to play a crucial role for the therapeutical spreading, especially, in the white-matter tracts, where a preferred distribution direction was

observed along the nervous fibres.

In terms of the numerical solution of the model, the resulting set of coupled partial differential equations is spatially discretised using mixed finite elements and solved in a monolithic manner with an implicit Euler time-integration scheme to obtain a robust simulation tool. Therefore, the implementation was realised within the in-house FE solver PANDAS and applied to selected IBVP. In this regard, patient-specific possibilities for the individual creation of meaningful brain geometries, based on medical imaging data, are discussed. Afterwards, the focus was placed on the numerical study of the basic material behaviour of the tissue-aggregate as well as on the numerical simulation of the drug-delivery problem within the tissue. For the latter issue, various numerical examples are presented, demonstrating the performance of the multicomponental formulation. Apart from all opportunities of the present model, the numerical studies are unfortunately still not able to provide validated quantitative predictions of the distribution of therapeutic agents. Certainly, this is partly caused by a lack of reliable patient-specific material parameters. Therefore, a numerical sensitivity analysis was additionally derived and the influence of certain material parameters and boundary conditions on the resulting therapeutical distribution was evaluated at local positions.

In conclusion, it can be stated that the theoretical and numerical investigations presented in this monograph can help to understand the complex processes occurring within the brain tissue. Moreover, the practising surgeon can benefit, in his decisions and in advance of a planned intervention, from pre-operative studies (predictions). In particular, this is urgently required for novel applications, such as the rarely applied and highly sensitive CED treatment.

7.2 Outlook

Up to now, the proposed model is able to describe the transport of applied therapeutic agents within the brain's tissue. In order to validate the obtained simulation results, a comparison with real clinical studies would be of great benefit. This may help to properly identify all relevant material parameters via additionally inserted tracers, which can be imaged in vivo and, therefore, allow for an assessment of the simulations. In this regard, different application sites (and application angles) as well as varying catheter designs can be tested to optimise the administration of therapeutics. Finally, this allows to answer the question of the spatial and temporal spreading and provides a local information of therapeutical concentration. However, the subsequently arising question concerns the response of a specific drug at a tumour site. Therefore, it is certainly necessary to include non-mechanical measures via systems-biological approaches. In general, such systems-biological relations are formulated via 0-d ordinary differential equations (ODE) and can, therefore, not be integrated into a spatially extended macroscopical approach. This can be rather investigated via a consideration in the manner of an interface solution, where the systems-biological equations are solved subsequently on Gauß point level, cf. Ehlers *et al.* [57]. Furthermore, the circumstances yielding a tumour growth or atrophy via apoptosis, need to be identified and included into the modelling approach via

the formulation of appropriate (constitutive) production terms in the constituent's mass balances. First investigations for avascular tumour growth by means of multicomponent modelling approaches are already made by, e. g., Ambrosi & Preziosi [6] or Ehlers *et al.* [57]. Furthermore, the mutual interaction of growth and atrophy processes of tumours with the occurring flow and transport mechanisms within the tissue is of fundamental interest since the originally healthy brain matrix can undergo large space-demanding deformations. This local displacement may influence the transport and diffusion properties within the ECS, resulting in a variation of the local anisotropic and heterogeneous permeabilities. Changes within the ECS may also influence the functionality of the brain and can effect the blood-vessel system and, hence, the initial blood perfusion.

Another important issue is the required computation time. Tracing in the direction of real-time applications for a convenient clinical usage, there are promising pathways such as parallel solution strategies or model-reduction techniques. Parallel solution strategies reduce the solution time via an appropriate distribution of numerical tasks to various processors in order to coordinate the computation in parallel. Since PANDAS is actually not designed for an internal parallel-solution procedure, it seems to be promising to combine PANDAS with a (commercial) FE package which already provides a parallel solution environment, such as ABAQUS[1]. This linkage allows for a straightforward transfer of material models from PANDAS with the convenient scripting environment for material definitions in PANDAS and, furthermore, for the use of a powerful graphical user interface (GUI) for pre- and post-processing purposes, cf. Schenke [136], Schenke & Ehlers [137]. Model-reduction methods aim to transform (or to approximate) a system to a low-dimensional subspace in order to minimise the computational effort while maintaining accuracy. In the meantime, various approaches have been developed. Therefore, the interested reader is referred to, e. g., Antoulas & Sorensen [8] for an overview, to Radermacher & Reese [124] for nonlinear elasticity with large deformations or to Wirtz *et al.* [172] for multiscale models using kernel methods.

[1] ABAQUS® (Dassault Systèmes, Vélizy-Villacoublay, France) is a commercial software package for finite-element analysis and computer-aided engineering, cf. http://www.3ds.com .

Appendix A:
Selected relations of tensor calculus

An excerpt of important vector and tensor operations is collected within this appendix. The chosen collection is strongly restricted to relations which are particularly required in the presented monograph. In general, the relations are extracted from the comprehensive work of Ehlers [45], which is partly based on the fundamental textbook of de Boer [19].

A.1 Tensor algebra

For the following considerations arbitrary **placeholders** are introduced, viz.:

$$
\begin{array}{lll}
\{\alpha, \beta\} & \in \mathbb{R} & : \text{scalars (zero-order tensors) as rational quantities,} \\
\{\mathbf{a}, \mathbf{b}, \mathbf{c}\} & \in \mathcal{V}^3 & : \text{vectors (first-order tensors) of the proper} \\
 & & \quad \text{Euklidian 3-d vector space } \mathcal{V}^3, \\
\{\mathbf{A}, \mathbf{B}, \mathbf{C}\} & \in \mathcal{V}^3 \otimes \mathcal{V}^3 & : \text{tensors (of second order) of the corresponding} \\
 & & \quad \text{dyadic product space } \mathcal{V}^3 \otimes \mathcal{V}^3.
\end{array}
$$

Collected rules for **products** of second-order tensors with scalars or vectors:

$$
\begin{array}{rcll}
\alpha\,(\beta\,\mathbf{A}) & = & (\alpha\,\beta)\,\mathbf{A} & : \text{associative law} \\
\mathbf{A}\,(\alpha\,\mathbf{a}) & = & \alpha(\mathbf{A}\,\mathbf{a}) \;=\; (\alpha\,\mathbf{A})\,\mathbf{a} & : \text{associative law} \\
(\alpha+\beta)\,\mathbf{A} & = & \alpha\,\mathbf{A} + \beta\,\mathbf{A} & : \text{distributive law} \\
\alpha\,(\mathbf{A}+\mathbf{B}) & = & \alpha\,\mathbf{A} + \alpha\,\mathbf{B} & : \text{distributive law} \\
\mathbf{A}\,(\mathbf{a}+\mathbf{b}) & = & \mathbf{A}\,\mathbf{a} + \mathbf{A}\,\mathbf{b} & : \text{distributive law} \\
(\mathbf{A}+\mathbf{B})\,\mathbf{a} & = & \mathbf{A}\,\mathbf{a} + \mathbf{B}\,\mathbf{a} & : \text{distributive law} \\
\alpha\,\mathbf{A} & = & \mathbf{A}\,\alpha & : \text{commutative law} \\
\mathbf{a} & = & \mathbf{A}\,\mathbf{b} & : \text{linear mapping} \\
\mathbf{I}\,\mathbf{a} & = & \mathbf{a} & : \mathbf{I} : \text{identical element (linear mapping)} \\
\mathbf{0}\,\mathbf{a} & = & \mathbf{0} & : \mathbf{0} : \text{zero element (linear mapping)}
\end{array}
\tag{A.1}
$$

Collected rules for **scalar (inner) products** of tensors:

$$
\begin{array}{rcll}
(\alpha\,\mathbf{A})\cdot\mathbf{B} & = & \mathbf{A}\cdot(\alpha\,\mathbf{B}) = \alpha\,(\mathbf{A}\cdot\mathbf{B}) & : \text{associative law} \\
\mathbf{A}\cdot(\mathbf{B}+\mathbf{C}) & = & \mathbf{A}\cdot\mathbf{B} + \mathbf{A}\cdot\mathbf{C} & : \text{distributive law} \\
\mathbf{A}\cdot\mathbf{B} & = & \mathbf{B}\cdot\mathbf{A} & : \text{commutative law} \\
\mathbf{A}\cdot\mathbf{B} & = & 0 \quad \forall\ \mathbf{A}\,, \text{ if } \mathbf{B} \equiv \mathbf{0} & \\
\mathbf{A}\cdot\mathbf{A} & > & 0 \quad \forall\ \mathbf{A} \neq \mathbf{0} &
\end{array}
\tag{A.2}
$$

Collected rules for **tensor products** of second-order tensors:

$$\begin{aligned}
\alpha\,(\mathbf{A}\,\mathbf{B}) &= (\alpha\,\mathbf{A})\,\mathbf{B} = \mathbf{A}\,(\alpha\,\mathbf{B}) && : \text{associate law}\\
(\mathbf{A}\,\mathbf{B})\,\mathbf{a} &= \mathbf{A}\,(\mathbf{B}\,\mathbf{a}) && : \text{associate law}\\
(\mathbf{A}\,\mathbf{B})\,\mathbf{C} &= \mathbf{A}\,(\mathbf{B}\,\mathbf{C}) && : \text{associate law}\\
\mathbf{A}\,(\mathbf{B}+\mathbf{C}) &= \mathbf{A}\,\mathbf{B}+\mathbf{A}\,\mathbf{C} && : \text{distributive law}\\
(\mathbf{A}+\mathbf{B})\,\mathbf{C} &= \mathbf{A}\,\mathbf{C}+\mathbf{B}\,\mathbf{C} && : \text{distributive law}\\
\mathbf{A}\,\mathbf{B} &\neq \mathbf{B}\,\mathbf{A} && : \textbf{no} \text{ commutative law}\\
\mathbf{I}\,\mathbf{A} &= \mathbf{A}\,\mathbf{I} = \mathbf{A} && : \mathbf{I} : \text{identical element (linear mapping)}\\
\mathbf{0}\,\mathbf{A} &= \mathbf{A}\,\mathbf{0} = \mathbf{0} && : \mathbf{0} : \text{zero element (linear mapping)}
\end{aligned} \tag{A.3}$$

Collected rules for **transposed** and **inverse** second-order tensors:

$$\begin{aligned}
(\mathbf{a}\otimes\mathbf{b})^T &= (\mathbf{b}\otimes\mathbf{a}) & \mathbf{A}^{-1} &= (\det\mathbf{A})^{-1}\,(\operatorname{cof}\mathbf{A})^T\\
(\alpha\,\mathbf{A})^T &= \alpha\,\mathbf{A}^T & &\rightarrow\ \mathbf{A}^{-1}\ \text{exists if}\ \det\mathbf{A}\neq 0\\
(\mathbf{A}\,\mathbf{B})^T &= \mathbf{B}^T\mathbf{A}^T &&\\
\mathbf{a}\cdot(\mathbf{B}\,\mathbf{b}) &= (\mathbf{B}^T\mathbf{a})\cdot\mathbf{b} & \mathbf{A}\,\mathbf{A}^{-1} &= \mathbf{A}^{-1}\,\mathbf{A} = \mathbf{I}\\
\mathbf{A}\cdot(\mathbf{B}\,\mathbf{C}) &= (\mathbf{B}^T\mathbf{A})\cdot\mathbf{C} & (\mathbf{A}^{-1})^T &= (\mathbf{A}^T)^{-1} =: \mathbf{A}^{T-1}\\
(\mathbf{A}+\mathbf{B})^T &= \mathbf{A}^T+\mathbf{B}^T & (\mathbf{A}\,\mathbf{B})^{-1} &= \mathbf{B}^{-1}\mathbf{A}^{-1}
\end{aligned} \tag{A.4}$$

The computation rules of the **determinant** and the **cofactor** are given via

$$\begin{aligned}
\det\mathbf{A} &= \tfrac{1}{6}\,(\mathbf{A}\between\mathbf{A})\cdot\mathbf{A} = \tfrac{1}{6}\,(\operatorname{tr}\mathbf{A})^3 - \tfrac{1}{2}\,(\operatorname{tr}\mathbf{A})\,(\mathbf{A}^T\cdot\mathbf{A}) + \tfrac{1}{3}\,(\mathbf{A}\mathbf{A})^T\cdot\mathbf{A}\\
\operatorname{cof}\mathbf{A} &= \tfrac{1}{2}\,\mathbf{A}\between\mathbf{A}\,,\quad \text{where}\quad \operatorname{cof}\mathbf{A} = \tfrac{1}{2}\,(a_{ik}\,a_{no}\,e_{inj}\,e_{kop})\,(\mathbf{e}_j\otimes\mathbf{e}_p) =: \overset{+}{a}_{jp}\,(\mathbf{e}_j\otimes\mathbf{e}_p)
\end{aligned}$$

can be evaluated using (A.8) and index notation. Thus, the coefficient matrix $\overset{+}{a}_{jp}$ contains at each position $(\,\cdot\,)_{jp}$ the corresponding subdeterminant, e. g., $\overset{+}{a}_{11} = a_{22}\,a_{33} - a_{23}\,a_{32}$.

Collected rules for the **determinant** and the **inverse** of second-order tensors:

$$\begin{aligned}
(\operatorname{cof}\mathbf{A})^T &= \operatorname{cof}\mathbf{A}^T & \det(\operatorname{cof}\mathbf{A}) &= (\det\mathbf{A})^2\\
\det\mathbf{A}^T &= \det\mathbf{A} & \det\mathbf{A}^{-1} &= (\det\mathbf{A})^{-1}\\
\det(\mathbf{A}\,\mathbf{B}) &= \det\mathbf{A}\,\det\mathbf{B} & \det(\mathbf{A}+\mathbf{B}) &= \det\mathbf{A} + \operatorname{cof}\mathbf{A}\cdot\mathbf{B} +\\
\det(\alpha\,\mathbf{A}) &= \alpha^3\,\det\mathbf{A} & &\quad + \mathbf{A}\cdot\operatorname{cof}\mathbf{B} + \det\mathbf{B}\\
\det\mathbf{I} &= 1 &&
\end{aligned} \tag{A.5}$$

Collected rules for the **trace** operator of second-order tensors:

$$\begin{aligned}
\operatorname{tr}\mathbf{A} &= \mathbf{A}\cdot\mathbf{I} & \operatorname{tr}(\alpha\,\mathbf{A}) &= \alpha\operatorname{tr}\mathbf{A}\\
\operatorname{tr}(\mathbf{a}\otimes\mathbf{b}) &= \mathbf{a}\cdot\mathbf{b} & \operatorname{tr}\mathbf{A}^T &= \operatorname{tr}\mathbf{A}\\
\operatorname{tr}(\mathbf{A}\,\mathbf{B}) &= \operatorname{tr}(\mathbf{B}\,\mathbf{A}) & \operatorname{tr}(\mathbf{A}\,\mathbf{B}\,\mathbf{C}) &= \operatorname{tr}(\mathbf{B}\,\mathbf{C}\,\mathbf{A})\\
&= \mathbf{A}\cdot\mathbf{B}^T = \mathbf{A}^T\cdot\mathbf{B} & &= \operatorname{tr}(\mathbf{C}\,\mathbf{A}\,\mathbf{B})
\end{aligned} \tag{A.6}$$

The third-order **fundamental (Ricci) tensor** and the **axial vector**:

$$\begin{aligned} \mathbf{a}\times\mathbf{b} &= \overset{3}{\mathbf{E}}(\mathbf{a}\otimes\mathbf{b}) && : \text{where } \overset{3}{\mathbf{E}} \text{ is the permutation tensor, cf. (A.8)} \\ \mathbf{A}\times\mathbf{B} &= \overset{3}{\mathbf{E}}(\mathbf{A}\,\mathbf{B}^T) && : \text{with the specific case } \mathbf{I}\times\mathbf{C} = \overset{3}{\mathbf{E}}\,\mathbf{C}^T = 2\,\overset{\mathrm{A}}{\mathbf{c}} \\ \overset{\mathrm{A}}{\mathbf{c}} &= \tfrac{1}{2}\overset{3}{\mathbf{E}}\,\mathbf{C}^T && : \text{where } \overset{A}{\mathbf{c}} \text{ is the axial vector of } \mathbf{C} \end{aligned} \tag{A.7}$$

In index notation, the properties of the permutation tensor are given, viz.:

$$\overset{3}{\mathbf{E}} = e_{ijk}\,(\mathbf{e}_i\otimes\mathbf{e}_j\otimes\mathbf{e}_k) \qquad \text{with the "permutation symbol" } e_{ijk}$$

$$e_{ijk} = \begin{cases} 1 & : \text{even permutation} \\ -1 & : \text{odd permutation} \\ 0 & : \text{double indexing} \end{cases} \longrightarrow \begin{cases} e_{123} = e_{231} = e_{312} = 1 \\ e_{321} = e_{213} = e_{132} = -1 \\ \text{all remaining } e_{ijk} \text{ vanish} \end{cases} \tag{A.8}$$

A.2 Tensor analysis

The **product rule** of derivatives of products of functions:

$$(\mathbf{a}\otimes\mathbf{b})' = \mathbf{a}'\otimes\mathbf{b} + \mathbf{a}\otimes\mathbf{b}' \qquad \text{and} \qquad (\mathbf{A}\,\mathbf{B})' = \mathbf{A}'\,\mathbf{B} + \mathbf{A}\,\mathbf{B}' \tag{A.9}$$

Collected **derivatives** of tensors and their invariants:

$$\begin{aligned} \frac{\partial\mathbf{A}}{\partial\mathbf{A}} &= (\mathbf{I}\otimes\mathbf{I})^{23}_{T} = \overset{4}{\mathbf{I}} & \frac{\partial\,\mathrm{tr}\,\mathbf{A}}{\partial\mathbf{A}} &= \mathbf{I} \\ \frac{\partial\mathbf{A}^T}{\partial\mathbf{A}} &= (\mathbf{I}\otimes\mathbf{I})^{24}_{T} & \frac{\partial\det\mathbf{A}}{\partial\mathbf{A}} &= \mathrm{cof}\,\mathbf{A} = (\det\mathbf{A})\,\mathbf{A}^{T-1} \\ \frac{\partial\mathbf{A}^{-1}}{\partial\mathbf{A}} &= -(\mathbf{A}^{-1}\otimes\mathbf{A}^{-1})^{23}_{T} & \frac{\partial\,\mathrm{cof}\,\mathbf{A}}{\partial\mathbf{A}} &= \det\mathbf{A}\,[(\mathbf{A}^{T-1}\otimes\mathbf{A}^{T-1}) - \\ & & & \quad -(\mathbf{A}^{T-1}\otimes\mathbf{A}^{T-1})^{24}_{T}] \end{aligned} \tag{A.10}$$

Selected computation rules for the **gradient** and the **divergence** operators:

$$\begin{aligned} \mathrm{grad}\,(\alpha\,\beta) &= \alpha\,\mathrm{grad}\,\beta + \beta\,\mathrm{grad}\,\alpha & \mathrm{div}\,(\mathbf{a}\otimes\mathbf{b}) &= \mathbf{a}\,\mathrm{div}\,\mathbf{b} + (\mathrm{grad}\,\mathbf{a})\,\mathbf{b} \\ \mathrm{grad}\,(\alpha\,\mathbf{b}) &= \mathbf{b}\otimes\mathrm{grad}\,\alpha + \alpha\,\mathrm{grad}\,\mathbf{b} & \mathrm{div}\,(\alpha\,\mathbf{B}) &= \mathbf{B}\,\mathrm{grad}\,\alpha + \alpha\,\mathrm{div}\,\mathbf{B} \\ \mathrm{grad}\,(\alpha\,\mathbf{B}) &= \mathbf{B}\otimes\mathrm{grad}\,\alpha + \alpha\,\mathrm{grad}\,\mathbf{B} & \mathrm{div}\,(\mathbf{A}\,\mathbf{b}) &= (\mathrm{div}\,\mathbf{A}^T)\cdot\mathbf{b} + \mathbf{A}^T\cdot\mathrm{grad}\,\mathbf{b} \\ \mathrm{div}\,(\alpha\,\mathbf{b}) &= \mathbf{b}\cdot\mathrm{grad}\,\alpha + \alpha\,\mathrm{div}\,\mathbf{b} & \mathrm{div}\left(\frac{\mathbf{b}}{\alpha}\right) &= \frac{1}{\alpha}\,\mathrm{div}\,\mathbf{b} - \frac{1}{\alpha^2}\,\mathbf{b}\cdot\mathrm{grad}\,\alpha \end{aligned} \tag{A.11}$$

Appendix B: Mechanical supplements

B.1 Polar decomposition of deformation tensors

In this section, a summary of the mathematical investigation for the polar decomposition, by means of the spectral decomposition, is derived. For a detailed discussion of this topic, the interested reader is referred to, e. g., Ehlers [45], Markert [105] or Karajan [87].

In the first instance, the eigenvalue problem is evaluated for the deformation tensors via

$$\begin{aligned} \mathbf{C}_\alpha\,\mathbf{m}_{\alpha(k)} &= \lambda_{\alpha(k)}\,\mathbf{m}_{\alpha(k)} \quad\leftrightarrow\quad (\mathbf{C}_\alpha - \lambda_\alpha\,\mathbf{I})\,\mathbf{m}_\alpha = \mathbf{0}\,, \\ \mathbf{B}_\alpha\,\mathbf{n}_{\alpha(k)} &= \lambda_{\alpha(k)}\,\mathbf{n}_{\alpha(k)} \quad\leftrightarrow\quad (\mathbf{B}_\alpha - \lambda_\alpha\,\mathbf{I})\,\mathbf{n}_\alpha = \mathbf{0}\,. \end{aligned} \tag{B.1}$$

Therein, $\lambda_{\alpha(k)} \in \mathbb{R}^+$ (for $k = 1,2,3$) denote the real and positive eigenvalues of the positive definite deformation tensors $\mathbf{C}_\alpha$ and $\mathbf{B}_\alpha$. If there are corresponding non-trivial orthogonal eigenvectors $\mathbf{m}_{\alpha(k)} \neq \mathbf{0}$ (reference configuration) and $\mathbf{n}_{\alpha(k)} \neq \mathbf{0}$ (actual configuration), the eigenvalue problem (B.1) can be solved via the characteristic polynomial

$$\det(\mathbf{C}_\alpha - \lambda_\alpha\,\mathbf{I}) = \det(\mathbf{B}_\alpha - \lambda_\alpha\,\mathbf{I}) = \lambda_\alpha^3 - I_{\alpha1}\,\lambda_\alpha^2 + I_{\alpha2}\,\lambda_\alpha - I_{\alpha3} = 0\,. \tag{B.2}$$

Therein, the principal invariants are given in terms of the deformation tensors, viz.:

$$\begin{aligned} I_{\alpha1} &= \operatorname{tr}\mathbf{C}_\alpha &&= \operatorname{tr}\mathbf{B}_\alpha &&= \mathbf{F}_\alpha \cdot \mathbf{F}_\alpha\,, \\ I_{\alpha2} &= \operatorname{tr}(\operatorname{cof}\mathbf{C}_\alpha) &&= \operatorname{tr}(\operatorname{cof}\mathbf{B}_\alpha) &&= \operatorname{cof}\mathbf{F}_\alpha \cdot \operatorname{cof}\mathbf{F}_\alpha\,, \\ I_{\alpha3} &= \det\mathbf{C}_\alpha &&= \det\mathbf{B}_\alpha &&= (\det\mathbf{F}_\alpha)^2\,. \end{aligned} \tag{B.3}$$

Moreover, the relation between the eigenvalues and the principal invariants

$$\begin{aligned} I_{\alpha1} &= \lambda_{\alpha(1)} + \lambda_{\alpha(2)} + \lambda_{\alpha(3)}\,, \\ I_{\alpha2} &= \lambda_{\alpha(1)}\,\lambda_{\alpha(2)} + \lambda_{\alpha(2)}\,\lambda_{\alpha(3)} + \lambda_{\alpha(3)}\,\lambda_{\alpha(1)}\,, \\ I_{\alpha3} &= \lambda_{\alpha(1)}\,\lambda_{\alpha(2)}\,\lambda_{\alpha(3)} \end{aligned} \tag{B.4}$$

holds. Based on this, the so-called spectral representation (of arbitrary real-valued powers $m \in \mathbb{R}$) of deformation tensors are expressed via

$$\begin{aligned} (\mathbf{C}_\alpha)^m &= \sum_{k=1}^{3} (\lambda_{\alpha(k)})^m\,\mathbf{M}_{\alpha(k)}\,, \qquad \text{with} \quad \mathbf{M}_{\alpha(k)} := \mathbf{m}_{\alpha(k)} \otimes \mathbf{m}_{\alpha(k)}\,, \\ (\mathbf{B}_\alpha)^m &= \sum_{k=1}^{3} (\lambda_{\alpha(k)})^m\,\mathbf{N}_{\alpha(k)}\,, \qquad \text{with} \quad \mathbf{N}_{\alpha(k)} := \mathbf{n}_{\alpha(k)} \otimes \mathbf{n}_{\alpha(k)}\,. \end{aligned} \tag{B.5}$$

Therefore, the right and left solid stretch tensors are directly obtained in spectral representation, viz.:

$$\begin{aligned} \mathbf{U}_\alpha &= (\mathbf{C}_\alpha)^{\frac{1}{2}} = \sum_{k=1}^{3} \sqrt{\lambda_{\alpha(k)}}\, \mathbf{M}_{\alpha(k)} \quad , \quad \mathbf{V}_\alpha = (\mathbf{B}_\alpha)^{\frac{1}{2}} = \sum_{k=1}^{3} \sqrt{\lambda_{\alpha(k)}}\, \mathbf{N}_{\alpha(k)} \,, \\ \mathbf{R}_\alpha &= \sum_{k=1}^{3} \mathbf{n}_{\alpha(k)} \otimes \mathbf{m}_{\alpha(k)} \qquad \rightarrow \qquad \mathbf{F}_\alpha = \sum_{k=1}^{3} \sqrt{\lambda_{\alpha(k)}}\, \mathbf{n}_{\alpha(k)} \otimes \mathbf{m}_{\alpha(k)} \,. \end{aligned} \tag{B.6}$$

From (B.6), it is easily concluded that the deformation gradient $\mathbf{F}_\alpha$ as well as the right and the left stretch tensors $\mathbf{U}_\alpha$ and $\mathbf{V}_\alpha$ share the same set of eigenvalues. Moreover, the eigenvalues of the deformation tensors are the squares of the these. To summarise, the evaluation of the spectral decomposition of the deformation tensors $\mathbf{C}_\alpha$ (or $\mathbf{B}_\alpha$) allows for an unique right (or left) decomposition of the deformation gradient $\mathbf{F}_\alpha$.

B.2 Natural basis representation of deformation and strain measures

The transport mechanisms performed by the material deformation gradient $\mathbf{F}_S$ and the association of the deformation and strain measures with its corresponding configuration can be illustrated using the natural basis representation, cf., e. g., Ehlers [45], Holzapfel [79], Karajan [87] or Markert [105].

In this regard, the covariant natural basis vectors are introduced with respect to postulated contravariant convective curvilinear coordinate lines θ^i_S, cf. Figure B.1, attached to the solid's reference configuration, which continuously follow the deformation of φ^S. In particular,

$$\mathbf{h}_{Si} := \frac{\partial \mathbf{X}_S}{\partial \theta^i_S} \quad \text{and} \quad \mathbf{a}_{Si} := \frac{\partial \mathbf{x}}{\partial \theta^i_S} \tag{B.7}$$

are defined, where $\mathbf{h}_{Si}$ is related to the reference configuration and $\mathbf{a}_{Si}$ to the actual configuration, respectively. In contrast, the contravariant basis vectors are derived by

$$\mathbf{h}^i_S = \frac{\partial \theta^i_S}{\partial \mathbf{X}_S} \quad \text{and} \quad \mathbf{a}^i_S = \frac{\partial \theta^i_S}{\partial \mathbf{x}} \,. \tag{B.8}$$

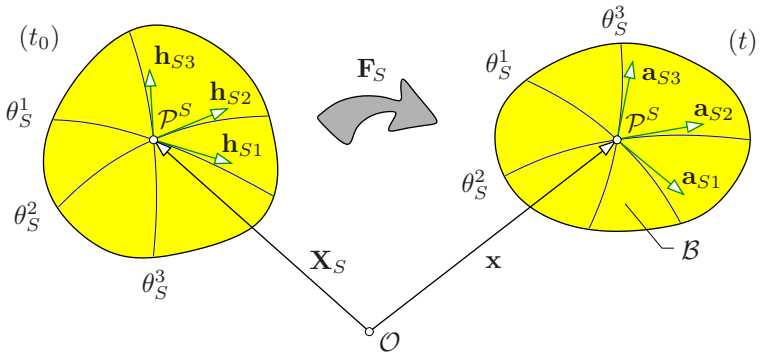

Figure B.1: *Natural basis representation.*

Although the co- and contravariant basis vectors do not constitute, in general, an orthonormal basis system, the tangent space (B.7) and the corresponding cotangent (dual) space (B.8) are conjugated by means of satisfying

$$\mathbf{h}_S^i \cdot \mathbf{h}_{Sk} = \delta_k^i \quad \text{and} \quad \mathbf{a}_S^i \cdot \mathbf{a}_{Sk} = \delta_k^i \,. \tag{B.9}$$

Therein, the mixed Kronecker delta δ_k^i yields either one, for the case of an equal indication ($i = k$), or zero for different indices ($i \neq k$). Thus, a contravariant basis vector $(\,\cdot\,)^i$ is, for $i \neq k$, always perpendicular to the covariant basis vectors $(\,\cdot\,)_k$. Proceeding from (3.29) and including the above considerations (B.7) and (B.8), it follows for the deformation gradient and its inverse

$$\begin{aligned} \mathbf{F}_S &= \frac{\partial \mathbf{x}}{\partial \mathbf{X}_S} = \frac{\partial \mathbf{x}}{\partial \theta_S^i} \otimes \frac{\partial \theta_S^i}{\partial \mathbf{X}_S} = \mathbf{a}_{Si} \otimes \mathbf{h}_S^i \,, \\ \mathbf{F}_S^{-1} &= \frac{\partial \mathbf{X}_S}{\partial \mathbf{x}} = \frac{\partial \mathbf{X}_S}{\partial \theta_S^i} \otimes \frac{\partial \theta_S^i}{\partial \mathbf{x}} = \mathbf{h}_{Si} \otimes \mathbf{a}_S^i \,. \end{aligned} \tag{B.10}$$

It is obvious, that $\mathbf{F}_S$ represents a two-field tensor and provides the (push-forward and pull-back) transformations of co- and contravariant basis vectors via

$$\begin{aligned} \mathbf{a}_{Si} &= \mathbf{F}_S \, \mathbf{h}_{Si} \qquad \longleftrightarrow \quad \mathbf{h}_{Si} = \mathbf{F}_S^{-1} \, \mathbf{a}_{Si} \,, \\ \mathbf{a}_S^i &= \mathbf{F}_S^{T-1} \, \mathbf{h}_S^i \qquad \longleftrightarrow \quad \mathbf{h}_S^i = \mathbf{F}_S^T \, \mathbf{a}_S^i \,. \end{aligned} \tag{B.11}$$

Moreover, the deformation and strain measures can be formulated in terms of the natural basis representation. Using the relations (B.10), one finds

$$\begin{aligned} \mathbf{C}_S &= \mathbf{F}_S^T \, \mathbf{F}_S &&= a_{Sik} \, (\mathbf{h}_S^i \otimes \mathbf{h}_S^k) \,, \\ \mathbf{B}_S &= \mathbf{F}_S \, \mathbf{F}_S^T &&= h_S^{ik} \, (\mathbf{a}_{Si} \otimes \mathbf{a}_{Sk}) \,, \\ \mathbf{C}_S^{-1} &= \mathbf{F}_S^{-1} \, \mathbf{F}_S^{T-1} &&= a_S^{ik} \, (\mathbf{h}_{Si} \otimes \mathbf{h}_{Sk}) \,, \\ \mathbf{B}_S^{-1} &= \mathbf{F}_S^{T-1} \, \mathbf{F}_S^{-1} &&= h_{Sik} \, (\mathbf{a}_S^i \otimes \mathbf{a}_S^k) \,, \\ \mathbf{E}_S &= \tfrac{1}{2} \, (\mathbf{C}_S - \mathbf{I}) &&= \tfrac{1}{2} \, (a_{Sik} - h_{Sik}) \, (\mathbf{h}_S^i \otimes \mathbf{h}_S^k) \,, \\ \mathbf{A}_S &= \tfrac{1}{2} \, (\mathbf{I} - \mathbf{B}_S^{-1}) &&= \tfrac{1}{2} \, (a_{Sik} - h_{Sik}) \, (\mathbf{a}_S^i \otimes \mathbf{a}_S^k) \,, \\ \overset{\text{R}}{\mathbf{K}}_S &= \tfrac{1}{2} \, (\mathbf{I} - \mathbf{C}_S^{-1}) &&= \tfrac{1}{2} \, (h_S^{ik} - a_S^{ik}) \, (\mathbf{h}_{Si} \otimes \mathbf{h}_{Sk}) \,, \\ \mathbf{K}_S &= \tfrac{1}{2} \, (\mathbf{B}_S - \mathbf{I}) &&= \tfrac{1}{2} \, (h_S^{ik} - a_S^{ik}) \, (\mathbf{a}_{Si} \otimes \mathbf{a}_{Sk}) \,. \end{aligned} \tag{B.12}$$

Therein, $(\,\cdot\,)_{Sik}$ and $(\,\cdot\,)_S^{ik}$ denote the co- and contravariant metric coefficients, constituted by the scalar product of the corresponding basis vectors. Note that in the representation derived in (B.12), one can clearly identify by the suffixed basis, in which configuration the quantities are defined. Moreover, the kind of variance of the measure is easily indicated.

B.3 Specific kinematical relations and transformations

Rate of the deformation gradient: Based on the material time derivative of the material deformation gradient, i. e. $(\mathbf{F}_\alpha)'_\alpha = \mathbf{L}_\alpha \mathbf{F}_\alpha$, the corresponding relations for the time derivative of its inverse and its transposed quantity are found via building the identity and take the material time derivative on both sides, viz.:

$$\begin{aligned}
\mathbf{I} = \mathbf{F}_\alpha^{-1}\mathbf{F}_\alpha \quad &\rightarrow \mathbf{0} = (\mathbf{F}_\alpha^{-1})'_\alpha \mathbf{F}_\alpha + \mathbf{F}_\alpha^{-1}(\mathbf{F}_\alpha)'_\alpha \\
&\rightarrow (\mathbf{F}_\alpha^{-1})'_\alpha = -\mathbf{F}_\alpha^{-1}(\mathbf{F}_\alpha)'_\alpha \mathbf{F}_\alpha^{-1} = -\mathbf{F}_\alpha^{-1}\mathbf{L}_\alpha\,, \\
\mathbf{I} = \mathbf{F}_\alpha^{T-1}\mathbf{F}_\alpha^{T} \quad &\rightarrow \mathbf{0} = (\mathbf{F}_\alpha^{T-1})'_\alpha \mathbf{F}_\alpha^{T} + \mathbf{F}_\alpha^{T-1}(\mathbf{F}_\alpha^{T})'_\alpha \\
&\rightarrow (\mathbf{F}_\alpha^{T-1})'_\alpha = -\mathbf{F}_\alpha^{T-1}(\mathbf{F}_\alpha^{T})'_\alpha \mathbf{F}_\alpha^{T-1} = -\mathbf{L}_\alpha^{T}\mathbf{F}_\alpha^{T-1} \\
&\rightarrow (\mathbf{F}_\alpha^{T})'_\alpha = -\mathbf{F}_\alpha^{T}(\mathbf{F}_\alpha^{T-1})'_\alpha \mathbf{F}_\alpha^{T} = \mathbf{F}_\alpha^{T}\mathbf{L}_\alpha^{T}\,.
\end{aligned} \tag{B.13}$$

Rearrangement of the blood's momentum balance: The transformation

$$\begin{aligned}
\frac{p_{\text{dif.}}}{s^B}\operatorname{grad} s^B &= \frac{p_{\text{dif.}}}{n^B}(n^F \operatorname{grad} s^B) \\
&= \frac{p_{\text{dif.}}}{n^B}(\operatorname{grad}(n^F s^B) - s^B \operatorname{grad} n^F) \\
&= \frac{p_{\text{dif.}}}{n^B}(\operatorname{grad} n^B - s^B \operatorname{grad} n^B - s^B \operatorname{grad} n^I) \\
&= \frac{p_{\text{dif.}}}{n^B}(s^I \operatorname{grad} n^B - s^B \operatorname{grad} n^I)
\end{aligned} \tag{B.14}$$

of the rightmost part in the parenthesis of $(4.76)_{3,4}$ is verified using the relations (3.6) and $(A.11)_1$.

Bibliography

[1] *PANDAS: Porous media Adaptive Nonlinear finite element solver based on Differential Algebraic Systems*. User manual. Institute of Applied Mechanics (CE), Chair of Continuum Mechanics, University of Stuttgart 2014.

[2] Abbott, N. J.: Evidence for bulk flow of brain interstitial fluid: significance for physiology and pathology. *Neurochemistry International* **45** (2004), 545–552.

[3] Acartürk, A.: *Simulation of Charged Hydrated Porous Media*. Dissertation, Report No. II-18 of the Institute of Applied Mechanics (CE), University of Stuttgart 2009.

[4] Adam, G.; Läuger, P. & Stark, G.: *Physikalische Chemie und Biophysik*. Springer-Verlag, Berlin 2009.

[5] Altenbach, H.: *Kontinuumsmechanik: Einführung in die materialunabhängigen und materialabhängigen Gleichungen*. Springer-Verlag, Berlin 2012.

[6] Ambrosi, D. & Preziosi, L.: On the closure of mass balance models for tumor growth. *Mathematical Models and Methods in Applied Sciences* **12** (2002), 737–754.

[7] Ammann, M.: *Parallel Finite Element Simulations of Localization Phenomena in Porous Media*. Dissertation, Report No. II-11 of the Institute of Applied Mechanics (CE), University of Stuttgart 2005.

[8] Antoulas, A. C. & Sorensen, D. C.: Approximation of large-scale dynamical systems: An overview. *Applied Mathematics and Computer Science* **11** (2001), 1093–1122.

[9] Ateshian, G. A. & Weiss, J. A.: Anisotropic hydraulic permeability under finite deformation. *Journal of Biomechanical Engineering* **132** (2010), 111004.

[10] Avci, O.: *Coupled Deformation and Flow Processes of Partial Saturated Soil: Experiments, Model Validation and Numerical Investigations*. Dissertation, Report No. II-26 of the Institute of Applied Mechanics (CE), University of Stuttgart 2013.

[11] Basser, P. J.: Interstitial pressure, volume, and flow during infusion into brain tissue. *Microvascular Research* **44** (1992), 143–165.

[12] Basser, P. J.; Mattielo, J. & Lebihan, D.: Estimation of effective self-diffusion tensor from the NMR spin-echo. *Journal of Magnetic Resonance* **103** (1994), 247–254.

[13] Basser, P. J.; Pajevic, S.; Pierpaoli, C.; Duda, J. & Aldroubi, A.: In vivo fiber tractography using DT-MRI data. *Magnetic Resonance in Medicine* **44** (2000), 625–632.

[14] Bathe, K. J.: *Finite-Elemente-Methoden*. 2nd edn. Springer-Verlag, Berlin 2002.

[15] Baxter, L. T. & Jain, R. K.: Transport of fluid and macromolecules in tumors: I. role of interstitial pressure and convection. *Microvascular Research* **37** (1989), 77–104.

[16] Blasberg, R.; Patlak, C. & Fenstermacher, J.: Intrathecal chemotherapy: brain tissue profiles after ventriculocisternal perfusion. *Journal of Pharmacology and Experimental Therapeutics* **195** (1975), 73–83.

[17] Bleiler, C.: *Application of medical imaging to simulate anisotropic flow in porous media*. Diplomarbeit, Report No. 12-II-9 of the Institute of Applied Mechanics (CE), University of Stuttgart 2012.

[18] Bobo, R. H.; Laske, D. W.; Akbasak, A.; Morrison, P. F.; Dedrick, R. L. & Oldfield, E. H.: Convection-enhanced delivery of macromolecules in the brain. *Proceedings of the National Academy of Sciences* **91** (1994), 2076–2080.

[19] de Boer, R.: *Vektor- und Tensorrechnung für Ingenieure*. Springer-Verlag, Berlin 1982.

[20] de Boer, R.: Highlights in the historical development of porous media theory: toward a consistent macroscopic theory. *Applied Mechanics Review* **49** (1996), 201–262.

[21] de Boer, R.: *Theory of Porous Media.* Springer-Verlag, Berlin 2000.

[22] de Boer, R.: *Trends in continuum mechanics of porous media, Vol. 18*. Theory and applications of transport in porous media, Springer, Dodrecht 2005.

[23] de Boer, R. & Ehlers, W.: *Theorie der Mehrkomponentenkontinua mit Anwendungen auf bodenmechanische Probleme*. Forschungsberichte aus dem Fachbereich Bauwesen, Heft 40, Universität-GH-Essen 1986.

[24] de Boer, R. & Ehlers, W.: A historical review of the formulation of porous media theories. *Acta Mechanica* **74** (1988), 1–8.

[25] Bowen, R. M.: Toward a thermodynamics and mechanics of mixtures. *Archive for Rational Mechanics and Analysis* **24** (1967), 370–403.

[26] Bowen, R. M.: Theory of mixtures. In Eringen, A. C. (ed.): *Continuum Physics, Vol. 3*. Academic Press, New York 1976, pp. 1–127.

[27] Bowen, R. M.: Incompressible porous media models by use of the theory of mixtures. *International Journal of Engineering Science* **18** (1980), 1129–1148.

[28] Bowen, R. M.: Compressible porous media models by use of the theory of mixtures. *International Journal of Engineering Science* **20** (1982), 697–735.

[29] Braess, D.: *Finite Elemente*. Springer-Verlag, Berlin 1997.

[30] Breasted, J. H.: *The Edwin Smith Surgical Papyrus*. University of Chicago Press, Chicago 1930.

[31] Brezzi, F. & Fortin, M.: *Mixed and Hybrid Finite Element Methods*. Springer-Verlag, New York 1991.

[32] Brooks, P. J.; Cheng, T.-F. & Cooper, L.: Do all of the neurologic diseases in patients with DNA repair gene mutations result from the accumulation of DNA damage? *DNA Repair* **7** (2008), 834–848.

[33] Cacioppo, J.; Tassinary, L. & Berntson, G.: *Handbook of Psychophysiology*. Cambridge University Press, Cambridge 2007.

[34] Chen, X. & Sarntinoranont, M.: Biphasic finite element model of solute transport for direct infusion into nervous tissue. *Annals of Biomedical Engineering* **35** (2007), 2145–2158.

[35] Chen, Z.; Broaddus, W. C.; Viswanathan, R. R.; Raghavan, R. & Gillies, G. T.: Intraparenchymal drug delivery via positive-pressure infusion: Experimental and modeling studies of poroelasticity in brain phantom gels. *IEEE Transactions on Biomedical Engineering* **49** (2002), 85–96.

[36] Coleman, B. D. & Noll, W.: The thermodynamics of elastic materials with heat conduction and viscosity. *Archive of Rational Mechanics and Analysis* **13** (1963), 167–178.

[37] Darcis, M.: *Erarbeitung und Implementierung eines Modellkonzepts zur Simulation von Strömungs- und Transportprozessen im menschlichen Gehirn*. Diplomarbeit, Institut für Wasser- und Umweltsystemmodellierung, University of Stuttgart 2007.

[38] Diebels, S.: *Mikropolare Zweiphasenmodelle: Formulierung auf der Basis der Theorie Poröser Medien*. Habilitation, Bericht Nr. II-4 aus dem Institut für Mechanik (Bauwesen), Universität Stuttgart 2000.

[39] Ding, D.; Kanaly, C. W.; Brady, M. L.; Mittermeyer, S.; Raghavan, R. & Sampson, J. H.: Convection-enhanced drug delivery to the brain. In Jain, K. K. (ed.): *Drug Delivery to the Central Nervous System*. Humana Press, New York 2010, pp. 291–318.

[40] Dolecek, T. A.; Propp, J. M.; Stroup, N. E. & Kruchko, C.: CBTRUS statistical report: Primary brain and central nervous system tumors diagnosed in the United States in 2005-2009. *Neuro-Oncology* **14** (2012), v1–v49.

[41] Dutta-Roy, T.; Wittek, A. & Miller, K.: Biomechanical modelling of normal pressure hydrocephalus. *Journal of Biomechanics* **41** (2008), 2263–2271.

[42] Duvernoy, H. M.; Delon, S. & Vannson, J.: Cortical blood vessels of the human brain. *Brain Research Bulletin* **7** (1981), 519–579.

[43] Effelsberg, J.: *Untersuchung der Diffusions- und Strömungsprozesse in der menschlichen Bandscheibe mittels Magnetresonanztomographie*. Diplomarbeit, Bericht Nr. 07-II-2 aus dem Institut für Mechanik (Bauwesen), Universität Stuttgart 2007.

[44] Ehlers, W.: *Poröse Medien – ein kontinuumsmechanisches Modell auf der Basis der Mischungstheorie*, 2012. Nachdruck der Habilitationsschrift aus dem Jahre 1989 (Forschungsbericht aus dem Fachbereich Bauwesen der Universität-GH-Essen, Heft 47, Essen 1989).

[45] Ehlers, W.: *Vector and Tensor Calculus: An Introduction*. Lecture notes, Institute of Applied Mechanics, Chair of Continuum Mechanics, University of Stuttgart 1995–2014.

[46] Ehlers, W.: *Elemente der nichtlinearen Kontinuumsthermodynamik*. Lecture notes, Institute of Applied Mechanics, Chair of Continuum Mechanics, University of Stuttgart 1996.

[47] Ehlers, W.: Grundlegende Konzepte in der Theorie Poröser Medien. *Technische Mechanik* **16** (1996), 63–76.

[48] Ehlers, W.: *Einführung in die Kontinuumsmechanik von Mehrphasenmaterialien*. Lecture notes, Institute of Applied Mechanics, Chair of Continuum Mechanics, University of Stuttgart 1997.

[49] Ehlers, W.: *Numerische Methoden in der Mechanik*. Lecture notes, Institute of Applied Mechanics, Chair of Continuum Mechanics, University of Stuttgart 1998.

[50] Ehlers, W.: Foundations of multiphasic and porous materials. In Ehlers, W. & Bluhm, J. (eds.): *Porous Media: Theory, Experiments and Numerical Applications*. Springer-Verlag, Berlin 2002, pp. 3–86.

[51] Ehlers, W.: Challenges of porous media models in geo- and biomechanical engineering including electro-chemically active polymers and gels. *International Journal of Advances in Engineering Sciences and Applied Mathematics* **1** (2009), 1–24.

[52] Ehlers, W. & Eipper, G.: Finite elastic deformations in liquid-saturated and empty porous solids. *Transport in Porous Media* **34** (1999), 179–191.

[53] Ehlers, W. & Ellsiepen, P.: PANDAS: Ein FE-System zur Simulation von Sonderproblemen der Bodenmechanik. In Wriggers, P.; Meiner, U.; Stein, E. & Wunderlich, W. (eds.): *Finite Elemente in der Baupraxis - FEM'98*. Ernst & Sohn, Berlin 1998, pp. 391–400.

[54] Ehlers, W.; Ellsiepen, P.; Blome, P.; Mahnkopf, D. & Markert, B.: *Theoretische und numerische Studien zur Lösung von Rand- und Anfangswertproblemen in der Theorie Poröser Medien, Abschlußbericht zum DFG-Forschungsvorhaben Eh 107/6-2*. Bericht Nr. 99-II-1 aus dem Institut für Mechanik (Bauwesen), Universität Stuttgart 1999.

[55] Ehlers, W.; Karajan, N. & Markert, B.: A porous media model describing the inhomogeneous behaviour of the human intervertebral disc. *Materials Science and Engineering Technology* **37** (2006), 546–551.

[56] Ehlers, W.; Karajan, N. & Markert, B.: An extended biphasic model for charged hydrated tissues with application to the intervertebral disc. *Biomechanics and Modeling in Mechanobiology* **8** (2009), 233–251.

[57] Ehlers, W.; Krause, R. & Markert, B.: Modelling and remodelling of biological tissue in the framework of continuum biomechanics. *Proceedings in Applied Mathematics and Mechanics* **11** (2011), 35–38.

[58] Ehlers, W.; Ramm, E.; Diebels, S. & D'Addetta, G. A.: From particle ensembles to cosserat continua: homogenization of contact forces towards stresses and couple stresses. *International Journal of Solids and Structures* **40** (2003), 6681–6702.

[59] Ehlers, W. & Wagner, A.: Constitutive and computational aspects in tumor therapies of multiphasic brain tissue. In Holzapfel, G. A. & Kuhl, E. (eds.): *Computer Models in Biomechanics*. Springer Netherlands, Dordrecht 2013, pp. 263–276.

[60] Ehlers, W. & Wagner, A.: Multi-component modelling of human brain tissue: a contribution to the constitutive and computational description of deformation, flow and diffusion processes with application to the invasive drug-delivery problem. *Computer Methods in Biomechanics and Biomedical Engineering* (2013), doi:10.1080/10255842.2013.853754.

[61] Ehlers, W.; Zinatbakhsh, S. & Markert, B.: Stability analysis of finite difference schemes revisited: A study of decoupled solution strategies for coupled multifield problems. *International Journal for Numerical Methods in Engineering* **94** (2013), 758–786.

[62] Eipper, G.: *Theorie und Numerik finiter elastischer Deformationen in fluidgesättigten porösen Festkörpern*. Dissertation, Bericht Nr. II-1 aus dem Institut für Mechanik (Bauwesen), Universität Stuttgart 1998.

[63] Ellsiepen, P.: *Zeit- und ortsadaptive Verfahren angewandt auf Mehrphasenprobleme poröser Medien*. Dissertation Bericht Nr. II-3 aus dem Institut für Mechanik (Bauwesen), Universität Stuttgart 1999.

[64] Eringen, A. C.: *Continuum Physics*. Academic Press, New York 1975.

[65] Fallenstein, G.; Hulce, V. & Melvin, J.: Dynamic mechanical properties of human brain tissue. *Journal of Biomechanics* **2** (1969), 217–226.

[66] Federico, S.: Porous fibre-reinforced materials under large deformations. In *Proceedings of the 2009 AIMETA Congress,* Ancona 2009, pp. 612–613.

[67] Franceschini, G.; Bigoni, D.; Regitnig, P. & Holzapfel, G. A.: Brain tissue deforms similarly to filled elastomers and follows consolidation theory. *Journal of Mechanics and Physics of Solids* **54** (2006), 2592–2620.

[68] Franke, E. K.: The response of the human skull to mechanical vibrations. *Journal of the Acoustical Society of America* **28** (1956), 1277–1284.

[69] Fredlund, D. G. & Rahardjo, H.: *Soil mechanics for unsaturated soils*. John Wiley & Sons, New York 1993.

[70] Graf, T.: *Multiphasic Flow Processes in Deformable Porous Media under Consideration of Fluid Phase Transitions*. Dissertation, Report No. II-17 of the Institute of Applied Mechanics (CE), University of Stuttgart 2008.

[71] Gray, H.: *Anatomy of the Human Body*. Lea & Febiger, Philadelphia 1918.

[72] Groothuis, D. R.; Benalcazar, H. & Allen, C. V.: Comparison of cytosine arabinoside delivery to rat brain by intraveneous, intrathecal, intraventricular and intraparenchymal routes of administration. *Brain Research* **856** (2000), 281–290.

[73] Hakim, S. & Adams, R. D.: The special clinical problem of symptomatic hydrocephalus with normal cerebrospinal fluid pressure - observations on cerebrospinal fluid hydrodynamics. *Journal of Neurological Sciences* **2** (1965), 307–327.

[74] Hall, W. A.; Rustamzadeh, E. & Asher, A. L.: Convection-enhanced delivery in clinical trials. *Neurosurgical Focus* **14** (2003), 1–4.

[75] Hassanizadeh, M. & Gray, W. M.: General conservation equations for muti-phase systems: 2. Mass, momenta, energy and entropy equations. *Advances in Water Resources* **2** (1979), 191–203.

[76] Haupt, P.: *Continuum Mechanics and Theory of Materials*. Springer 2002.

[77] Heider, Y.: *Saturated Porous Media Dynamics with Application to Earthquake Engineering*. Dissertation, Report No. II-25 of the Institute of Applied Mechanics (CE), University of Stuttgart 2012.

[78] Hlawatsch, M.; Vollrath, J. E.; Sadlo, F. & Weiskopf, D.: Coherent structures of characteristic curves in symmetric second order tensor fields. *IEEE Transactions on Visualization and Computer Graphics* **17** (2011), 781–794.

[79] Holzapfel, G. A.: *Nonlinear Solid Mechanics: A Continuum Approach for Engineering*. Wiley, Chichester 2000.

[80] Hughes, T. J. R.: *The Finite Element Method: Linear Static and Dynamic Finite Element Analysis*. Dover Publications, New York 2012.

[81] Ivanchenko, O.; Sindhwani, N. & Linninger, A.: Experimental techniques for studying poroelasticity in brain phantom gels under high flow microinfusion. *Journal of Biomechanical Engineering* **132** (2010), 051008.

[82] Jain, R. K.: Transport of molecules across tumor vasculature. *Cancer and Metastasis Reviews* **6** (1987), 559–593.

[83] Jain, R. K.: Determinants of tumor blood flow: a review. *Cancer Research* **48** (1988), 2641–2658.

[84] Kaatsch, P.; Spix, C.; Katalinic, A.; Hentschel, S.; Baras, N.; Barnes, B.; Bertz, J.; Dahm, S.; Haberland, J.; Kraywinkel, K.; Laudi, A. & Wolf, U.: *Krebs in Deutschland 2007/2008*, 8th edn. Robert-Koch-Institut und die Gesellschaft der epidemiologischen Krebsregister in Deutschland e. V., Berlin 2012.

[85] Kaczmarek, M.; Subramaniam, R. P. & Neff, S. R.: The hydromechanics of hydrocephalus: steady-state solutions for cylindrical geometry. *Bulletin of Mathematical Biology* **59** (1997), 295–323.

[86] Karajan, N.: *Finite elasticity of fibre-reinforced materials*. Diploma thesis, Report No. II-12 of the Institute of Applied Mechanics (CE), University of Stuttgart 2003.

[87] Karajan, N.: *An Extended Biphasic Description of the Inhomogeneous and Anisotropic Intervertebral Disc*. Dissertation, Report No. II-19 of the Institute of Applied Mechanics (CE), University of Stuttgart 2009.

[88] Kawakami, K.; Kawakami, M. & Kioi, M.: Distribution kinetics of targeted cytotoxin in glioma by bolus or convection-enhanced delivery in a murine model. *Journal of Neurosurgery* **101** (2004), 1004–1011.

[89] Kedem, O. & Katchalsky, A.: Thermodynamic analysis of the permeability of biological membranes to non-electrolytes. *Biochimica et Biophysica Acta* **27** (1958), 229–246.

[90] Kelly, P. D.: A reacting continuum. *International Journal of Engineering Science* **2** (1964), 129–153.

[91] Kim, J. H.; Mareci, T. H. & Sarntinoranont, M.: A voxelized model of direct infusion into the corpus callosum and hippocampus of the rat brain: model development and parameter analysis. *Medical and Biological Engineering and Computing* **48** (2010), 203–214.

[92] Kunwar, S.; Prados, M. D.; Chang, S. M.; Berger, M. S.; Lang, F. F.; Piepmeier, J. M.; Sampson, J. H.; Ram, Z.; Gutin, P. H.; Gibbons, R. D.; Aldape, K. D.; Croteau, D. J.; Sherman, J. W. & Puri, R. K.: Direct intracerebral delivery of cintredekin besudotox (IL13-PE38QQR) in recurrent malignant glioma: a report by the cintredekin besudotox intraparenchymal study group. *Journal of Clinical Oncology* **25** (2007), 837–844.

[93] Laske, D. W.; Youle, R. J. & Oldfield, E. H.: Tumor regression with regional distribution of the targeted toxin TF-CRM107 in patients with malignant brain tumors. *Nature Medicine* **3** (1997), 1362–1368.

[94] Le Bihan, D.; Mangin, J.-F.; Poupon, C.; Clark, C. A.; Pappata, S.; Molko, N. & Chabriat, H.: Diffusion tensor imaging: Concepts and applications. *Journal of Magnetic Resonance Imaging* **13** (2001), 534–546.

[95] Lewin, R.: Is your brain really necessary? *Science* **210** (1980), 1232–1234.

[96] Linninger, A.; Gould, I.; Marinnan, T.; Hsu, C.-Y.; Chojecki, M. & Alaraj, A.: Cerebral microcirculation and oxygen tension in the human secondary cortex. *Annals of Biomedical Engineering* (2013), 1–21.

[97] Linninger, A. A.; Somayaji, M. R.; Erickson, T.; Guo, X. & Penn, R.: Computational methods for predicting drug transport in anisotropic and heterogeneous brain tissue. *Journal of Biomechanics* **41** (2008), 2176–2187.

[98] Linninger, A. A.; Somayaji, M. R.; Mekarsk, M. & Zhang, L.: Prediction of convection-enhanced drug delivery to the human brain. *Journal of Theoretical Biology* **250** (2008), 125–138.

[99] Linninger, A. A.; Somayaji, M. R.; Zhang, L.; Hariharan, M. S. & Penn, R. D.: Rigorous mathematical modeling techniques for optimal delivery of macromolecules to the brain. *IEEE Transactions on Biomedical Engineering* **55** (2008), 2303–2313.

[100] Lippert, H.: *Lehrbuch Anatomie*, 8th edn. Elsevier, München 2011.

[101] Liu, I.-S.: Method of Lagrange multipliers for exploitation of entropy principle. *Archive for Rational Mechanics and Analysis* **46** (1972), 131–148.

[102] Mabuma, J.; Markert, B. & Ehlers, W.: Towards a method for parameter estimation of articular cartilage and a staggered procedure for synovial fluid-cartilage interaction. *Proceedings in Applied Mathematics and Mechanics* **12** (2012), 129–130.

[103] Magdoom, K.; Pishko, G. L.; Hwan, K. J. & Sarntinoranont, M.: Evaluation of a voxelized model based on DCE-MRI for tracer transport in tumor. *Journal of Biomechanical Engineering* **134** (2012), 091004.

[104] Margulies, S. S. & Prange, M.: Regional, directional, and age-dependent properties of the brain undergoing large deformation. *Journal of Biomechanical Engineering* **124** (2002), 244–252.

[105] Markert, B.: *Porous Media Viscoelasticity with Application to Polymeric Foams.* Dissertation, Report No. II-12 of the Institute of Applied Mechanics (CE), University of Stuttgart 2005.

[106] Markert, B.: A constitutive approach to 3-d nonlinear fluid flow through finite deformable porous continua. *Transport in Porous Media* **70** (2007), 427–450.

[107] Markert, B.; Ehlers, W. & Karajan, N.: A general polyconvex strain-energy function for fiber-reinforced materials. *Proceedings in Applied Mathematics and Mechanics* **5** (2005), 245–246.

[108] Markert, B.; Heider, Y. & Ehlers, W.: Comparison of monolithic and splitting solution schemes for dynamic porous media problems. *International Journal for Numerical Methods in Engineering* **82** (2010), 1341–1383.

[109] Mehta, A. I.; Choi, B. D.; Raghavan, R.; Brady, M.; Friedman, A. H.; Bigner, D. D.; Pastan, I. & Sampson, J. H.: Imaging of convection enhanced delivery of toxins in humans. *Toxins* **3** (2011), 201–206.

[110] Miller, K.: Modelling soft tissue using biphasic theory – a word of caution. *Computer Methods in Biomechanics and Biomedical Engineering* **1** (1998), 261–263.

[111] Miller, K.: Method of testing very soft biological tissues in compression. *Journal of Biomechanics* **38** (2005), 153–158.

[112] Miller, K. & Chinzei, K.: Constitutive modelling of brain tissue: experiment and theory. *Journal of Biomechanics* **30** (1997), 1115–1121.

[113] Miller, K. & Chinzei, K.: Mechanical properties of brain tissue in tension. *Journal of Biomechanics* **35** (2002), 483–490.

[114] Mills, N.: Incompressible mixture of Newtonian fluids. *International Journal of Engineering Science* **4** (1966), 97–112.

[115] Morrison, P. F.; Chen, M. Y.; Chadwick, R. S.; Lonser, R. R. & Oldfield, E. H.: Focal delivery during direct infusion to brain: role of flow rate, catheter diameter, and tissue mechanics. *American Journal of Physiology - Regulatory, Integrative and Comparative Physiology* **277** (1999), 1218–1229.

[116] Morrison, P. F.; Laske, D. W.; Bobo, H.; Oldfield, E. H. & Dedrick, R. L.: High-flow microinfusion: tissue penetration and pharmacodynamics. *American Journal of Physiology* **266** (1994), 292–305.

[117] Muthupillai, R.; Lomas, D. J.; Rossman, P. J.; Greenleaf, J. F.; Manduca, A. & Ehman, R. L.: Magnetic resonance elastography by direct visualization of propagating acoustic strain waves. *Science* **269** (1995), 1854–1857.

[118] Nagashima, T.; Tamaki, N.; Matsumoto, S.; Horwitz, B. & Seguchi, Y.: Biomechanics of hydrocephalus: A new theoretical model. *Neurosurgery* **21** (1987), 898–903.

[119] Noll, W.: On the continuity of the solid and fluid states. *Journal of Rational Mechanics and Analysis* **4** (1955), 3–81.

[120] Noll, W.: A mathematical theory of the mechanical behavior of continous media. *Archives for Rational Mechanics and Analysis* **2** (1958), 197–226.

[121] Pardridge, W. M.: Physiologic-based strategies for protein drug delivery to the brain. *Journal of Controlled Release* **39** (1996), 281–286.

[122] Pierpaoli, C.; Jezzard, P.; Basser, P. J.; Barnett, A. & Di Chiro, G.: Diffusion tensor MR imaging of the human brain. *Radiology* **201** (1996), 637–648.

[123] Pishko, G.; Astary, G.; Mareci, T. & Sarntinoranont, M.: Sensitivity analysis of an image-based solid tumor computational model with heterogeneous vasculature and porosity. *Annals of Biomedical Engineering* **39** (2011), 2360–2373.

[124] Radermacher, A. & Reese, S.: Model reduction for complex continua – at the example of modeling soft tissue in the nasal area. In Markert, B. (ed.): *Advances in Extended and Multifield Theories for Continua*. Springer, Berlin 2011, pp. 197–217.

[125] Raghavan, R.; Brady, M. L.; Rodriguez-Ponce, M. I.; Hartlep, A.; Pedain, C. & Sampson, J. H.: Convection enhanced delivery of therapeutics for brain disease and its optimization. *Neurosurgical Focus* **20** (2006), E12.

[126] Rainov, N. G. & Heidecke, V.: Long term survival in a patient with recurrent malignantc glioma treated with intratumoral infusion of an IL4-targeted toxin (NBI-3001). *Journal of Neuro-Oncology* **66** (2004), 197–201.

[127] Rathakrishnan, E.: *Fundamentals of Engineering Thermodynamics*, 2nd edn. Prentice-Hall of India, New Delhi 2006.

[128] Rempler, H.-U.: *Visualisierung von Ergebnissen aus numerischen Berechnungen*. Diplomarbeit, Bericht Nr. 04-II-13 aus dem Institut für Mechanik (Bauwesen), Universität Stuttgart 2004.

[129] Rempler, H.-U.: *Damage in Multi-Phasic Materials Computed with the Extended Finite-Element Method*. Dissertation, Report No. II-23 of the Institute of Applied Mechanics (CE), Universität Stuttgart 2012.

[130] Ricken, T. & Bluhm, J.: Remodeling and growth of living tissue: a multiphase theory. *Archive of Applied Mechanics* **80** (2010), 453–465.

[131] Ricken, T. & de Boer, R.: Multiphase flow in a capillary porous medium. *Computational Materials Science* **28** (2003), 704–713.

[132] Ricken, T.; Dahmen, U. & Dirsch, O.: A biphasic model for sinusoidal liver perfusion remodeling after outflow obstruction. *Biomechanics and Modeling in Mechanobiology* **9** (2010), 435–450.

[133] Ricken, T.; Schwarz, A. & Bluhm, J.: A triphasic model of transversely isotropic biological tissue with applications to stress and biologically induced growth. *Computational Materials Science* **39** (2007), 124–136.

[134] Sampson, J. H.; Raghavan, R.; Brady, M. L.; Provenzale, J. M.; Herndon, J. E.; Croteau, D.; Friedman, A. H.; Reardon, D. A.; Coleman, R. E.; Wong, T.; Bigner, D. D.; Pastan, I.; Rodriguez-Ponce, M. I.; Tanner, P.; Puri, R. & Pedain, C.: Clinical utility of a patient-specific algorithm for simulating intracerebral drug infusions. *Neuro-Oncology* **9** (2007), 343–353.

[135] Sarntinoranont, M.; Chen, X.; Zhao, J. & Mareci, T. M.: Computational model of interstitial transport in the spinal cord using diffusion tensor imaging. *Annals of Biomedical Engineering* **34** (2006), 1304–1321.

[136] Schenke, M.: *Development of an interface between ABAQUS and PANDAS*. Master thesis, Report Nr. 08-II-12 of the Institute of Applied Mechanics (CE), University of Stuttgart 2008.

[137] Schenke, M. & Ehlers, W.: On the analysis of soils using an Abaqus-PANDAS interface. *Proceedings in Applied Mathematics and Mechanics* **11** (2011), 431–432.

[138] Schick, F.: Grundlagen der Magnetresonanztomographie (MRT). *Der Radiologe* **45** (2005), 69–88.

[139] Schlegel, U. & Wiestler, D.: *Gehirntumoren - Ein Ratgeber für Betroffene, Angehörige und Interessierte*. Deutsche Krebshilfe e. V. 2009.

[140] Scholz, B.: *Application of a Micropolar Model to the Localization Phenomena in Granular Materials: General Model, Sensitivity Analysis and Parameter Optimization*. Dissertation, Report No. II-15 of the Institute of Applied Mechanics (CE), University of Stuttgart 2007.

[141] Schröder, J.: *Theoretische und algorithmische Konzepte zur phänomenologischen Beschreibung anisotropen Materialverhaltens*. Dissertation, Bericht Nr. I-1 aus dem Institut für Mechanik (Bauwesen), Universität Stuttgart 1996.

[142] Schünke, M.; Schulte, E. & Schumacher, U.: *Prometheus: LernAtlas der Anatomie, Kopf und Neuroanatomie*. Georg Thieme Verlag, Stuttgart 2006.

[143] Schwarz, H. R.: *Methode der finiten Elemente*. Teubner, Stuttgart 1991.

[144] Shahar, T.; Ram, Z. & Kanner, A. A.: Convection-enhanced delivery catheter placements for high-grade gliomas: complications and pitfalls. *Journal of Neuro-Oncology* **107** (2012), 373–378.

[145] Sierra, R.: *Nonrigid Registration of Diffusion Tensor Images*. Master thesis, Swiss Federal Institute of Technology (ETHZ), Computer Vision Laboratory, Medical Image Analysis and Visualization Group, Zürich (2001).

[146] Sindhwani, N.; Ivanchenko, O.; Lueshen, E.; Prem, K. & Linninger, A. A.: Methods for determining agent concentration profiles in agarose gel during convection-enhanced delivery. *IEEE Transactions on Biomedical Engineering* **58** (2011), 626–632.

[147] Smith, J. H. & Humphrey, J. A.: Interstitial transport and transvascular fluid exchange during infusion into brain and tumor tissue. *Microvascular Research* **73** (2007), 58–73.

[148] Spencer, A. J. M.: Theory of Invariants. In Eringen, A. C. (ed.): *Continuum Physics, Vol. 1*. Academic Press, New York 1971, pp. 239–353.

[149] Spencer, A. J. M.: Constitutive theory for strongly anisotropic solids. In Spencer, A. J. M. (ed.): *Continuum Theory of the Mechanics of Fibre Reinforced Composites*. Springer-Verlag, Wien 1984, CISM Courses and Lectures No. 282, pp. 1–32.

[150] Stefan, J.: Über das Gleichgewicht und die Bewegung, insbesondere die Diffusion von Gasgemengen. *Sitzungsbericht Akademie der Wissenschaften (Wien), mathematisch-naturwissenschaftliche Klasse, Abteilung II* **63** (1871), 63–124.

[151] Støverud, K. H.: *Modeling Convection-Enhanced Delivery into Brain Tissue using Information from Magnetic Resonance Imaging*. Master thesis, Department of Earth Sciences, Utrecht University 2009.

[152] Støverud, K. H.; Darcis, M.; Helmig, R. & Hassanizadeh, S. M.: Modeling concentration distribution and deformation during convection-enhanced drug delivery into brain tissue. *Transport in Porous Media* **92** (2011), 119–143.

[153] Su, S.-W. & Payne, S. J.: A two phase model of oxygen transport in cerebral tissue. In *Annual International Conference of the Engineering in Medicine and Biology Society*, 2009, pp. 4921–4924.

[154] Syková, E. & Nicholson, C.: Diffusion in brain extracellular space. *Physiological reviews* **88** (2008), 1277–1340.

[155] Tada, Y. & Nagashima, T.: Modeling and simulation of brain lesions by the finite-element method. *Engineering in Medicine and Biology Magazine* **13** (1994), 497–503.

[156] Tamaraz, J. C. & Comair, Y. G.: *Atlas of Regional Anatomy of the Brain Using MRI*. Springer-Verlag, Berlin 2006.

[157] Taylor, Z. & Miller, K.: Reassessment of brain elasticity for analysis of biomechanics of hydocephalus. *Journal of Biomechanics* **37** (2004), 1263–1269.

[158] Truesdell, C.: *Rational Thermodynamics*, 2nd edn. Springer-Verlag, New York 1984.

[159] Truesdell, C. & Noll, W.: *The nonlinear field theories of mechanics, Vol. III/3*. Springer-Verlag, Berlin 1965.

[160] Truesdell, C. & Toupin, R. A.: The classical field theories. In Flügge, S. (ed.): *Handbuch der Physik, Vol. III/1*. Springer-Verlag, Berlin-Göttingen-Heidelberg 1960, pp. 226–902.

[161] Tuch, D. S.; Wedeen, V. J. & Dale, A. M.: Conductive tensor mapping of the human brain using diffusion tensor MRI. *Proceedings of the National Academy of Sciences USA* **98** (2001), 11697–11701.

[162] Vankan, W.; Huyghe, J.; Janssen, J. & Huson, A.: Poroelasticity of saturated solids with an application to blood perfusion. *International Journal of Engineering Science* **34** (1996), 1019–1031.

[163] Vankan, W.; Huyghe, J.; Janssen, J.; Huson, A.; Hacking, W. & Schreiner, W.: Finite element analysis of blood flow through biological tissue. *International Journal of Engineering Science* **35** (1997), 375–385.

[164] Vogelbaum, M. A.: Convection enhanced delivery for treating brain tumors and selected neurological disorders: symposium review. *Journal of Neuro-Oncology* **83** (2007), 97–109.

[165] Voges, J.; Reszka, R.; Gossmann, A.; Dittmar, C.; Richter, R.; Garlip, G.; Kracht, L.; Coenen, H. H.; Sturm, V.; Wienhard, K.; Heiss, W.-D. & Jacobs, A. H.: Imaging-guided convection-enhanced delivery and gene therapy of glioblastoma. *Annals of Neurology* **54** (2003), 479–487.

[166] Wagner, A.; Bleiler, C.; Stadelmann, V.; Windolf, M.; Gueorguiev-Rüegg, B.; Köstler, H.; Boger, A.; Röhrle, O. & Ehlers, W.: Porous-media simulation of bone-cement spreading during vertebroplasty. *Proceedings in Applied Mathematics and Mechanics* **13** (2013), 67–68.

[167] Wagner, A. & Ehlers, W.: A porous media model to describe the behaviour of brain tissue. *Proceedings in Applied Mathematics and Mechanics* **8** (2008), 10201–10202.

[168] Wagner, A. & Ehlers, W.: Continuum-mechanical analysis of human brain tissue. *Proceedings in Applied Mathematics and Mechanics* **10** (2010), 99–100.

[169] Wagner, A. & Ehlers, W.: Computational modelling of drug infusion into the anisotropic white-matter tracts of the human brain. *Proceedings in Applied Mathematics and Mechanics* **11** (2011), 133–134.

[170] Wagner, A. & Ehlers, W.: Multiphasic modelling of human brain tissue for intracranial drug-infusion studies. *Proceedings in Applied Mathematics and Mechanics* **12** (2012), 107–110.

[171] Wirth, B. & Sobey, I.: Analytic solution during an infusion test of the linear unsteady poroelastic equations in a spherically symmetric model of the brain. *Mathematical Medicine and Biology* **26** (2009), 25–61.

[172] Wirtz, D.; Karajan, N. & Haasdonk, B.: Model order reduction of multiscale models using kernel methods. *Preprint, University of Stuttgart, SRC SimTech* (2013).

[173] Zienkiewicz, O. C. & Taylor, R. L.: *The Finite Element Method*, 5th edn. Butterworth-Heinemann, Oxford 2000.

List of Figures

List of Tables

Curriculum Vitae

Personal data:

Name:	Arndt Wagner
Date of birth:	October 10, 1980
Place of birth:	Waiblingen, Germany
Nationality:	German
Parents:	Henry Wagner and Ingrid Wagner
Siblings:	Lutz Wagner and Heiko Wagner
Marital status:	married, with Sabine Wagner
Children:	one child, Jana Wagner

Education:

09/1987 – 06/1991	elementary school "Anne-Frank-Grundschule", Fellbach, Germany
09/1991 – 06/2000	secondary school "Gustav-Stresemann-Gymnasium", Fellbach, Germany
06/2000	degree: "Allgemeine Hochschulreife" (high school diploma)
10/2001 – 09/2006	studies in civil engineering at the University of Stuttgart, Germany major subject: "Konstruktiver Ingenieurbau"
09/2006	degree: "Diplom-Ingenieur (Dipl.-Ing.) Bauingenieurwesen"

Civilian service:

07/2000 – 05/2001	civilian service (agricultural activity), Winterbach, Germany

Professional occupation:

11/2006 – 09/2013	teaching assistant and research associate at the Institute of Applied Mechanics (Civil Engineering) at the University of Stuttgart, Germany
10/2013	nomination as "Akademischer Rat" at the Institute of Applied Mechanics (Civil Engineering) at the University of Stuttgart, Germany

Presently published contributions in this report series

II-1 Gernot Eipper: *Theorie und Numerik finiter elastischer Deformationen in fluidgesättigten porösen Festkörpern*, 1998.

II-2 Wolfram Volk: *Untersuchung des Lokalisierungsverhaltens mikropolarer poröser Medien mit Hilfe der Cosserat-Theorie*, 1999.

II-3 Peter Ellsiepen: *Zeit- und ortsadaptive Verfahren angewandt auf Mehrphasenprobleme poröser Medien*, 1999.

II-4 Stefan Diebels: *Mikropolare Zweiphasenmodelle: Formulierung auf der Basis der Theorie Poröser Medien*, 2000.

II-5 Dirk Mahnkopf: *Lokalisierung fluidgesättigter poröser Festkörper bei finiten elastoplastischen Deformationen*, 2000.

II-6 Heiner Müllerschön: *Spannungs-Verformungsverhalten granularer Materialien am Beispiel von Berliner Sand*, 2000.

II-7 Stefan Diebels (Ed.): *Zur Beschreibung komplexen Materialverhaltens: Beiträge anläßlich des 50. Geburtstages von Herrn Prof. Dr.-Ing. Wolfgang Ehlers*, 2001.

II-8 Jack Widjajakusuma: *Quantitative Prediction of Effective Material Parameters of Heterogeneous Materials*, 2002.

II-9 Alexander Droste: *Beschreibung und Anwendung eines elastisch-plastischen Materialmodells mit Schädigung für hochporöse Metallschäume*, 2002.

II-10 Peter Blome: *Ein Mehrphasen-Stoffmodell für Böden mit Übergang auf Interface-Gesetze*, 2003.

II-11 Martin Ammann: *Parallel Finite Element Simulations of Localization Phenomena in Porous Media*, 2005.

II-12 Bernd Markert: *Porous Media Viscoelasticity with Application to Polymeric Foams*, 2005.

II-13 Saeed Reza Ghadiani: *A Multiphasic Continuum Mechanical Model for Design Investigations of an Effusion-Cooled Rocket Thrust Chamber*, 2005.

II-14 Wolfgang Ehlers & Bernd Markert (Eds.): *Proceedings of the 1st GAMM Seminar on Continuum Biomechanics*, 2005.

II-15 Bernd Scholz: *Application of a Micropolar Model to the Localization Phenomena in Granular Materials: General Model, Sensitivity Analysis and Parameter Optimization*, 2007.

II-16 Wolfgang Ehlers & Nils Karajan (Eds.): *Proceedings of the 2nd GAMM Seminar on Continuum Biomechanics*, 2007.

II-17 Tobias Graf: *Multiphasic Flow Processes in Deformable Porous Media under Consideration of Fluid Phase Transitions*, 2008.

II-18 Ayhan Acartürk: *Simulation of Charged Hydrated Porous Materials*, 2009.

II-19 Nils Karajan: *An Extended Biphasic Description of the Inhomogeneous and Anisotropic Intervertebral Disc*, 2009.

II-20 Bernd Markert: *Weak or Strong – On Coupled Problems In Continuum Mechanics*, 2010.

II-21 Wolfgang Ehlers & Bernd Markert (Eds.): *Proceedings of the 3rd GAMM Seminar on Continuum Biomechanics*, 2012.

II-22 Wolfgang Ehlers: *Poröse Medien – ein kontinuumsmechanisches Modell auf der Basis der Mischungstheorie*, 2012. Nachdruck der Habilitationsschrift aus dem Jahr 1989 (Forschungsberichte aus dem Fachbereich Bauwesen der Universität-GH-Essen **47**, Essen 1989).

II-23 Hans-Uwe Rempler: *Damage in multi-phasic Materials Computed with the Extended Finite-Element Method*, 2012.

II-24 Irina Komarova: *Carbon-Dioxide Storage in the Subsurface: A Fully Coupled Analysis of Transport Phenomena and Solid Deformation*, 2012.

II-25 Yousef Heider: *Saturated Porous Media Dynamics with Application to Earthquake Engineering*, 2012.

II-26 Okan Avci: *Coupled Deformation and Flow Processes of Partial Saturated Soil: Experiments, Model Validation and Numerical Investigations*, 2013.

II-27 Arndt Wagner: *Extended Modelling of the Multiphasic Human Brain Tissue with Application to Drug-Infusion Processes*, 2014.